

# General Index

<b>Chapter 1 Introduction</b> .....	3
Production storage and transport of H <sub>2</sub> .....	4
Steam reforming.....	5
Ethanol steam reforming (ESR).....	9
Aim of the PhD thesis.....	13
<b>Chapter 2 Catalysts synthesis</b> .....	15
Flame Spray Pyrolysis (FSP).....	15
FSP recipes.....	17
Operatives parameters for the FSP synthesis (if not else specified).....	18
1) Al <sub>2</sub> O <sub>3</sub> .....	18
2) TiO <sub>2</sub> .....	18
3) La <sub>2</sub> O <sub>3</sub> .....	19
4) X wt % Ni/Al <sub>2</sub> O <sub>3</sub> (X= 5;10;15).....	19
5) X wt%Ni/TiO <sub>2</sub> (X= 5;10;15) .....	20
6) X wt% Ni/La <sub>2</sub> O <sub>3</sub> (X= 5;10;15) and LaNiO <sub>3</sub> .....	20
7) LaCoO <sub>3</sub> .....	21
8) 10%Ni/SiO <sub>2</sub> .....	21
9) 10%Co/SiO <sub>2</sub> .....	22
10) 10%Cu/SiO <sub>2</sub> .....	22
11) 10% Co/TiO <sub>2</sub> .....	23
12) 10% Cu/TiO <sub>2</sub> .....	23
13) Pt/CeO <sub>2</sub> .....	23
14) 10%Ni/ZrO <sub>2</sub> .....	24
15) La <sub>0.6</sub> Zr <sub>1.4</sub> O <sub>3</sub> /Ni10% .....	24
16) La <sub>0.8</sub> Sr <sub>0.2</sub> NiO <sub>3</sub> .....	25
17)La <sub>0.3</sub> Ce <sub>0.7</sub> NiO <sub>3</sub> .....	25
18) 10% Ni /La <sub>0.6</sub> Ce <sub>1.4</sub> O <sub>3</sub> .....	26
FSP support + deposition of active phase.....	27
1) X wt% Ni/Al <sub>2</sub> O <sub>3</sub> (X= 5;10;15).....	27
2) X wt% Ni/TiO <sub>2</sub> (X= 5;10;15) .....	27
3) X wt% Ni/La <sub>2</sub> O <sub>3</sub> (X= 5;10;15) .....	27
Catalysts prepared at UniVe .....	27

TiO <sub>2</sub> -based catalysts.....	27
SBA-15-based catalysts.....	28
ZrO <sub>2</sub> -based catalysts.....	28
Addition of the active phase.....	28
Samples table.....	31
<b>Chapter 3 Experimental methods.....</b>	<b>33</b>
Characterisation.....	33
Atomic absorption spectroscopy.....	33
X-ray Powder Diffraction (XRPD).....	33
Nitrogen physisorption .....	34
Scanning Electron microscopy/Transmission electron microscopy (SEM-TEM) .....	34
X-ray Photoelectron Spectroscopy XPS .....	34
Temperature programmed Reduction, Oxidation and Desorption (TPR-TPO- TPD).....	35
Chemisorption .....	35
Fourier Transform Infrared Spectroscopy (FT-IR) .....	36
Activity test.....	37
1st set up for ESR (Milan, IT).....	37
2nd set up for ESR tests (Belfast UK) .....	45
<b>Chapter 4 Results.....</b>	<b>48</b>
Atomic absorption spectroscopy.....	49
XRD.....	50
BET.....	64
SEM-TEM.....	73
XPS .....	81
TPR-TPO-TPD.....	82
Chemisorption .....	94
FT-IR.....	95
Activity test in Milan .....	122
Blank test.....	123
Group 1.....	123
Group 2.....	135
Group 3.....	142

Group 4.....	152
Activity test in Belfast :.....	156
<b>Chapter 5 Integrated energy co-generation device.....</b>	<b>167</b>
GH2-BE-500 unit .....	168
<b>Chapter 6: Conclusions.....</b>	<b>173</b>
Working temperature .....	173
Synthesis methods .....	173
Specific surface area.....	174
Metal reducibility.....	174
Active phase.....	175
Supports.....	175
Surface acidity.....	177
General conclusions .....	178
<b>Appendix 1 :proceedings and publications.....</b>	<b>179</b>
Proceedings:.....	179
Pubblications:.....	180
<b>Bibliography .....</b>	<b>181</b>

# Chapter 1 Introduction

There are several reasons why the research of alternative energy sources, different from fossil fuels, enhanced year per year. At first economic reasons, since energy demand is raising up also thanks to the industrial development of countries such as China and India. The availability of traditional fuels is gradually decreasing and the cost for extraction, of oil in particular, is increasing. Indeed deposits in very extreme conditions (i.e. deep sea deposits), in the past considered profitless, are now available. There are also very pressing environmental reasons, such as the worldwide policy for the control of CO<sub>2</sub> emissions (Kyoto protocol 1997) and the public opinion interest for the environment and the public health. Moreover, there are political reasons: most of the reserves of fossil fuels are located in countries that do not have a stable political situation and the supplies may not always be granted. Therefore many countries are promoting research on alternative sources of energy to become more independent from the energetic point of view.

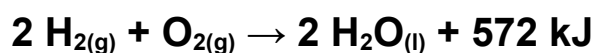
For all those reasons this new sources must be renewable and when they are used as fuels they should not produce any, or at least as few as possible, poisoning sub-products. Another key point is to reduce the net emission of CO<sub>2</sub> that is the main greenhouse gas produced by mankind activity. To be convenient from an economical point of view, they should be cheaper than fossil fuels that, despite all the problems cited above, are still the source of energy with the lowest cost/earnings ratio.

The field of these researches is very wide and deals with different disciplines such as chemistry, physics, biology.

Many of these researches are focused on the production of H<sub>2</sub> as energy vector. In the mid-1970s [1] for the first time the conception of a clean hydrogen energy system arose as a natural response of part of the scientific community to the impending environmental disaster, the dwindling of natural resources of fossil fuels (initially oil and gas), and on the world-wide energy crisis at that time.

Hydrogen is the lightest and most abundant chemical element, constituting roughly 75% of the Universe's chemical elemental mass, is very common on earth, but only in its compounds (H<sub>2</sub>O, minerals, hydrocarbons,...) not in its free bi-atomic molecular form H<sub>2</sub>. For this reason hydrogen couldn't be considered a source of energy

because energy should be spent to produce it, so it could be considered only a way to store energy as an energy vector. The use of hydrogen as energy vector is very interesting since its combustion/oxidation with O<sub>2</sub> is highly exothermic and the only product is water.



$$\Delta H_{\text{comb}} = -286 \text{ kJ/mol}$$

## **Production storage and transport of H<sub>2</sub>**

Even if the combustion of H<sub>2</sub> is carbon free we can not define the whole H<sub>2</sub> economy free from CO<sub>2</sub> emission especially the production step. Moreover to consider hydrogen a good energy vector its production should consume less energy than that obtained by the use of H<sub>2</sub> as fuel. Conventional hydrogen production methods and their shortcomings can be classified as follows [2-3]:

- 1) Water electrolysis: efficient, but it requires a great amount of electrical energy that is produced using oil, coal or nuclear power. It could be possible to produce the electricity required for the process using some renewable sources (wind, sun) but nowadays these sources are still site-specific and intermittent not suitable for a large scale continuous production of H<sub>2</sub>.
- 2) Water photolysis, under lab-scale development at present. The hydrogen production rate is still low due to quick electron/hole recombination in the bulk or on the surface of semiconductor particles, quick back reaction of oxygen and hydrogen to form water on the surface of the catalyst and poor use of visible light.
- 3) Thermal pyrolysis and reforming of organic compounds : these are the most common processes for H<sub>2</sub> production and they are carried out at high temperature. The reactants are mainly water and hydrocarbons (usually derived by oil, natural gas or coal), so they are not CO<sub>2</sub> neutral and renewable. The most used and well known of these methods are Steam reforming (SR) [4] and Partial Oxidation (Pox) [5]

- 4) Biological hydrogen production using processes such as the direct bio-photolysis, indirect bio-photolysis, biological water–gas shift reaction, photo-fermentation, and dark fermentation. However all these processes are still under laboratory development.

## Steam reforming

Currently the global annual production of H<sub>2</sub> is c-a 500 billion Nm<sup>3</sup>. 190 billion come from sub-products of chemical industry, while the greater portion is derived from fossil fuels, natural gas and heavy oil through the SR and POx processes.

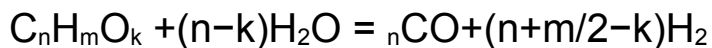
The first consumers of H<sub>2</sub> are the ammonia production plants, followed by the methanol manufacturers. Hydrogenation processes in petroleum refineries also require great amount of H<sub>2</sub>, that are raising since the demand for cleaner distillates has increased. Many other industries utilize hydrogen such as food and metallurgic industries, pure hydrogen chloride manufacturers. H<sub>2</sub> is also used liquid as fuel for rocket.

SR is a well know and commercialised reaction involving fossil fuels, most commonly CH<sub>4</sub> from natural gas, and water. The reaction is highly endothermic and is typically carried out at approximately 800°C over nickel-based catalyst packed into the tubes of a reforming furnace.

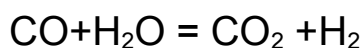
The general formula for the reaction is reported below:



$$\Delta H_{298K}^0 = +206 \text{ kJ/mol} \quad (n = 1, m = 4)$$



products of the reaction are CO and H<sub>2</sub>. The yield of H<sub>2</sub> is increased by the reaction of water gas shift (WGS) which extracts additional H<sub>2</sub> from water, oxidizing CO to CO<sub>2</sub>:



$$\Delta H_{298K}^0 = -41 \text{ kJ/mol}$$

This reaction is weakly exothermic, and so slightly inhibited at the high SR reaction temperature, but anyway it consumes part of the CO produced by SR and contributes to the total H<sub>2</sub> production. To minimize catalyst amount, hence reactor size, the water gas shift reaction can be carried out in two steps. The first one at 350–450 °C (HTS, High Temperature Shift) employs Fe/Cr catalysts and allows high reaction rate, but very high conversions cannot be obtained because of thermodynamic limitations. A second step at 200–250°C (LTS, Low Temperature Shift) on Cu/Zn based catalyst considerably increases CO conversion level. The water gas shift process is not sufficient to guarantee an adequate CO abatement in most cases (at LTS stage outlet CO concentration of 0.3%–1% can be reached), thus a further purification treatment is required to further reduce CO concentration when H<sub>2</sub> should be used in a PEM fuel cell. The heat required for SR is provided by the combustion of part of the hydrocarbon used for the H<sub>2</sub> production [6]. A simplified scheme of a typical set up for an industrial steam reforming reactor is reported in Figure 1

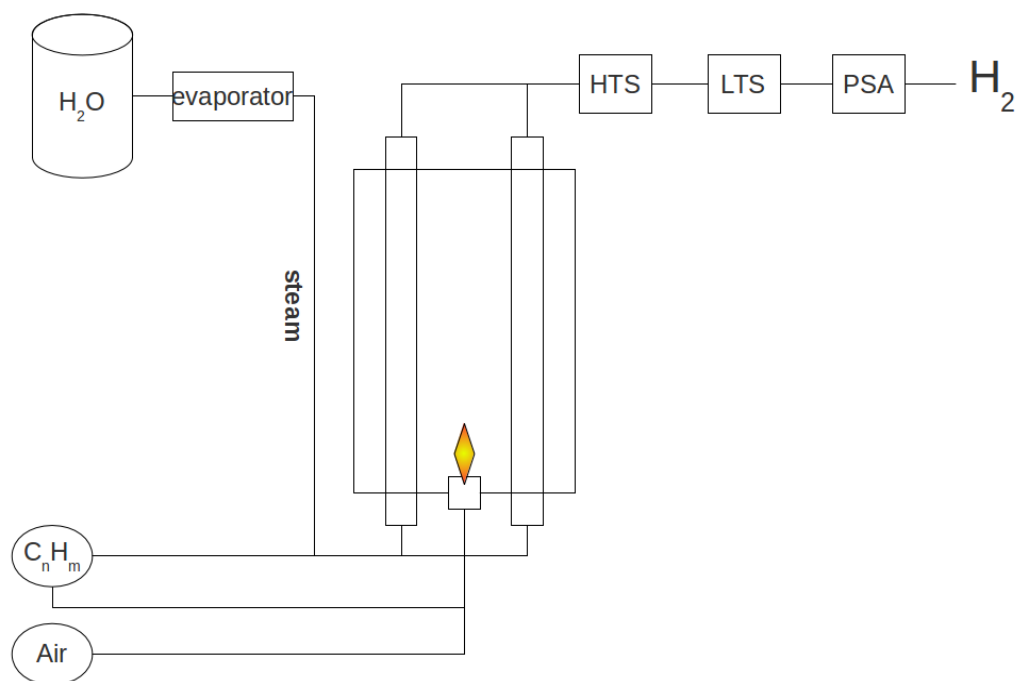


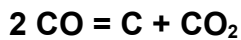
Figure 1: Typical scheme of industrial SR reactor

Because of the high temperature, hydrocarbons also undergo a complex series of cracking reaction generating carbon deposition on catalyst surface. It is widely accepted that hydrocarbons in the absence of air and water vapour can undergo decomposition above 650 °C according to the cracking reaction:



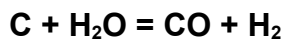
$$\mathbf{\Delta H^0_{298K} = +75 \text{ kJ/mol (n = 1, m = 4)}}$$

Another source of carbon formation is the CO disproportionation reaction (Boudouard equilibrium), which is catalysed by the same Ni catalyst used for SR



$$\mathbf{\Delta H^0_{298K} = -172 \text{ kJ/mol}}$$

As a consequence carbon filaments can rapidly grow attached on catalyst surface, giving rise to its fast deactivation and pressure drop increase. In order to reduce carbon deposition, an excess of steam can be added to the fuel stream. The main effect is reducing the partial pressure of CO in the gas stream by shifting water gas shift equilibrium towards CO<sub>2</sub> and H<sub>2</sub>. Besides, carbon can be consumed by the gasification reaction, which is also very fast:



$$\mathbf{\Delta H^0_{298K} = 131 \text{ kJ/mol}}$$

The tendency of hydrocarbons to produce coke increases with molecular weight and unsaturation. Therefore, the risk of producing carbon is higher when a mixture of liquid hydrocarbons such as gasoline or diesel fuel is used instead of methane. Regarding the formation of carbon oxides, it is important to notice that these compounds are not avoidable in the effluents of steam reforming.

Hot spots in the catalyst's reactor can allow the formation of coke too, so the catalysts are used packed in radiant tubes and inserted in a furnace (Figure 1). The pressure drop is typically around 2.8 kg/cm<sup>2</sup> and the temperature is very high. Thermal cycling is hard on the catalyst: when the tubes are heated, they expand and the catalyst tends to settle in the tube; then when the tube cools and the tubes contracts the catalyst is crushed. Due to this severe operation condition catalyst's support is an alumina ceramic that grants good mechanical and thermal stability, in addition, the catalyst is extruded in rings to increase the heat and mass transfer with the minimum allowable pressure drop.

The active phase usually is Ni, that is most cost effective than other more active metals. Supplied in form of Ni oxide, during the start up operation the catalyst is heated in a stream of inert gas. Near the normal operation temperature, hydrogen or a light hydrocarbon is added to reduce the nickel oxide to metallic nickel. The main poisons are sulphur and chlorides, which are present in small amounts in most feedstocks. Sulphur poisoning is theoretically reversible, and the catalyst can often



be restored to near full activity by steaming. However in practice the deactivation may cause catalyst overheating and coking making poisoning irreversible.

## **Ethanol steam reforming (ESR)**

To make carbon neutral the SR process, it is possible to use feedstocks derived from biomass. The latter could approach an almost 0 CO<sub>2</sub> balance, since the CO<sub>2</sub> produced by SR is reused in photosynthesis during biomass growth. Among all the feedstocks the most promising is ethanol.

Ethanol was first used as transport fuel in the 20 's when Henry Ford's Model T, called "Quadricycle", built in 1908, was fuelled with ethanol.

Ethanol has been used on a large scale as fuel since the early 20th century, particularly in Europe. In 1902 there was an exhibition in Paris dedicated to alcohol fuels (including cars, farm, machinery, lamps, stoves, heaters). To give an idea of the widespread use of fuel ethanol, in Germany alone more than 95,000 stoves and 37,000 spirit lamps were made in 1902; ethanol production increased from about 38 million litres (MI) in 1887 to 98.5 MI in 1904 [7].

Fuel ethanol played a key role in the first four decades of the 20th century. By the mid-1920s ethanol was widely blended with petrol in almost all industrial countries, except in the USA. In the Scandinavian countries 10-20 % blend was common and ethanol was mostly produced from paper mill waste. While in most of continental Europe ethanol was obtained from surplus grapes, potatoes, wheat, etc., in Australia, Brazil and many other countries, ethanol was produced from sugar cane juice and molasses.

In the USA, the combination of raising taxes, a concerted campaign by major oil producers and availability of cheap petrol effectively killed off ethanol as a major transport fuel in the early part of the 20<sup>th</sup> century. Ethanol achieved some prominence only during the Second World War, particularly in Brazil and in the USA due to fuel shortages. When the conflict was over, the availability of cheap oil effectively eclipsed the use of ethanol as fuel for nearly three decades in most countries. Contrariwise, in Brazil, due to the vital role of the sugar cane industry, government intervention was frequent as ethanol production was seen as an instrument of policy to achieve the rationalization of the sugar industry since the early 20<sup>th</sup> century [7].

Nowadays ethanol seems to be one of the most effective and immediate solution to partially replace oil-based fuels. Ethanol is a non toxic liquid easy to transport and store, since the current system for storage, transportation and utilization of fossil fuels could be adapted to ethanol with low investments. Despite all the benefits, 1<sup>st</sup> generation bio-ethanol was not without incongruities. At first it is derived from crops that are used as food and feed (corn, soy bean, etc..) and with the growing demand of bio-fuels around the world there is the fear that it will cause the price of the raw amtherial to rise tremendously. Since 1<sup>st</sup> generation ethanol is derived from crops, it is necessary to increase the surface for plantation causing the tropical forest destruction and this will jeopardize the environmental benefits of the ethanol production.

2<sup>nd</sup> generation bioethanol instead seem to be free of all those problems since it is derived from less expensive cellulosic biomass. Cellulose is an organic compound with the formula  $(C_6H_{10}O_5)_n$  and is one of the most common organic compound on earth. Nowadays it is mainly used for paper and paper board production.

Candidate biomass for 2<sup>nd</sup> generation ethanol production is constituted of waste material (from agriculture or municipal waste) or of some particular vegetables very rich in cellulose that have a very fast life cycle, which could live in areas not suitable for agriculture and that does not need forest destruction (marginals lands).

The use of cellulose for bio-fuel production is still under experimentation. E.g., on April 2011 near Tortona, Italy, Mossi &Ghisolfi group started the construction of the first 2<sup>nd</sup> generation bio-ethanol plant of the world. This plant will use as feedstock waste materials from the crops near its site (corn stalk, straw, rice straw), giant cane (*Arundo donax*) and biomass poplar that will be cultivated in unproductive land.

Because of the extreme dilution of the raw product ( $H_2O/C_2H_5OH$  molar ratio = 8.4 mol/mol) and the possible co-production of hardly separable toxic products, direct use of ethanol/water mixtures as fuel for internal combustion engines is not advisable at the present moment [8]. As an alternative to distillation and addition of additives to make the bio-ethanol suitable as fuel, the transformation trough SR into hydrogen seems to be a good way for the in situ production of clean  $H_2$ .

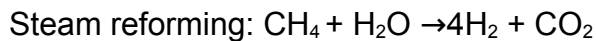
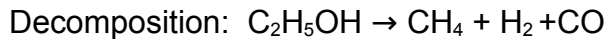
The whole reaction could be written in the following way:



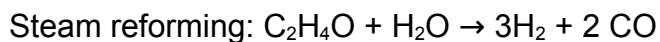
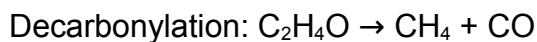
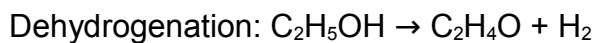
$$\Delta H^{\circ}_{298} = +347.4 \text{ kJ/mol}$$

Even if depending on the catalyst used, a lot of different reaction pathways could occur in a ESR reactor.

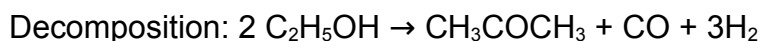
A possible pathway could start with the decomposition of ethanol followed by steam reforming of methane:



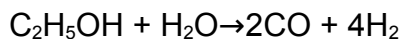
The H<sub>2</sub> production could also start with the ethanol dehydrogenation to acetaldehyde followed by decarbonylation or steam reforming of acetaldehyde:



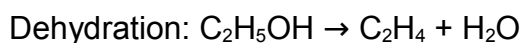
It is possible that the ethanol is also first decomposed into acetone and then reformed:



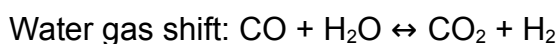
A fifth pathway of reaction starts with the simple steam reforming of ethanol to produce syngas:



Dehydration of ethanol to ethylene may occur, followed by C<sub>2</sub>H<sub>4</sub> polymerization generating coke.



Those alternatives [9] show how the ESR reaction looks simple, though, depending on the catalyst used and on the working conditions the pathways that lead to H<sub>2</sub> are very wide and different. Inside the ESR reactor other reactions take place [10]. As mentioned, water gas shift contributes to increasing in the yield of H<sub>2</sub> and to eliminate the CO present in the reactor.

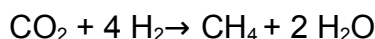
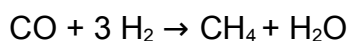


This reaction is slightly exothermic,  $\Delta H^{\circ}_{298} -41. \text{ kJ/mol}$  and to shift the equilibrium towards the H<sub>2</sub> production it necessary to lower the usual SR temperature (800°C).

Due to high temperature and to the nature of the metallic catalyst in some cases it is

also possible that methanation takes place consuming H<sub>2</sub>.

Methanation:



As for the SR of oil derived hydrocarbons some reactions inside the reactor could generate coke that accumulate over the surface of the catalyst causing its deactivation.



Therefore the choice of the catalyst plays a vital role in the construction of a plant for ESR, that's why there is a wide variety of studies on different active phases. In 2005 a review [10] gave a general overview of different metal catalysts for ESR (Table 1)

**Table 1: general overview of ESR catalysts [10].**

Catalysts	Research highlight	Ref.
MgO; Al <sub>2</sub> O <sub>3</sub> ; V <sub>2</sub> O <sub>5</sub> ; ZnO; TiO <sub>2</sub> ; La <sub>2</sub> O <sub>3</sub> ; CeO <sub>2</sub> ; Sm <sub>2</sub> O <sub>3</sub> ; La <sub>2</sub> O <sub>3</sub> -Al <sub>2</sub> O <sub>3</sub> ; CeO <sub>2</sub> -Al <sub>2</sub> O <sub>3</sub> ; MgO-Al <sub>2</sub> O <sub>3</sub>	Oxide Catalyst Group ZnO is the most promising catalyst. At 723 K, ZnO catalyst converts C <sub>2</sub> H <sub>5</sub> OH totally and produces H <sub>2</sub> with no CO. H <sub>2</sub> yield is 5.1 mol per mol of reacted C <sub>2</sub> H <sub>5</sub> OH.	11-13
Co/Al <sub>2</sub> O <sub>3</sub> ; Co/La <sub>2</sub> O <sub>3</sub> ; Co/SiO <sub>2</sub> ; Co/MgO; Co/ZrO <sub>2</sub> ; Co-ZnO; Co/TiO <sub>2</sub> , Co/V <sub>2</sub> O <sub>5</sub> , Co/CeO <sub>2</sub> ; Co/Sm <sub>2</sub> O <sub>3</sub> ; Co/CeO <sub>2</sub> -ZrO <sub>2</sub> ; Co/C	Co-oxide Catalyst Group Haga reported Co/Al <sub>2</sub> O <sub>3</sub> showed high selectivity by suppressing the methanation of CO and decomposition of C <sub>2</sub> H <sub>5</sub> OH. Llorca reported that Co/ZnO as the best for C <sub>2</sub> H <sub>5</sub> OH steam reforming. Co/ZnO catalyst produces 5.51 mol H <sub>2</sub> and 1.87 mol CO <sub>2</sub> , which converts to 92% of stoichiometrical coefficients	14-21
Ni/La <sub>2</sub> O <sub>3</sub> ; Ni/(La <sub>2</sub> O <sub>3</sub> - Al <sub>2</sub> O <sub>3</sub> ); Ni/Al <sub>2</sub> O <sub>3</sub> ; Ni/MgO; Ni-Cu/SiO <sub>2</sub> ; Ni-Cu/γ- Al <sub>2</sub> O <sub>3</sub> ; Ni-Cu-K/γ-Al <sub>2</sub> O <sub>3</sub>	Ni-oxide Catalyst Group Ni/Al <sub>2</sub> O <sub>3</sub> converted 100% C <sub>2</sub> H <sub>5</sub> OH and produced 70 vol % H <sub>2</sub> . At a temperature higher than 773K and steam to C <sub>2</sub> H <sub>5</sub> OH molar ratio 6:1, Ni/γAl <sub>2</sub> O <sub>3</sub> gave 5.2 mol H <sub>2</sub> with 91% H <sub>2</sub> selectivity. Ni/Al <sub>2</sub> O <sub>3</sub> deactivated because of coke formation. Ni/(La <sub>2</sub> O <sub>3</sub> -Al <sub>2</sub> O <sub>3</sub> ) showed good activity and stability. At temperatures of >600 °C, C <sub>2</sub> H <sub>5</sub> OH conversion was 100% and H <sub>2</sub> selectivity 95%, with CH <sub>4</sub> as the only undesirable product.	12,14,15,22-27

	However, a small deactivation was observed.	
Rh/TiO <sub>2</sub> ; Rh/SiO <sub>2</sub> ; Rh/CeO <sub>2</sub> ; Rh/ZrO <sub>2</sub> ; Rh/Al <sub>2</sub> O <sub>3</sub> ; Rh/MgO; Rh/Al <sub>2</sub> O <sub>3</sub> ; Rh/CeO <sub>2</sub> -ZrO <sub>2</sub> ; Rh-Au/CeO <sub>2</sub> ; Rh-Pt/CeO <sub>2</sub>	Rh-oxide Catalyst Group Rh/CeO <sub>2</sub> showed good performance for oxidative steam reforming with 100% activity and produced 5 mol H <sub>2</sub> . At high Rh loading, Rh/Al <sub>2</sub> O <sub>3</sub> was promising for C <sub>2</sub> H <sub>5</sub> OH steam reforming. H <sub>2</sub> yield was 5.5 mol (very close to the maximum stoichiometric coefficient of 6)	11,26, 28-31
Pd/CeO <sub>2</sub> ; Pt/CeO <sub>2</sub> ; Au/CeO <sub>2</sub> ; Pd/Al <sub>2</sub> O <sub>3</sub> ; Pt- Pd/CeO <sub>2</sub> ; Cu/Nb <sub>2</sub> O <sub>5</sub> - Al <sub>2</sub> O <sub>3</sub> ; Cu-Ni-Al-Zn; NiO- CeO <sub>2</sub> -ZrO <sub>2</sub> ; Pd/C; Rh(2,2'-bipyridyl) <sub>2</sub> Cl; Group VIII (Fe,Ru, Os) [Rh(bipy) <sub>2</sub> ]Cl	Other Catalyst Groups The performance of these catalysts were inferior compared to the aforementioned catalysts.	28, 32- 39

## Aim of the PhD thesis

My PhD project deals with ESR and its application for a small de-localized system for energy production. It is divided in two parts that were developed in parallel.

The first parts involved the investigation on a semi-commercial device (GH2-5000 Energy System provided by Helbio S.A) composed by a polymer electrolyte membrane fuel-cell (PEM) integrated in a steam reforming + H<sub>2</sub> purification system. The device has a nominal output of 5 kW electrical + 5kW thermal power. This system is designed to produce energy for civil de-localized uses, variable electricity and heat loads and discontinuous. Future applications of this device have driven the choice of a PEM fuel cell. This type of cell, although not characterised by the highest efficiency has two nice features : operation at low temperature, 80 °C, and prompt answer to large load variations [40]. However, it is very sensitive to CO poisoning, so is necessary to purify the reformat before supplying hydrogen to the FC.

A scheme of the part of this system investigated is presented in Figure 2:

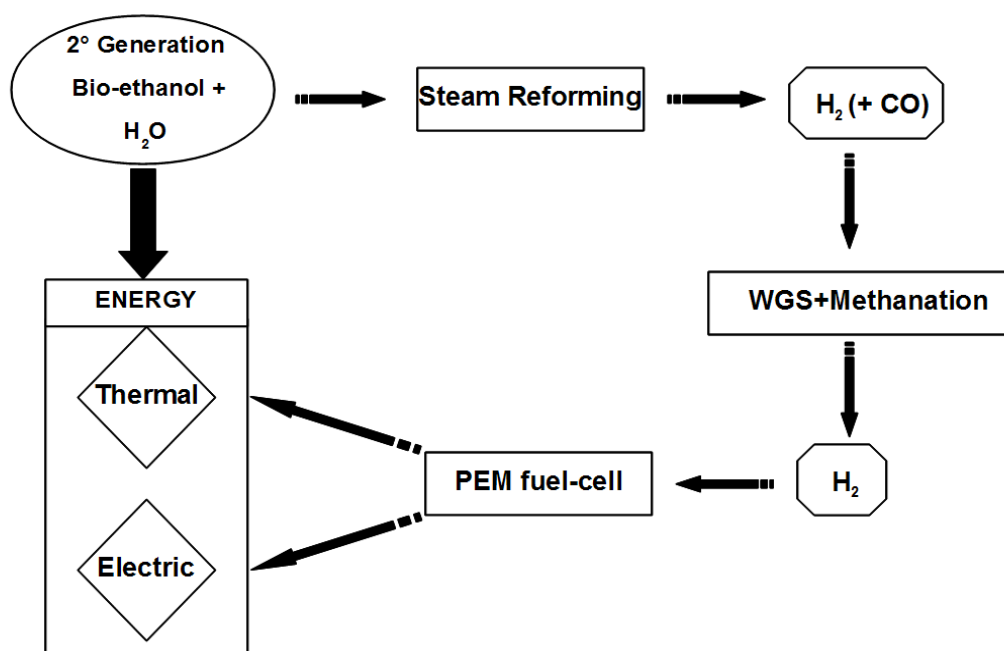


Figure 2 : Scheme of the integrated system

The second part of the project deals with the synthesis of catalysts for low temperature steam reforming of ethanol. Verykios et al. studied H<sub>2</sub> production by SR of bioethanol [41-43] at first focusing on Ni as active phase, loaded on different supports [41-42], then on supported noble metals [43]. The main issue was to reduce coke formation and to lower the reaction temperature. Other investigations on low temperature SR were carried out by Llorca et al. [44-45], using Co-based catalysts loaded in microreactors.

The strong interest in low temperature SR is due to the working temperature of the PEM fuel-cells that is ca. 80°C. Therefore, it is necessary to reduce the thermal gradient between the different process steps to obtain an efficient system (SR-PEMFC). Lowering the ESR working temperature (usually around 800°C) could give some advantages. First of all it is possible to reduce the thermal gradient between the different stages of the device and to increase the overall energetic balance. At lower temperature the equilibrium of WGS is shifted towards the products, this increases the amount of H<sub>2</sub> produced and consumes CO, making its elimination lighter in subsequent reactors. Different series of catalysts were synthesised with different methods and formulation. All of them were characterised and tested for ESR reaction under different operating conditions.

# Chapter 2 Catalysts synthesis

The main method used was Flame Spray Pyrolysis (FSP). This method was chosen because it produces metal oxides with features suitable for ESR: high thermal stability and high surface area [46-53].

To check the influence of the method of preparation on the catalytic performances, some catalysts were prepared also in other ways, e.g. at first preparing the support by FSP and then loading the active phase by impregnation, to be compared with direct preparation by FP.

Furthermore, in the frame of a collaboration between University of Milan (UniMi), University of Venice (UniVE) and University of Genoa (UniGe), a project started focused on the design, synthesis and characterization of heterogeneous catalysts for the steam reforming of ethanol and glycerol. Some of the samples were synthesised by FSP and compared with samples synthesised at UniVE by impregnation of the active metals on supports prepared in liquid phase.

## Flame Spray Pyrolysis (FSP)

This method allows to synthesize single and mixed oxides with a high phase purity. It is a one step synthesis, since at the same time the sample is synthesised and calcined.

Proper precursor salt of the elements constituting the oxide are dissolved in an organic solvent. The solution is fed, using a syringe pump, through a capillary needle to the centre of a vertical nozzle in the middle of a burner. The end of the needle is skirt by a coaxial flow of oxygen. This intense flow acts both as dispersing agent and as comburent for the organic fuel. The solution is dispersed in very small droplets and the mixture is ignited by twelve small flames that surround the nozzle. The main flame generated is characterised by a different temperature depending on the nature of the solvent [46,47],  $O_2$ /fuel ratio and on the different flow of the solution or of the gases. Inside the flame the droplets are instantly evaporated and the precursor is thermally decomposed (pyrolysis) generating the first oxide nuclei. Those nuclei grow

for coalescence and condensation. The nano particles generated at the beginning of the flame aggregate in the final part of the flame generating the final oxides powder (Fig.3).

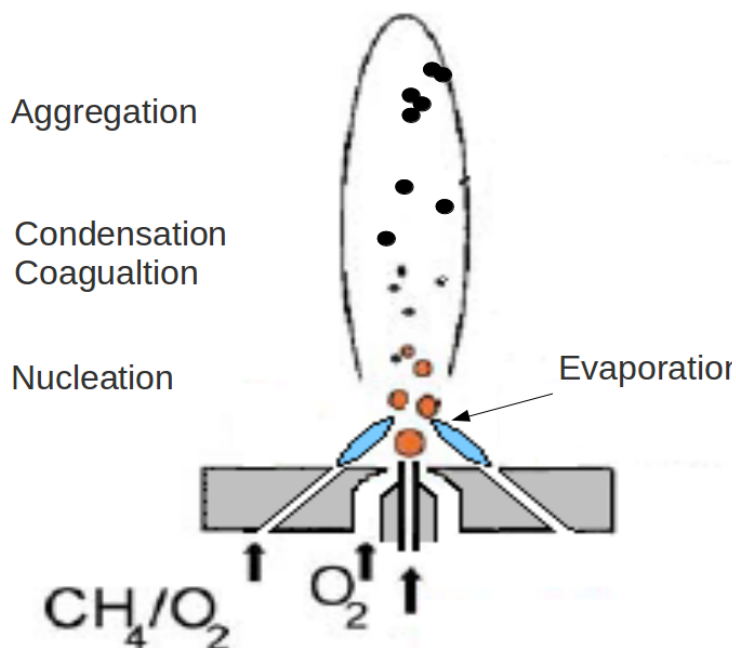


Figure 3: Formation, condensation and aggregation of the particles inside the flame

Three different factors influence the size of the particles : the time of flight inside the main flame, the temperature of the flame and the density of the particles inside the flame. If the temperature is too high, or if the particle spend too much time inside the flame or if there are too many particles inside it, the probability of particles sintering rise up, generating samples made of bigger particles and lower surface area.

This three phenomena could be controlled by properly setting the right operative parameters:

1. flow of the organic solution
2. concentration of the precursors solution
3. pressure drop at the nozzle
4. nature of the solvent
5. flow of  $\text{CH}_4/\text{O}_2$  for the small support flames
6. main flow of  $\text{O}_2$

All these parameters were optimized in previous investigations made in our laboratories [46-51] and all the conditions used in the recipes for each catalyst were the optimal ones.

In Figure 4 there is a schematic view of the FSP apparatus:



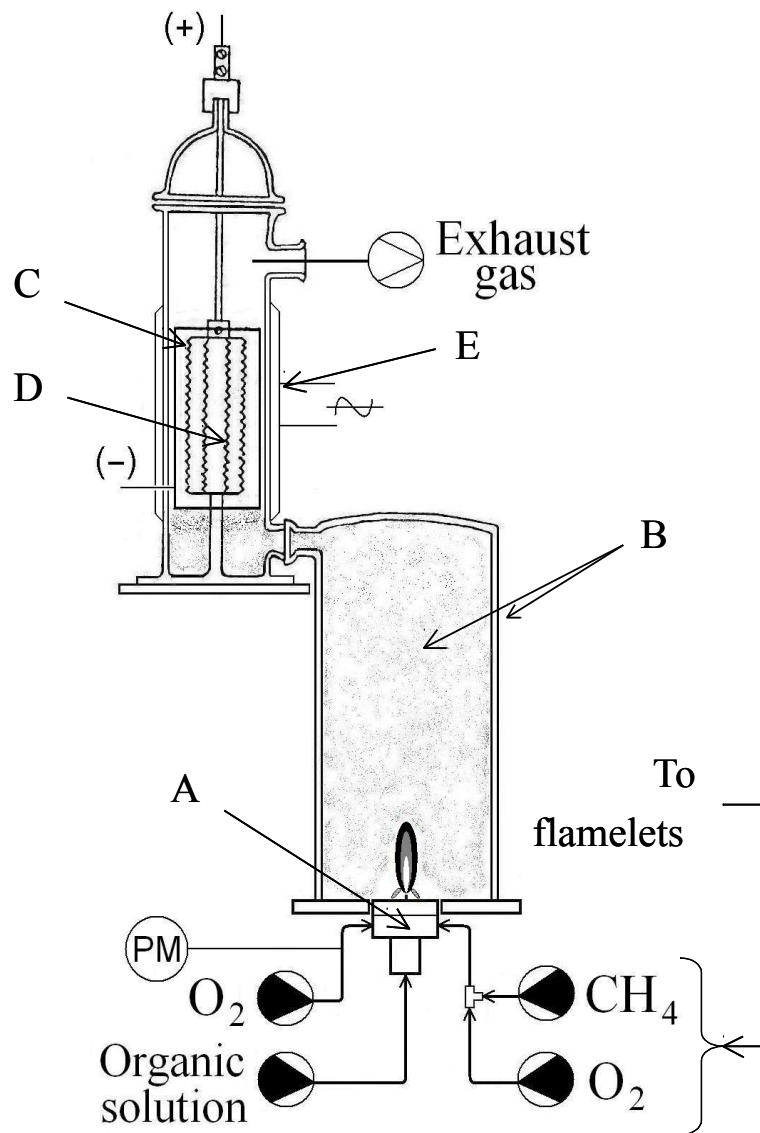


Figure 4: Schematic view of the FSP apparatus: the burner (A); the pyrex collector (B); the electrostatic precipitator (E) composed by the negative (C) and the positive poles (D)

## FSP recipes

Every solution of precursors must satisfy some features before it could be sprayed to the burner: it has to be clear with no particles in suspension, it has to be stable (no precipitation during the synthesis) and it should not possess high viscosity. All conditions prevent the blocking of the needle during synthesis causing damages to the experimental apparatus.

## Operatives parameters for the FSP synthesis (if not else specified)

Flow support flames: CH<sub>4</sub> 500 ml/min

O<sub>2</sub> 1000ml/min

O<sub>2</sub> main flow : 5.00 L/min

Syringe volume :50 ml

Syringe pump flow: 2.2 ml/min ( level 10)

Pressure drop at the nozzle : 1.5 bar

### 1) Al<sub>2</sub>O<sub>3</sub>

Precursor solution:

Precursor: Aluminum tri-sec-butoxide (Aldrich) 97%

Solvent: O-Xylene (Aldrich pur. 97%)

concentration of Al<sub>2</sub>O<sub>3</sub> in solution : 0.1 mmol/ml

To prepare the solution the Al precursor, which is a liquid with high viscosity, is disperse in Xylene

Notes: this preparation is quite tricky and requires a constant monitoring of the outlet of the needle, since during the combustion is it possible to form some carbon residual that could stop the flow of the main solution

### 2) TiO<sub>2</sub>

Precursor solution:

Precursor: Titanium isopropoxide Ti (IV) (C<sub>3</sub>H<sub>7</sub>O)<sub>4</sub> (Aldrich 97%)

Solvent: O-Xylene (Aldrich pur. 97%)

concentration of TiO<sub>2</sub> in solution : 0.1 mmol/ml

To prepare the solution the liquid Titanium precursor is dispersed in Xylene

### 3) $\text{La}_2\text{O}_3$

Precursor solution:

Precursor:	Lanthanum acetate La (III) $(\text{CH}_3\text{COO})_3 \cdot \text{H}_2\text{O}$ (Aldrich 99,9%, )
Solvent:	Propionic acid (Aldrich pur. 97%) O-Xylene (Aldrich pur. 97%)

concentration of  $\text{La}_2\text{O}_3$  in solution : 0.1 mmol/ml

To prepare the solution the Lanthanum precursor is dissolved in propionic acid. The solution must be heated till from pale white it becomes clear. After checking that there are no deposit xylene is added to the solution.

Propionic acid and xylene were in volume ratio 1:1 and the concentration of  $\text{La}_2\text{O}_3$  is calculated on the final volume

### 4) X wt % Ni/ $\text{Al}_2\text{O}_3$ (X= 5;10;15)

Precursor solution:

Precursor:	Aluminum tri-sec-butoxide (Aldrich) 97% Nickel acetate Ni(II) $(\text{CH}_3\text{CO}_2)_2 \cdot 4\text{H}_2\text{O}$ (Aldrich 98%)
Solvent:	Propionic acid (Aldrich pur. 97%) O-Xylene (Aldrich pur. 97%)

concentration of X%Ni/ $\text{Al}_2\text{O}_3$  in solution : 0.1 mmol/ml

To prepare the solution the aluminium precursor, is dispersed in xylene and the nickel precursor is dissolved in propionic acid. These two solutions have the same volume, so the ratio between propionic acid and xylene is 1:1. Before spraying in the burner the solutions were put in the same Becker and keep under vigorous stirring until they were uniformly mixed.

Notes: This preparation is not suitable for the flame because the precursor solution is not stable, when Propionic acid is added to Xylene the solution becomes very viscous and it is impossible to spray it in the flame.

### 5) X wt%Ni/TiO<sub>2</sub> (X= 5;10;15)

Precursor solution:

Precursor:	Titanium isopropoxide Ti (IV) (C <sub>3</sub> H <sub>7</sub> O) <sub>4</sub> (Aldrich 97%) Nickel acetate Ni(II) (CH <sub>3</sub> CO <sub>2</sub> ) <sub>2</sub> *4H <sub>2</sub> O (Aldrich 98%)
Solvent:	Propionic acid (Aldrich pur. 97%) O-Xylene (Aldrich pur. 97%)

concentration of X%Ni/TiO<sub>2</sub> in solution : 0.1 mmol/ml

To prepare the solution titanium isopropoxide, is dispersed in xylene and the nickel precursor is dissolved in propionic acid. These two solution have the same volume, so the ratio between propionic acid and xylene is 1:1. Before spraying in the burner the solutions were put in the same Becker and keep under vigorous stirring until they were uniformly mixed. The amount of Ni acetate was calculate time to time to obtain the right percentage of Ni inside the catalysts.

### 6) X wt% Ni/La<sub>2</sub>O<sub>3</sub> (X= 5;10;15) and LaNiO<sub>3</sub>

Precursor solution:

Precursor:	Lanthanum acetate La (III) (CH <sub>3</sub> COO) <sub>3</sub> *H <sub>2</sub> O (Aldrich 99,9%, ) Nickel acetate Ni(II) (CH <sub>3</sub> CO <sub>2</sub> ) <sub>2</sub> *4H <sub>2</sub> O (Aldrich 98%)
Solvent:	Propionic acid (Aldrich pur. 97%) O-Xylene (Aldrich pur. 97%)

concentration of X%Ni/La<sub>2</sub>O<sub>3</sub> in solution : 0.1 mmol/ml

To prepare the solution first lanthanum acetate is dissolved in propionic acid, the solution is heated till from pale white it becomes colourless. Then Ni acetate is added to the propionic solution. Before spraying the solution in the burner it is diluted 1:1 (vol/vol) with xylene. Concentration is referred to the final volume of the precursor solution in which xylene and propionic acid are in volume ratio 1:1. The amount of Ni acetate was calculated from time to time to obtain the right percentage of Ni inside the catalysts. For the perovskitic catalyst (LaNiO<sub>3</sub>) the precursors solution was prepared so as to obtain a molar ratio La/Ni=1.

Notes: Xylene in this preparation is used to increase the flame temperature since

none of the precursors could be dissolved in it. It is very important to dissolve first the La acetate and after the Ni acetate. Because the nickel precursor gives to the solution a green colour that makes hard the detection the presence of deposit of salt on the bottom of the becker.

## 7) LaCoO<sub>3</sub>

Precursor solution:

Precursor: Lanthanum acetate La (III) (CH<sub>3</sub>COO)<sub>3</sub> \*H<sub>2</sub>O (Aldrich 99,9%, )

Cobalt acetate Co(II) (CH<sub>3</sub>CO<sub>2</sub>)<sub>2</sub>\*4H<sub>2</sub>O (Fluka 99%)

Solvent: Propionic acid (Aldrich pur. 97%)

O-Xylene (Aldrich pur. 97%)

concentration of LaCoO<sub>3</sub> in solution : 0.1 mmol/ml

To prepare the solution first lanthanum acetate is dissolved in propionic acid, the solution is heated till from pale white it becomes colourless. Then cobalt acetate is added to the propionic solution. Before spraying the solution in the burner it is diluted 1:1 with xylene. Concentration of LaCoO<sub>3</sub> is referred to the final volume of the precursor solution in which xylene and propionic acid are in volume ratio 1:1. Precursors solution was prepared so as to obtain a molar ratio La/Co=1.

Notes: xylene in this preparation is used to increase the heat of the flame since none of the precursors could be dissolved in it. It is very important to dissolve first the lanthanum acetate and after the cobalt acetate. Indeed the cobalt precursor gives to the solution a dark purple colour that makes makes hard the detection of deposit of salt on the bottom of the becker.

## 8) 10%Ni/SiO<sub>2</sub>

Precursor solution:

Precursor: Nickel acetate Ni(II) (CH<sub>3</sub>CO<sub>2</sub>)<sub>2</sub>\*4H<sub>2</sub>O (Aldrich 98%)

Tetraethyl ortosilicate (TEOS) Si(OC<sub>2</sub>H<sub>5</sub>)<sub>4</sub> (Aldrich 98%)

Solvent: Propionic acid (Aldrich pur. 97%)

O-Xylene (Aldrich pur. 97%)

concentration of 10%Ni/SiO<sub>2</sub> in solution : 0.1 mmol/ml

To prepare the solution TEOS is dispersed in xylene and the nickel precursor is dissolved in propionic acid. These two solutions have the same volume, so the ratio between propionic acid and xylene is 1:1. Before spraying the solution in the burner they were mixed in the same beaker and kept under vigorous stirring until they became a uniform solution.

### 9) 10%Co/SiO<sub>2</sub>

Precursor solution:

Precursor:	Cobalt acetate Co(II) (CH <sub>3</sub> CO <sub>2</sub> ) <sub>2</sub> *4H <sub>2</sub> O (Fluka 99%) Tetraethyl ortosilicate (TEOS) Si(OC <sub>2</sub> H <sub>5</sub> ) <sub>4</sub> (Aldrich 98%)
Solvent:	Propionic acid (Aldrich pur. 97%) O-Xylene (Aldrich pur. 97%)

concentration of 10%Co/SiO<sub>2</sub> in solution : 0.1 mmol/ml

TEOS is diluted in xylene and the cobalt precursor is dissolved in propionic acid. These two solutions have the same volume, so the ratio between propionic acid and xylene is 1:1. Before spraying the solution in the burner the solutions were put in the same beaker and kept under vigorous stirring until they were uniformly mixed.

### 10) 10%Cu/SiO<sub>2</sub>

Precursor solution:

Precursor:	Copper acetate (II) (CH <sub>3</sub> CO <sub>2</sub> ) <sub>2</sub> *H <sub>2</sub> O (Ciba purissimum) Tetraethyl ortosilicate (TEOS) Si(OC <sub>2</sub> H <sub>5</sub> ) <sub>4</sub> (Aldrich 98%)
Solvent:	Propionic acid (Aldrich pur. 97%) O-Xylene (Aldrich pur. 97%)

concentration of 10%Cu/SiO<sub>2</sub> in solution : 0.1 mmol/ml

TEOS is diluted in xylene and the copper precursor is dissolved in propionic acid. These two solutions have the same volume, so the ratio between propionic acid and xylene is 1:1. Before spraying the solution in the burner the solutions were put in the same beaker and kept under vigorous stirring until they were uniformly mixed.

### 11) 10% Co/TiO<sub>2</sub>

Precursor solution:

Precursor:	Titanium isopropoxide Ti (IV) (C <sub>3</sub> H <sub>7</sub> O) <sub>4</sub> (Aldrich 97%) Cobalt acetate Co(II) (CH <sub>3</sub> CO <sub>2</sub> ) <sub>2</sub> *4H <sub>2</sub> O (Fluka 99%)
Solvent:	Propionic acid (Aldrich pur. 97%) O-Xylene (Aldrich pur. 97%)

concentration of 10%Co/TiO<sub>2</sub> in solution : 0.1 mmol/ml

To prepare the solution titanium isopropoxide, is dispersed in xylene and the cobalt precursor is dissolved in propionic acid. These two solutions have the same volume, so the ratio between propionic acid and xylene is 1:1. Before spraying the solution in the burner they were put in the same becker and kept under vigorous stirring until they became an uniform solution.

### 12) 10% Cu/TiO<sub>2</sub>

Precursor solution:

Precursor:	Titanium isopropoxide Ti (IV) (C <sub>3</sub> H <sub>7</sub> O) <sub>4</sub> (Aldrich 97%) Copper acetate (II) (CH <sub>3</sub> CO <sub>2</sub> ) <sub>2</sub> *H <sub>2</sub> O (Ciba purissimum)
Solvent:	Propionic acid (Aldrich pur. 97%) O-Xylene (Aldrich pur. 97%)

concentration of 10%Cu/TiO<sub>2</sub> in solution : 0.1 mmol/ml

To prepare the solution titanium isopropoxide, is dispersed in xylene and the copper precursor is dissolved in propionic acid. These two solution have the same volume, so the ratio between propionic acid and xyline is 1:1. Before spraying the solution in the burner they were put in the same becker and kept under vigorous stirring until they became an uniform solution.

### 13) Pt/CeO<sub>2</sub>

Precursor solution:

Precursor: :	Cerium acetate Ce (III) (CH <sub>3</sub> CO <sub>2</sub> ) <sub>3</sub> * H <sub>2</sub> O (Aldrich 99,9%) Platinum acetyl-acetonate Pt (II) (C <sub>5</sub> H <sub>7</sub> O <sub>2</sub> ) <sub>2</sub> (Aldrich 97%)
--------------	--

Solvent: Propionic acid (Aldrich pur. 97%)  
O-Xylene (Aldrich pur. 97%)

concentration of CeO<sub>2</sub> in solution : 0.1 mmol/ml

To prepare the solution first cerium acetate is dissolved in propionic acid, the solution is heated till the salt is dissolved. Platinum acetate is added to the propionic solution. Before spraying the precursors in the burner the solution is diluted 1:1 with xylene. Concentration of CeO<sub>2</sub> is referred to the final volume of the precursor solution in which xylene and propionic acid are in volume ratio 1:1.

#### **14) 10%Ni/ZrO<sub>2</sub>**

Precursor solution:

Precursor: Nickel acetate Ni(II) (CH<sub>3</sub>CO<sub>2</sub>)<sub>2</sub>\*4H<sub>2</sub>O (Aldrich 98%)  
Zirconium acetyl-acetonate Zr (CH<sub>3</sub>COCH<sub>3</sub>COO)  
(Aldrich +99%)  
Solvent: Propionic acid (Aldrich pur. 97%)  
O-Xylene (Aldrich pur. 97%)

concentration of 10%Ni/ZrO<sub>2</sub> in solution : 0.1 mmol/ml

First the zirconium precursor is dissolved in propionic acid, after the whole salt is dissolved and the solution looks clear nickel precursor is added and dissolved in the solution.

Before spraying the solution in the burner it is dilute 1:1 with xylene

#### **15) La<sub>0,6</sub>Zr<sub>1,4</sub>O<sub>3</sub> /Ni10%**

Precursor solution:

Precursor: Nickel acetate Ni(II) (CH<sub>3</sub>CO<sub>2</sub>)<sub>2</sub>\*4H<sub>2</sub>O (Aldrich 98%)  
Zirconium acetyl-acetonate Zr (CH<sub>3</sub>COCH<sub>3</sub>COO)  
(Aldrich +99%)  
Lanthanum acetate La (III) (CH<sub>3</sub>COO)<sub>3</sub> \*H<sub>2</sub>O  
(Aldrich 99,9%, )  
Solvent: Propionic acid (Aldrich pur. 97%)



O-Xylene (Aldrich pur. 97%)

concentration of 10%Ni/La<sub>0,6</sub>Zr<sub>1,4</sub>O<sub>3</sub> in solution : 0.1 mmol/ml

To prepare the solution first lanthanum acetate is dissolved in propionic acid, the solution is heated till from pale white it becomes colourless, after checking the whole salt is dissolved zirconium precursor is added to the solution, at the end when it is sure that the solution is clear the Ni precursor is added and dissolve. Before spray the solution in the burner it is dilute 1:1 with xylene. Concentration of 10%Ni/La<sub>0,6</sub>Zr<sub>1,4</sub>O<sub>3</sub> is referred to the final volume of the precursor solution in which xylene and propionic acid are in volume ratio 1:1. The amount of nickel acetate is calculated to obtain the right percentage in the catalyst.

### 16) La<sub>0,8</sub>Sr<sub>0,2</sub>NiO<sub>3</sub>

Precursor solution:

Precursor:	Nickel acetate Ni(II) (CH <sub>3</sub> CO <sub>2</sub> ) <sub>2</sub> *4H <sub>2</sub> O (Aldrich 98%)
	Strontium acetate Sr (II) (CH <sub>3</sub> CO <sub>2</sub> ) <sub>2</sub> (Aldrich )
	Lanthanum acetate La (III) (CH <sub>3</sub> COO) <sub>3</sub> *H <sub>2</sub> O (Aldrich 99,9%, )
Solvent:	Propionic acid (Aldrich pur. 97%)
	O-Xylene (Aldrich pur. 97%)

concentration of La<sub>0,8</sub>Sr<sub>0,2</sub>NiO<sub>3</sub> in solution : 0.1 mmol/ml

To prepare the solution first lanthanum acetate is dissolved in propionic acid, the solution is heated till from pale white it becomes colourless, after checking the whole salt is dissolved zirconium precursor is added to the solution, at the end when it is sure that the solution is clear the Ni precursor is added and dissolved. Before spraying the solution in the burner it is diluted 1:1 with xylene. Concentration of La<sub>0,8</sub>Sr<sub>0,2</sub>NiO<sub>3</sub> is referred to the final volume of the precursor solution in which xylene and propionic acid are in volume ratio 1:1.

### 17)La<sub>0,3</sub>Ce<sub>0,7</sub>NiO<sub>3</sub>

Precursor solution:

Precursor:	Nickel acetate Ni(II) (CH <sub>3</sub> CO <sub>2</sub> ) <sub>2</sub> *4H <sub>2</sub> O (Aldrich 98%)
------------	--

Cerium acetate Ce (III)  $(\text{CH}_3\text{CO}_2)_3 \cdot \text{H}_2\text{O}$  (Aldrich 99,9%)

Lanthanum acetate La (III)  $(\text{CH}_3\text{COO})_3 \cdot \text{H}_2\text{O}$

(Aldrich 99,9%, )

Solvent: Propionic acid (Aldrich pur. 97%)

O-Xylene (Aldrich pur. 97%)

concentration of  $\text{La}_{0.3}\text{Ce}_{0.7}\text{NiO}_3$  in solution : 0.1 mmol/ml

To prepare the solution first lanthanum acetate is dissolved in propionic acid, the solution is heated till from pale white it becomes colourless, after checking the whole salt is dissolved cerium precursor is added to the solution, at the end when it is sure that the solution is clear the Ni precursor is added and dissolved. Before spraying the solution in the burner it is diluted 1:1 with xylene. Concentration of  $\text{La}_{0.3}\text{Ce}_{0.7}\text{NiO}_3$  is referred to the final volume of the precursor solution in which xylene and propionic acid are in volume ratio 1:1.

### **18) 10% Ni / $\text{La}_{0.6}\text{Ce}_{1.4}\text{O}_3$**

Precursor solution:

Precursor: Nickel acetate Ni(II)  $(\text{CH}_3\text{CO}_2)_2 \cdot 4\text{H}_2\text{O}$  (Aldrich 98%)

Cerium acetate Ce (III)  $(\text{CH}_3\text{CO}_2)_3 \cdot \text{H}_2\text{O}$  (Aldrich 99,9%)

Lanthanum acetate La (III)  $(\text{CH}_3\text{COO})_3 \cdot \text{H}_2\text{O}$

(Aldrich 99,9%, )

Solvent: Propionic acid (Aldrich pur. 97%)

O-Xylene (Aldrich pur. 97%)

concentration of 10%Ni/  $\text{La}_{0.6}\text{Ce}_{1.4}\text{O}_3$  in solution : 0.1 mmol/ml

To prepare the solution first lanthanum acetate is dissolved in propionic acid, the solution is heated till from pale white it becomes colourless, after checking the whole salt is dissolved cerium precursor is added to the solution, at the end when it is sure that the solution is clear the Ni precursor is added and dissolved. Before spraying the solution in the burner it is diluted 1:1 with xylene. Concentration of 10%Ni/  $\text{La}_{0.6}\text{Ce}_{1.4}\text{O}_3$  is referred to the final volume of the precursor solution in which xylene and propionic acid are in volume ratio 1:1. The amount of nickel acetate is calculated to obtain the right percentage in the catalyst.

## FSP support + deposition of active phase

Some catalysts were prepared by impregnation of the Ni on FSP made supports (recipes 1;2;3). The method of preparation was the same for all the three series of catalysts. A proper amount of  $\text{Ni}(\text{NO}_3)_2 \cdot 6\text{H}_2\text{O}$  was dissolved in 100ml of distilled water. After the salt was completely dissolved 3.7 g of FSP oxide were put in the solution and water was evaporated under vigorous magnetic stirring. The sample was dried in an oven at 200°C for one night. Calcination of the sample was carried out in the reactor during the activation procedure.

### 1) X wt% Ni/ $\text{Al}_2\text{O}_3$ (X= 5;10;15)

- $\text{Al}_2\text{O}_3$  FSP made (recipe1)
- $\text{Ni}(\text{NO}_3)_2 \cdot 6\text{H}_2\text{O}$  (Merck)
- $\text{H}_2\text{O}$  distilled

### 2) X wt% Ni/ $\text{TiO}_2$ (X= 5;10;15)

- $\text{TiO}_2$  FSP made (recipe2)
- $\text{Ni}(\text{NO}_3)_2 \cdot 6\text{H}_2\text{O}$  (Merck)
- $\text{H}_2\text{O}$  distilled

### 3) X wt% Ni/ $\text{La}_2\text{O}_3$ (X= 5;10;15)

- $\text{La}_2\text{O}_3$  FSP made (recipe 3)
- $\text{Ni}(\text{NO}_3)_2 \cdot 6\text{H}_2\text{O}$  (Merck)
- $\text{H}_2\text{O}$  distilled

## ***Catalysts prepared at UniVe***

### **TiO<sub>2</sub>-based catalysts**

$\text{TiO}_2$  was prepared through a conventional precipitation method.

20 g of  $\text{TiOSO}_4 \cdot x\text{H}_2\text{SO}_4 \cdot x\text{H}_2\text{O}$  (Aldrich, purity synthesis grade) were dissolved in 300 mL of distilled water at room temperature, then NaOH (Carlo Erba, 9 M) or  $\text{NH}_3$

(*Riedel-de Haën*, 9 M) was added dropwise until the system reached a pH of 5.5.

The precipitate was aged at 60°C for 20 hours, then repeatedly washed with distilled water and finally dried overnight at 110°C.

The samples were named **TxCy-Me**, where T refers to the TiO<sub>2</sub> carrier, x is a series number progressively assigned, y represents the calcination temperature, and Me the metal used as active phase.

### **SBA-15-based catalysts**

8 g of Pluronic 123 (P123, *Aldrich*) were dissolved in an aqueous solution of HCl (*Sigma - Aldrich*) at 45°C, then the silica precursor (TEOS, *Aldrich*) was added dropwise. The system was aged at 45°C for 20 hours, then aged at 100°C for 48 hours in a hermetically sealed vessel.

The solid was extensively washed with distilled water and dried at room temperature for several days, then calcined at 500°C or 800°C for 6 hours.

Catalysts were named **SxCy-Me**, where S refers to the SBA-15 carrier, x is a series number progressively assigned, y represents the calcination temperature and Me the metal used as active phase.

### **ZrO<sub>2</sub>-based catalysts**

ZrO<sub>2</sub> was prepared by a conventional precipitation method.

A solution of 26 g of ZrOCl<sub>2</sub>·8 H<sub>2</sub>O (Fluka, purity ≥99%) in 100 mL of distilled water was added with a peristaltic pump under vigorous stirring to an ammonia solution. During the entire course of the precipitation, the pH value was kept constant at 10.0 by the continuous addition of a 33% ammonia solution (*Riedel-de Haën*). After the complete addition of the salt solution, the hydroxide suspension was aged for 20 h at 90°C. The aged hydroxide was filtered and washed with warm distilled water until it was free from chloride ions (AgNO<sub>3</sub> test), then dried overnight at 110°C.

Catalysts were named **ZxCy-Me**, where Z refers to the ZrO<sub>2</sub> carrier, x is a series number progressively assigned, y represents the calcination temperature and Me the metal used as active phase.

### **Addition of the active phase**

The active phase was added to each support by incipient wetness impregnation with

an aqueous solution of the metallic precursors  $\text{Ni}(\text{NO}_3)_2 \cdot 6\text{H}_2\text{O}$ ,  $\text{Co}(\text{NO}_3)_2 \cdot 6\text{H}_2\text{O}$  or  $\text{Cu}(\text{NO}_3)_2 \cdot 3\text{H}_2\text{O}$  and in the proper concentration in order to obtain the desired Me loading (10 wt%). The catalyst was dried overnight at 110°C and then calcined at 500°C or 800°C ( $\text{TiO}_2$ , SBA-15) for 4 hours.

In Table 2 there is a synoptic overview of all the catalysts. The last column contains the metal loading as detected by atomic absorption.

**Table 2 : overview of recipes and real metal loadings of all UniVe samples**

NI-BASED CATALYSTS	<i>Support:</i> $\text{TiO}_2$	<b>T1C500 - Ni</b>	$\text{TiO}_2$ prepared by precipitation with NaOH, calcined at 500°C; actual concentration of Ni 7.8 wt %.	
		<b>T2C500 - Ni</b>	$\text{TiO}_2$ prepared by precipitation with $\text{NH}_3$ , calcined at 500°C; actual concentration of Ni 7.5 wt %.	
		<b>T4C800 - Ni</b>	$\text{TiO}_2$ prepared by precipitation with NaOH, calcined at 800°C; actual concentration of Ni 6.7 wt %.	
		<b>T3C800 - Ni</b>	$\text{TiO}_2$ prepared by precipitation with $\text{NH}_3$ , calcined at 800°C; actual concentration of Ni 7.3 wt %.	
	<i>Support:</i> SBA-15	<b>S1C500 - Ni</b>	SBA-15 calcined at 500°C; actual concentration of Ni 9.2 wt %.	
		<b>S2C800 - Ni</b>	SBA-15 calcined at 800°C; actual concentration of Ni 8.9 wt %.	
	<i>Support:</i> $\text{ZrO}_2$	<b>Z1C500 - Ni</b>	$\text{ZrO}_2$ prepared by precipitation with $\text{NH}_3$ , calcined at 500°C; actual concentration of Ni 9.7 wt %.	
		<b>Z2C800 - Ni</b>	$\text{ZrO}_2$ prepared by precipitation with $\text{NH}_3$ , calcined at 500°C; actual concentration of Ni 9.7 wt %.	
	CO-BASED CATALYSTS	<i>Support:</i> $\text{TiO}_2$	<b>T6C500 - Co</b>	$\text{TiO}_2$ prepared by precipitation with $\text{NH}_3$ , impregnated by incipient wetness with $\text{Co}(\text{NO}_3)_2 \cdot 6\text{H}_2\text{O}$ , calcined at 500°C; Co loading 6.6wt%.

		<b>T8C500 - Co</b>	TiO <sub>2</sub> prepared by precipitation with NaOH, impregnated by incipient wetness with Co(NO <sub>3</sub> ) <sub>2</sub> *6H <sub>2</sub> O, calcined at 500°C; Co loading 9.6wt%.
	<i>Support:</i> <i>SBA-15</i>	<b>S4C500 - Co</b>	SBA-15 calcined at 500°C; impregnated by incipient wetness with Co(NO <sub>3</sub> ) <sub>2</sub> *6H <sub>2</sub> O and further calcined at 500°C; Co loading 7.8wt%.
CU-BASED CATALYSTS	<i>Support:</i> <i>TiO<sub>2</sub></i>	<b>T9C500 - Cu</b>	TiO <sub>2</sub> prepared by precipitation with NH <sub>3</sub> , impregnated by incipient wetness with Cu(NO <sub>3</sub> ) <sub>2</sub> *3H <sub>2</sub> O, calcined at 500°C; Cu loading 5.6wt%.
		<b>T11C500-Cu</b>	TiO <sub>2</sub> prepared by precipitation with NaOH, impregnated by incipient wetness with Cu(NO <sub>3</sub> ) <sub>2</sub> *3H <sub>2</sub> O, calcined at 500°C; Cu loading 5.6wt%.
	<i>Support:</i> <i>SBA-15</i>	<b>S3C500-Cu</b>	SBA-15 calcined at 500°C; impregnated by incipient wetness with Cu(NO <sub>3</sub> ) <sub>2</sub> *3H <sub>2</sub> O, and further calcined at 500°C; Cu loading 6.8wt%.

## Samples table

**Table 3 : complete overview of all the samples name, composition and synthesis method**

Name	Formula	Synthesis method
DAL8p0	Al <sub>2</sub> O <sub>3</sub>	FSP
DTi0	TiO <sub>2</sub>	FSP
LAD0	La <sub>2</sub> O <sub>3</sub>	FSP
DAL8p2	10% Ni /Al <sub>2</sub> O <sub>3</sub>	Support made by FSP , Ni added by impregnation
DTi1	5% Ni /TiO <sub>2</sub>	Support made by FSP , Ni added by impregnation
DTi2	10% Ni /TiO <sub>2</sub>	Support made by FSP , Ni added by impregnation
DTi3	15% Ni /TiO <sub>2</sub>	Support made by FSP , Ni added by impregnation
FTi1	5% Ni /TiO <sub>2</sub>	FSP
FTi2	10% Ni /TiO <sub>2</sub>	FSP
FTi3	15% Ni /TiO <sub>2</sub>	FSP
LAD1	5% Ni /La <sub>2</sub> O <sub>3</sub>	Support made by FSP , Ni added by impregnation
LAD2	10% Ni /La <sub>2</sub> O <sub>3</sub>	Support made by FSP , Ni added by impregnation
LAD3	15% Ni /La <sub>2</sub> O <sub>3</sub>	Support made by FSP , Ni addde by impregnation
FLA1	5% Ni /La <sub>2</sub> O <sub>3</sub>	FSP
FLA2	10% Ni /La <sub>2</sub> O <sub>3</sub>	FSP
FLA3	15% Ni /La <sub>2</sub> O <sub>3</sub>	FSP
DPLN	LaNiO <sub>3</sub>	FSP
FLC	LaCoO <sub>3</sub>	FSP
MC12	10.9% Co /TiO <sub>2</sub>	FSP
MC13	8.3% Cu /TiO <sub>2</sub>	FSP
MC10	9.6% Ni /SiO <sub>2</sub>	FSP
MC11	8.7% Co /SiO <sub>2</sub>	FSP
MC14	9.2% Cu /SiO <sub>2</sub>	FSP
MC15	8.8% Ni /ZrO <sub>3</sub>	FSP
T1C500	7.8%Ni/TiO <sub>2</sub>	Incipient wetness impregnation+ calcination 500°C
T2C500	7.5%Ni/TiO <sub>2</sub>	Incipient wetness impregnation+ calcination 500°C
T3C800	7.3%Ni/TiO <sub>2</sub>	Incipient wetness impregnation+ calcination 800°C
T4C800	6.7%Ni/TiO <sub>2</sub>	Incipient wetness impregnation+ calcination 800°C
T6C500	6.6%Co/TiO <sub>2</sub>	Incipient wetness impregnation+ calcination 500°C

T8C500	9.6%Co/TiO <sub>2</sub>	Incipient wetness impregnation+ calcination 500°C
T9C500	5.6%Cu/TiO <sub>2</sub>	Incipient wetness impregnation+ calcination 500°C
T11C500	5.6%Cu/TiO <sub>2</sub>	Incipient wetness impregnation+ calcination 500°C
S1C500	9.2%Ni/SiO <sub>2</sub>	Incipient wetness impregnation+ calcination 500°C
S2C800	8.9%Ni/SiO <sub>2</sub>	Incipient wetness impregnation+ calcination 800°C
S3C500	6.7%Ni/TiO <sub>2</sub>	Incipient wetness impregnation+ calcination 500°C
S4C500	7.8%Co/SiO <sub>2</sub>	Incipient wetness impregnation+ calcination 500°C
Z1C500	9.7%Ni/ZrO <sub>2</sub>	Incipient wetness impregnation+ calcination 500°C
Z2C800	8.8%Ni/ZrO <sub>2</sub>	Incipient wetness impregnation+ calcination 800°C
MC2	10% Ni/La <sub>0.6</sub> Zr <sub>1.4</sub> O <sub>3</sub>	FSP
MC3	La <sub>0.8</sub> Sr <sub>0.2</sub> NiO <sub>3</sub>	FSP
MC5	LaCeNiO <sub>3</sub>	FSP
MC6	10% Ni/La <sub>0.6</sub> Ce <sub>1.4</sub> O <sub>3</sub>	FSP
MC8	3%Pt/Ce <sub>2</sub> O <sub>3</sub>	FSP



# Chapter 3 Experimental methods

## Characterisation

In this paragraph I will illustrate all the techniques used to characterise the different samples tested in this PhD project.

### Atomic absorption spectroscopy

In order to evaluate the real metal concentration in the catalysts, atomic absorption spectroscopy measurements were carried out on a Perkin Elemer AAnalysis instrument after dissolution of each sample.

### X-ray Powder Diffraction (XRPD)

It is a non-destructive technique used to characterise the crystallographic structure, crystallite size and preferred orientation in polycrystalline or powdered solid samples. It is used to identify unknown phases or, as in this case, to confirm the structure of a laboratory made sample, by comparing diffraction data with a database maintained by the International Centre for Diffraction Data. It is also possible to determine the size of the crystallites using the Scherrer Equation. In most of the cases XRPD analyses were here made on the as prepared catalysts, though in some cases the analysis was performed after a pretreatment of 1h at 800°C in a 20vol% H<sub>2</sub> in N<sub>2</sub> gas flow to check the catalysts structure after activation.

XRPD analysis has been carried out by means of 3 different instruments:

- 1) Philips PW3020 powder diffractometer, by selecting the Ni-filtered Cu K<sub>α</sub> radiation ( $\lambda = 0.15148$  nm) and using a monochromator on the diffracted beam.
- 2) Bruker D8 Advance diffractometer equipped with a Si(Li) solid state detector (SOL-X) and a sealed tube providing the Cu K<sub>α</sub> radiation
- 3) PANanalytical X'PERT PRO

The diffractograms have been compared with literature data for phase recognition [54]

### **Nitrogen physisorption**

Specific surface area and pore size distribution were evaluated through the collection of N<sub>2</sub> adsorption-desorption isotherms at 77K. Surface area was calculated on the basis of the Brunauer, Emmet and Teller equation (BET), whereas the pores size distribution was determined by the BJH method, applied to the N<sub>2</sub> desorption branch of the isotherm.

Two instruments were used for this analysis, a MICROMERITICS ASAP 2010 instrument, and prior the analysis sample was outgassed at 300°C for 4/8h; MICROMERITICS, ASAP 2000 Analyser, and prior to the analysis the sample was dried overnight at 110°C and then outgassed at 110°C for 2 hours.

### **Scanning Electron microscopy/Transmission electron microscopy (SEM-TEM)**

SEM and TEM analysis were carried out at the University of Perugia. A scanning electron microscope (SEM) images a sample by scanning it with a high-energy beam of electrons in a raster scan pattern. The electrons interact with the atoms with an energy range between 5-50 kV. Electrons are reflected or emitted. Reflected beams are collected and conveyed to a cathode ray tube, in which there is a beam of electron synchronized with it. This produces a high resolution image of the surface of the catalyst. An Energy-dispersive X-ray spectroscope (EDX) is coupled to the SEM microscope. This technique is used for the elemental analysis or chemical characterization of a sample. In transmission electron microscopy instead a beam of electrons is transmitted through an ultra-thin sample interacting with it as it passes through. An image is formed from the interaction of the electrons transmitted across the sample; the image is magnified and focused onto an imaging device, such as a fluorescent screen, on a layer of photographic film, or to be detected by a sensor such as a CCD camera. TEM microscopy acquire images with very high resolution This enables to examine fine details as small as a single column of atoms. SEM images have been obtained using a Philips XL-30CP electron microscope and the surface and elemental composition of the catalysts was determined using energy

dispersive X-ray measurements (EDX). TEM images have been obtained using a Philips 208 Transmission Electron Microscope. The samples were prepared by putting one drop of an ethanol dispersion of the catalysts on a copper grid pre-coated with a Formvar film and dried in air.

### **X-ray Photoelectron Spectroscopy XPS**

XPS analysis is a quantitative spectroscopic technique for surface chemical analysis measures the elemental composition, chemical state and electronic state of elements present in a sample. XPS spectra are obtained by irradiating a material with a beam of X-rays while simultaneously measuring the kinetic energy and number of electrons that escape from the top 1 to 10 nm of the material being analysed. XPS requires ultra-high vacuum (UHV) conditions. XPS analysis on the present catalysts has been carried out by means of an Al-source Surface Science Instrument (M-Probe) instrument.

### **Temperature programmed Reduction, Oxidation and Desorption (TPR-TPO-TPD)**

Temperature programme techniques are employed to check thermal stability of the sample (TPD) to identify the different species present in the catalysts according to the different reduction temperatures (TPR) or to test the resistance of a reduced sample to oxidation (TPO) ; moreover, this technique allows to evaluate the existence of potential interactions between the active phase and the support.

The catalyst was placed in a quartz reactor and heated at 10 °C/min.

Temperature programmed analysis were carried out on ca. 0.15 g of catalyst, loaded into a continuous, tubular quartz microreactor, and heated in a mixed gas stream flowing at 40 mL/min. Heat was provided by means of an electric furnace, controlled by an Eurotherm 2408 TRC. Heating rate was 10°C/min from 25 to 800°C, composition of mixed gas stream changed depending of the analysis for TPR 5% H<sub>2</sub>/Ar, TPO Air and TPD He.

The outlet gas was continuously monitored by means of a quadrupolar mass spectrometer (MS) (MKS, PPT Residual Gas Analyser). For TPR and TPO analysis it was also use a parallel device equipped with thermal conductivity detector (TCD), allowing to quantify hydrogen consumption after proper calibration with CuO. TPR

analysis was mainly used to identify the lowest temperature at which all the active phase present in each sample was completely reduced while TPO was used to test how stable is the reduced state of those metals.

### **Chemisorption**

O<sub>2</sub> pulse chemisorption measurements were performed at 298 K. A home-made equipment was used for pulse chemisorption.

All the samples were first reduced at 500°C under pure H<sub>2</sub> for 1 hour and then evacuated under helium gas at 500°C for 2 hours to remove all physisorbed hydrogen. O<sub>2</sub> chemisorption was performed at 25°C. An O<sub>2</sub>/Ni chemisorption stoichiometry = 2 was used.

This analysis was made to determine the size and the total surface area of the metallic particles over the surface of each sample (especially Ni and Cu). For samples giving no O<sub>2</sub> chemisorption, reduction at 800°C was also tried, according to the previous inspection of the TPR pattern, to ensure complete metal reduction before chemisorption.

### **Fourier Transform Infrared Spectroscopy (FT-IR)**

FT-IR analysis were made to investigate the surface interaction of the samples with CO, to identify Ni species and qualitatively estimate their size. CO adsorption and mostly spectra collected after dosage of pivalonitrile (PN) allowed to assess the nature and strength of the active active sites.

FT-IR spectra have been recorded in static conditions by a Nicolet Nexus Fourier transform instrument, using conventional IR cells connected to a gas manipulation apparatus. Pressed disks of pure catalyst and support powders (~20 mg) were thermally pretreated in the IR cell by heating in vacuum at 773 K (723 for the Ti1C500 samples series). For reducing the samples, after this pretreatment, they were heated in pure H<sub>2</sub> at 773 K (600 Torr, two cycles, 30 min each) followed by an evacuation step at the same temperature. CO adsorption experiments have been performed at 77K, and following out gassing until room temperature, recording different spectra at 133, 153, 163, 225, 273 K and r.t..

Pivalonitrile (PN) adsorption experiments have been performed over the reduced samples at room temperature and following out gassing at increasing temperatures.

Skeletal spectra have been recorded in air, after dilution of the catalyst powder with KBr (0.1% w/w).

## Activity test

Activity test were carried out in a home-made micro pilot plant for steam reforming, set up during the first six months of my thesis. During the 3<sup>rd</sup> year of this thesis I've spent six months at the Queen's University of Belfast, where I've tested some catalysts on a different plant already set up.

### 1<sup>st</sup> set up for ESR (Milan, IT)

The apparatus (Fig. 5) is composed by four mass flow meters (Brooks mod. SLA5850S), controlled by a mass-flow controller (Brooks, mod. 0154). The system is equipped with different gas lines, in particular carbon dioxide, carbon monoxide, hydrogen and helium. An Incoloy 800 reactor, where the catalyst is placed, is located in an electric oven, controlled by an Eurotherm 3204 TIC. An HPLC pump (Waters mod. 501) is used to feed water/ethanol liquid mixtures with various compositions. In Figure 6 there is the scheme of the micro plant



*Figure 5: Picture of the plant for the activity tests*

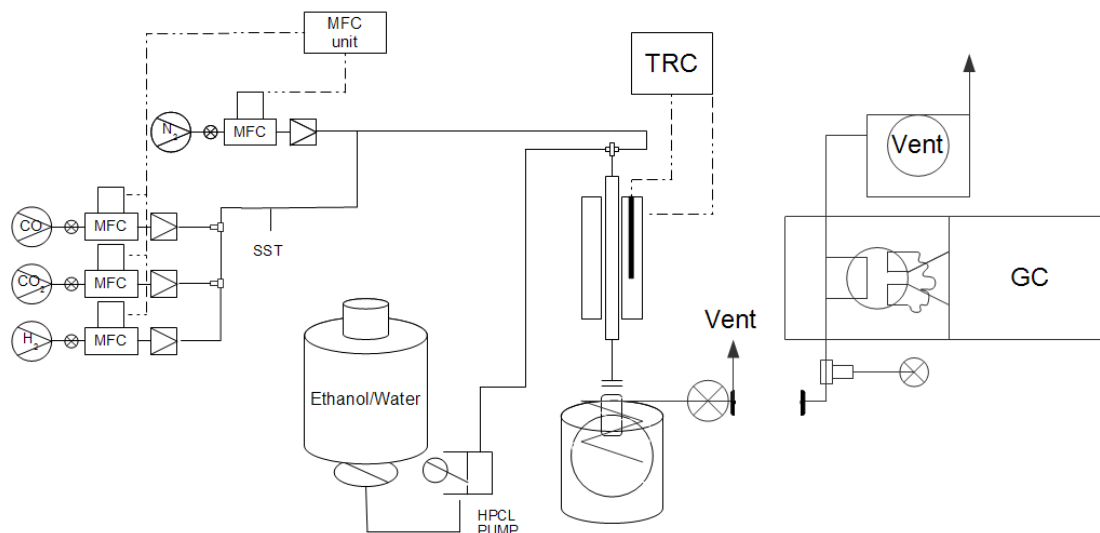


Figure 6: Scheme of the plant for the activity tests

The reactor effluent is sampled using a 25 ml gas syringe.

Analysis are carried out by means of a two channel Gas Chromatograph (Agilent 7890), both of them equipped with two columns connected in series (MS and PoraplotQ). The first channel drives the gas to a thermal conductivity detector (TCD) and is used for the determination of the composition of the gas mixture where CO concentration is relatively high ( $> 1\%$  vol). The second channel is connected to a flame ionization detector (FID) combined with a methanator device, allowing the determination of very low amounts of CO (a few ppm).

All the activity tests were made on the TCD channel by referring to an internal standard ( $N_2$ ). This channel is provided with two columns: i) HP-PLOT/Q that separates the gaseous sample in components on the basis of their polarity. So this first column separates carbon dioxide, water, permanent gases ( $O_2$ ,  $N_2$ ,  $CO$ ,  $CH_4$ ,  $H_2$ ), heavy polar organic compounds (in this case  $CH_3CHO$  and  $CH_3CH_2OH$ ) ii) HP-MOLESIEVE, which separates the permanent gases on the basis of their dimension.

In Figure 7 and 8 the configuration of the valves V2 and V3 of the GC are reported, valves are open when they allow the sample inside the column.

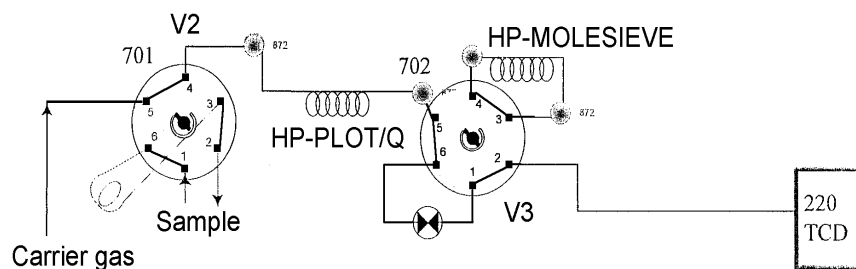


Figure 7: V2 and V3 closed.

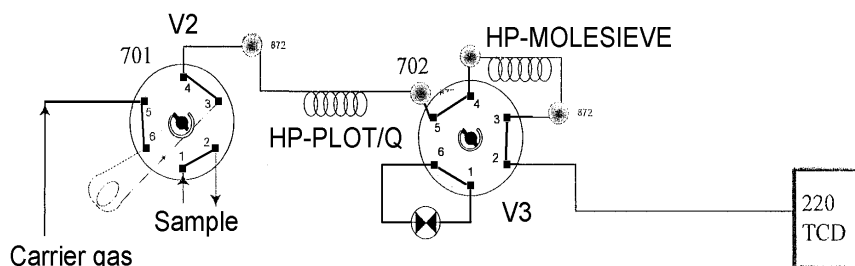


Figure 8: V2 and V3 open

Analysis time is 16.7 min oven temperature of the GC is 70 °C from the beginning of the analysis until 11 min, after rise up to 200°C with a slope of 35 °C/min. The oven remains at 200 °C for 2 min. Carrier gas is helium, flowing at 12 ml/min. The gaseous sample is injected inside the auto-sampler loop. The analysis method is set up to avoid the introduction inside the molecular sieves column of CO<sub>2</sub>, H<sub>2</sub>O and organic compounds, These species, especially water, could deactivate the molecular sieves column.

After the sampling the valves change operates as shown in Table 4

**Table 4: operating time of GC valves**

	State of the valve							
Time min	0	0.01	0.02	0.1	0.6	2.2	7	11
Valve 2	closed	closed	open	open	open	close	open	close
Valve 3	open	closed	closed	open	closed	closed	closed	closed

Set-up of the plant included the calibration of the mass-flow meters and of the HPLC pump, the determination of the temperature profile inside the oven, to evaluate the isothermal zone where the catalyst should be located and the GC calibration.

GC calibration was carried out for CO, CO<sub>2</sub>, H<sub>2</sub>, H<sub>2</sub>O<sub>(g)</sub>, CH<sub>4</sub>, CH<sub>3</sub>CH<sub>2</sub>OH<sub>(g)</sub> and CH<sub>3</sub>COH<sub>(g)</sub> on the TCD channel by referring to an internal standard (N<sub>2</sub>). Particular care was

put in the calibration procedure allowing to detect at once in vapour phase an originally heterogeneous mixture. The problem was overcome by setting up a saturation and condensation device and by calculating the vapour pressure of the different compounds at various operating temperature. Calibration were made by analysing mixture of gases or gas+ vapour (using a saturator shown in Figure 9) of known composition. Analysis were carried out with the same method used for the activity tests. Peaks were identified by retention time previously determined by injection of single components (Table 5).

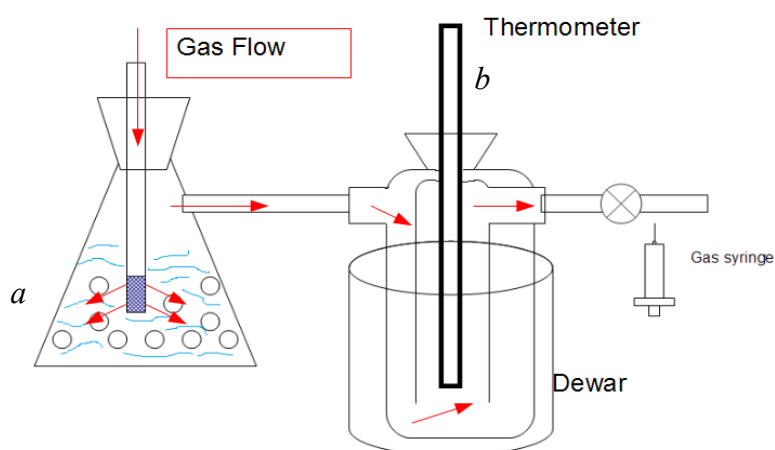


Figure 9: Scheme of the saturator. Gas flow ( red arrows) pass throughout a liquid (a) an goes to a refrigerated trap in which there is a thermometer (b) . The partial pressure of the vapour in the carrier gas was calculated from the temperature detected.

**Table 5: retention time of the reformat species [method file : Altaconc 4]**

Components	Retention time (min)
CO <sub>2</sub>	2-2.5
H <sub>2</sub> O	5.6-6.5
H <sub>2</sub>	8.3
N <sub>2</sub>	8.7
CH <sub>4</sub>	9.33
CO	9.5-10
CH <sub>3</sub> CHO	11.4
CH <sub>3</sub> CH <sub>2</sub> OH	12.7

For each gaseous product the calibration was made by changing the ratio between its flow and that of nitrogen (*i.e.* Figure 10 and Figure 11) a. With interpolating curves



(Table 6) it was possible to determine the composition of the gaseous outlet of the SR reactor knowing the area of the peaks (chromatograph analysis) and the flow of  $N_2$ .

**Table 6: interpolated curves for reformat species**

$X = \text{area of } n \text{ peak} / \text{area of } N_2 \text{ peak}$

$Y = \text{flow of } n \text{ species} / \text{flow of } N_2$

of  $N_2$

Specie (n)	equation	R <sup>2</sup>
CO <sub>2</sub>	Y= 0.8386*X	0.99
H <sub>2</sub> O	Y= 2.3077*X	0.98
H <sub>2</sub>	Y=-305.2*X <sup>2</sup> +78.031*X	0.99
CH <sub>4</sub>	Y= 1.3623*X	0.99
CO	Y= 0.9969*X	0.99
CH <sub>3</sub> CHO	Y=-0.7849*X <sup>2</sup> +0.5961*X	0.99
CH <sub>3</sub> CH <sub>2</sub> OH	Y= 0.8499X	0.99

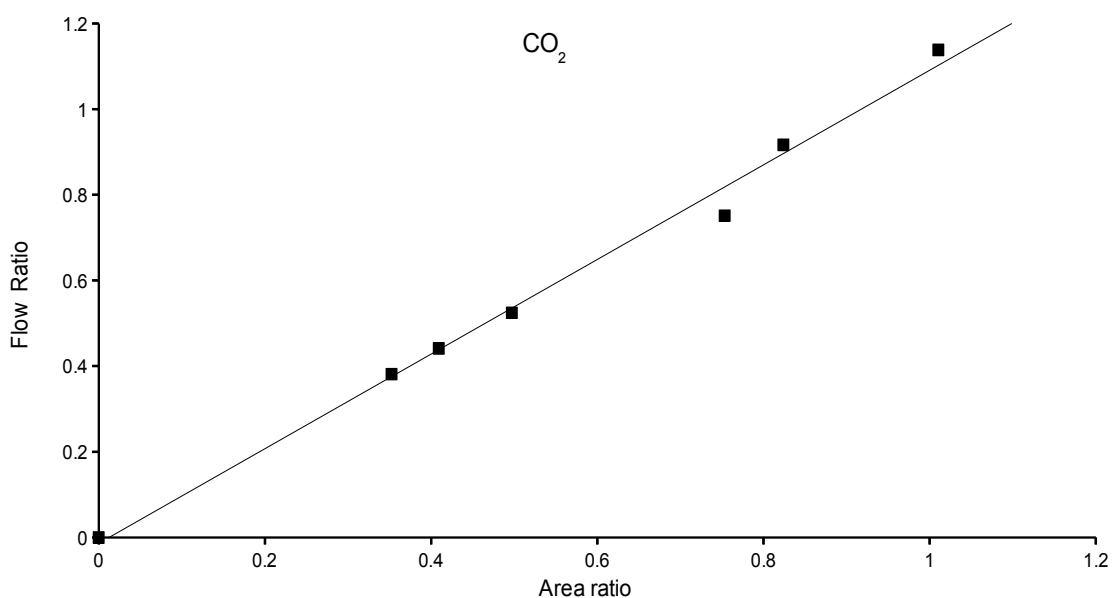


Figure 10: Interpolated curve of CO<sub>2</sub>

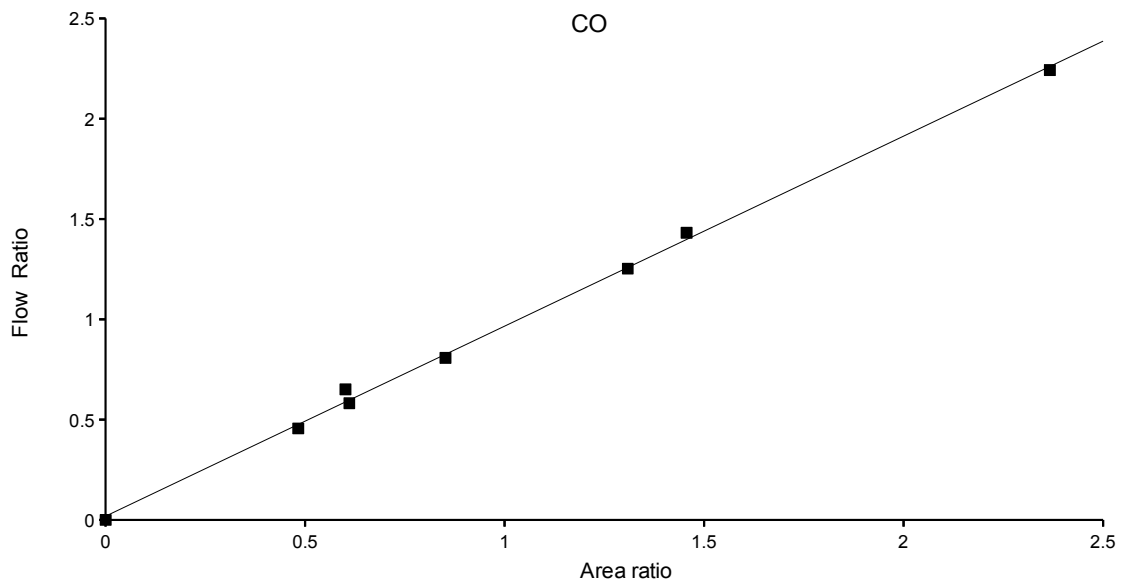


Figure 11: Interpolated curve of CO

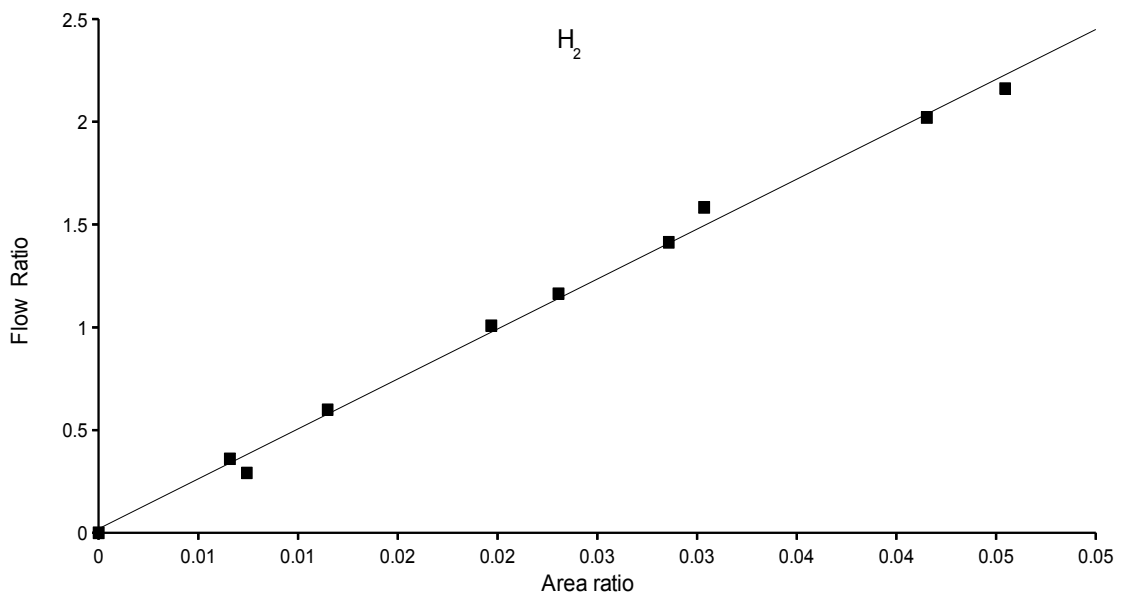


Figure 12: Interpolated curve of H<sub>2</sub>

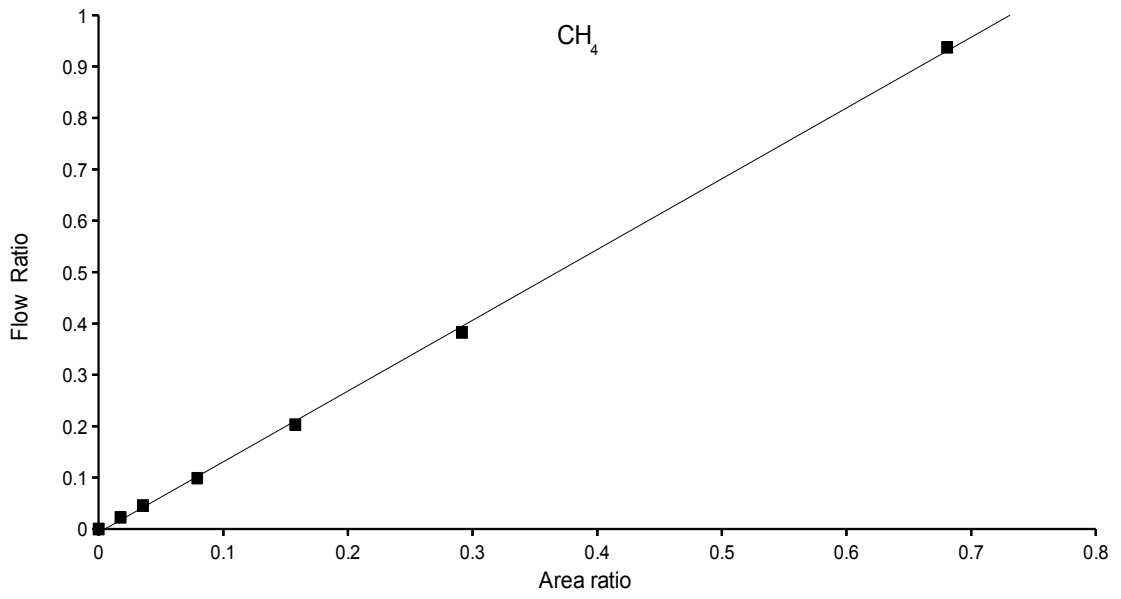


Figure 13: Interpolated curve of  $\text{CH}_4$

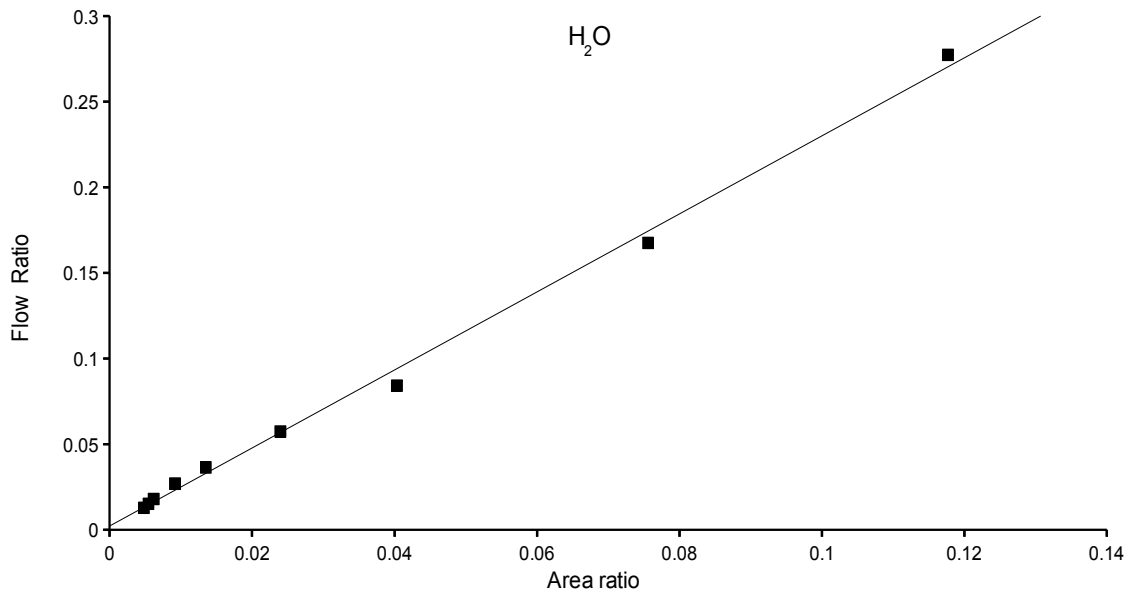


Figure 14: Interpolated curve of  $\text{H}_2\text{O}$

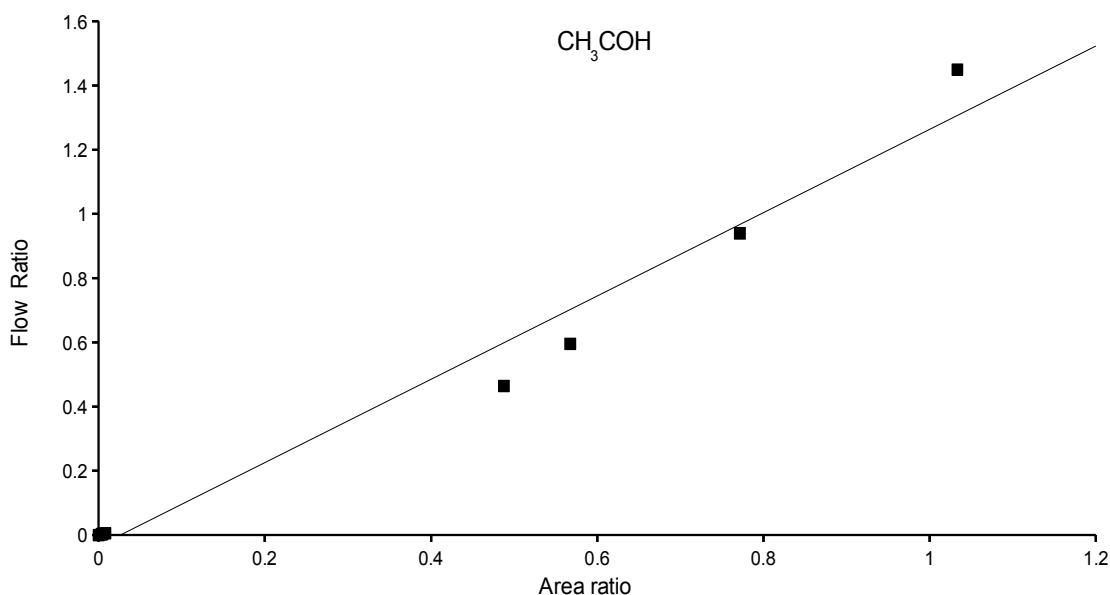


Figure 15: Interpolated curve of  $CH_3CHO$

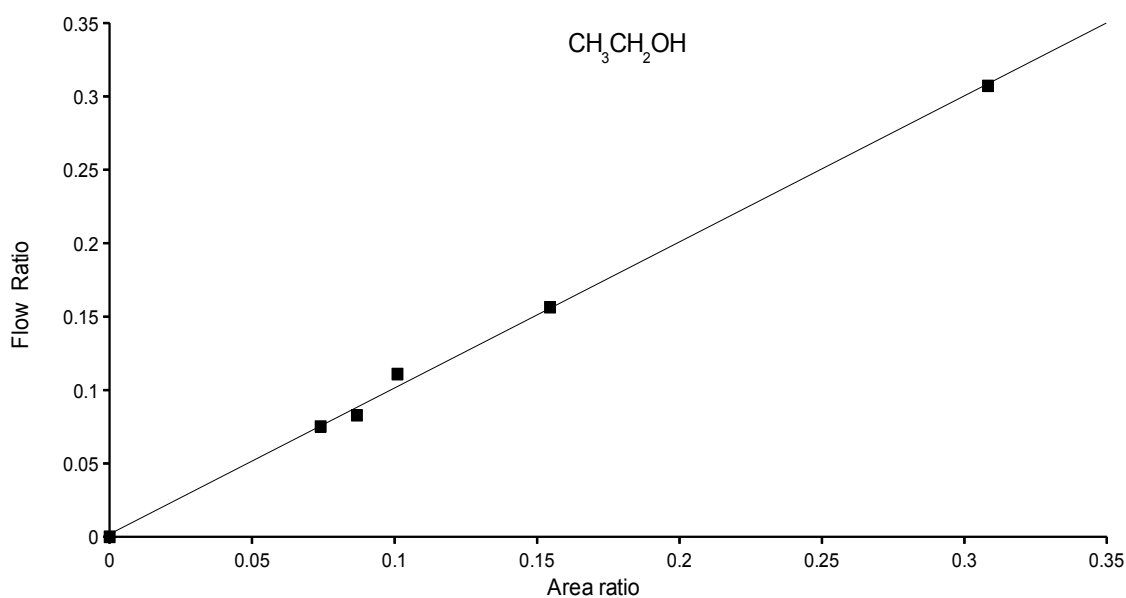


Figure 16: Interpolated curve of  $CH_3CH_2OH$

Activity testing were made focused the attention on the  $H_2$  productivity (mol/minkgcat), the  $CO/CO_2$  ratio and the formation of coke, estimated on the basis of C balance. A good catalyst should have a high  $H_2$  productivity, a low  $CO/CO_2$  ratio that means low production of CO, hence easier  $H_2$  purification and a good resistance towards coking.

The procedure for the activity test was the same for all catalysts and, it lasted about 80h for each sample. First the catalyst was pressed, ground and sieved (sieves 60-100 mesh), dilute 1:3 (in volume) with SiC to increase the volume of the working

zone inside the reactor. Activation is accomplished by reduction for 1h at 800°C in a flow of 50ml/min 1:4 (vol/vol) H<sub>2</sub> in N<sub>2</sub>. During activity testing a liquid mixture H<sub>2</sub>O:CH<sub>3</sub>CH<sub>2</sub>OH= 3:1 mol/mol (if not else specified) was fed to the reactor added with a gaseous mixture composed of 277 ml/min He and 50 ml/min N<sub>2</sub>. He acted as diluent to decrease the partial pressure of ethanol and water, below saturation under most conditions, so allowing the analysis of the whole mixture in gas phase, whereas N<sub>2</sub> was the internal standard for GC analysis.

A 1<sup>st</sup> test was made at 750°C, the 2<sup>nd</sup> at 500°C and the 3<sup>th</sup> at 625°C. Every test lasted about 7 hours and between the tests the catalyst was kept in temperature and fed with a very mild flow of He. After the third test the catalyst was activated again and the test at 750°C was repeated. Some modifications to this testing procedure were made for low temperature testing. For some catalysts after the reduction (1h at 800°C in a flux 1:4 H<sub>2</sub>) only one test at 500°C was made. Furthermore, for some of the catalysts prepared in collaboration with UniVe and calcined at 500°C the procedure was slightly different: after reduction of the active phase 1h at 500°C in a flow of 50ml/min 1:4 H<sub>2</sub> in N<sub>2</sub>, a liquid mixture 3:1 mol H<sub>2</sub>O:CH<sub>3</sub>CH<sub>2</sub>OH and a gaseous mixture 277 ml/min He and 50 ml/min N<sub>2</sub> were fed to the reactor. The 1<sup>st</sup> test was made at 500°C, the 2<sup>nd</sup> at 400°C and the 3<sup>rd</sup> at 300°C. Every test lasted about 7 hours. GC analyses on each sample were made every 30-60 min and the results are tabulated as average value among all the data collected after 4-7 h-on-stream.

## **2<sup>nd</sup> set up for ESR tests (Belfast UK)**

Between the second and the third year of my PhD thesis I've spent 6 months at The Queen's University of Belfast. During this period some of the catalysts already tested in Milan were compared (Group 1) by using a different set up and some different operative parameters.

The reaction was performed in a fixed bed reactor. A scheme of the set-up is presented in Figure 17. All the tubing and connections were made from stainless steel supplied by Swagelok. The reactor used was a quartz tube (internal diameter 2 cm), where the catalytic bed was held by some quartz wool previously calcined at 900°C. The temperature inside and outside the catalytic bed was recorded by a thermocouple (type K) connected to the software Pico Technology. The temperature of the oven was controlled by a programmable temperature controller Eurotherm

2630. The gas flow was controlled by a series of mass flow controllers (EL-Flow from Bronkhorst or FC-7700C from Aera). The liquid feed mixture was fed to the system by a syringe-free liquid pump from Valco Instruments Co. Inc. (VICI) connected to a home-made evaporator in which the liquid feed was evaporated and mixed with the inert gas at 100 °C. All the pipes were heated using heating tapes to prevent any condensation. Finally, the gas mixture was analysed on-line by a gas chromatograph.

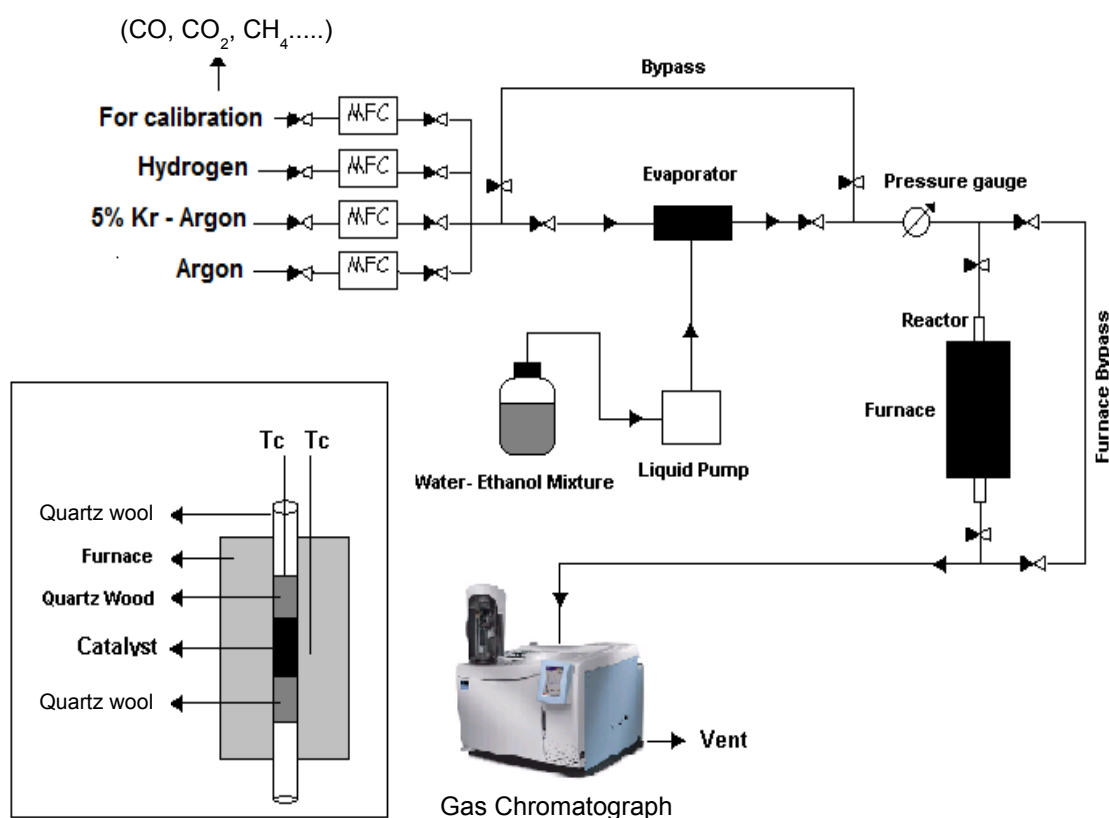


Figure 17: Scheme of the plant activity testing in Belfast

The Gas Chromatograph (GC) used was a Clarus 500 supplied by PerkinElmer, and controlled by the software TotalChrom. The carrier gas used was Argon supplied by BOC ( $\geq 99.9\%$  purity) used without further purification. The injector was an automatic 6 ways valve (heated at 200°C) provided by Valco and the on-line sampling was carried out by a loop sampling as shown in figure 18

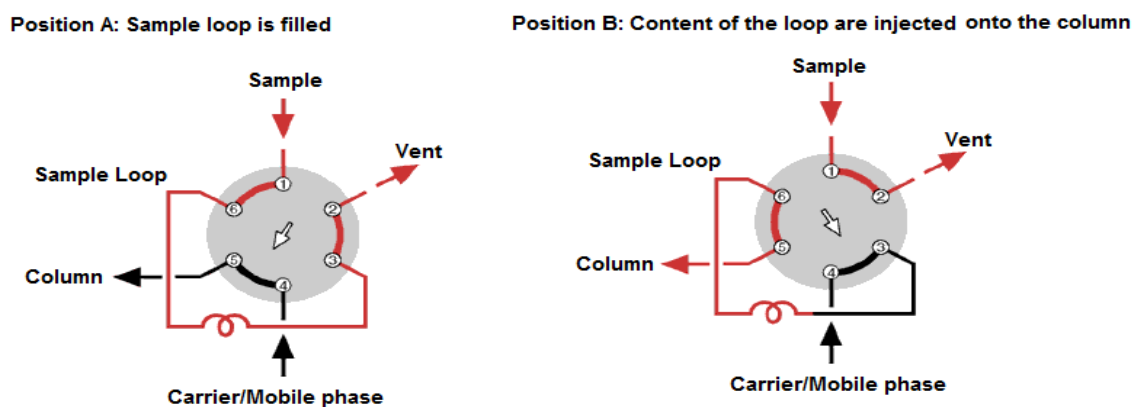


Figure 18: Scheme of the GC valves in Belfast

The column used is HaySep DB (10 m, 1/8 in OD, mesh range: 100-120, 2 mm ID) in which all gaseous components are separated and pass through it directly to the detectors. Two detectors were used consecutively, a Thermal Conductivity Detector (TCD) and a Flame-Ionization Detector (FID). The temperature of the TCD was 250°C and the range used was 4. The FID was coupled with a methanizer which converts CO and CO<sub>2</sub> to methane, thereby allowing their detection by the FID. The temperature of the FID was fixed at 350°C; the range was 20 and the flows of air and H<sub>2</sub> were fixed at 400 and 40 ml/min respectively. Air was supplied by an air compressor and H<sub>2</sub> was supplied by BOC (>99.9) and used without purification. Eight gaseous compounds were separated and analysed during this experiment: H<sub>2</sub>, CO, Ar, CH<sub>4</sub>, CO<sub>2</sub>, CH<sub>2</sub>CH<sub>2</sub>, H<sub>2</sub>O, CH<sub>3</sub>CHO and CH<sub>3</sub>CH<sub>2</sub>OH in a run of 40 minutes total time. Oven temperature was first set at 85°C for 5 min and then increased to 245°C with a heating rate of 40°C/min and kept at 245°C for 31 min. Retention times of the components were as follows (Table 7):

**Table 7: Retention time of the gaseous compounds during testing in Belfast**

Components	Retention time (min)
H <sub>2</sub>	5.5
CO	7.3
CH <sub>4</sub>	9.33
Ar	10.9
CO <sub>2</sub>	14.3
CH <sub>2</sub> CH <sub>2</sub>	18.3

H <sub>2</sub> O	19.5
CH <sub>3</sub> CHO	31
CH <sub>3</sub> CH <sub>2</sub> OH	36.1

A feed of 20 vol% water-ethanol mixture, 3.75 vol% Kr (as internal standard) and 76.25 vol% Ar was fed at a rate of 80 ml/min through the catalyst. For all the tests the water/ethanol molar ratio was 3. Ar and Kr were supplied by BOC (research grade, >99.9) and used without further purification. 200 mg of catalyst was reduced with a flow of 50ml/min 1:4 H<sub>2</sub> in Ar (vol/vol) and the activity towards ethanol steam reforming was measured at 500°C only. Analysis on each sample were made every 15-30 min and results are reported as average value among all the analyses.



# Chapter 4 Results

## Atomic absorption spectroscopy

The results are reported in Table 8

**Table 8: Actual meta metal concentration of the samples.**

Sample	Me loading wt%
T1C500	<b>Ni 7.8</b>
T2C500	<b>Ni 7.5</b>
T4C800	<b>Ni 6.7</b>
T3C800	<b>Ni 7.3</b>
S1C500	<b>Ni 9.2</b>
S2C800	<b>Ni 8.9</b>
Z1C500	<b>Ni 9.7</b>
Z1C800	<b>Ni 8.8</b>
10%Ni / TiO <sub>2</sub>	<b>Ni 8.2</b>
10%Ni / SiO <sub>2</sub>	<b>Ni 9.6</b>
T6C500	<b>Co 6.6</b>
T8C500	<b>Co 9.6</b>
S4C500	<b>Co 7.8</b>
10%Co/TiO <sub>2</sub>	<b>Co 10.9</b>
10%Co/SiO <sub>2</sub>	<b>Co 8.7</b>
T9C500	<b>Cu 5.6</b>
T11C500	<b>Cu 5.6</b>
S3C500	<b>Cu 6.8</b>
10%Cu/TiO <sub>2</sub>	<b>Cu 8.3</b>
10%Cu/SiO <sub>2</sub>	<b>Cu 9.2</b>

The amount of Ni in TiO<sub>2</sub> obtained by precipitation was lower than for the other supported samples. This is congruent with the preparation method and it may be ascribed to a

difficulty in the estimation of the real amount of Ti(OH)<sub>4</sub> present in the support, some

of that possibly being yet transformed into  $\text{TiO}_2$  during the drying step. Also for Cu and Co samples catalysts made by impregnation showed a lower metal concentration, attributed to the preparation method. By contrast catalysts made by FP showed an average active phase between 8-9 wt%.

## XRD

Figure 19 refers to the  $\text{Al}_2\text{O}_3$  support. The sample is mainly composed by  $\gamma$  alumina (JCPDS file 00-010-0425 ( $\diamond$ )) with a small contribution of  $\delta$  alumina (JCPDS file 00-050-0741( $\blacklozenge$ )) even if the shape of the spectra, with broad reflections and a high background noise, suggest nanostructuring of the sample.

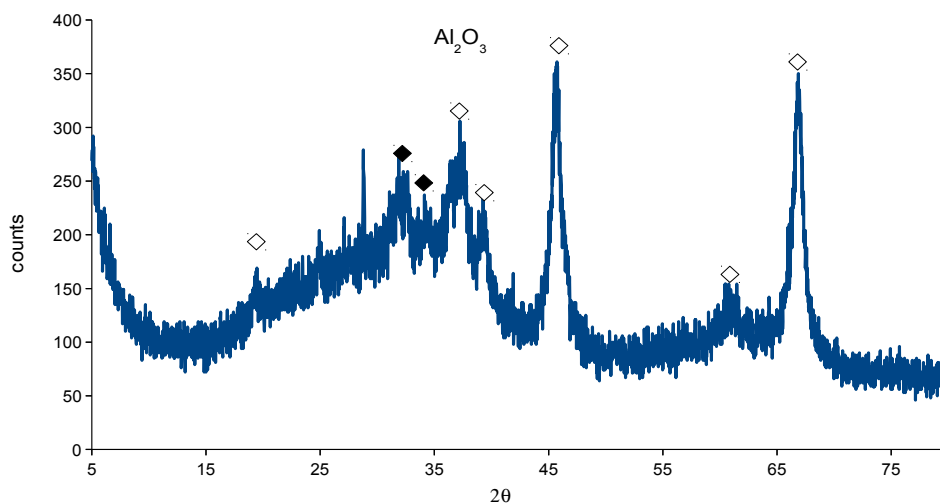


Figure 19: XRD pattern of FP made  $\text{Al}_2\text{O}_3$

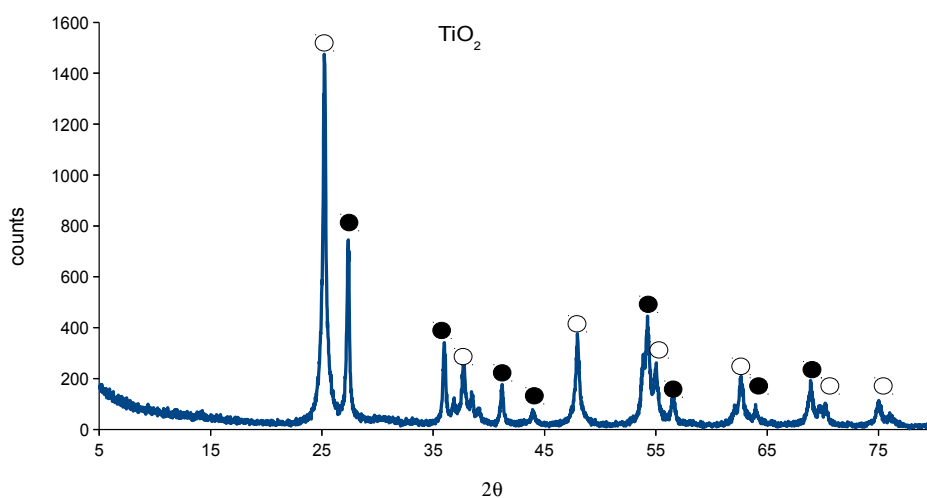


Figure 20: XRD pattern of FP made  $\text{TiO}_2$

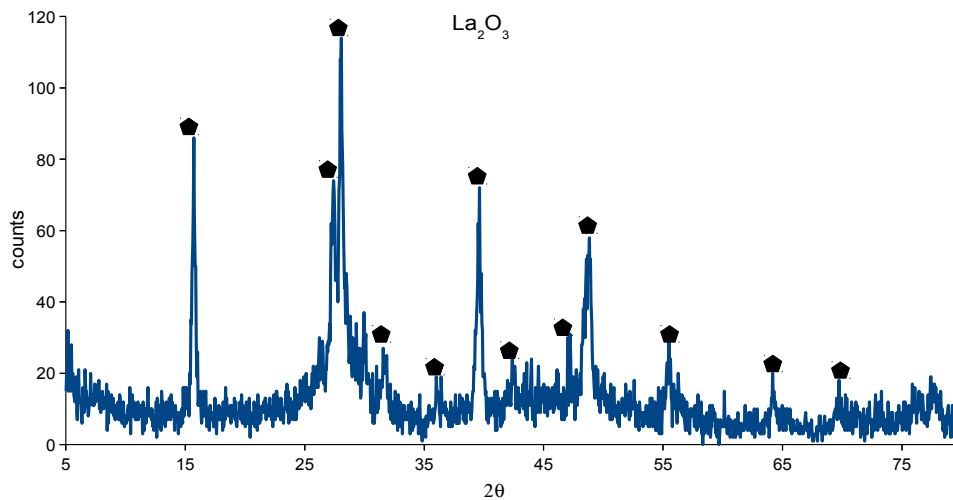


Figure 21: XRD pattern of FP made  $\text{La}_2\text{O}_3$

The  $\text{TiO}_2$  sample (Figure 20) showed a highly crystalline structure composed by two different phases:  $\text{TiO}_2$  rutile (JCPDS file 00-021-1276 (●)) and  $\text{TiO}_2$  anatase (JCPDS file 00-021-1272 (○)), the latter being the main component.

$\text{La}_2\text{O}_3$  (Figure 21) seems composed by  $\text{La}(\text{OH})_3$  only (JCPDS file 00-036-1481 (◆)).

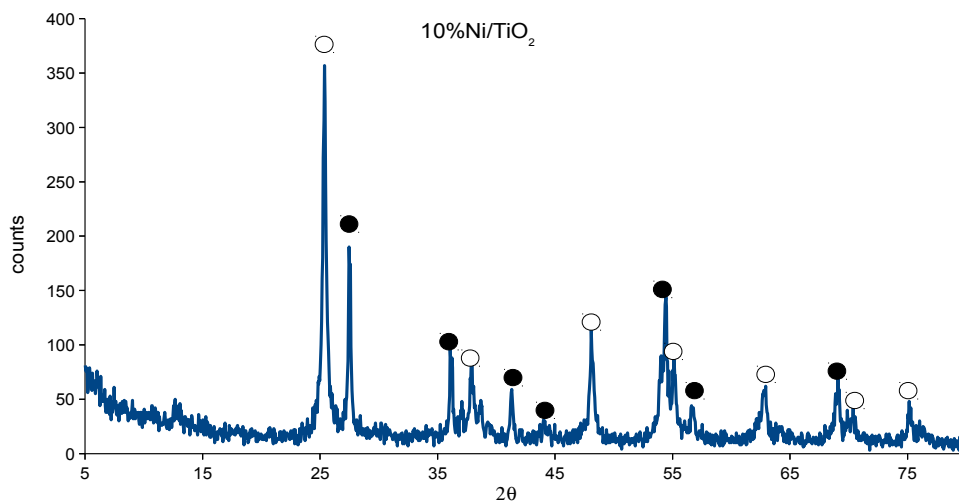


Figure 22: XRD pattern of 10%Ni/ $\text{TiO}_2$  made by impregnation; as prepared

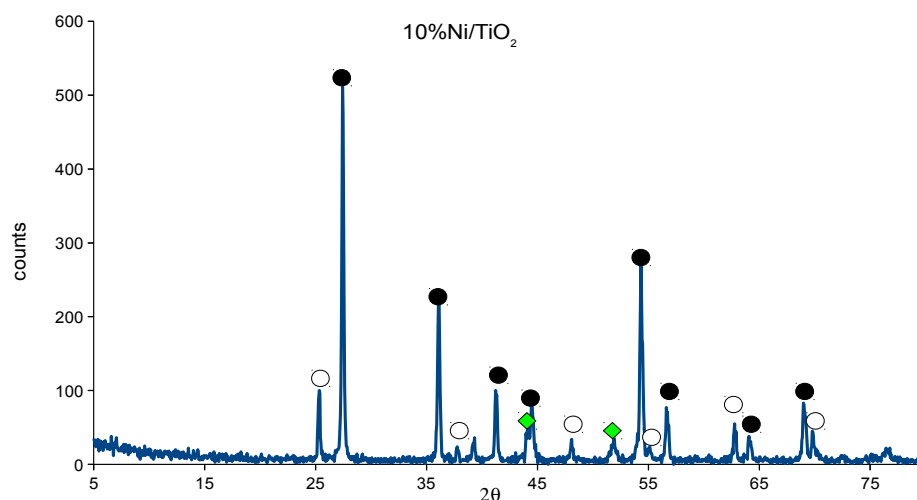


Figure 23: XRD pattern of 10%Ni/TiO<sub>2</sub> made by impregnation; reduced

The XRD spectra of 10wt%Ni/TiO<sub>2</sub> obtained by impregnation of the FP made TiO<sub>2</sub> is reported in Figure 22. Impregnation of the active phase seems to not affect the crystalline structure of the support and there is no evidence of peaks that could be attributed to Ni oxides or metallic Ni. The same sample after activation at 800° for 1h under flow of 20 vol% H<sub>2</sub> in N<sub>2</sub> is depicted in Figure 23. The ratio between rutile and anatase changes, with increasing intensity of rutile and the appearance of two small peaks ascribable to metallic nickel Ni (JCPDS File 00-001-1260 (♦)).

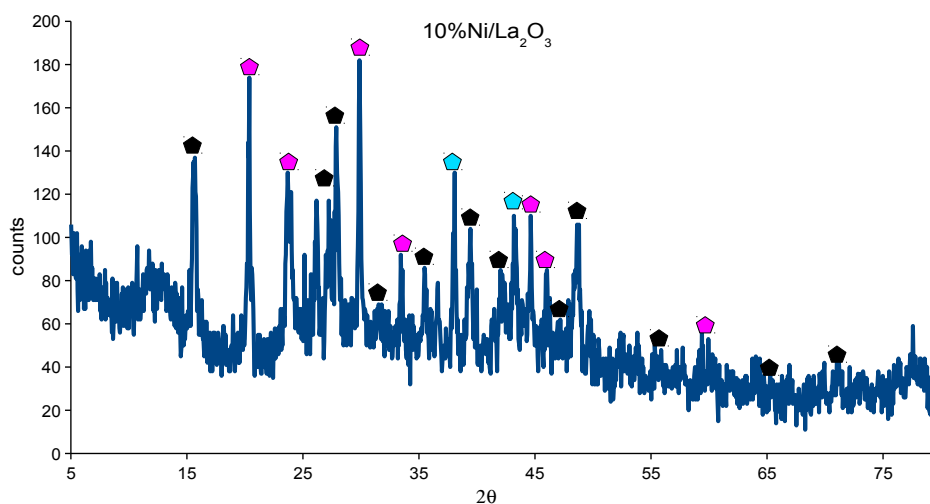


Figure 24: XRD pattern of 10%Ni/La<sub>2</sub>O<sub>3</sub> made by impregnation; as prepared

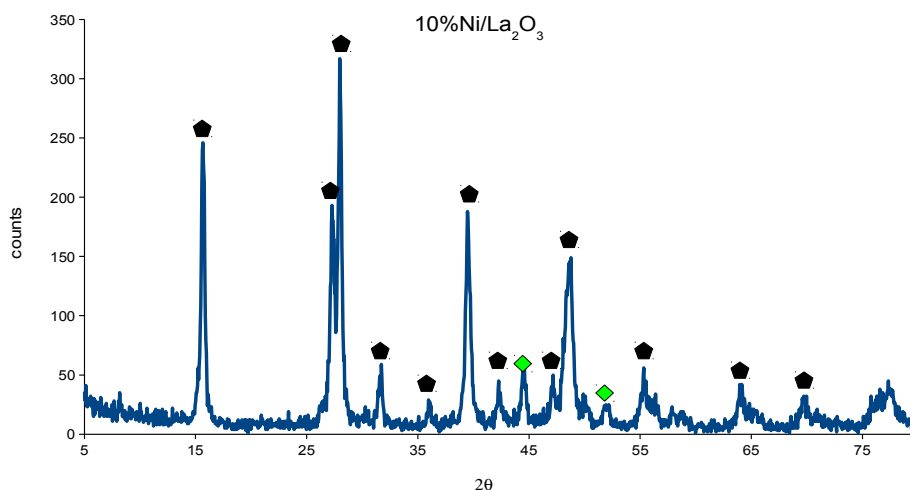





Figure 25: XRD pattern of 10%Ni/La<sub>2</sub>O<sub>3</sub> made by impregnation; reduced

In Figure 24 we report the XRD spectra of 10wt%Ni/La<sub>2</sub>O<sub>3</sub>. The addition of the active phase to the FP made support generates a lot of new peaks that could be attributed to NiO:

La<sub>2</sub>NiO<sub>4</sub> or NiO/La<sub>2</sub>O<sub>3</sub> (JCPDS file 00-011-0557 (  ))

NiO (JCPDS file 00-001-1239 (  )).

After activation (Figure 25) the sample appeared more crystalline and the only visible reflections were La(OH)<sub>3</sub> (  ) and metallic Ni (  ). In figure 6 there is the XRD spectra of 10%Ni/La<sub>2</sub>O<sub>3</sub>.

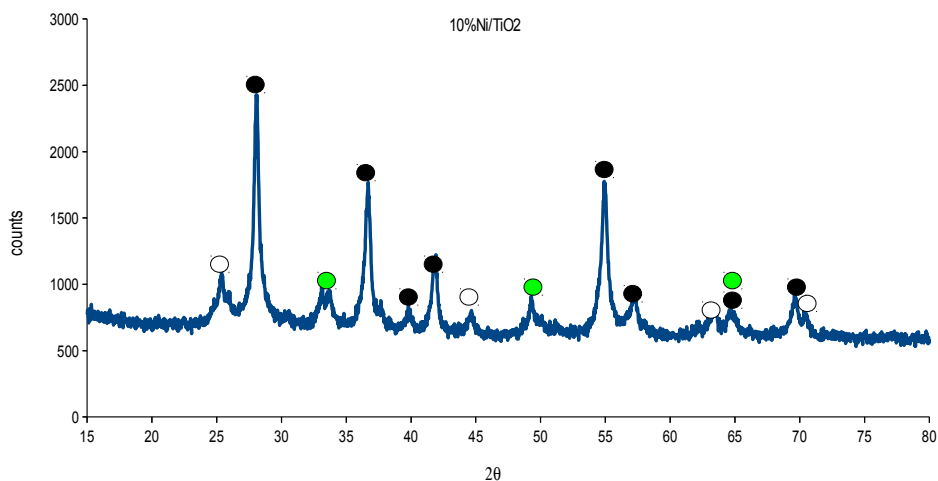


Figure 26: XRD pattern of 10%Ni/TiO<sub>2</sub> FP made

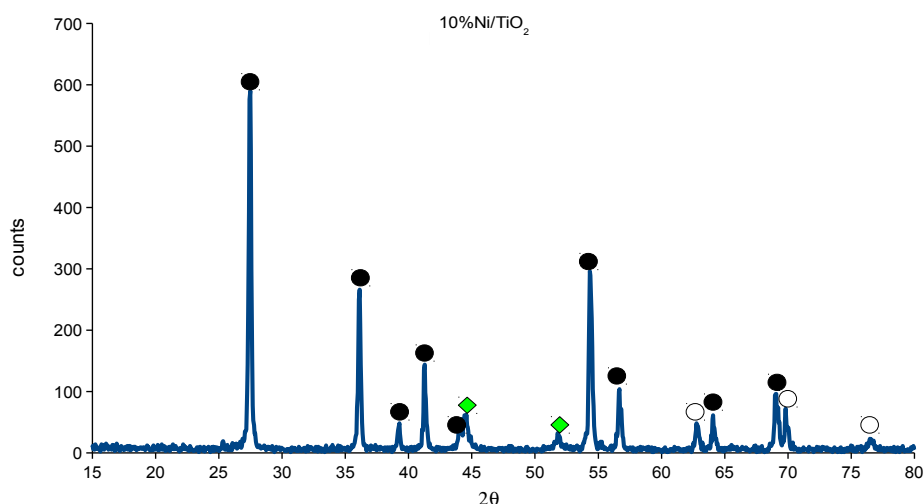


Figure 27: XRD pattern of 10%Ni/TiO<sub>2</sub> FP made reduced

The XRD spectra of 10wt%Ni/TiO<sub>2</sub> prepared directly by flame pyrolysis (FP made) is depicted in Figure 26 and in Figure 27 after activation. First of all there is much more rutile than anatase in the FP made catalysts and in Figure 26 some peaks are also visible that could be attributed to either a mixed oxide of Ti and Ni or to nickel oxide and titanium oxide:

NiTiO<sub>3</sub> or NiO/TiO<sub>2</sub> (JCPDS file 00-003-1154 (●))

After reduction (Figure 27) anatase reflections almost disappeared, as in the case of the impregnated catalysts (Figure 23), and two signals of metallic Ni (◆) were visible.

The pattern of 10%Ni/La<sub>2</sub>O<sub>3</sub> made by FP is reported in Figure 28 and in Figure 29 after activation. As for 10%Ni/La<sub>2</sub>O<sub>3</sub> made by impregnation (Figure 24) most of the sample is composed by LaOH<sub>3</sub> (◆). In the FP sample there was no trace of NiO, but La<sub>2</sub>NiO<sub>4</sub> formed during the synthesis La<sub>2</sub>NiO<sub>4</sub> JCPDS file 01-070-1333 (◆). After activation (Figure 29) the XRD spectrum was quite similar to that obtained for the impregnated sample (Figure 25). After the reduction the sample resulted mainly composed by LaOH<sub>3</sub> with two small peaks that could be attributed to metallic Ni (◆). Some La<sub>2</sub>NiO<sub>4</sub> was still visible, indicating that part of this species resisted even after the reduction at 800°C.

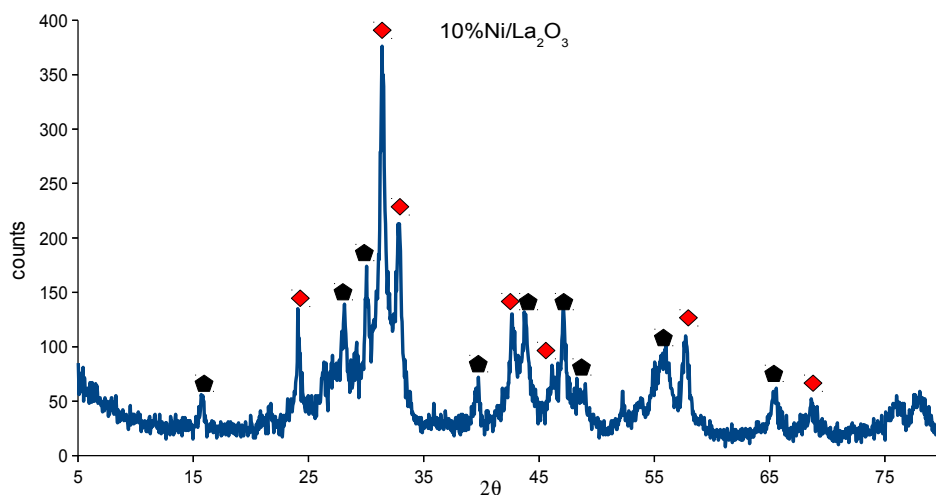


Figure 28: XRD pattern of 10%Ni/La<sub>2</sub>O<sub>3</sub> FP made

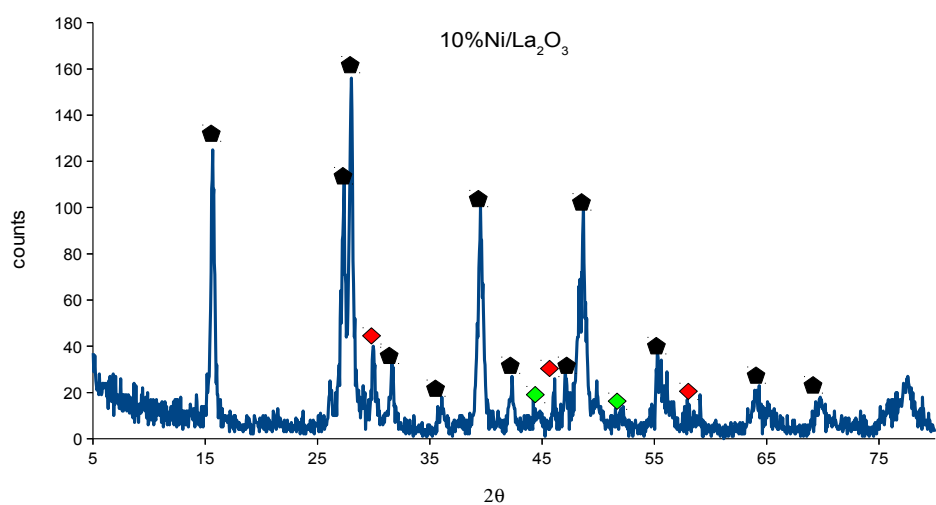


Figure 29: XRD pattern of 10%Ni/La<sub>2</sub>O<sub>3</sub> FP made; reduced

The XRD diffractograms of Xwt%Ni/TiO<sub>2</sub> (x= 5,10,15) are reported in Figure 12, as prepared by flame pyrolysis. Anatase (○) in the structure decreased as the nickel loading increased, while peaks of rutile (●) and of NiO/TiO<sub>2</sub> (●) increased.

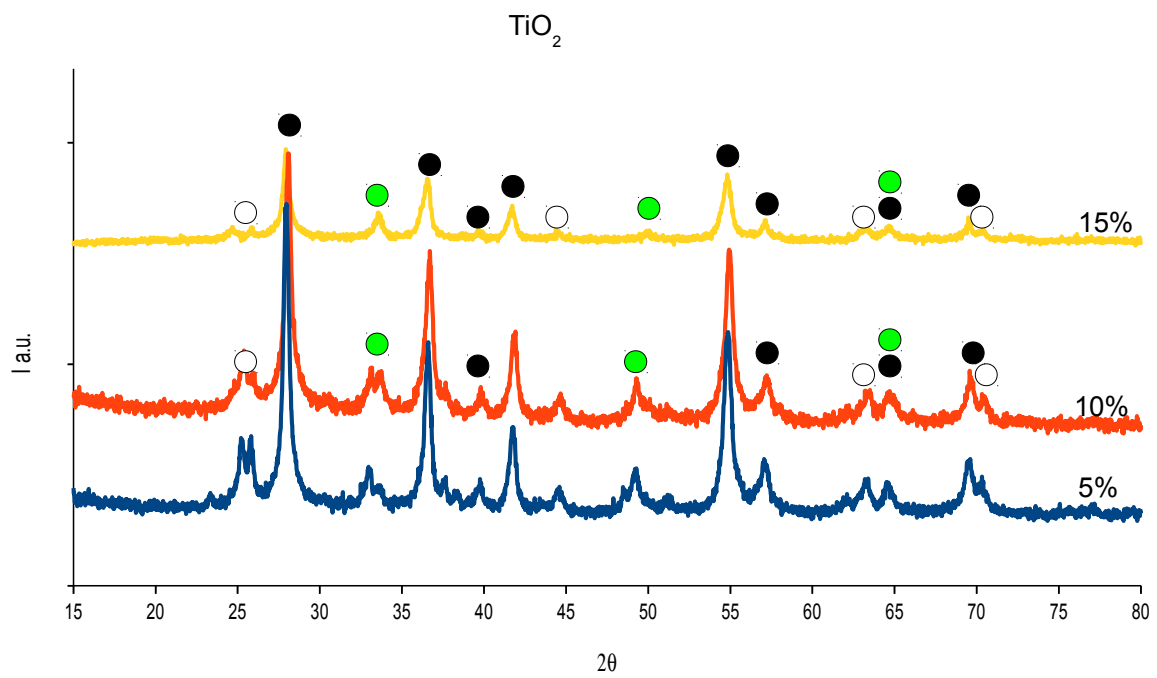


Figure 30: XRD pattern of FP made 5%Ni/TiO<sub>2</sub>(blue line); 10%Ni/TiO<sub>2</sub>(red line); 15%Ni/TiO<sub>2</sub>(yellow line): comparison

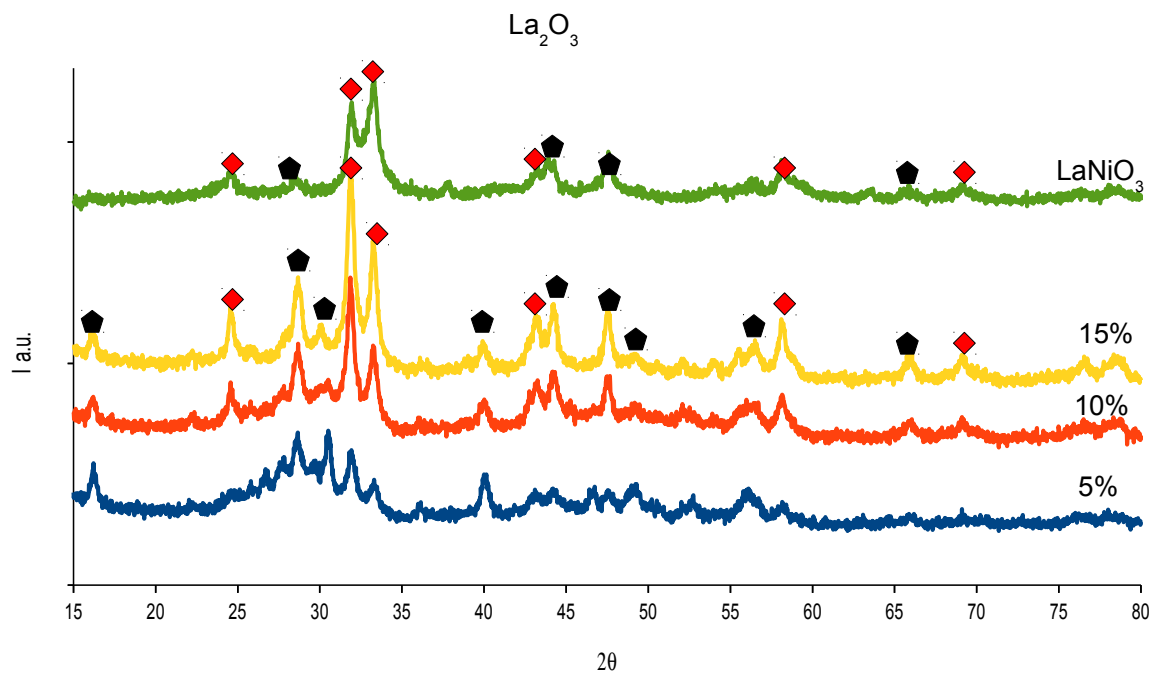


Figure 31: XRD pattern of FP made 5%Ni/La<sub>2</sub>O<sub>3</sub>(blue line); 10%Ni/La<sub>2</sub>O<sub>3</sub>(red line); 15%Ni/La<sub>2</sub>O<sub>3</sub>(yellow line); LaNiO<sub>3</sub> (green line): comparison



The same comparison between FP made catalysts supported on  $\text{La}_2\text{O}_3$  (5,10 and 15 wt% Ni;  $\text{LaNiO}_3$ ) is depicted in Figure 31. As the Amount of nickel increased  $\text{La}(\text{OH})_3$  (◆) reflections decreased until disappearing for the sample with the highest Ni content,  $\text{LaNiO}_3$  (La:Ni= 1:1). At the same time, the signal of  $\text{La}_2\text{NiO}_4$  (◇) increased with the Ni loading.

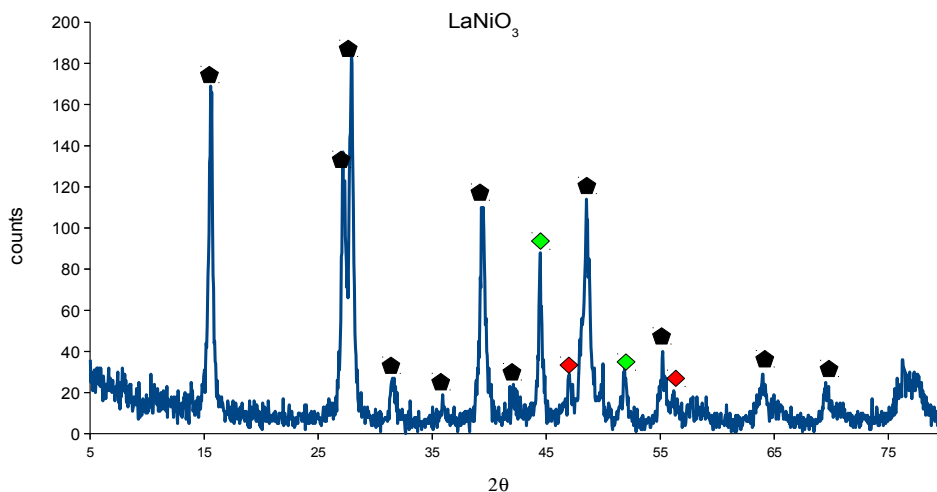


Figure 32: XRD pattern of FP made  $\text{LaNiO}_3$ ; reduced

After reduction (Figure 32),  $\text{La}(\text{OH})_3$  became the main phase, even with  $\text{LaNiO}_3$ , while  $\text{La}_2\text{NiO}_4$  almost disappeared and reflections of metallic nickel became more intense.

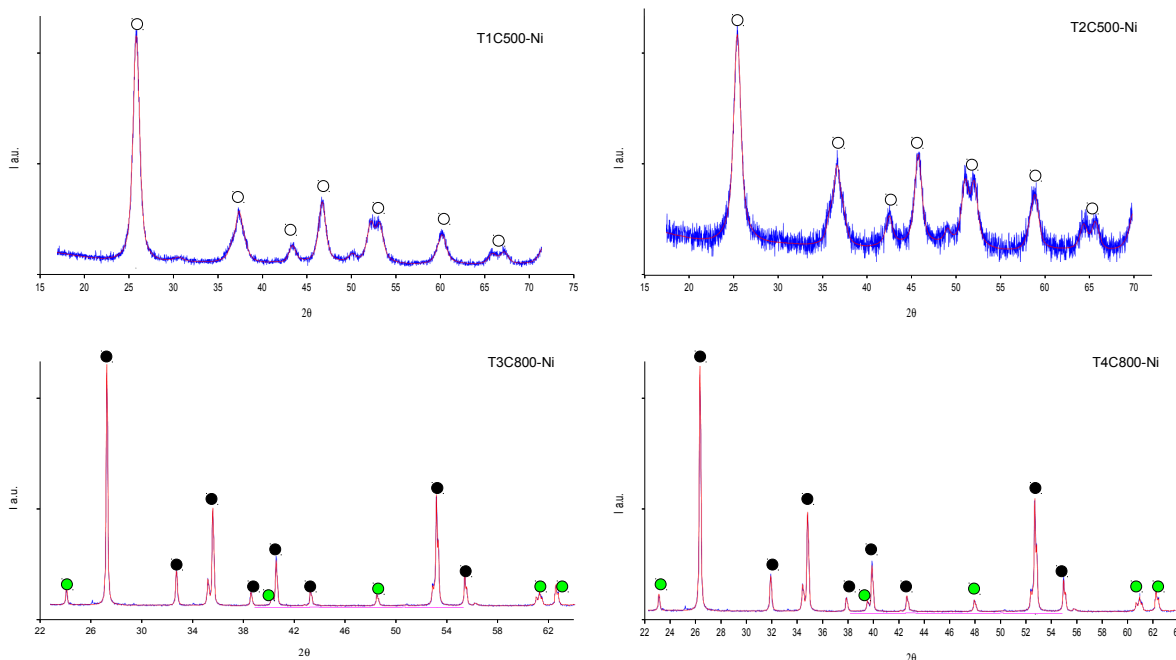


Figure 33: XRD pattern of 10%Ni/ $\text{TiO}_2$  samples made at UniVe

10wt%Ni/ $\text{TiO}_2$  was also prepared by impregnation of titania made by precipitation

Università Cà Foscari (Venezia). The XRD patterns of four samples with nominal composition 10wt%Ni/TiO<sub>2</sub>, but prepared on differently synthesised or calcined TiO<sub>2</sub> are reported in Figure 33. The phase composition was determined by Rietveld refinement. Sample T1C500, calcined at 500°C, was mainly constituted by anatase (○), 86% with ca.10wt% of brookite. The size of Ni crystallites was 6.6 nm. By contrast, sample T2C500 fully consisted of anatase ca. 96% with dimension of Ni crystallite 6.6 nm. The quantitative XRD analyses of both samples calcined at 500°C underestimated the Ni amount (ca. 4 wt%). By contrast, both the samples T3C800 and T4C800, calcined at 800°C, were constituted by rutile (●), plus ca. 15-17 wt% of ilmenite (NiTiO<sub>3</sub>) with bigger particle size than previous samples (T3C800 = 10.8nm and T4C800 = 12nm). Samples calcined at 800°C possess a structure more similar to the one showed by FP made 10%Ni/TiO<sub>2</sub> (Figure 30) as expected on the basis of the high temperature attained in the flame.

TiO<sub>2</sub>-supported samples with different active phase (Co and Cu) were also prepared., whose diffractograms are reported in the following Figures.

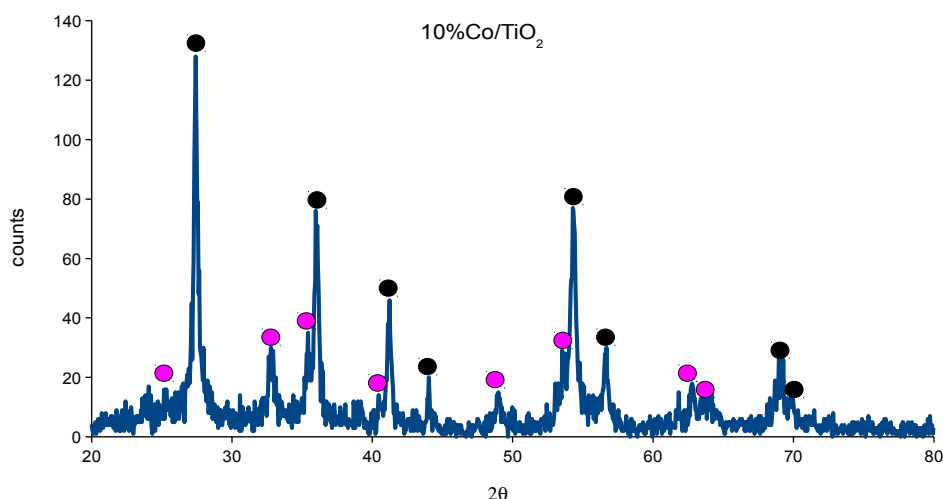


Figure 34: XRD pattern of 10%Co/TiO<sub>2</sub> FP made

The XRD of 10wt%Co/TiO<sub>2</sub> made by FP is depicted in figure 34, composed mainly by rutile (●), though very small reflections of anatase were hardly visible. Some mixed oxide CoTiO<sub>3</sub> JCPDS file 00-002-1216 (●) was also present.

In the case of 10wt%Cu/TiO<sub>2</sub> the main component was rutile, though there were still some reflections attributed to anatase (○). The other component of the structure was identified with CuO JCPDS file 00-089-5899 (●).

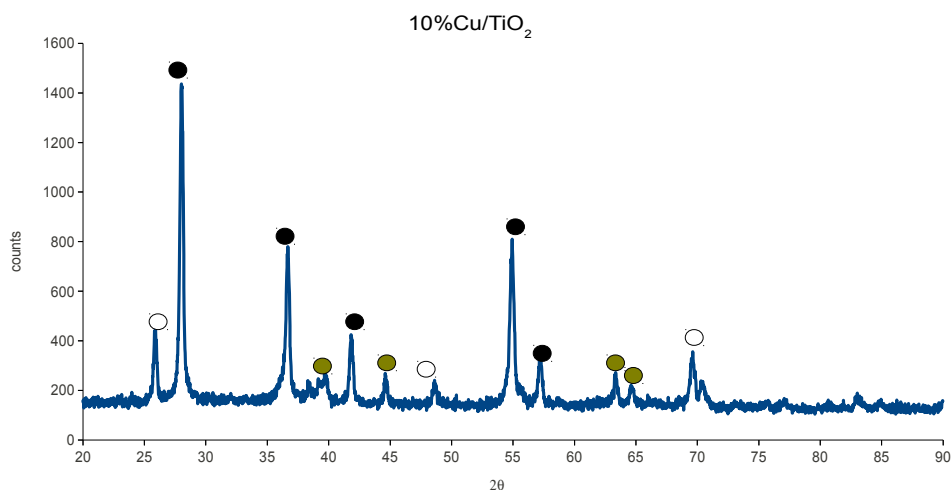


Figure 35: XRD pattern of 10%Cu/TiO<sub>2</sub> FP made

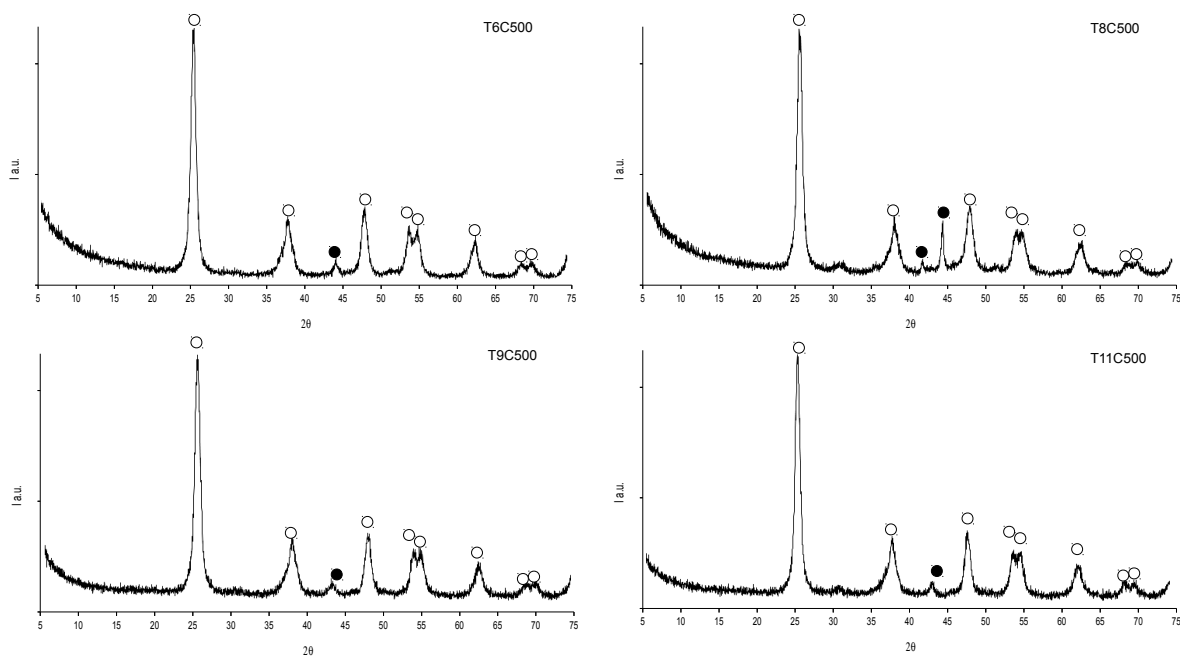


Figure 36: XRD pattern of 10%Co/TiO<sub>2</sub> samples made at UniVe (T6C500; T8C500); and of 10%Cu/TiO<sub>2</sub> made at UniVe (T9C500; T11C500)

In Figure 36 we report the XRD patterns of samples made by impregnation at UniVe. It seems there is no differences between the two Co-based catalysts (T6C500 and T8C500) and the two Cu-based ones (T9C500 and T11C500). The main component was anatase (○) with some contribution of rutile (●).

Dimension of crystallites evaluated through the Scherrer equation were T6C500 = 8 nm; T8C500 = 21.2 nm; T9C500 = 6.7 nm and T11C500 = 10.3 nm. Rietvel refinement also evidenced that in two samples there was also a percentage of

brookite, in particular T8C500 = 19.4% and T11C500 = 9.3%.

Other samples were supported on SiO<sub>2</sub> for each active phase (Ni, Co and Cu).

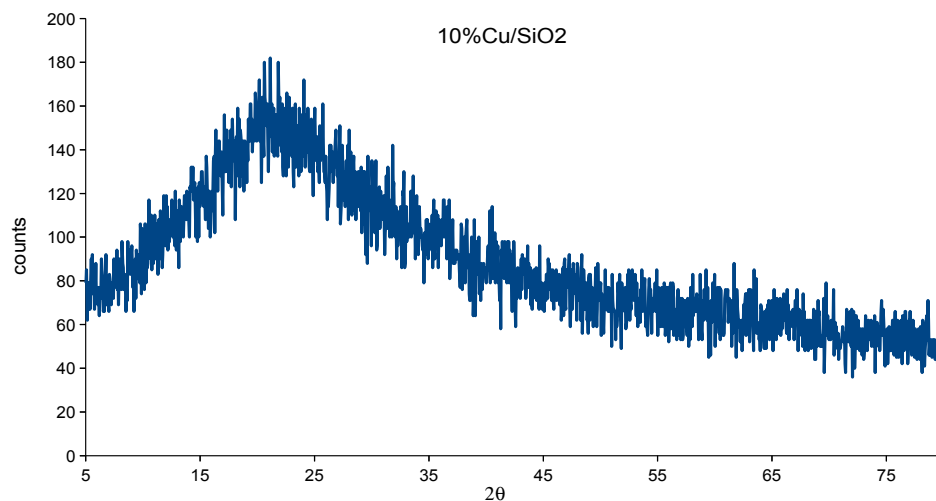


Figure 37: XRD pattern of 10%Cu/SiO<sub>2</sub> FP made

As for the previously described samples, a first group of silica based catalysts was synthesised by FP 10wt%Me /SiO<sub>2</sub> (Me = Ni, Co, Cu). XRD analysis on these samples showed an amorphous component due to SiO<sub>2</sub> and no evidence of metal oxides (Figure 37). Similar samples were synthesised by wet impregnation at UniVE by impregnation of the active phase over SBA-15 mesoporous silica (Figure 38 and 39).

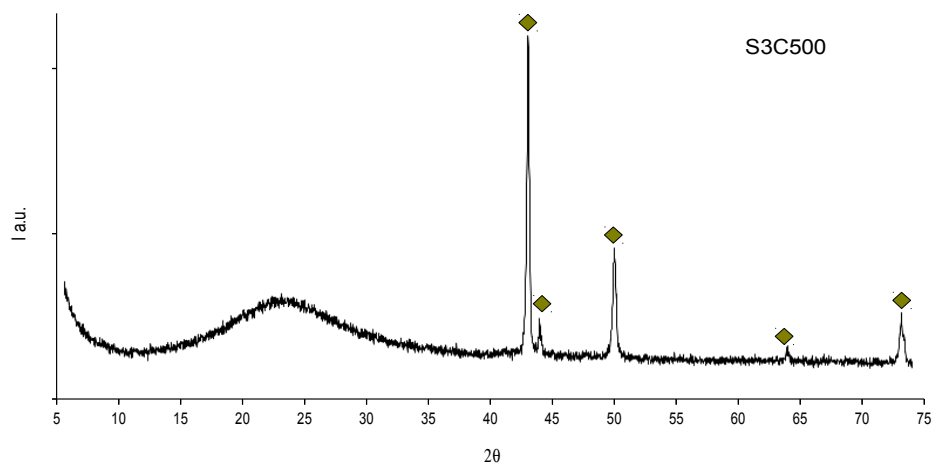


Figure 38: XRD pattern of 10%Cu/SiO<sub>2</sub> made at UniVe

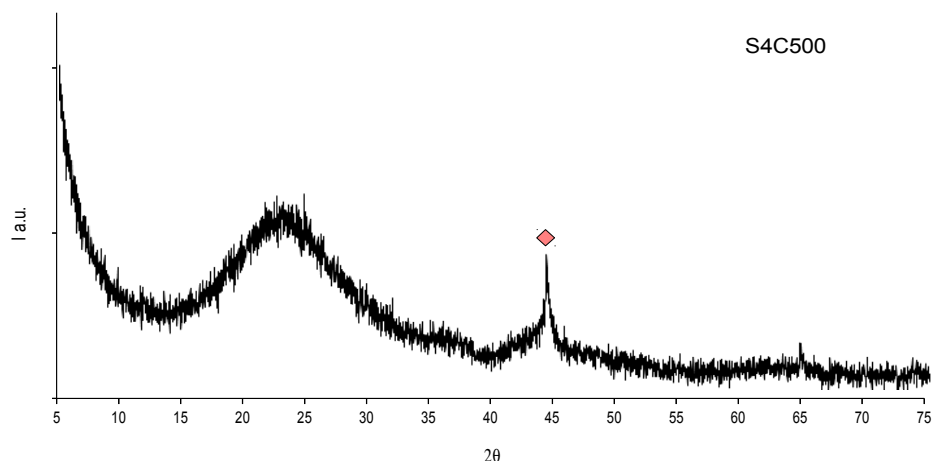


Figure 39: XRD pattern of 10%Co/SiO<sub>2</sub> made at UniVe

In Figure 38 (sample S3C500 10wt%Cu/SiO<sub>2</sub>) were visible reflections of Cu JCPDS 00-085-1326 (◊), while for the 10wt%Co/SiO<sub>2</sub> (Figure 39) only one peak of αCo JCPDS file 00-089-4307 (◊) was visible.

Finally, catalysts were prepared with formulation 10%Ni/ZrO<sub>2</sub> both using wet impregnation (after calcination at 500 and 800°C) and FP.

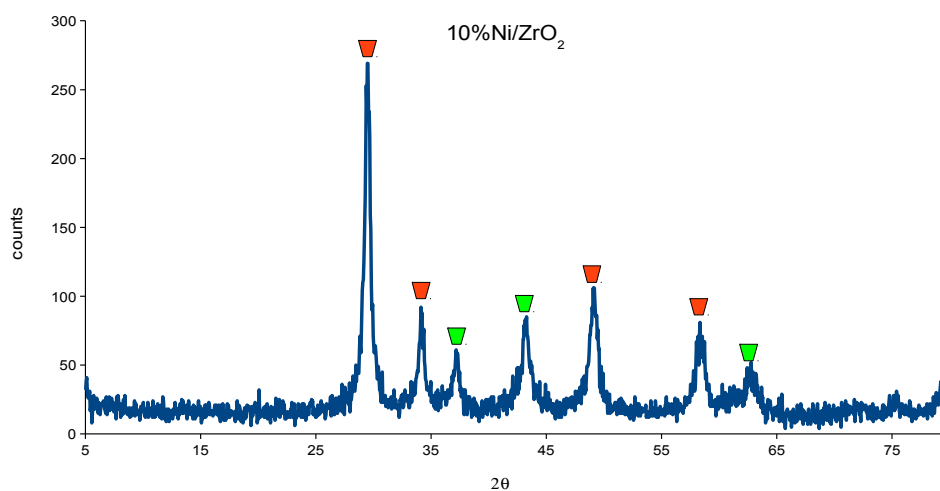


Figure 40: XRD pattern of 10%Ni/ZrO<sub>2</sub> FP made

The diffractogram of the FP made 10wt%Ni/ZrO<sub>2</sub> is reported in Figure 40, while in Figure 41 the same sample made by impregnation of the support obtained by precipitation and calcined at 500°C. They showed to be constituted by the same components, in particular ZrO<sub>2</sub> JCPDS file 00-002-0733 (▼) and NiO JCPDS file 00-04-0850 (▼). Also sample Z2C800 showed the same XRD structure (here not reported) and nickel dispersion seemed unaffected by the calcination temperature.

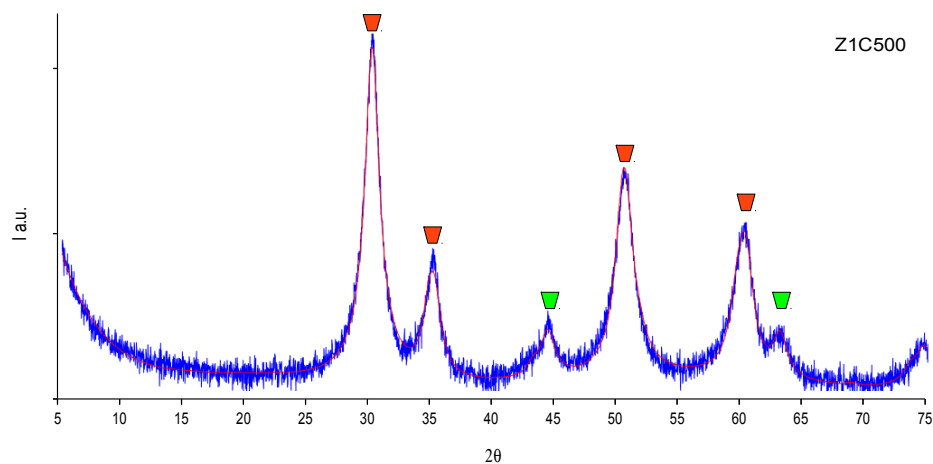


Figure 41: XRD pattern of 10%Ni/ZrO<sub>2</sub> made at UniVe

LaMeOx cataòysts were also synthesised by FP.

The XRD pattern of the FP-made LaCoO<sub>3</sub> is reported in Figure 42. The main component identified was LaCoO<sub>3</sub> JCPDS file 00-025-1060 (◀). In Figure 43 we report the same sample after reduction at 800°C with H<sub>2</sub>. As in the case of LaNiO<sub>3</sub> (Figure 32) the main phase became La(OH)<sub>3</sub> (▶) with a signal attributed to αCo JCPDS file 00-089-4307 (◀).

The XRD of La<sub>0.4</sub>Sr<sub>0.2</sub>NiO<sub>3</sub> made by FP is reported in Figure 44. The introduction of Sr atoms seems not to change the structure of the sample that is composed mainly by La<sub>2</sub>NiO<sub>4</sub> JCPDS file 01-070-1333 (◀) with some reflections attributed to nickel oxide NiO JCPDS file 00-002-1216 (◀). By contrast, La<sub>0.7</sub>Ce<sub>0.3</sub>NiO<sub>3</sub> (Figure 45) showed composed by LaNiO<sub>3</sub> JCPDS file 01-034-1181 (◀), CeO<sub>2</sub> JCPDS file 00-004-0593 (◀) and NiO (◀). Therefore no complete Ce incorporation into the perovskite structure was obtained.

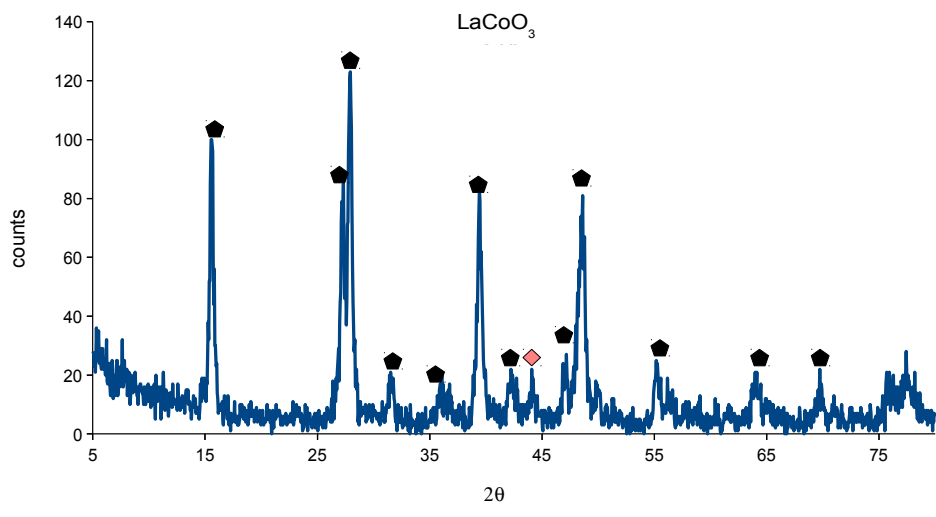


Figure 42: XRD pattern of  $\text{LaCoO}_3$  FP made, activated

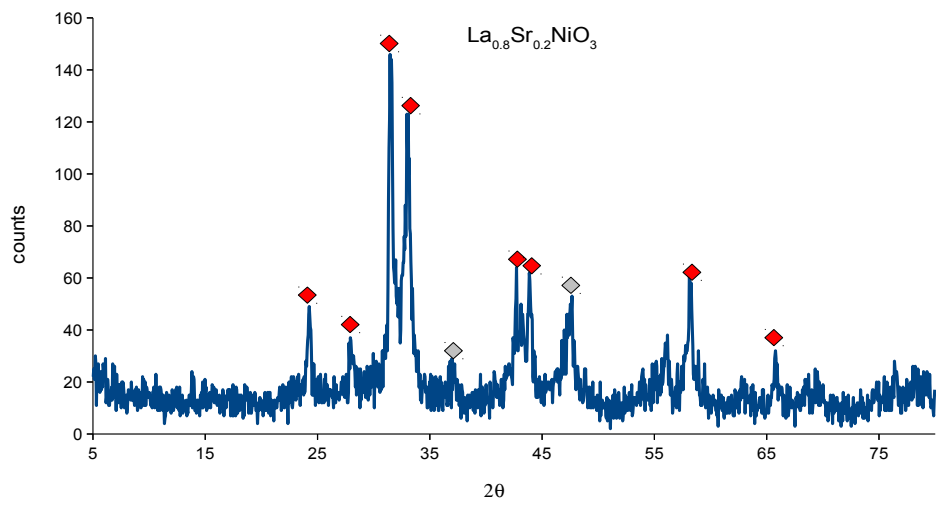


Figure 43: XRD pattern of FP made  $\text{La}_{0.8}\text{Sr}_{0.2}\text{NiO}_3$

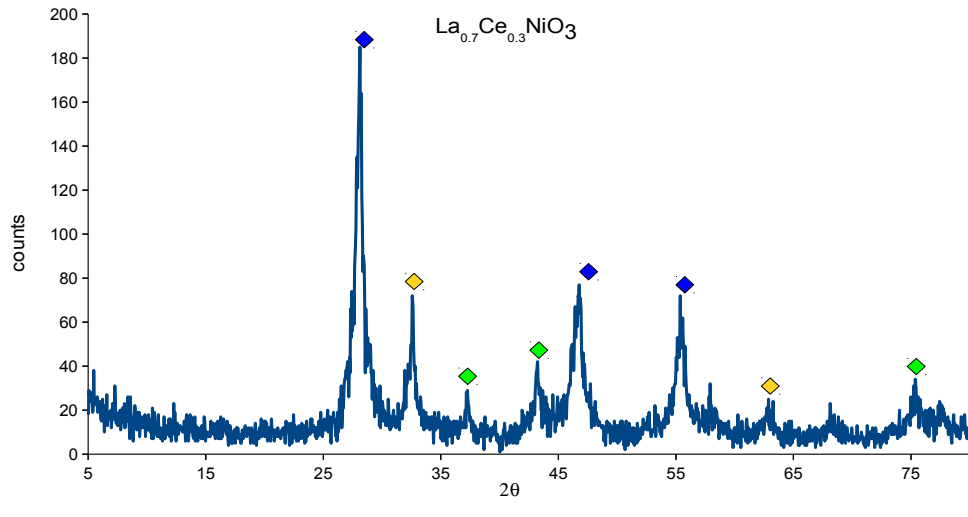


Figure 44: XRD pattern of FP made  $\text{La}_{0.7}\text{Ce}_{0.3}\text{NiO}_3$

## BET

**Table 8 :specific surface area of the samples**

Key legend

SSA= specific surface area

d= pore dimension

FP= one step flame pyrolysis synthesis

FP+IMP= impregnation on FP made support

IW IMP + calc= incipient wetness impregnation + calcination at xxx°C

Name	composition	Synthesis	SSA (m <sup>2</sup> /g)	d (nm)
Al <sub>2</sub> O <sub>3</sub>	Al <sub>2</sub> O <sub>3</sub>	FP	180	13
TiO <sub>2</sub>	TiO <sub>2</sub>	FP	84	nd
La <sub>2</sub> O <sub>3</sub>	La <sub>2</sub> O <sub>3</sub>	FP	41	nd
DTI2	10%NiTiO <sub>2</sub>	FP+ IMP	6.4	15
LAD2	10%Ni/La <sub>2</sub> O <sub>3</sub>	FP+ IMP	11	7.4
FTI2	10%Ni/TiO <sub>2</sub>	FP	62	10.5
FLAD2	10%Ni/La <sub>2</sub> O <sub>3</sub>	FP	42	21
MC10	10%Ni/SiO <sub>2</sub>	FP	221	13.1
MC12	10%Co/TiO <sub>2</sub>	FP	57	11.9
MC11	10%Co/SiO <sub>2</sub>	FP	174	14.9
MC13	10%Cu/TiO <sub>2</sub>	FP	44	12.8
MC14	10%Cu/SiO <sub>2</sub>	FP	163	13.6
MC15	10%Ni/ZrO <sub>2</sub>	FP	83	13.1
T1C500	10%Ni/TiO <sub>2</sub>	IW IMP + calc 500°C	101	4.1
T2C500	10%Ni/TiO <sub>2</sub>	IW IMP + calc 500°C	100	4.5
T3C800	10%Ni/TiO <sub>2</sub>	IW IMP + calc 800°C	4	32
T4C800	10%Ni/TiO <sub>2</sub>	IW IMP + calc 800°C	7	nd
S1C500	10%Ni/SiO <sub>2</sub>	IW IMP + calc 500°C	709	6
S2C800	10%Ni/SiO <sub>2</sub>	IW IMP + calc 800°C	309	6.3
Z1C500	10%Ni/ZrO <sub>2</sub>	IW IMP + calc 500°C	158	10.1
Z2C800	10%Ni/ZrO <sub>2</sub>	IW IMP + calc 800°C	43	18.7
T6C500	10%Co/TiO <sub>2</sub>	IW IMP + calc 500°C	63	10.5
T8C500	10%Co/TiO <sub>2</sub>	IW IMP + calc 500°C	211	13.1
S1C500	10%Co/SiO <sub>2</sub>	IW IMP + calc 500°C	629	6.4
T9C500	10%Cu/TiO <sub>2</sub>	IW IMP + calc 500°C	73	8.1
T11C500	10%Cu/TiO <sub>2</sub>	IW IMP + calc 500°C	49	12



S3C500	10%Cu/SiO <sub>2</sub>	IW IMP + calc 500°C	667	6.2
--------	------------------------	---------------------	-----	-----

First preliminary analysis were made on instrument 1 on the sample as prepared : support oxides showed SSA between 46 (TiO<sub>2</sub>) and 180 (Al<sub>2</sub>O<sub>3</sub>)m<sup>2</sup>/g. After deposition of the active phase by impregnation the SSA decrease (Table 7)

Instead samples made directly by-FP showed SSA values higher than their corresponding ones made by impregnation of the FP-made support (Table 7). Catalyst made by impregnation calcined at 500°C showed higher SSA than the corresponding samples calcined at 800°C. Among the support chosen SiO<sub>2</sub> exhibited the highest surface area ( around 700 m<sup>2</sup>/g when calcined at 500°C, but still over 200 m<sup>2</sup>/g when directly prepared by FP). As a general conclusion one may notice that for TiO<sub>2</sub> supported samples obtained by precipitation and calcined at 500°C the surface area was ca. double than for the FP prepared one, but it dropped to a few m<sup>2</sup>/g after calcination at 800°C, compatible with the working temperature of the high temperature SR tests.

Analysis on FP made catalysts 10%Ni/TiO<sub>2</sub> and 10%Ni/SiO<sub>2</sub> are reported in figure 45. For this catalysts only interparticle porosity was found. The pore distribution showed very broad for both kinds of supports. In particular it could be noticed that the value of the SSA of 10%Ni/TiO<sub>2</sub> is quite the same measured with instrument 1 = 62 m<sup>2</sup>/g or with instrument 2 = 63m<sup>2</sup>/g. This indicates that the sample is stable and the condition of degassing does not affect the SSA. Analysis on FP made catalysts supported on TiO<sub>2</sub> and SiO<sub>2</sub> with cobalt as active phase are reported in figure 46 (MC11; MC12) was evidenced adsorption at high relative pressure, indicating a substantially macroporous system. This is congruent with the formation of dense nanoparticles forming agglomerates. Accordingly, the pore size distribution was broad and not uniform, thus indicating that the porosity here evidenced was secondary. The surface area of the titania based catalysts was around 50 m<sup>2</sup>/g, whereas that of the silica based ones ranged around 160-175 m<sup>2</sup>/g (Table 8). The same behaviour is showed by Cu catalysts (MC13-MC14).

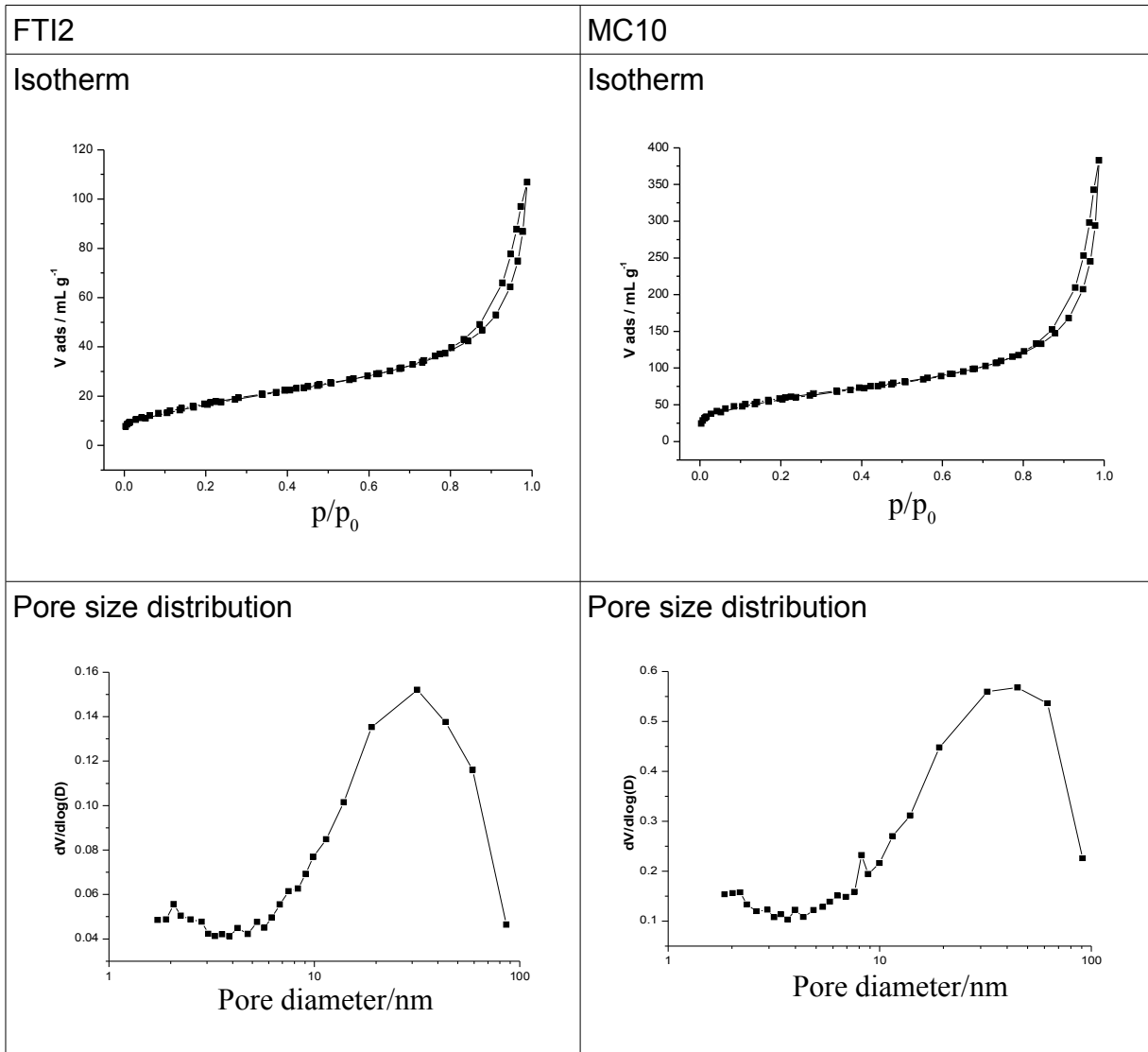
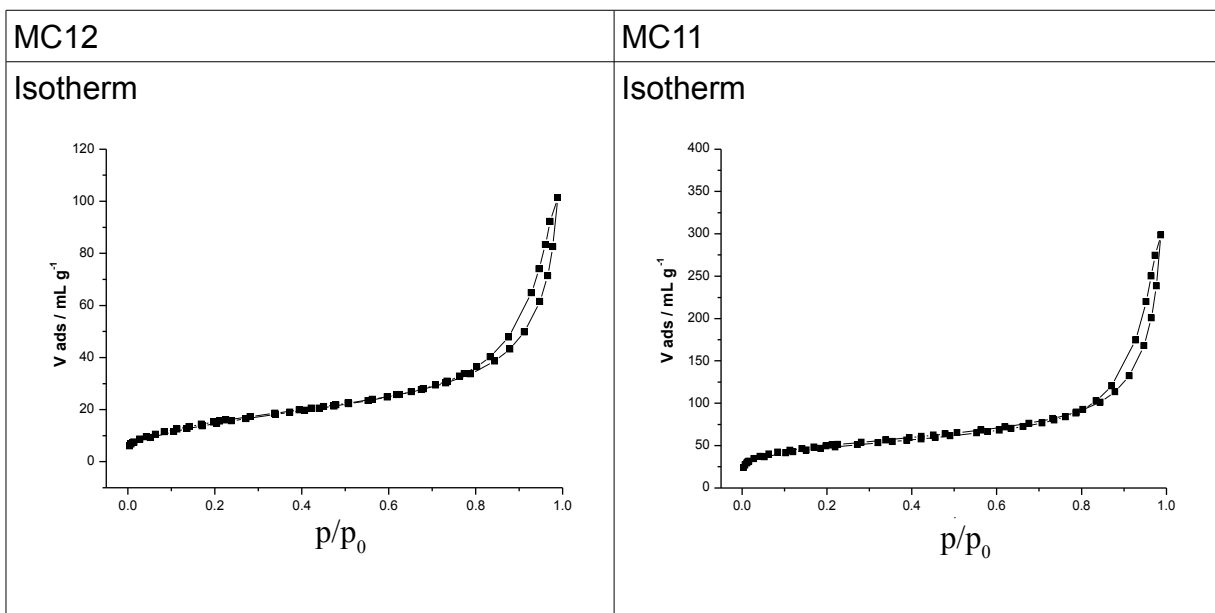


Figure 45: Adsorption/desorption isotherm and pores size distribution of FTI2 and MC10



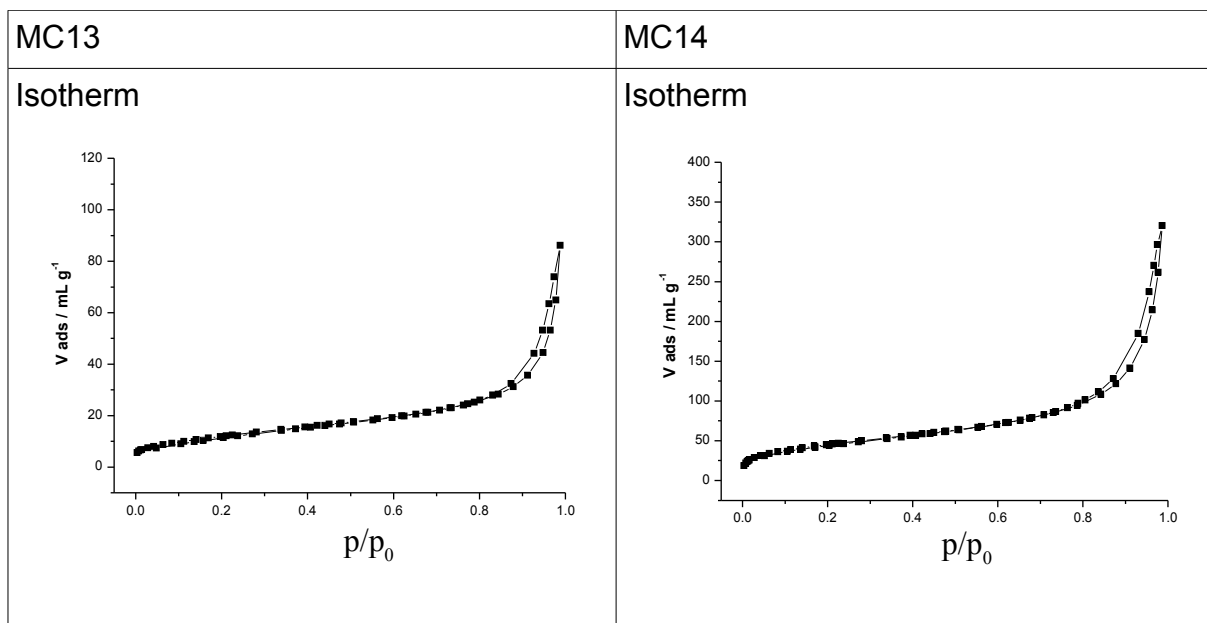


Figure 46: Adsorption/desorption isotherm of FP made Co catalysts MC11-MC12 and of FP made Cu catalysts MC13-MC14.

Results of analysis made on catalysts made by incipient wetness impregnation on  $\text{TiO}_2$  and calcined at  $500^\circ\text{C}$  are reported in Figure 47. Both samples show a IV-type isotherm, which is typical of mesoporous materials characterized by a quite high surface area and an unimodal pores size distribution.

High temperature calcination caused the collapse of the porous structure of the oxides, thus obtaining a substantially non-porous materials (Figure 48). Samples calcined at  $800^\circ\text{C}$  shows a SSA similar to the value of the sample made by impregnation on FP made  $\text{TiO}_2$  (Table 8)

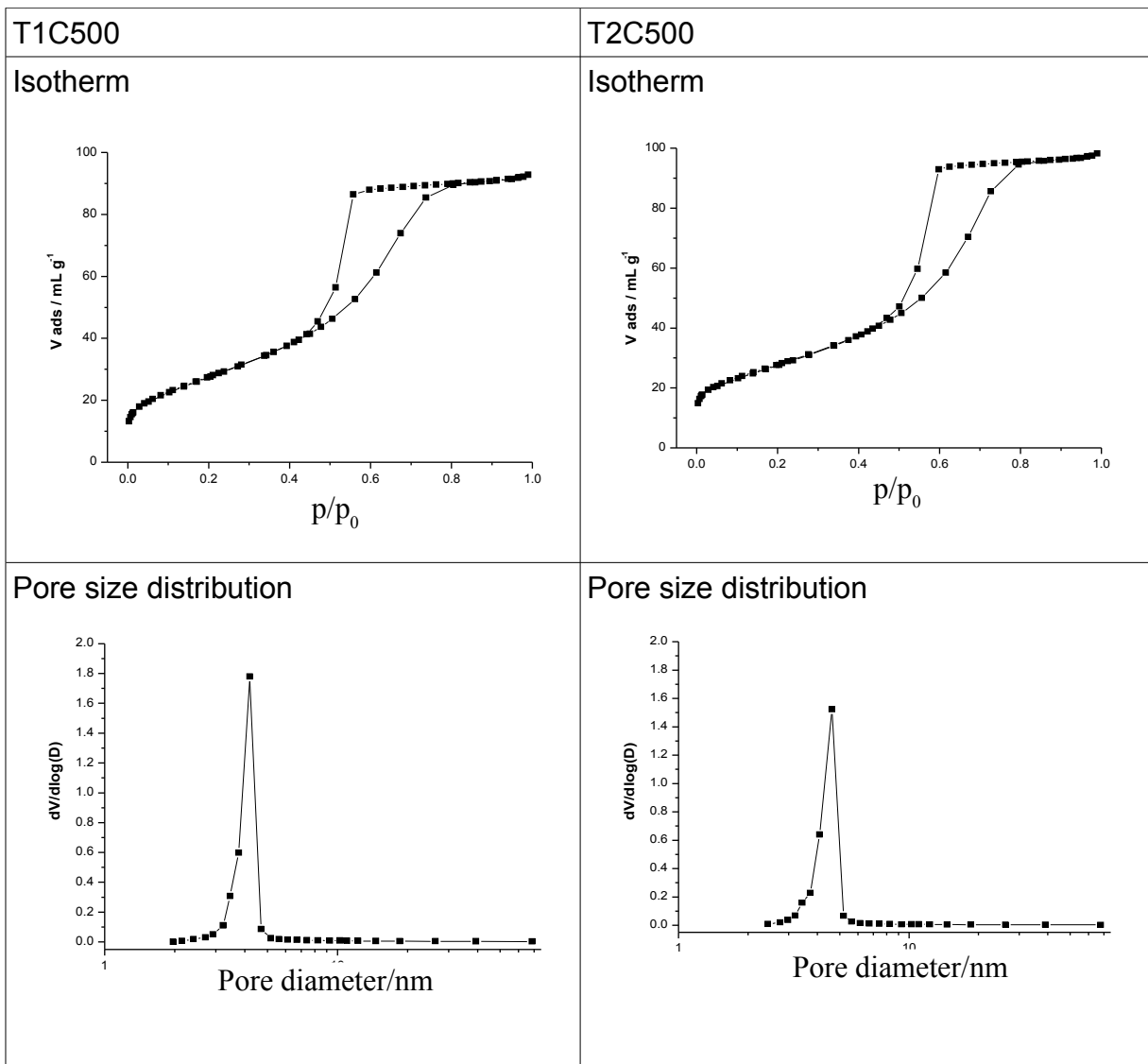
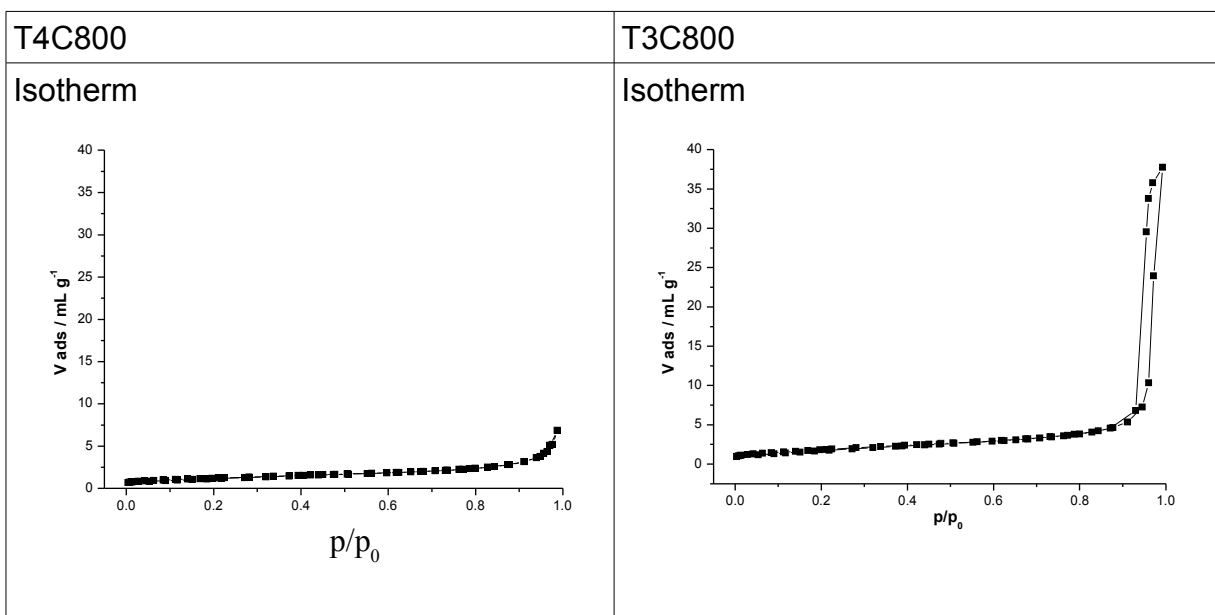


Figure 47: Adsorption/desorption isotherm and pore distribution of catalyst made by wetness impregnation and calcined at 500°C



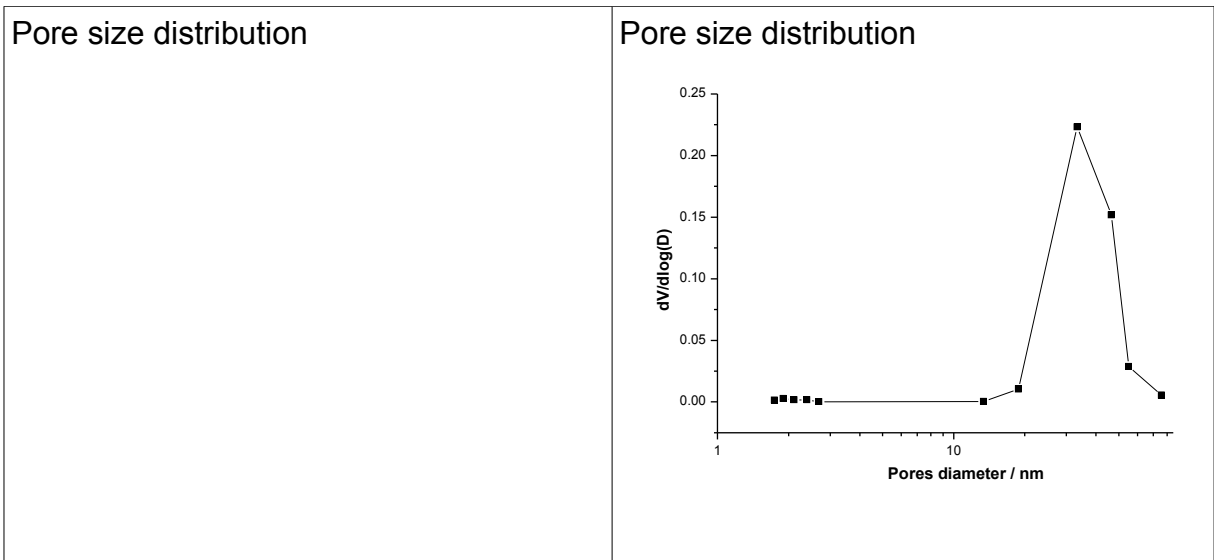


Figure 48: Adsorption/desorption isotherm and pore distribution of catalyst made by wetness impregnation and calcined at 800°C

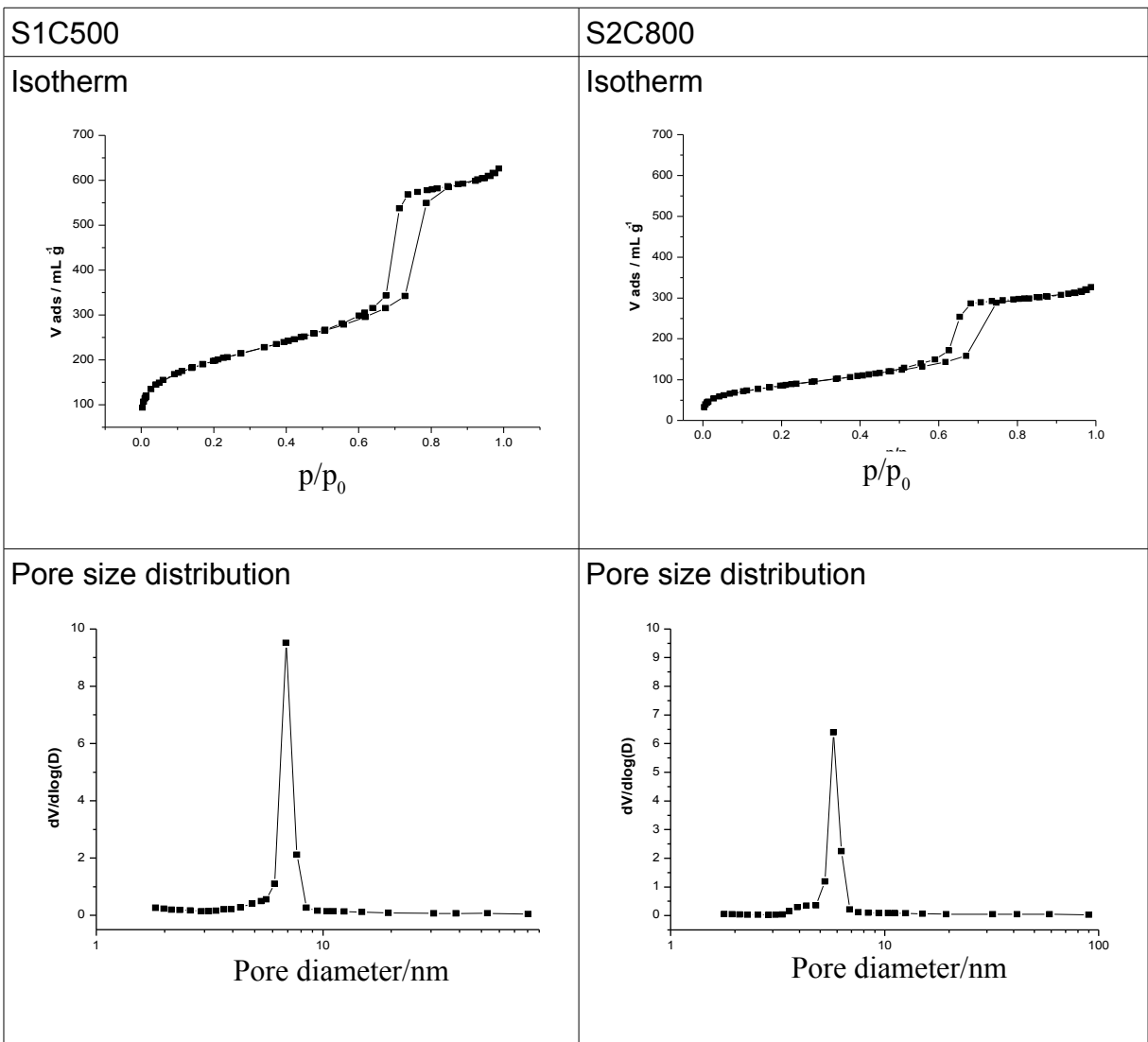


Figure 49: Adsorption/desorption isotherm and pore distribution of catalyst made by wetness impregnation on SiO<sub>2</sub> calcined at 500°C and at 800°C

The adsorption/desorption isotherms and the pores size distribution of the SBA-15 supported catalysts are reported in Figure 49. Sample S1C500 shows a IV-type isotherm with a H1-type hysteresis, which is typical of this support, a mesoporous material with a high surface area ( $\approx 700 \text{ m}^2/\text{g}$ ) and a sharp pores size distribution with a maximum at 6 nm (Table 8). The shape of the isotherm of S2C800 remained unchanged, so it is possible to suppose that the mesoporous structure of the material has been preserved, as demonstrated also by TEM microscopy (*vide infra*) but the high temperature calcination caused a significant contraction of the surface area (down to *ca.*  $300 \text{ m}^2/\text{g}$ ). The pores size distribution was still sharp with a maximum at 6 nm.

The adsorption/desorption isotherm and the pores size distribution of the  $\text{ZrO}_2$  supported catalyst are reported in Figure 50. Sample Z1C500 exhibits a IV-type isotherm containing a H3-type hysteresis, typical of materials that do not possess a well-defined mesoporous structure.

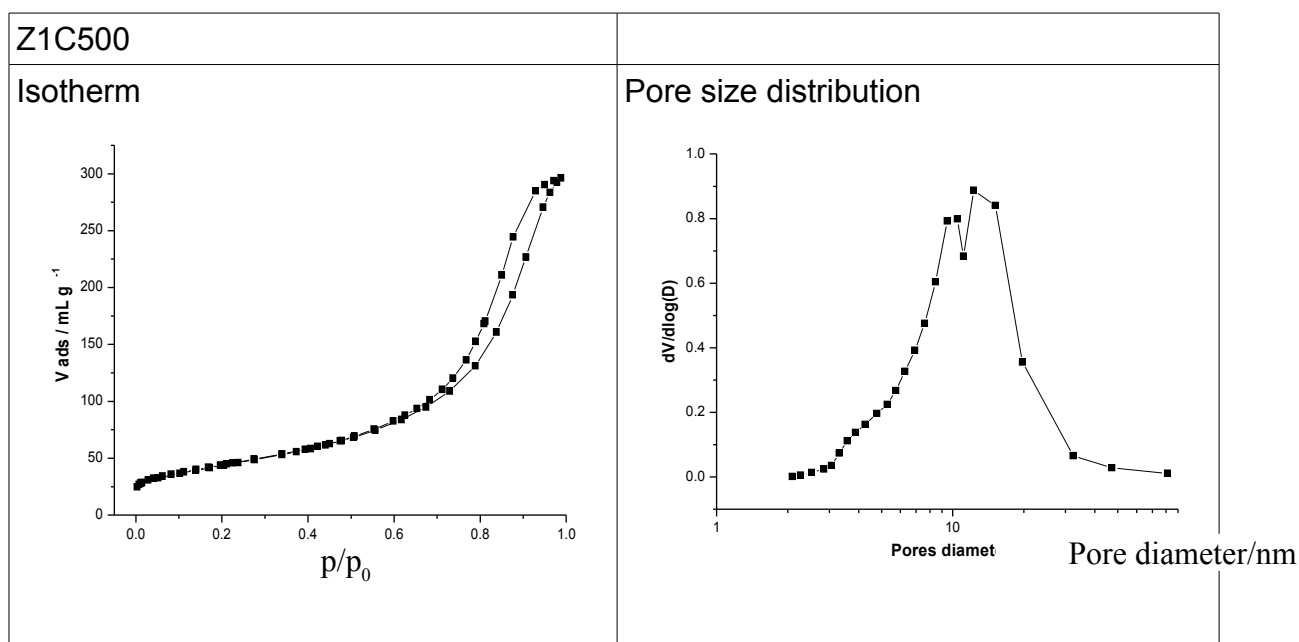


Figure 50: Adsorption/desorption isotherm and pore distribution of catalyst made by wetness impregnation on  $\text{ZrO}_2$  calcined at  $500^\circ\text{C}$

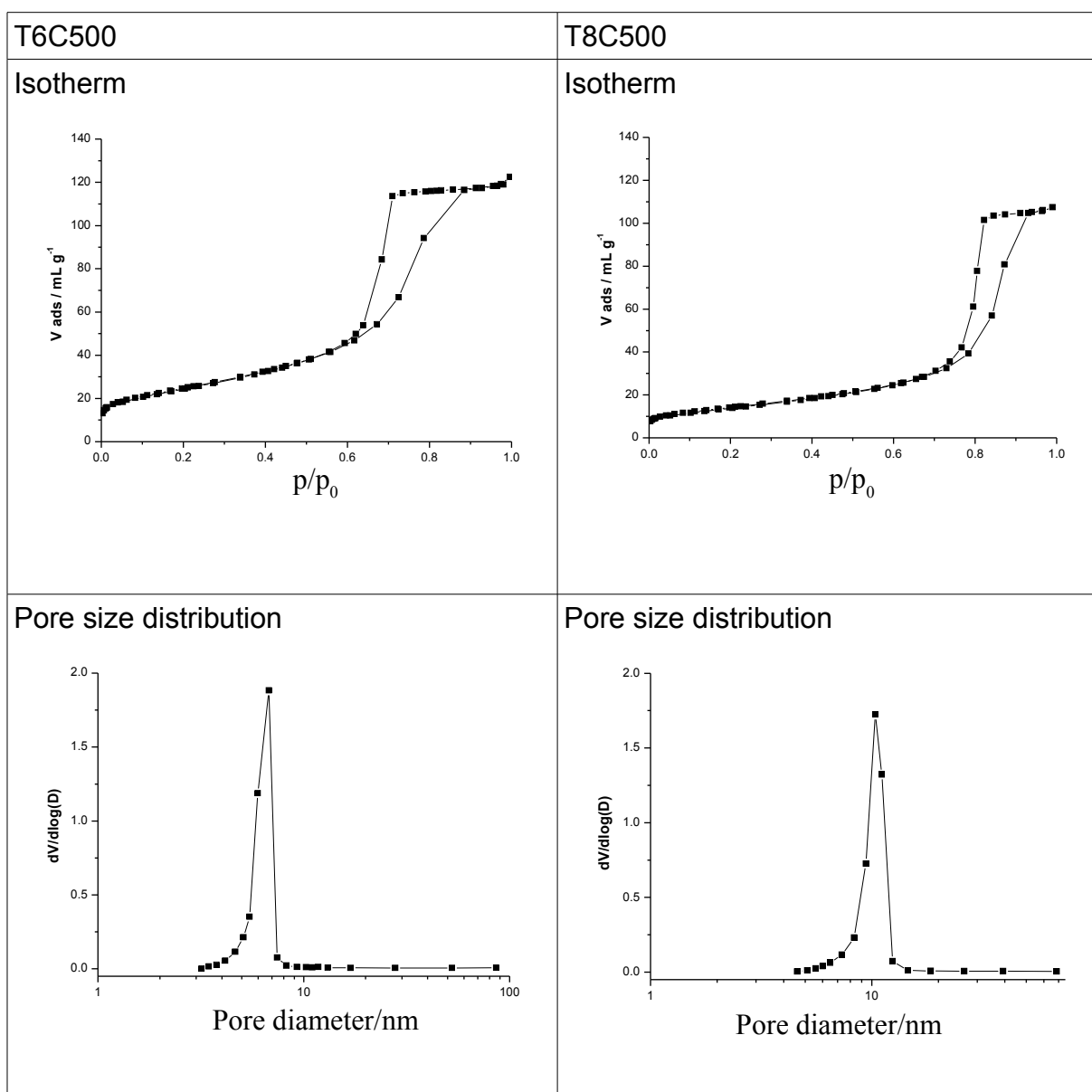


Figure 51 Adsorption/desorption isotherm and pore distribution of catalyst made by wetness impregnation of Co on  $\text{TiO}_2$  calcined at  $500^\circ\text{C}$

Samples T6C500 and T8C500 showed a IV-type isotherm, indicating a mesoporous system. A H1 hysteresis suggests a uniform distribution of mesopores. The SSA was not very high, lower than that of Ni-based samples (table 8), with a correspondingly higher mean pore size.

Sample S4C500 (figure 52) showed a IV-type isotherm, typical of this support. The specific surface area was high ( $\approx 630 \text{ m}^2/\text{g}$ ) and a sharp and unimodal pore size distribution was observed, centred around 6.4 nm.

The same comments hold for the homologue Cu-based samples, whose results are reported below ( Fig 53-54).

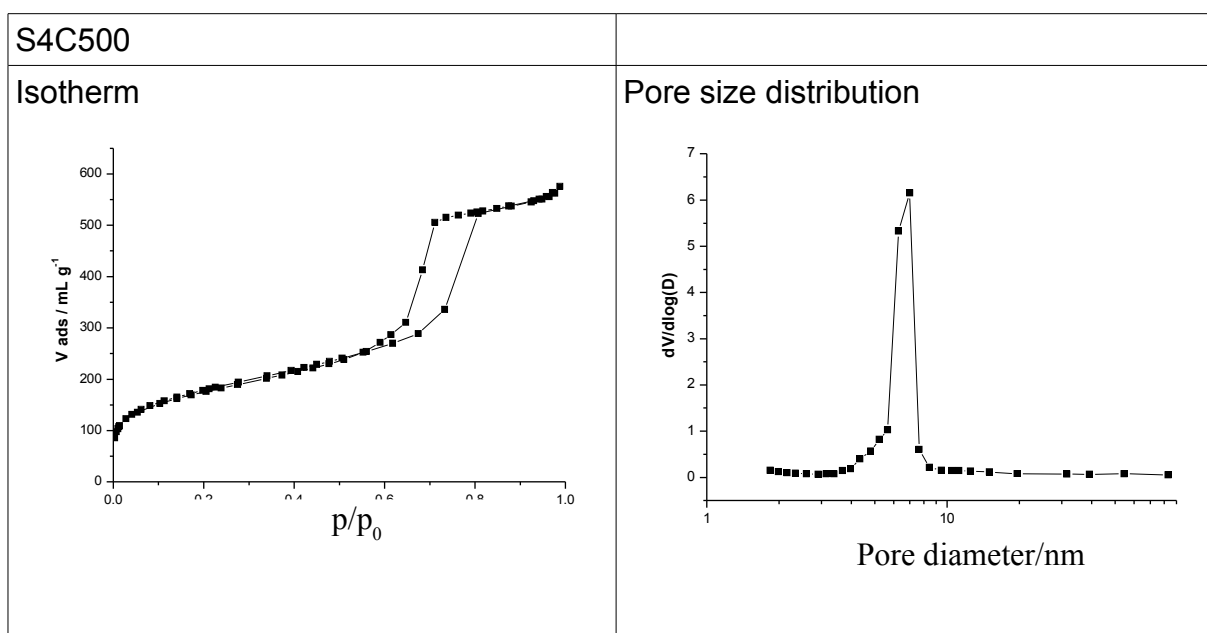


Figure 52 Adsorption/desorption isotherm and pore distribution of catalyst made by wetness impregnation of Co on SiO<sub>2</sub> calcined at 500°C

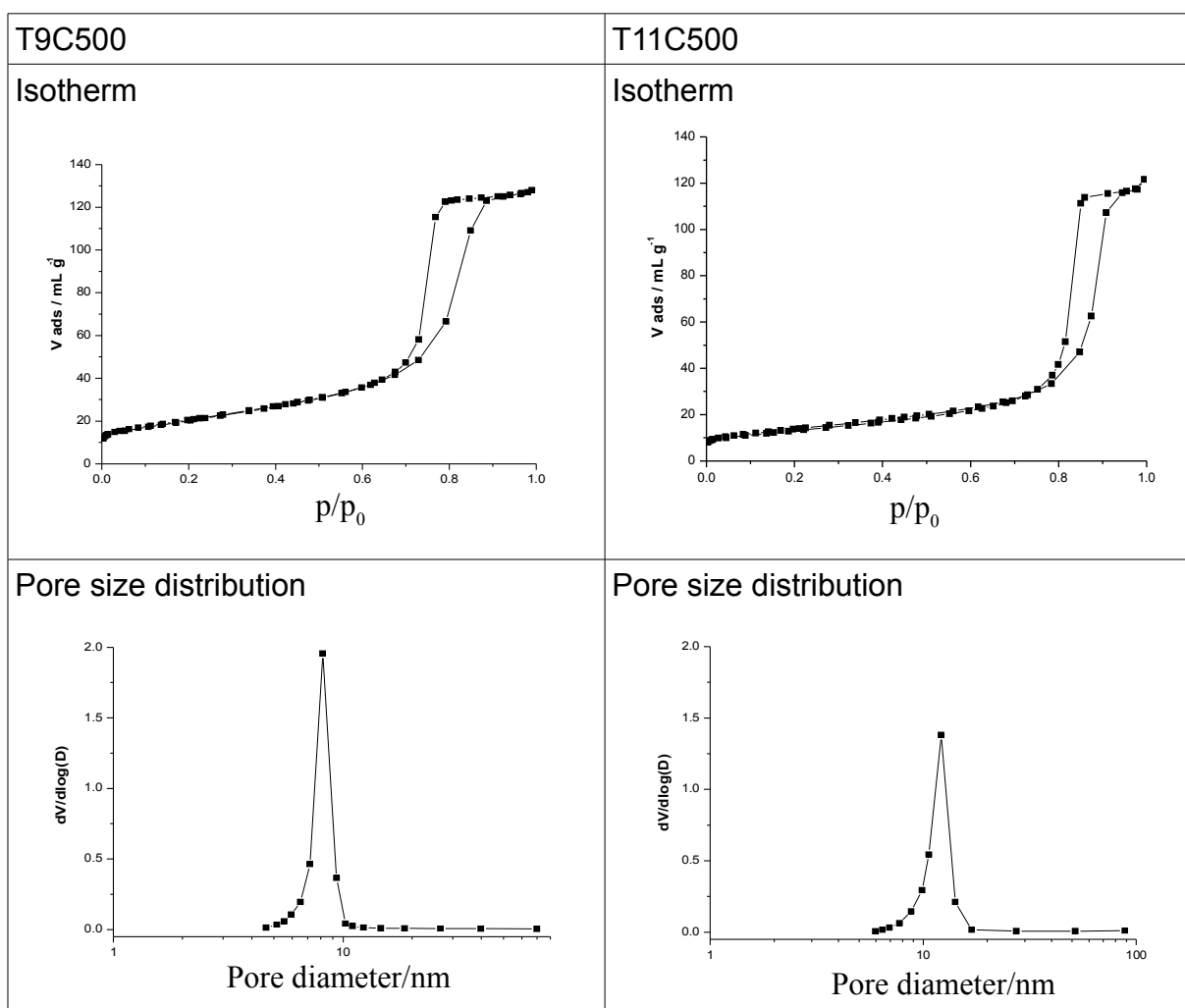




Figure 53 Adsorption/desorption isotherm and pore distribution of catalyst made by wetness impregnation of Cu on TiO<sub>2</sub> calcined at 500°C

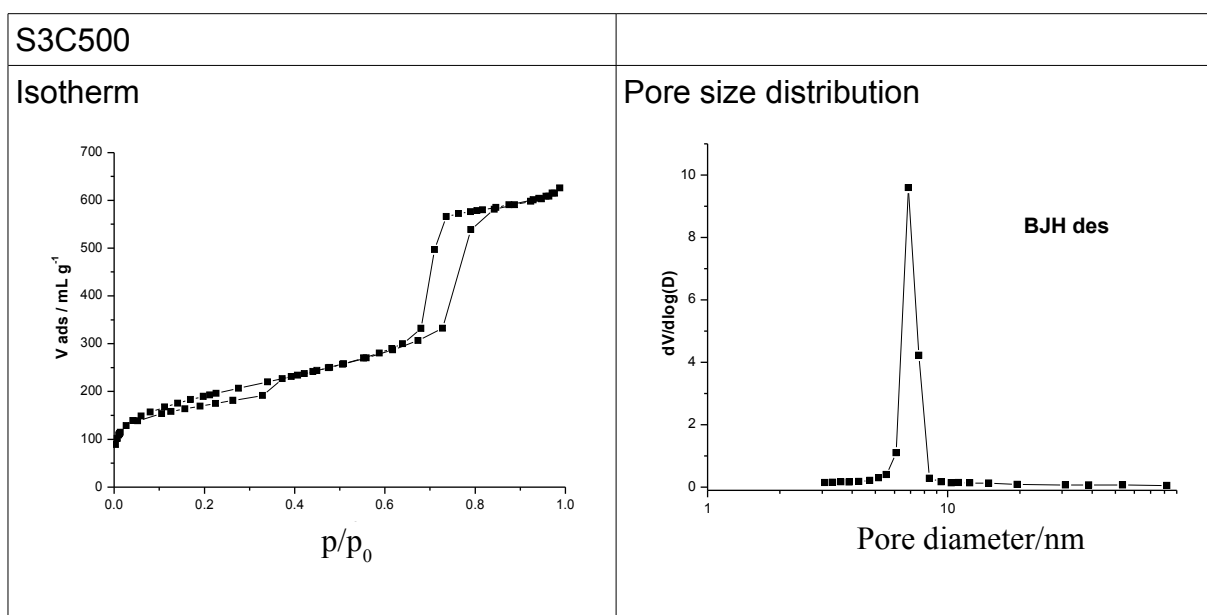


Figure 54 Adsorption/desorption isotherm and pore distribution of catalyst made by wetness impregnation of Cu on SiO<sub>2</sub> calcined at 500°C.

## SEM-TEM

EDX analysis was used to semiquantitatively assess sample composition. Spot and mapping analyses also allowed to check the uniformity of composition. Usually 1 μm cube of the sample is interested by this analysis, values are therefore an average on such zone. Composition of the samples are quite different from the theoretical formula, i.e TiO<sub>2</sub> should possessed an atomic ratio of 1:2 Ti:O, while in Table 9 it showed a ratio of 1:3,5 Ti:O this is due to a bad detection of the oxygen. As detected also by atomic absorption the is not 10% depending on the synthesis procedure.

**Table 9: EDX analysis on the samples**

Sample	Atoms	Weigh %	Atomic %
TiO <sub>2</sub>	O	44.26	70.39
	Ti	55.74	20.61
La <sub>2</sub> O <sub>3</sub>	O	15.88	62.11
	La	84.12	37.89
10 wt% Ni/TiO <sub>2</sub>	O	36-46	73-64
	Ti	44-37	19-26
	Ni	19-16	7-9
10 wt% Ni/La <sub>2</sub> O <sub>3</sub>	O	19-23	65-70

	La	73-71	28-24
	Ni	7-5	6-5
FP-10 wt% Ni/TiO <sub>2</sub>	O	37-38	64-65
	Ti	59-55	33-31
	Ni	6-7	3
FP-10 wt% Ni/La <sub>2</sub> O <sub>3</sub>	O	9-13	43-53
	La	86-78	45-57
	Ni	8	9-10
FP10 wt% Ni/SiO <sub>2</sub>	O	44.58	60.49
	Si	47.16	36.46
	Ni	8.26	3.05
FP-10 wt% Co/SiO <sub>2</sub>	O	32-36	47-44
	Si	65-55	50-52
	Co	5-8	2-3
FP-10 wt% Cu/SiO <sub>2</sub>	O	40-43	57-58
	Si	45-46	37-36
	Cu	14-10	5-4
FP-10 wt% Co/TiO <sub>2</sub>	O	49-31	69-58
	Ti	47-38	26-36
	Co	11	5
FP-10 wt% Cu/TiO <sub>2</sub>	O	35-37	4
	Ti	55	32
	Cu	10-9	64-62
FP-LaNiO <sub>3</sub>	O	12.82	48.10
	La	63.08	27.26
	Ni	24.10	24.64
FP-La <sub>0.8</sub> Sr <sub>0.2</sub> NiO <sub>3</sub>	O	14-11	49-43
	La	52-49	6-4
	Sr	9-6	21-22
	Ni	25-23	24
FP- La <sub>0.7</sub> Ce <sub>0.3</sub> NiO <sub>3</sub>	O	17.32	56.65
	La	17.54	6.1
	Ce	41.13	15.36
	Ni	24	21.39

SEM and TEM pictures of various samples are reported in the following figures.

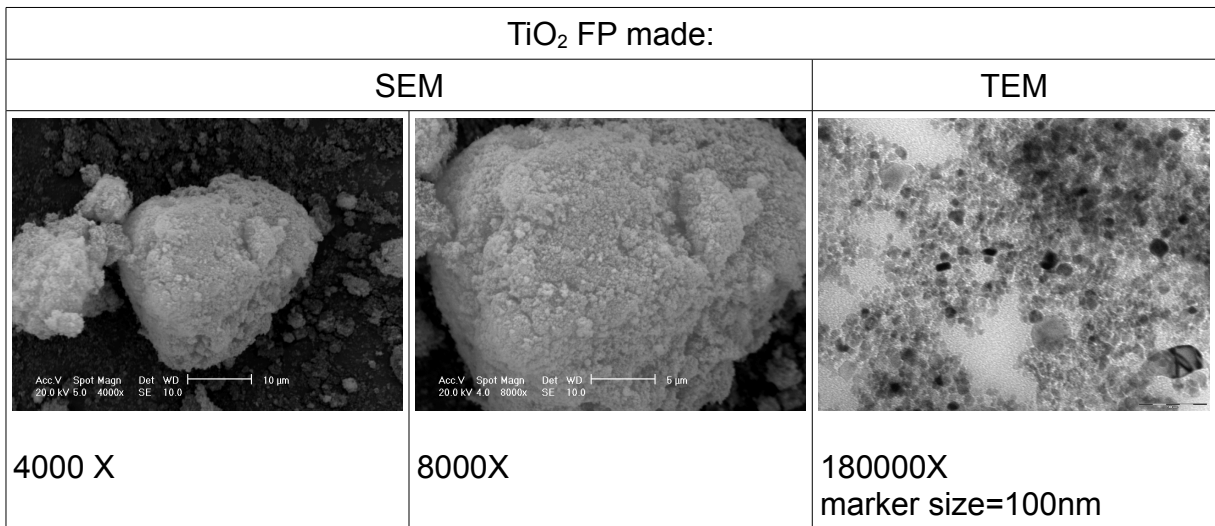


Figure 55: SEM-TEM pictures of FP made TiO<sub>2</sub>

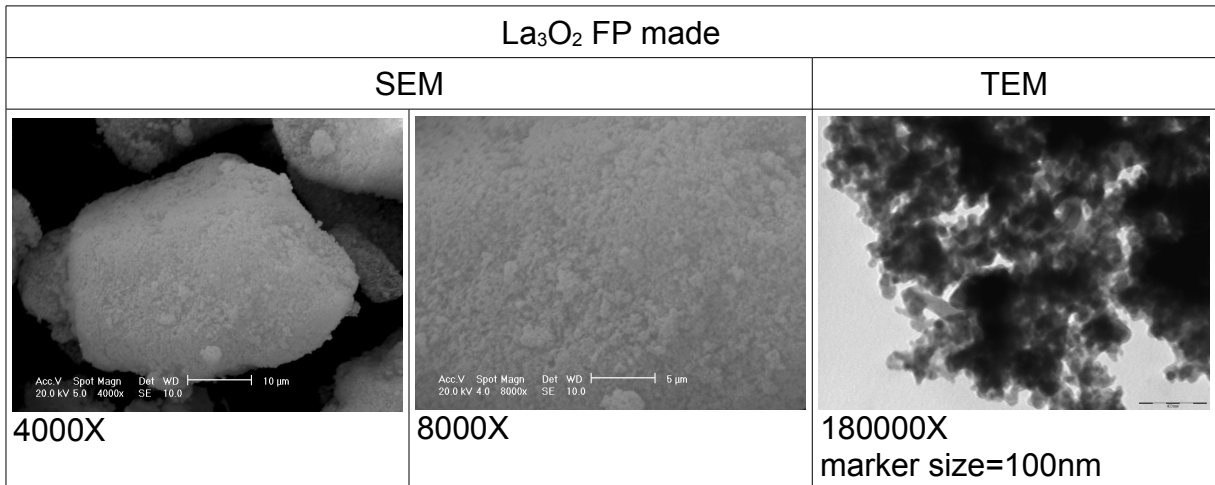
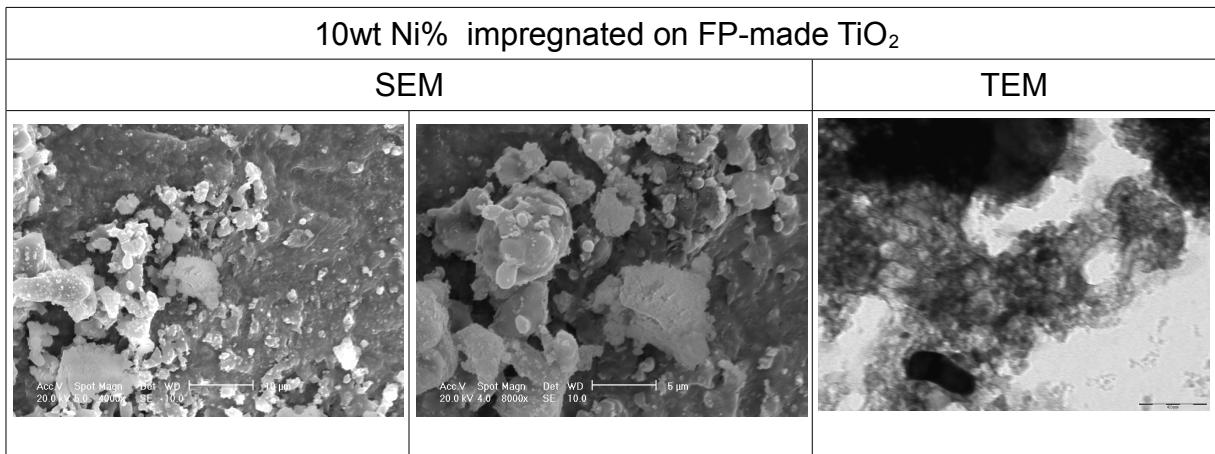


Figure 56 : SEM-TEM pictures of FP made La<sub>2</sub>O<sub>3</sub>

Both samples seem composed of agglomerates of small particles (10-20nm), but those of TiO<sub>2</sub> are more defined than the ones of La<sub>2</sub>O<sub>3</sub>. This could explain the bigger SSA shown above.



4000X	8000X	180000X marker size=100nm
-------	-------	------------------------------

Figure 57: SEM-TEM pictures of 10%Ni/TiO<sub>2</sub> impregnation of FP made support

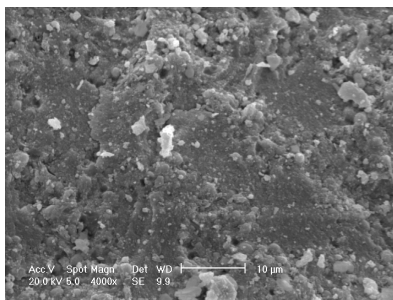
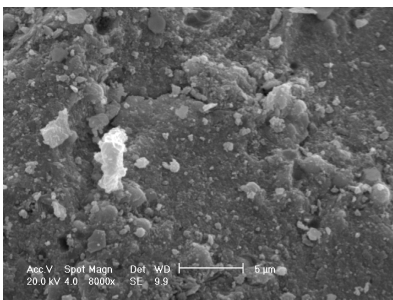
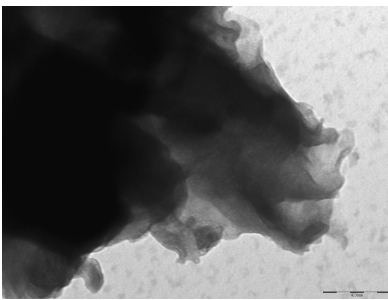
10wt Ni% impregnated on FP made La <sub>2</sub> O <sub>3</sub>		
SEM		TEM
		
4000X	8000X	180000X marker size=100nm
EDX		

Figure 58: SEM-TEM pictures of 10%Ni/La<sub>2</sub>O<sub>3</sub> impregnation of FP made support

Deposition of active phase over FP-made support generate a loss of definition especially in TEM images for both the catalyst. For 10%Ni/TiO<sub>2</sub> it could be noticed how particle were not defined neither uniform (Figure 57, TEM image). This could explain also the variation in EDX analysis made on different spots of the sample. Even for 10%Ni/La<sub>2</sub>O<sub>3</sub> TEM analysis did not show well defined particles, but characterised by to small differences in the spot EDX analysis.

Differences in composition of the sample with respect to the nominal value could also be due to the fact that analyses were made on as prepared samples, with oxidise Ni. SEM-TEM analysis on direct FP-made catalyst are reported in Figure 59 (10%Ni/TiO<sub>2</sub>) and in Figure 60 (10%Ni/La<sub>2</sub>O<sub>3</sub>). These catalysts shows a composition more similar to the one of the FP-made support (Figure 55 and 56). They are composed by agglomerates of small particles. For 10%Ni/TiO<sub>2</sub> TEM image showed the presence of well shaped spherical particles. In the image Figure 59 two different dimension distributions are visible: there are bigger particles with diameter of 100nm and smaller particle with diameter between 10-20nm.

By contrast, Figure 60 much more uniform particles with between 10-20nm. EDX analysis (Table 9) shows that composition was not very uniform especially for La and

O. This could be due to the presence of  $\text{La}_2\text{NiO}_4$  and  $\text{La}(\text{OH})_3$ , as detected by XRD analysis (Figure 28), which modifies the stoichiometric composition of the sample with respect the nominal value.

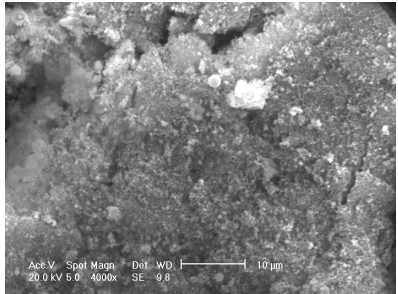
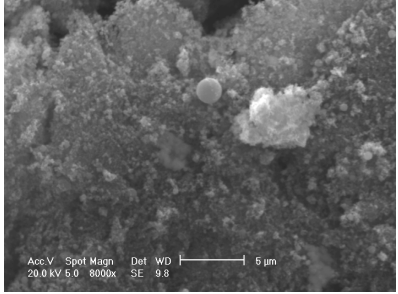
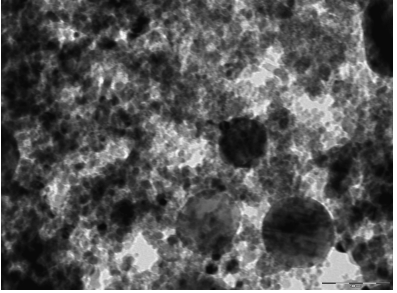
FP made 10wt Ni% /TiO <sub>2</sub>		
SEM	TEM	
		
4000X	8000X	180000X marker size=100nm

Figure 59: SEM-TEM pictures and EDX analysis of FP made 10%Ni/TiO<sub>2</sub>

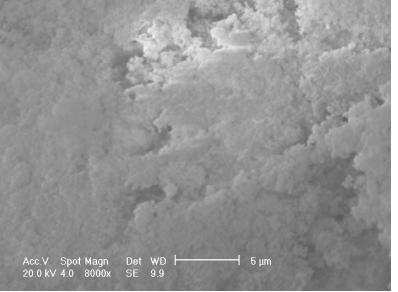
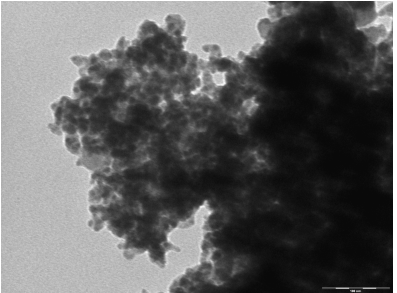
FP made 10wt Ni% /La <sub>2</sub> O <sub>3</sub>		
SEM	TEM	
N.D. 4000X		
	8000X	180000X marker size=100nm

Figure 60: SEM-TEM pictures and EDX analysis of FP made 10%Ni/La<sub>2</sub>O<sub>3</sub>

Different nickel in La-based samples or in Ti-based ones does not change the morphology with respect of what reported for the 10wt% samples.

SEM-EDX-TEM analysis on FP made SiO<sub>2</sub> based catalysts are reported in Figures 61-63 for samples 10%Ni, 10%Co, 10%Cu, respectively.

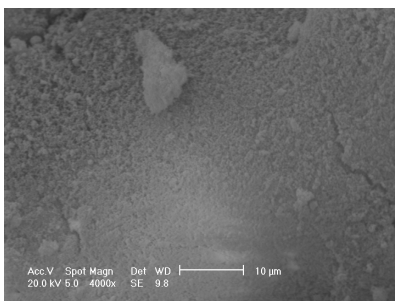
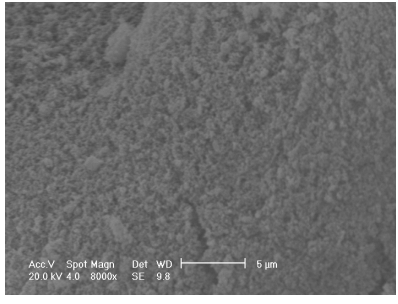
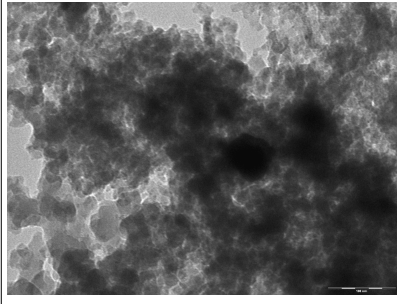
FP made 10wt Ni%/SiO <sub>2</sub>		
SEM		TEM
		
4000X	8000X	180000X marker size=100nm

Figure 61: SEM-TEM pictures of FP made 10%Ni/SiO<sub>2</sub>

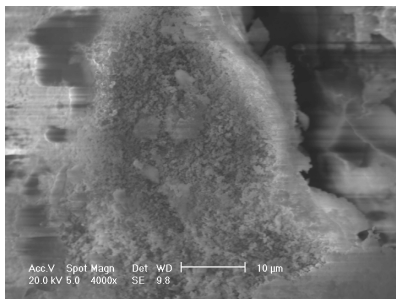
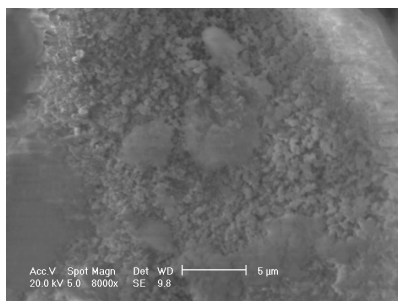
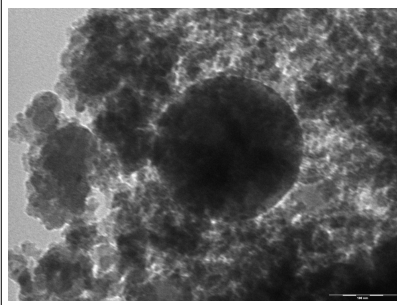
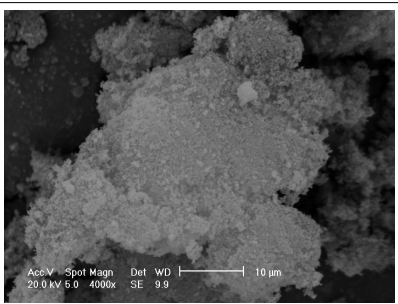
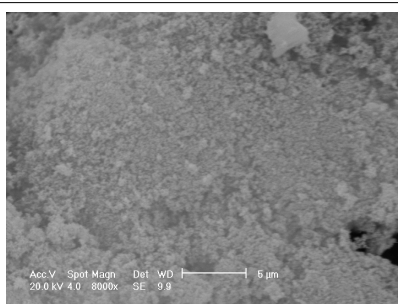
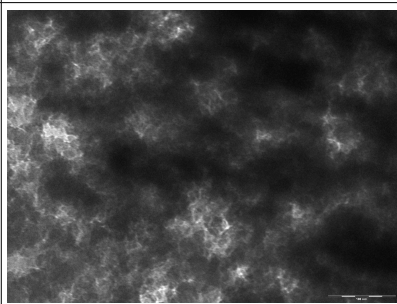
FP made 10wt Co%/SiO <sub>2</sub>		
SEM		TEM
		
4000X	8000X	180000X marker size=100nm

Figure 62: SEM-TEM pictures of FP made 10%Co/SiO<sub>2</sub>

FP made 10 wt Cu %/SiO <sub>2</sub>		
SEM		TEM
		
4000X	8000X	180000X

	marker size=100nm
--	-------------------

Figure 63: SEM-TEM pictures and EDX analysis of FP made 10%Cu/SiO<sub>2</sub>

As enlightened by XRD analysis (Figure 41), all these catalysts show a big component of amorphous phase in their structure indeed also the TEM pictures shows particles with not well defined shape and with variable size. Ni/SiO<sub>2</sub> (Figure 61) seems to be the most uniform among these three samples showing some particles of 60nm. In Co/SiO<sub>2</sub> TEM image shows the presence of a big spherical particle with a diameter bigger than 200nm.

Co (Figure 69) and Cu (figure 70) were also supported on TiO<sub>2</sub>.

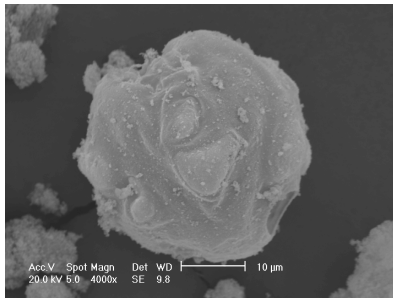
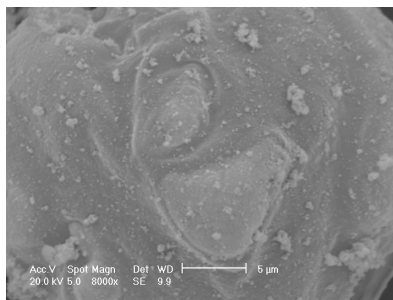
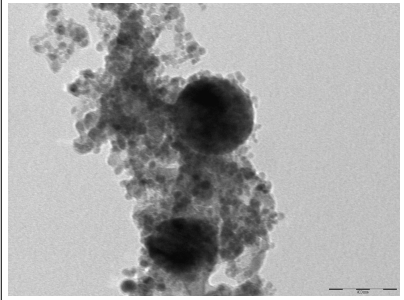
FP made 10wt Co %/TiO <sub>2</sub>		
SEM		TEM
		
4000X	8000X	180000X marker size=100nm

Figure 64: SEM-TEM pictures of FP made 10%Co/TiO<sub>2</sub>

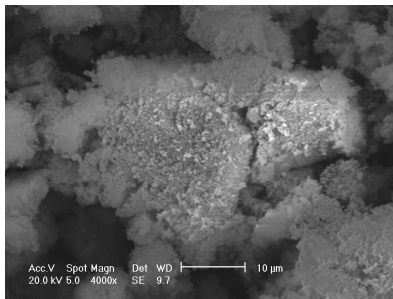
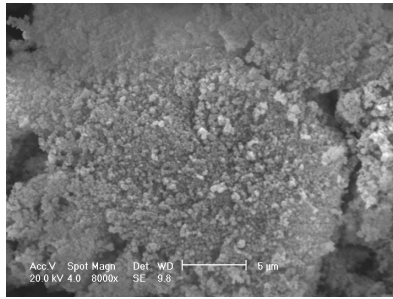
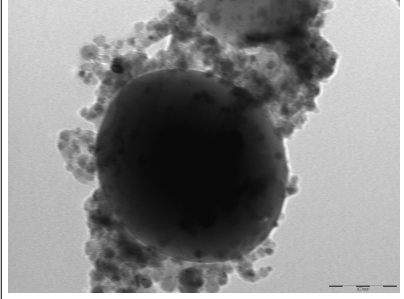
FP made 10wt Cu %/TiO <sub>2</sub>		
SEM		TEM
		
4000X	8000X	180000X marker size=100nm

Figure 65: SEM-TEM pictures of FP made 10%Cu/TiO<sub>2</sub>

As it was for bare TiO<sub>2</sub> and for 10%Ni/TiO<sub>2</sub> TEM micrographs enlighten the presence of agglomerates formed by spherical particles with two different sizes. For Co (Fig 64 ) there are particles with diameter of 10-20nm and bigger particle with a diameter of c.a. 120nm.

Furthermore, TEM images of Cu catalyst shows a presence of even bigger spherical particle with diameter > 240nm.

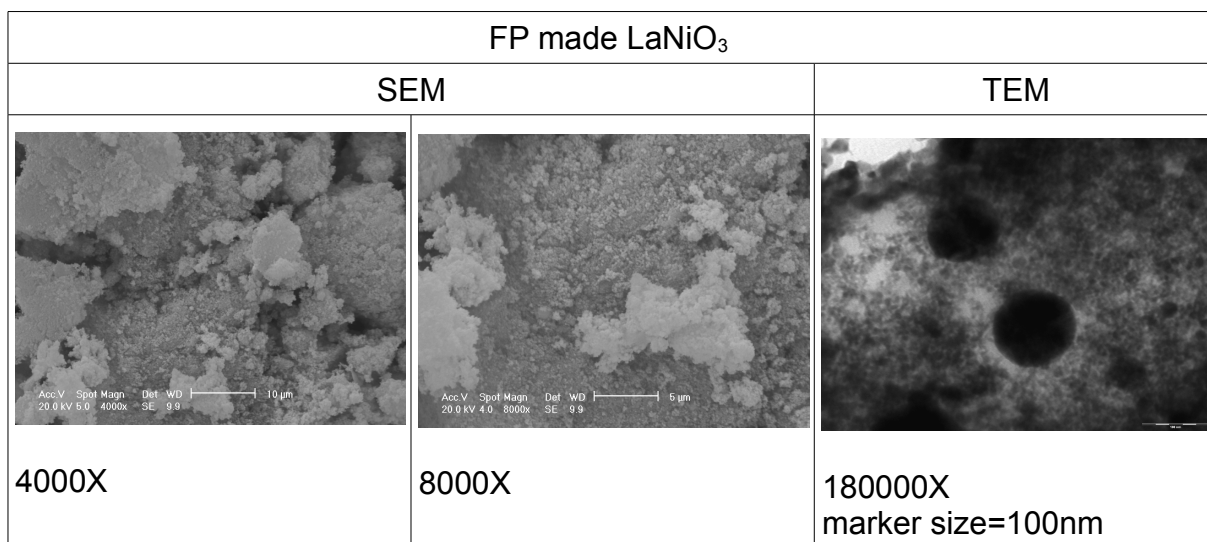


Figure 66: SEM-TEM pictures of FP made LaNiO<sub>3</sub>

Pictures in Figure 66 show that the sample is formed mainly by agglomeration of smaller spherical particles. Size distribution of these particles is very wide: 10-20nm, 30-60nm and some > 200nm.

When substituting La with Sr or Ce, even if XRD analysis showed a change in the structure when La was substituted with Ce (Figures 42-44), from SEM-TEM analysis no change in particle size or distribution was observed with the undoped sample.

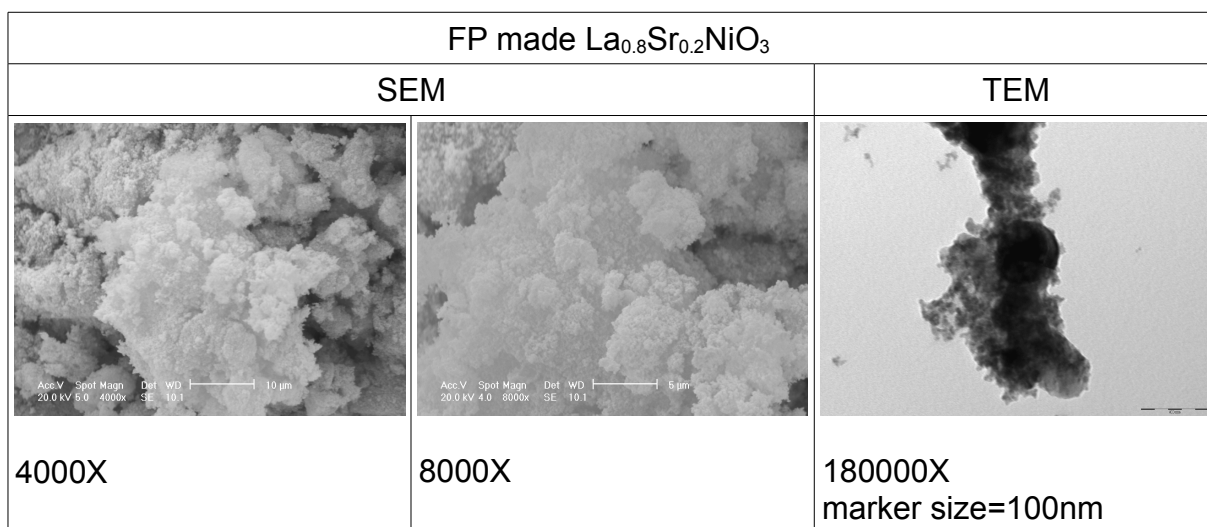


Figure 67: SEM-TEM pictures of FP made La<sub>0.8</sub>Sr<sub>0.2</sub>NiO<sub>3</sub>



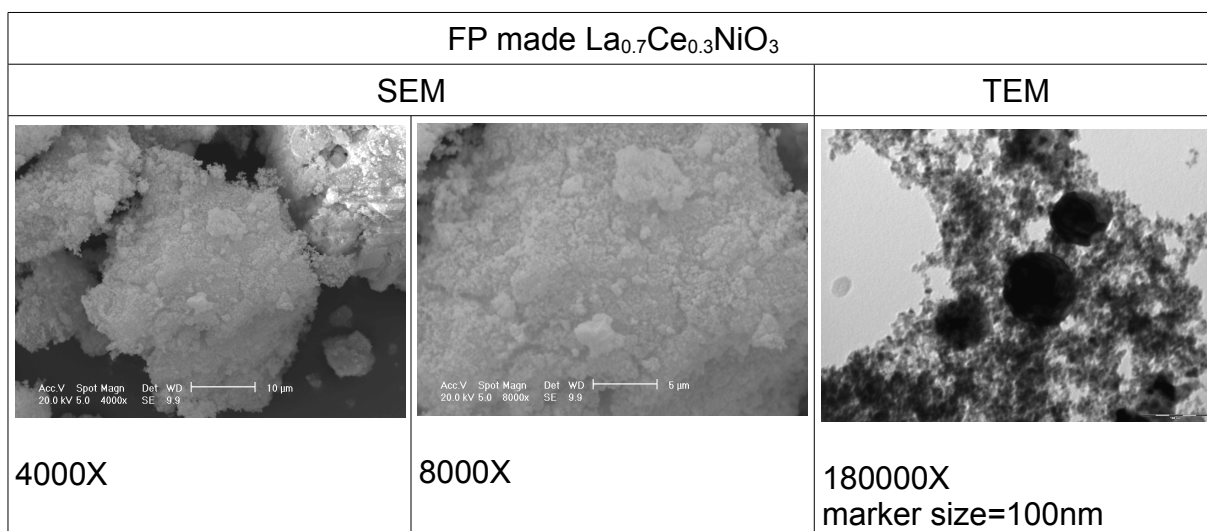


Figure 68: SEM-TEM pictures of FP made  $\text{La}_{0.7}\text{Ce}_{0.3}\text{NiO}_3$

## XPS

Table 10: surface composition of sample involved in INSTM project by XPS analysis

SAMPLE	Surface Metal	Support Ion	O	C	Others	Metal/Support Ion
S1C500-Ni	0.9	30.3	54.4	14.4	-	0.03
S2C800-Ni	0.8	33.5	-	-	-	0.04
S3C500-Cu	0.5	32.9	58	8.6	-	0.015
T1C500-Ni	0.5	11.6	31.7	54.9	S 1.3	0.04
T2C500-Ni	2.7	20.3	45.1	30.8	-	0.13
T3C800-Ni	2.4	7.1	52.8	37.7	-	0.34
T4C800-Ni	0.9	4.5	-	-	Na 1.5 N 1.9	0.20
T11C500-Cu	3.9	16.6	51.8	24.0	Na 3.7	0.23
Z1C500-Ni	1.7	19.8	43.1	35.5	-	0.09
Z2C500-Ni	1.2	14.4	-	-	S 2.6 Si 3.2	0.083
10%Ni/TiO <sub>2</sub>	1.0	7.4	23.9	65.4	N 2.4	0.14
10%Co/TiO <sub>2</sub>	0	0.9	14.0	81.9	N 32	-
10%Ni/SiO <sub>2</sub>	1.4	30.3	-	-	N 0.7	0.05
10%Co/SiO <sub>2</sub>	0.7	0.9	14	81.9	N32	-

10%Cu/SiO <sub>2</sub>	0	9.2	24.7	63.2	N29	-
------------------------	---	-----	------	------	-----	---

The Ni fraction exposed on the support surface is relatively similar for the samples obtained by FP. This is reasonable considering the direct incorporation of the metallic active phase during the synthesis of the support. By contrast, the TiO<sub>2</sub> supported samples obtained by impregnation, though characterised by a lower total Ni content, showed a higher surface concentration of the metal. In particular, it may be noticed that samples T1 and T2, prepared by precipitation with NaOH or NH<sub>3</sub>, respectively, and calcined at 500°C exposed the same surface area (*ca.* 100 m<sup>2</sup>/g). By contrast sample T3, precipitated with NH<sub>3</sub> but calcined at 800°C has a negligible surface area. In spite of this, samples T2 and T3 are more prone to expose Ni at the surface.

### TPR-TPO-TPD

First TPR analysis was made to detect the reduction temperature of Ni for each sample. The H<sub>2</sub> consumption of 10%Ni deposited by impregnation on the FP made Al<sub>2</sub>O<sub>3</sub>, TiO<sub>2</sub> and La<sub>2</sub>O<sub>3</sub> are reported in Figure 69. Titania-loaded sample showed the lowest reduction temperature with a sharp peaks starting at 200°C and with the maximum at *c.a* 250°C (red arrow Fig. 69) This main peak was associated with a small broad peak closing at 400°C. These two peaks could indicate the presence of free NiO (first peak) and some Ni oxide more tied to the surface (second peak). Al<sub>2</sub>O<sub>3</sub> supported samples showed a sharper peak with a maximum at *c.a* 300°C (blue arrow Fig.69) indicating that on the surface only one NiO species was present. Finally, the La<sub>2</sub>O<sub>3</sub>-supported catalyst evinced two broad peaks, a more intense one between 300°C and 450°C and a second feature between 600-700°C (green arrows). This indicates the presence of two different species of Ni oxides, one of which showing a much stronger interaction with the support. Comparing the TPR pattern with literature those catalysts show a reduction temperature at least 100°C lower [55-56]

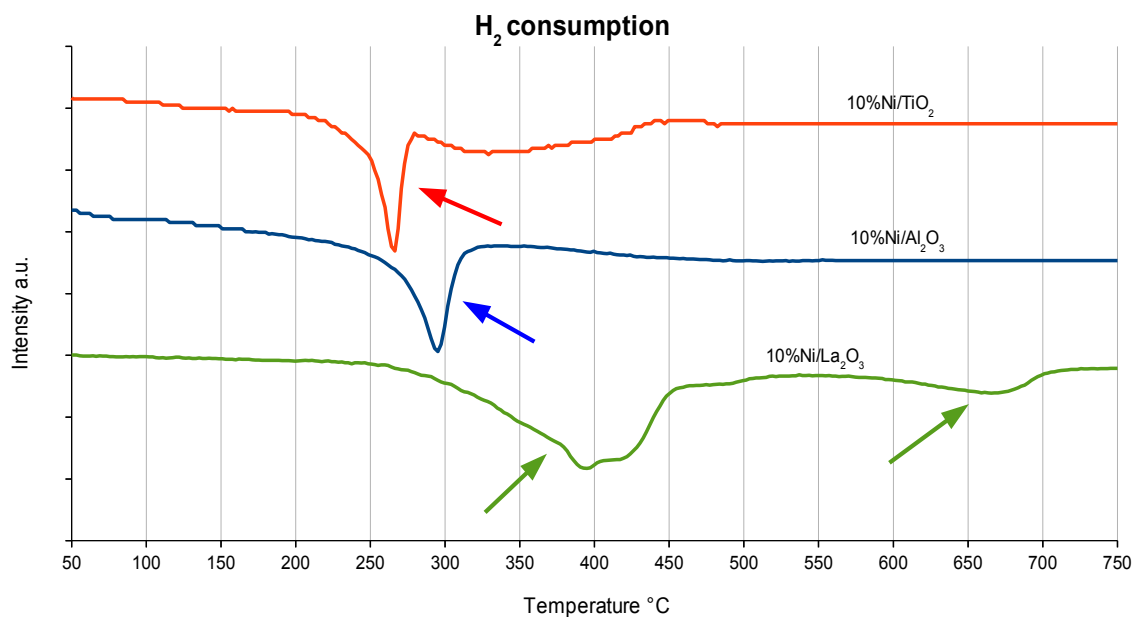


Figure 69:  $H_2$  consumption of 10%Ni/OX; OX=  $Al_2O_3$ (blue line);  $TiO_2$  (red line) ;  $La_2O_3$  (green line)

Hydrogen consumption of FP-made catalysts are reported in Fig 70. The first thing to notice is the increasing in the reduction temperature ( $>350^\circ C$ ). This was ascribed to stronger interaction between Ni and the support due to the high temperature attained during FP synthesis. Variations of Ni loading do not affect the shape or the temperature of the TPR profile, but only in the intensity of the peaks proportionally to the amount of nickel.

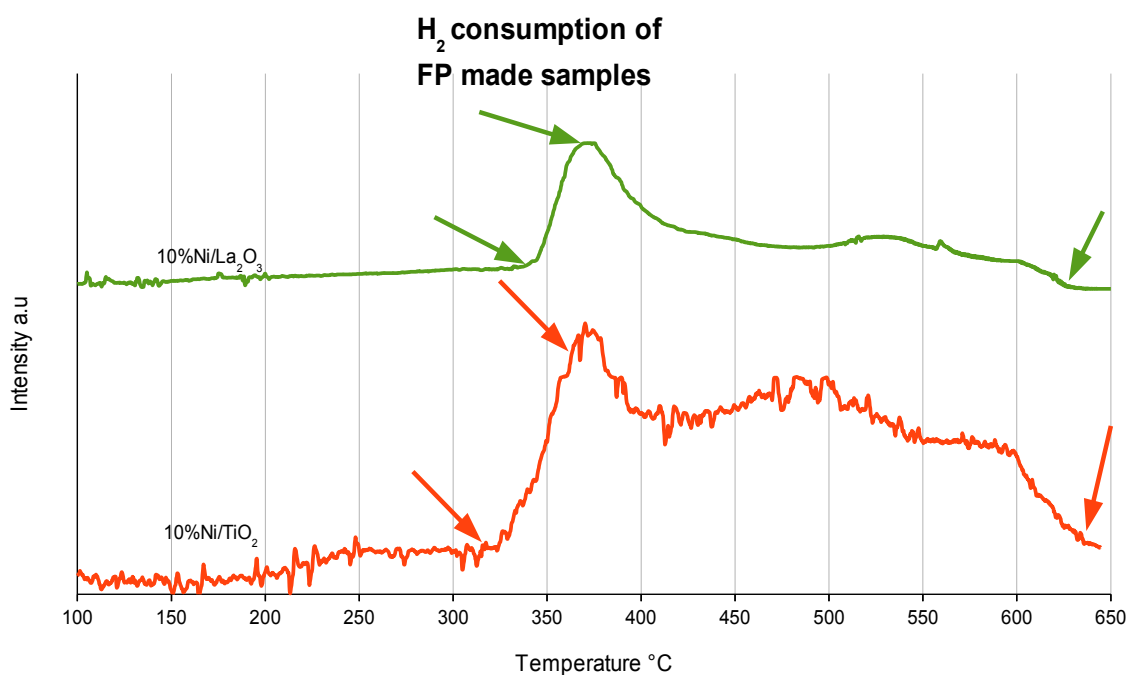


Figure 70:  $H_2$  consumption of FP-made 10%Ni/ $TiO_2$  (red line) ; 10%Ni / $La_2O_3$  (green line)

TPR analysis of 10%Ni/ZrO<sub>2</sub> is reported in figure 76 Ni/Zi catalysts showed a TPR pattern similar to the ones of Ni/Ti and Ni/La (Figure 70) a peak followed by a shoulder. In those samples there was also a small peak before the main one (between 300-350°C) and in the shoulder around 500°C there were 2 more peaks. This indicates the presence of at least 4 types of Ni oxides from the free NiO, the more easy to reduce, to some NiO exhibiting strong interaction with the support which reduces over 450°C.

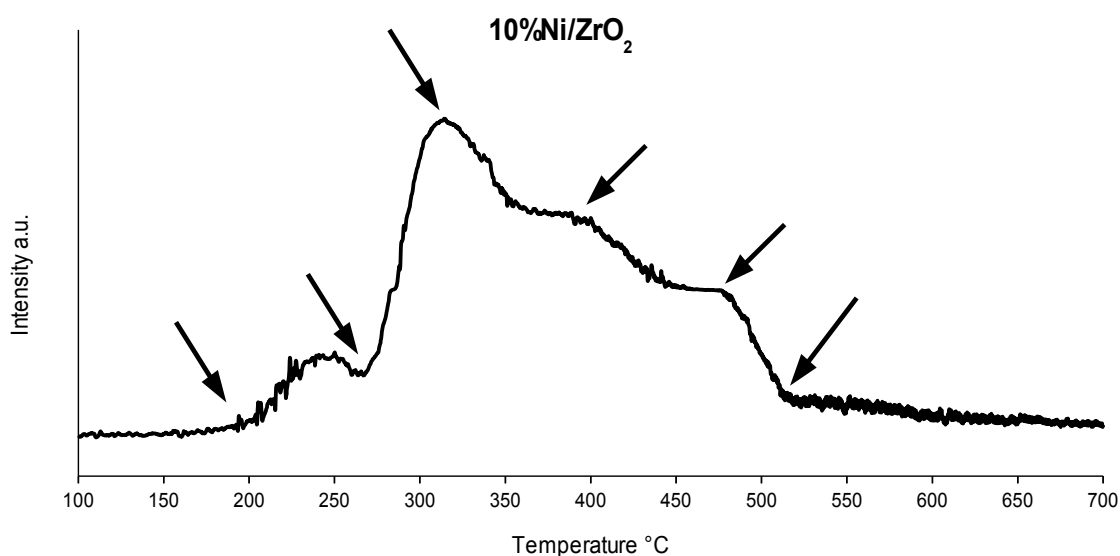


Figure 71: H<sub>2</sub> consumption of FP-made 10%Ni/ZrO<sub>2</sub>

Different from the others FP-made catalysts is the shape of the H<sub>2</sub> consumption of 10%Ni/SiO<sub>2</sub> (Figure 72), which showed a very broad peak centered around 450°C and attributed to the reduction of very heterogeneous NiO species. This may be connected with the amorphous structure of the support, which do not impart a well defined structure and interaction with the active phase.

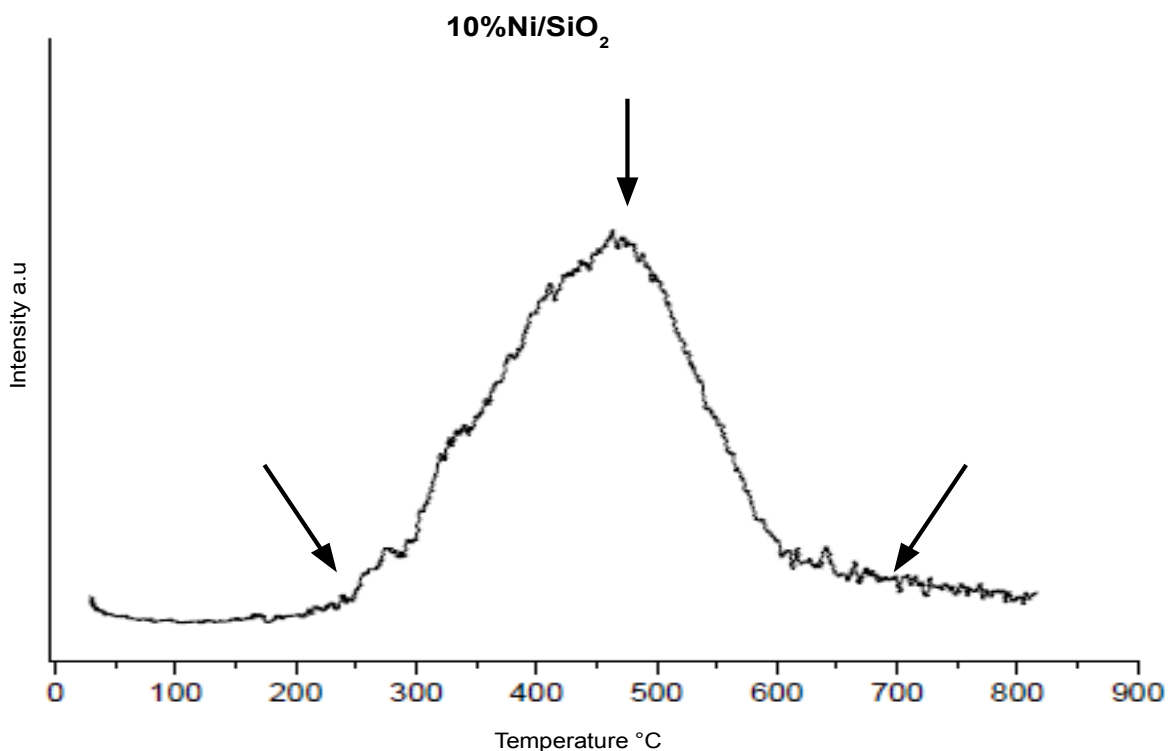


Figure 72: H<sub>2</sub> consumption of FP-made 10%Ni/SiO<sub>2</sub>

To test the stability of the reduced catalysts and characterised the Ni species after activation some TPR-TPO-TPR cycles were made on Ni, Co and Cu based catalyst:

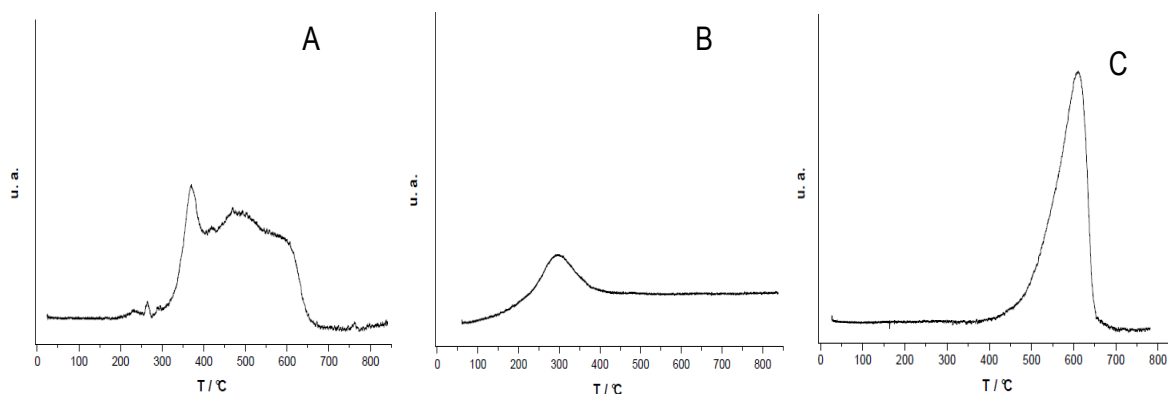


Figure 73: 10%Ni/TiO<sub>2</sub>, first TPR(A); TPO(B); second TPR(C)

First reduction of the FP made 10%Ni/TiO<sub>2</sub> (Fig 73 A) shows a very broad peak ascribable to reduction of different Ni species, NiO, bulk NiO and NiO<sub>2</sub> interacting with TiO<sub>2</sub>. Metallic nickel is oxidised back at 300°C (Fig 73 B), and the second TPR pattern (Fig 73 C) showed a much more uniform pattern with a peak at 600°C. This may indicate an increasing interaction with the support and suggested the need of higher reduction temperature to reduce Ni after the first redox cycle. This feature also indicated the irreversibility of the process with transformation of the “free” NiO

particles into species more strongly bound to the support, maybe as a mixed oxide.

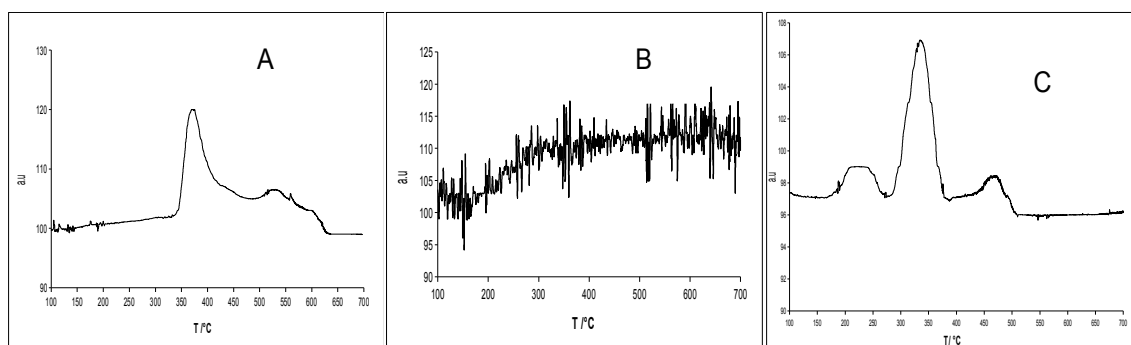


Figure 74: 10%Ni/La<sub>2</sub>O<sub>3</sub>, first TPR(A); TPO(B); second TPR(C)

TPR-TPO-TPO cycle of the FP-made 10%Ni/La<sub>2</sub>O<sub>3</sub> is reported in Figure 74. As already observed first TPR shows a peak with one/two shoulders that indicates the production of different Ni species. TPO (Fig. 74 B) was not well defined with a shape that could indicate a progressive oxidation of the metallic Ni present in the sample. The second TPR showed the presence of more easily reducible species since a first peak appeared around 200°C. And in general we observed a shift of the whole pattern towards lower temperature. This may be ascribed to sintering of Ni particles after the first activation, since bigger metal particles show a lower metal-support interface and thus more easily reduced. [57-58]

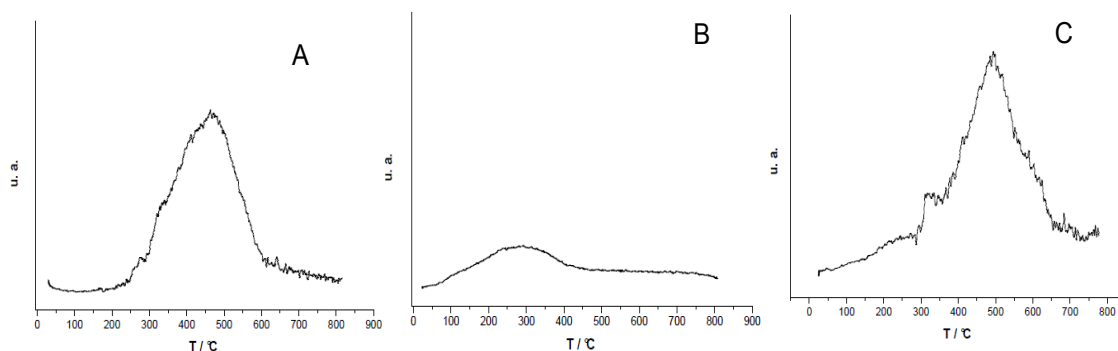


Figure 75: 10%Ni/SiO<sub>2</sub>, first TPR(A); TPO(B); second TPR(C)

The first TPR run carried out on the FP-prepared 10%Ni/SiO<sub>2</sub> catalyst revealed, as told previously, an almost featureless broad peak centred around 450°C, to NiO reduction (Fig. 75 A). The metal may be oxidised back at ca. 300°C (Fig. 75 B), as in the case of the titania support sample and the second reduction (Fig. 75 C) resulted almost equivalent to the fresh sample, indicating on one hand a reversible reduction/oxidation cycle, on the other hand the retention of a very broad heterogeneity of Ni oxide species even after activation. A slight shift of the TPR

pattern towards higher temperature indicated the establishment of stronger metal support interaction upon activation and so a high dispersion of the active phase over activated surface.

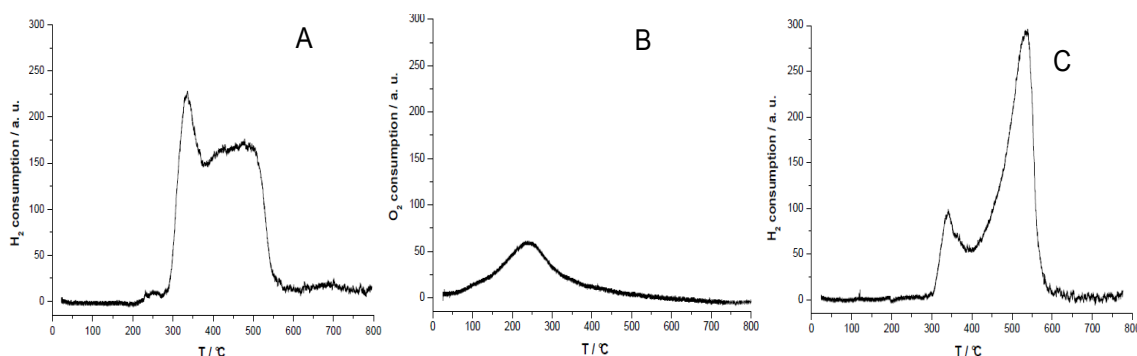


Figure 76: 10%Ni/ZrO<sub>2</sub>, first TPR(A); TPO(B); second TPR(C)

TPR-TPO-TPR cycle for 10%Ni/ZrO<sub>2</sub> is reported in Figure 79. First reduction indicates the presence of different species of Ni, metallic Nickel is oxidise (Fig 76 B) at 200°C instead of 300°C Also in this case the second TPR Ni species with stronger interaction with ZrO<sub>2</sub> is formed, i.e. reducing at higher temperature as the second TPR shows (Fig. 76 C).

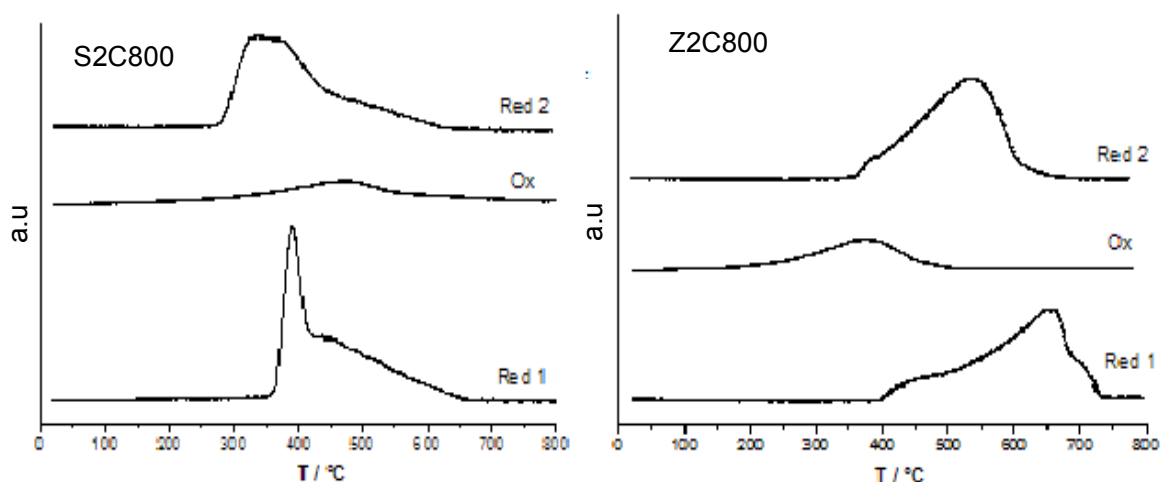


Figure 77 TPR-TPO-TPR cycle of 10%Ni/SiO<sub>2</sub> (S2C800) and 10%Ni/ZrO<sub>2</sub> (Z2C800) made by impregnation at UniVE

TPR-TPO-TPR cycle for catalyst made by impregnation and calcined at 800°C instead showed a shift towards lower temperature for the second reduction due to the sintering of the active phase (low metal dispersion).

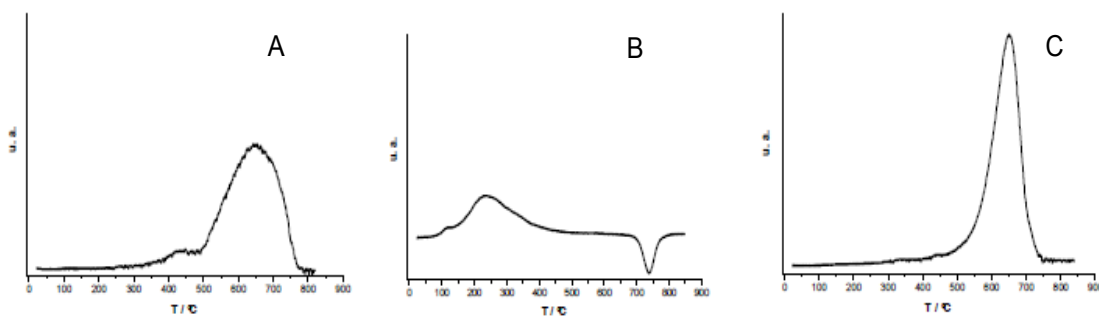


Figure 78: 10%Co/TiO<sub>2</sub>, first TPR(A); TPO(B); second TPR(C)

The first TPR( Fig. 78A) pattern shows one broad peak centred around 650°C, due to the reduction of the oxide to metallic Co. The metal was oxidized back over a broad temperature range. In addition, the TPO (Fig. 78B) showed a sharp peak corresponding to oxygen release at ca. 750°C. This may be due to the formation of some mixed oxide between Co and Ti, where Co was stable in a lower oxidation state (likely CoTiO<sub>3</sub>). The second reduction treatment started at higher temperature (ca. 500°C), but it was characterized by a bit sharper profile, suggesting the formation of homogeneous Co species more strongly interacting with the support after activation

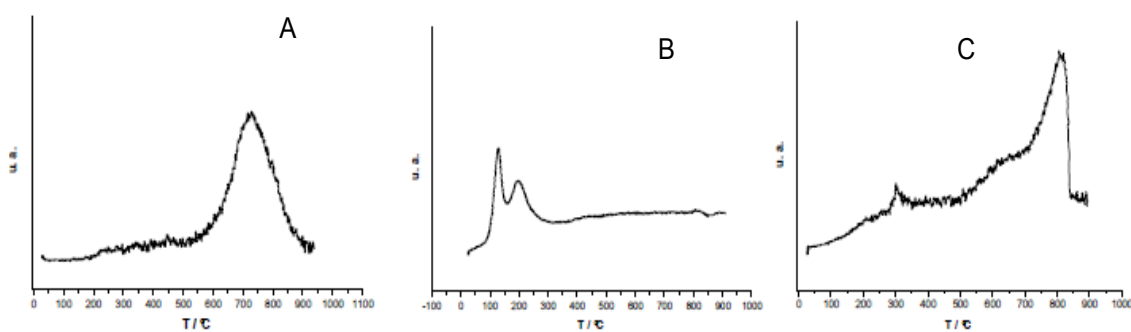


Figure 79: 10%Co/SiO<sub>2</sub>, first TPR(A); TPO(B); second TPR(C)

The first TPR (Fig 79 A) of sample 10%Co/SiO<sub>2</sub> evidenced one peak, relatively broad, always due to the amorphous structure of SiO<sub>2</sub>, centred at 750°C due to the reduction of a single cobalt oxide to metallic Co. Its re-oxidation (Fig 79 B) was complete at ca. 300°C, with formation of two species, CoO and Co<sub>3</sub>O<sub>4</sub>. The second reduction treatment was completed at 900°C, also in this case highlighting the formation of less reducible species, more strongly interacting with the support upon catalyst activation



in reducing atmosphere.

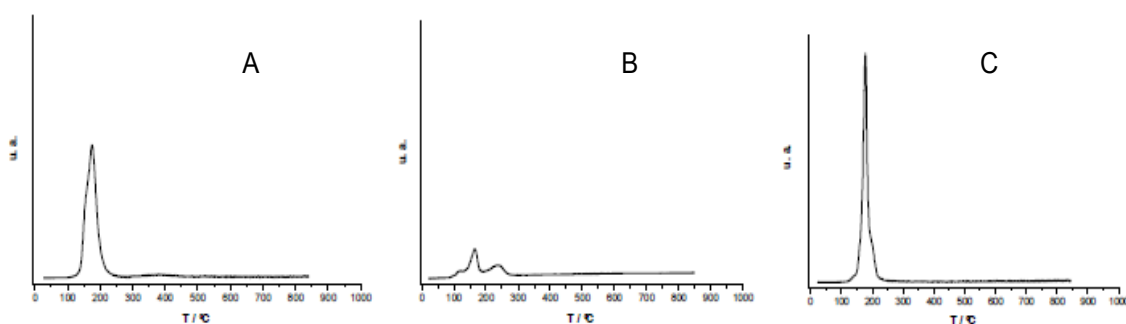


Figure 80: 10%Cu/TiO<sub>2</sub>, first TPR(A); TPO(B); second TPR(C)

Cu showed a much lower interaction with the support, evidenced with very sharp reduction peaks at low temperature (200°C), very reproducible when comparing subsequent reduction cycles. Therefore, the formation of mixed oxides with the support, as well as the formation of strong surface interactions may be ruled out. The reoxidation of the metal occurred step-wise and completed at ca. 300°C.

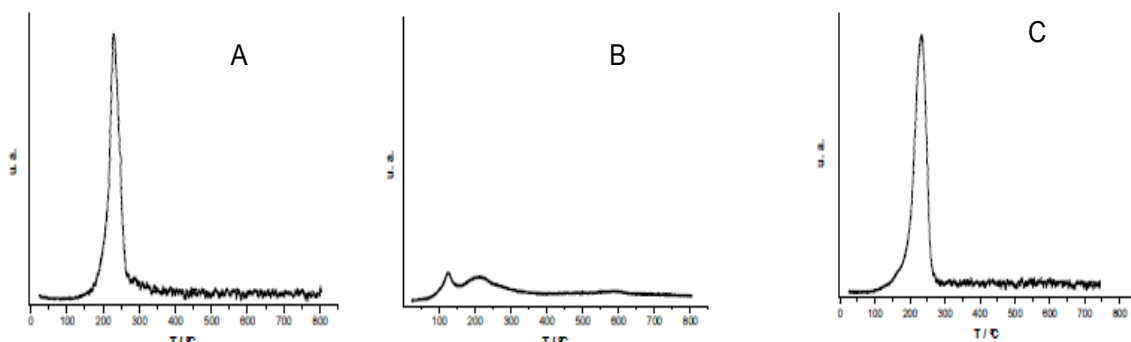


Figure 81: 10%Cu/SiO<sub>2</sub>, first TPR(A); TPO(B); second TPR(C)

The first and last TPR (Fig 81 A,C) patterns of sample 10%Cu/SiO<sub>2</sub> identically showed one sharp peak centred around 220°C due to the reduction of CuO to metallic Cu. Metal re-oxidation was as expected more difficult than with Co and completed at 400°C.

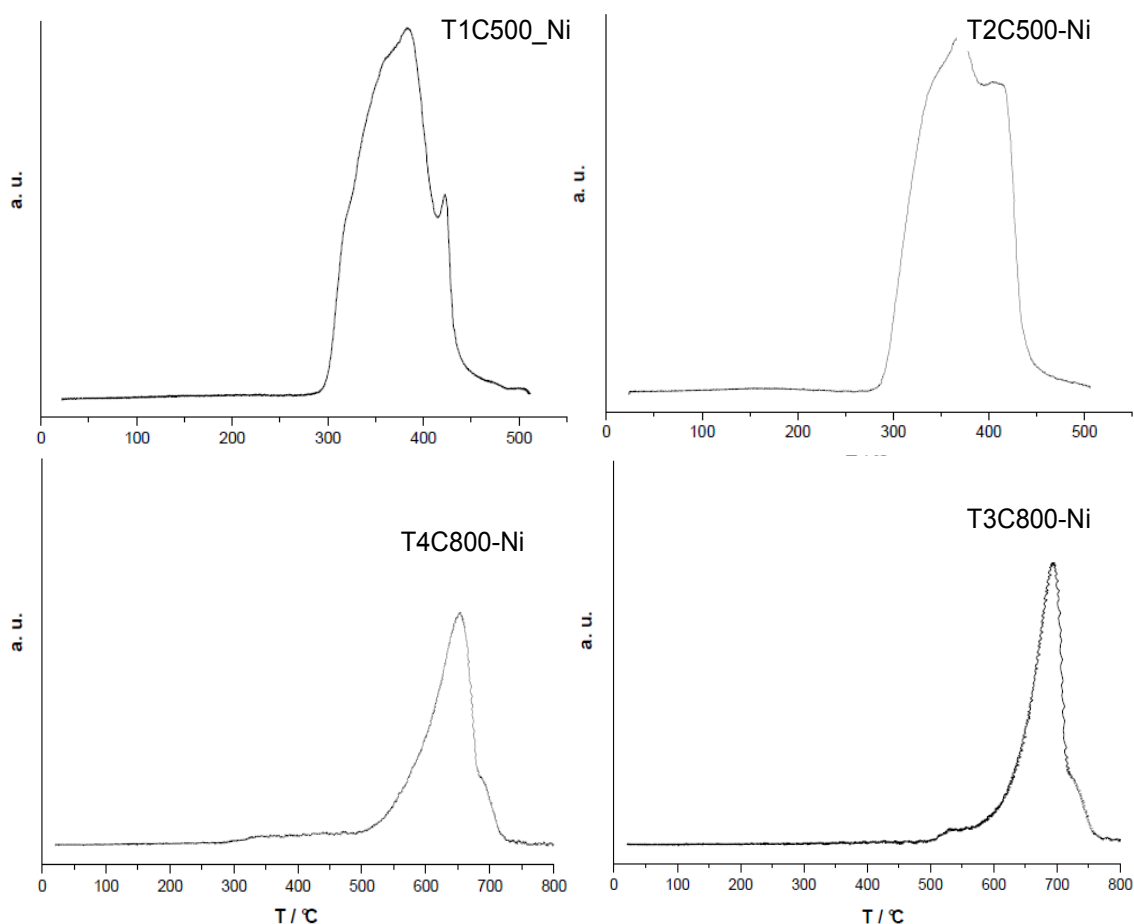


Figure 82: TPR profiles of Ni/Ti based catalysts made by impregnation at UniVE.

The TPR patterns of the Ni-TiO<sub>2</sub> samples calcined at 500°C (Fig 82 T1 and T2) showed a broad reduction region, in the range 300-500°C. Two NiO species, corresponding to two different peaks, were detected. The peak located at the lowest temperature can be attributed to the reduction of “free” NiO, which was not interacting with the support (unsupported NiO has a reduction temperature of about 280°C [59]). By contrast, the peak at higher temperature was related to NiO particles having significant interaction with titania [60]. The TPR patterns of the catalysts calcined at 800°C (Fig. 82 T3 and T4) show a shift of the reduction peaks towards higher temperatures. It is well-known that the interaction between metal and support increases with calcination temperature. The present TPR profiles thus suggest an increase of the interactions between NiO particles and TiO<sub>2</sub>, as well as the possible formation of the species NiTiO<sub>3</sub> [61], as confirmed by XRD analysis.

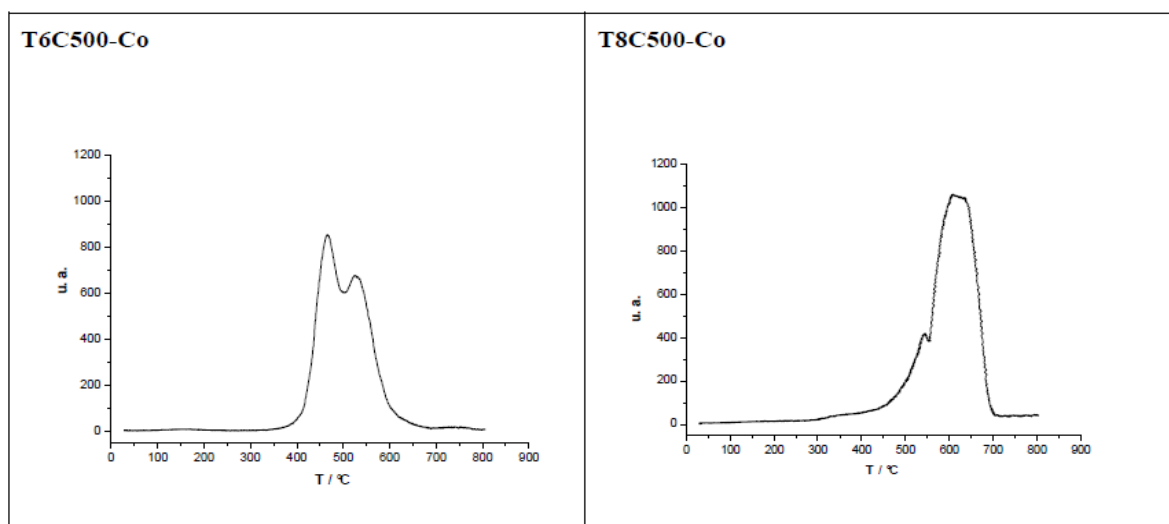


Figure 83: TPR profiles of Co/Ti based catalysts made by impregnation.

The TPR patterns of samples T6C500-Co e T8C500-Co (Fig. 83) show two main peaks between 400 and 700°C, which may refer to the reduction of  $\text{Co}_3\text{O}_4$  e  $\text{CoO}$  [62]. The shift of the reduction temperatures on the two supports may be ascribed to the different crystal phases of  $\text{TiO}_2$ . At 700°C Co is fully reduced.

The TPR patterns of Cu samples supported on  $\text{TiO}_2$  (Fig 84) showed three peaks. One at 170°C, was attributed to the reduction of CuO interacting with the support; The second, at 190°C, to the reduction of small and dispersed CuO clusters and the latter, at 210°C referred to CuO crystallites [63]. In sample T11C500-Cu the peaks shifted towards slightly higher temperature with respect to T9C500-Cu. Likely, also in this case it may be due to the different crystal phases of  $\text{TiO}_2$ . Much lower metal support interaction was concluded for Cu-based catalysts.

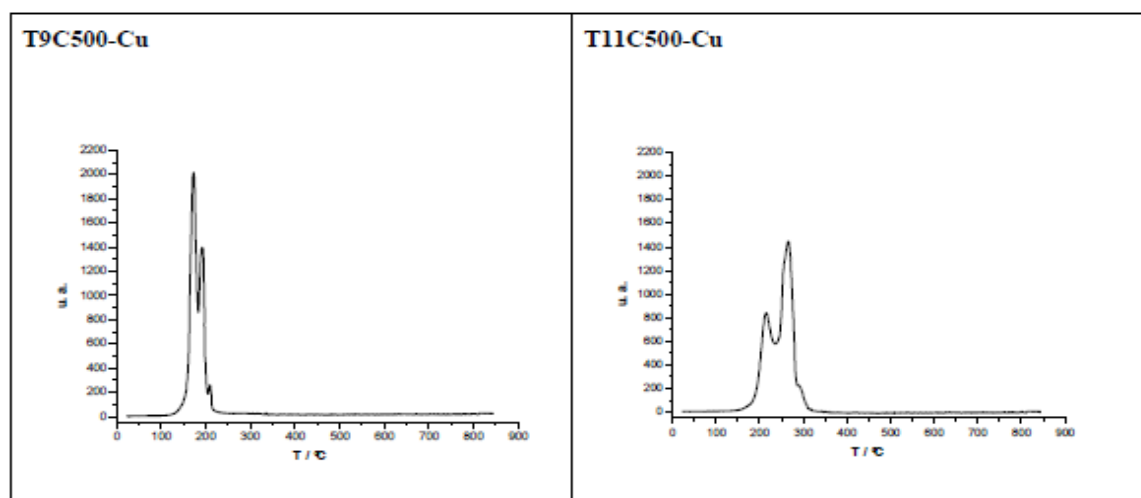


Figure 84: TPR profiles of Cu/Ti based catalysts made by impregnation.

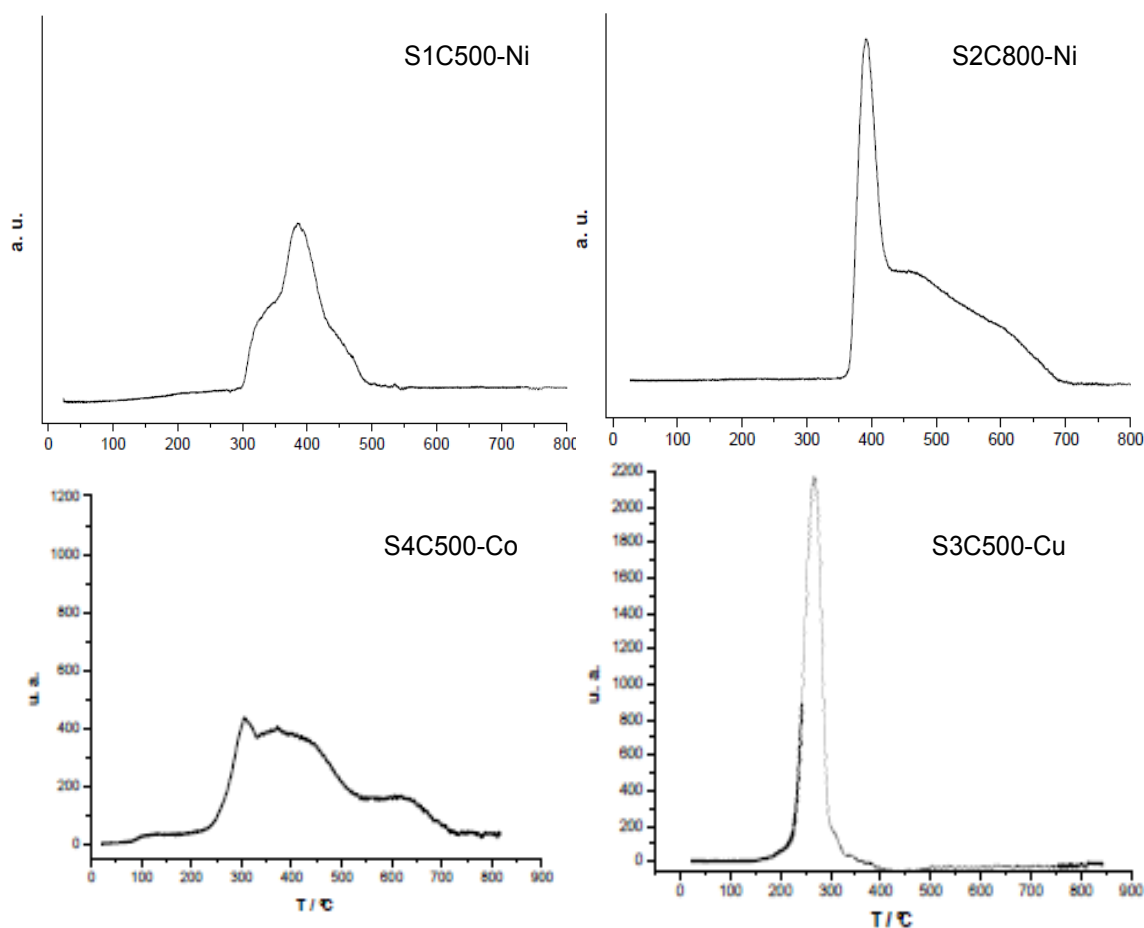


Figure 85: TPR profiles of  $\text{SiO}_2$  based catalysts made by impregnation; S1-S2 10%Ni; S3 10%Cu; S4 10%Co

TPR profiles of catalysts supported on  $\text{SiO}_2$  are reported in Figure 85:

S1C500-Ni gave rise to a rather broad reduction feature in the range 300 - 500°C. A well-defined peak with its maximum at 390°C was indeed detected, with a shoulder between 300 and 360°C, indicating that different NiO species were present on the support also in this case. So, at least two reduction zones could be distinguished: the first, at a lower temperature, related to “free” NiO particles not interacting with the support and therefore more easily reduced; the second, at a higher temperature, ascribable to NiO particles with stronger interactions with the silica support [64,65]. In the TPR diagram of the sample calcined at 800°C the first peak was well-defined, while the second peak transformed in a broad shoulder in the temperature range between 420 and 700°C. Two different reduction species seemed still present and the fact that the second peak was much broader than the first one implicates that only a small fraction of NiO particles was characterised by weak interactions with the

support, while a great portion of metal oxide particles strongly interacted with silica. This confirms that an increase of the calcination temperature during the synthesis allowed to establish stronger metal support interactions.

The TPR of sample S4C500-Co showed broad and overlapping peaks, which may be attributed to the progressive reduction of  $\text{Co}^{3+}$  to  $\text{Co}^{2+}$  and of  $\text{Co}^{2+}$  to  $\text{Co}^0$  [66]. The peak at the highest temperature may be ascribed to particles strongly interacting with the support [67,68]. The reduction pattern of sample S3C500-Cu revealed a single peak at  $260^\circ\text{C}$ , corresponding to the reduction of CuO to metallic Cu [69].

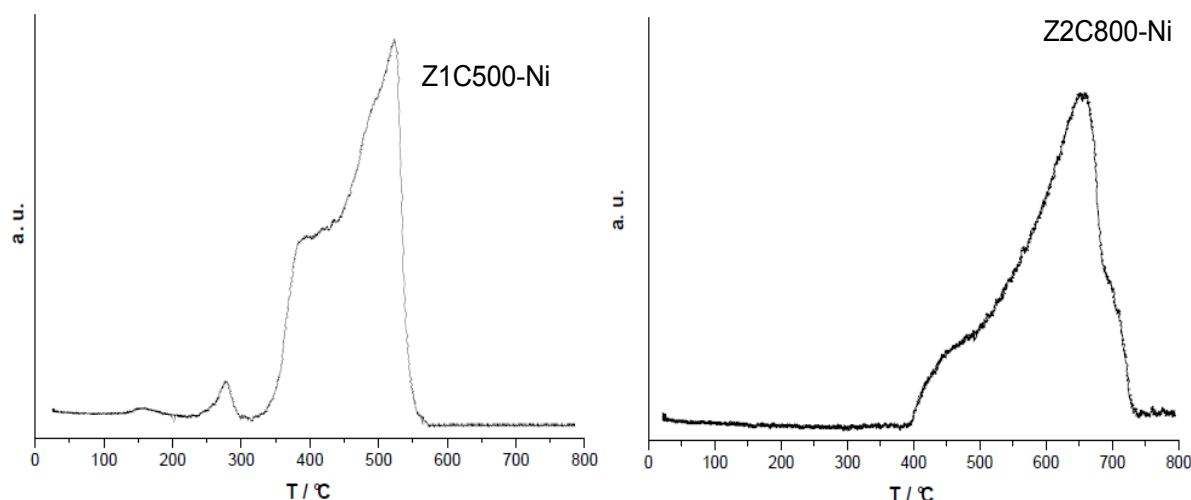


Figure 86: TPR profiles of 10%Ni/ZrO<sub>2</sub> catalysts made by impregnation at UniVe.

The TPR profiles of Ni/Zr catalysts made by impregnation and calcined at  $500^\circ\text{C}$  (Z1C500-Ni) and at  $800^\circ\text{C}$  (Z2C800-Ni) are reported in Figure 85. The TPR profile of Ni-ZrO<sub>2</sub> sample calcined at  $500^\circ\text{C}$  suggests the existence of three different NiO species on the zirconia surface. According to the pertinent literature, the higher temperature peak (with its maximum at  $520^\circ\text{C}$ ) could be assigned to NiO particles strongly interacting with the ZrO<sub>2</sub> surface, while the peak at  $380^\circ\text{C}$  was probably due to NiO species weakly interacting with the support. The peak at the lowest temperature ( $280^\circ\text{C}$ ) is ascribable to “free” metal oxide particles, more easily reduced [70,71]. In general the present sample seems less reducible than the previous ones. The TPR profile of Z2C800 suggests the existence of at least two different NiO species on the zirconia surface. The higher temperature peak (with its maximum at  $655^\circ\text{C}$ ) can be assigned to NiO particles strongly interacting with the ZrO<sub>2</sub> surface, while the shoulder at about  $450^\circ\text{C}$  is due to NiO species weakly interacting with the

support. Compared to the sample calcined at 500°C, a shift of the reduction peaks towards higher temperatures can be noticed. As mentioned, it is well-known that the interaction between metal and support increases with calcination temperature and the TPR profile thus suggests an increasingly strong interaction between NiO particles and ZrO<sub>2</sub>.

## Chemisorption

**Table 11: O<sub>2</sub> chemisorption for Ni and Cu-based catalysts.**

T1C500-Ni	mL O <sub>2</sub> (0°C)/g <sub>Ni</sub> = 30.26 A (m <sup>2</sup> /g <sub>Ni</sub> ) = 106 m <sup>2</sup> /g <sub>Ni</sub> d (nm) = 5.3 nm
T2C500-Ni	mL O <sub>2</sub> (0°C)/g <sub>Ni</sub> = 18.99 A (m <sup>2</sup> /g <sub>Ni</sub> ) = 66 m <sup>2</sup> /g <sub>Ni</sub> d (nm) = 8.5 nm
T4C800-Ni	No chemisorption occurs.
T3C800-Ni	mL O <sub>2</sub> (0°C)/g <sub>Ni</sub> = 0.61 A (m <sup>2</sup> /g <sub>Ni</sub> ) = 2 m <sup>2</sup> /g <sub>Ni</sub> /
S1C500-Ni	No chemisorption occurs
S2C800-Ni	No chemisorption occurs
Z1C500-Ni	mL O <sub>2</sub> (0°C)/g <sub>Ni</sub> = 17.18 A (m <sup>2</sup> /g <sub>Ni</sub> ) = 60 m <sup>2</sup> /g <sub>Ni</sub> d (nm) = 9.4 nm
Ni / TiO <sub>2</sub>	mL O <sub>2</sub> (0°C)/g <sub>Ni</sub> = 14.5 Area (m <sup>2</sup> /g <sub>Ni</sub> ) = 51 m <sup>2</sup> /g <sub>Ni</sub> d (nm) = 11 nm
Ni / SiO <sub>2</sub>	mL O <sub>2</sub> (0°C)/g <sub>Ni</sub> = 0.40 Area (m <sup>2</sup> /g <sub>Ni</sub> ) = 1 m <sup>2</sup> /g <sub>Ni</sub> d (nm) = 401 nm
Ni / TiO <sub>2</sub> – Red. 800°C	mL O <sub>2</sub> (0°C)/g <sub>Ni</sub> = 0.18 Area (m <sup>2</sup> /g <sub>Ni</sub> ) = 0.6 m <sup>2</sup> /g <sub>Ni</sub> d (nm) = 891 nm
T9C500-Cu	mL O <sub>2</sub> (0°C)/g <sub>Cu</sub> = 1.3 d (nm) = 99 nm
T11C500-Cu	mL O <sub>2</sub> (0°C)/g <sub>Cu</sub> = 3.85 d (nm) = 34 nm
S3C500-Cu	No chemisorption

10%Cu/TiO <sub>2</sub>	mL O <sub>2</sub> (0°C)/g <sub>Cu</sub> = 0.43 d (nm) = 304 nm
10%Cu/SiO <sub>2</sub>	Immediately saturated.

O<sub>2</sub> chemisorption on TiO<sub>2</sub> supported Ni, calcined at 500°C, reveals the presence of small metal particles, with an average diameter of 5 nm (T1C500-Ni) and 8 nm (T2C500-Ni). The stronger interactions between NiO particles and the support in T1C500-Ni revealed by TPR analyses can be explained in terms of size, due to smaller Ni particles.

For the samples T3 and T4 calcined at 800°C no chemisorption occurred, since the thermal treatment caused a severe sintering of the Ni particles.

Unexpectedly, for the SBA-15-based catalysts no chemisorption occurred at all, independently from the calcination temperature.

A very different dispersion was observed for the FP-prepared samples. A higher dispersion was achieved for the TiO<sub>2</sub>-supported catalyst with respect to the silica based one, as it was observed by SEM-TEM analysis. Nevertheless, an attempt of reduction at 800°C, to reproduce the activation procedure of the catalyst, has been carried out for the Ni/TiO<sub>2</sub> sample, confirming the expected extensive sintering of the active phase. As for Cu-based catalysts results revealed the presence of relatively big metal particles, identified also in SEM-TEM analysis, likely due to the easy sintering of copper also at relatively low temperature.

## FT-IR

### ***Ni based catalysts:***

Following a thermal treatment at 500°C, pure powders spectra of activated and reduced

10%Ni/TiO<sub>2</sub> catalyst showed a clean surface almost completely dehydroxylated (Fig. 86).

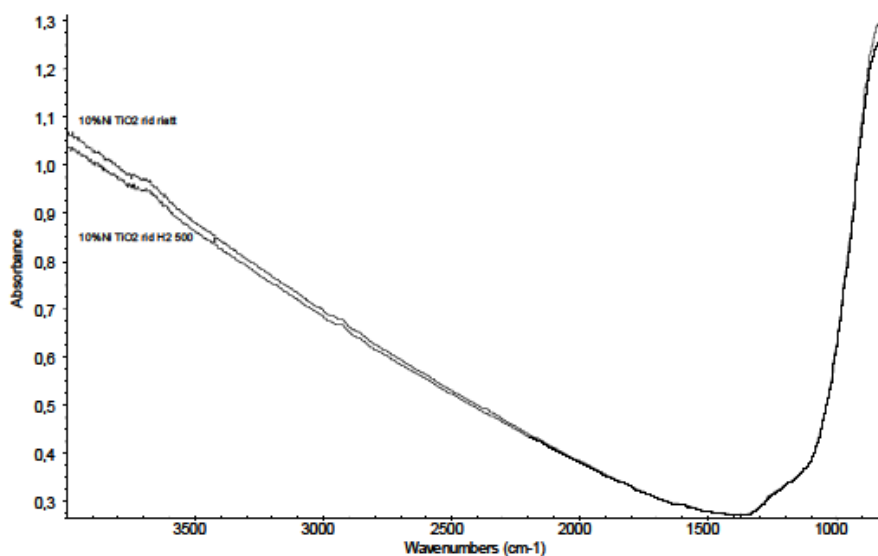


Figure 87 : FT-IR spectra of activated and H<sub>2</sub>-reduced 10%Ni/TiO<sub>2</sub> FP-prepared catalyst

Low temperature CO adsorption over 10%Ni/TiO<sub>2</sub> support gave rise to several IR bands in the C-O carbonyl spectral region (Fig. 87). As widely reported in the literature and summarised by Hadjiivanov et al. [72] bands at 2184, shifting to 2191 cm<sup>-1</sup> at decreasing coverage, characterise acidic c.u.s. Ti cations acting as Lewis sites of different strength (Ti<sup>4+</sup>).

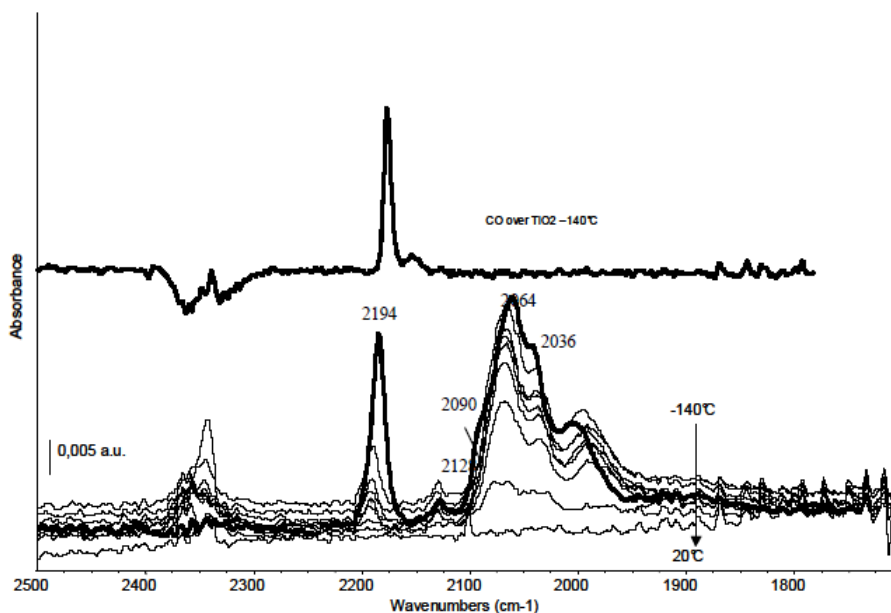


Figure 88 :FT-IR subtraction spectra of surface species arising from CO adsorption over the 10%Ni/TiO<sub>2</sub> (FP) reduced catalyst . Spectrum of CO adsorbed over pure titania has been reported for comparison

Another weak component at 2165 cm<sup>-1</sup>, here detected as a broad shoulder, tailing to



2139  $\text{cm}^{-1}$ , was due to CO interacting with residual OH groups. These assignments were also confirmed by the behaviour of the bands following outgassing: bands due to carbonyl

interacting with Lewis sites were more resistant, while bands due to H-bonded CO readily disappear, as long as the weak bands due to isolated OH stretching mode were restored in the spectra. It can be observed that few different bands related to Ni species can be identified in the region 1850-2130  $\text{cm}^{-1}$ . The weak band at 2128  $\text{cm}^{-1}$  indicate the presence of gem dicarbonyls over  $\text{Ni}^+$  ions, where the associated band located around 2090  $\text{cm}^{-1}$  could be masked by the strong band at 2057  $\text{cm}^{-1}$ . This band disappeared only after evacuation at room temperature, in agreement with literature findings that reported  $\text{Ni}^+$ -CO complexes being much more stable than  $\text{Ni}^{2+}$ -CO complexes. Two intense bands at 2064  $\text{cm}^{-1}$  and 2036  $\text{cm}^{-1}$ , with similar resistance to outgassing, were registered in the region 2000-2100  $\text{cm}^{-1}$ . These features were associated with CO linearly adsorbed on  $\text{Ni}^0$  small clusters with different crystal face exposure, size and possibly different metal-support interaction. Besides, an additional broad band at 2003  $\text{cm}^{-1}$ , shifting to 1992  $\text{cm}^{-1}$  at decreasing coverage, was detected in the region 2000-1980  $\text{cm}^{-1}$ . This band corresponds to bridging CO over larger metal  $\text{Ni}^0$  centers. No bands associated with the presence of residual  $\text{Ni}^{2+}$ -CO species of NiO were detected following the reduction treatment. Thus, Ni was broadly reduced at the catalyst surface. On the other side, then heterogeneity of the Ni species is in agreement with TPR results, pointing out the presence of at least three kinds of Ni metal particles, metal clusters strongly interacting with the support, Ni ions having different reducibility. In fact upon outgassing and warming,  $\text{CO}_2$  was formed (band around 2350  $\text{cm}^{-1}$ ) as a result of CO oxidation by Ni ions. Exposed  $\text{Ti}^{4+}$  ions acting as Lewis acidic sites were also detected. Following PN adsorption (Fig. 89), two complex bands were detected in the CN stretching region at 2278 and 2247  $\text{cm}^{-1}$  (with a shoulder at lower frequency). The former was due to PN interacting with medium strength Lewis sites (Ti ions), while the latter, strongly decreasing following outgassing at room temperature, was due to PN H-bound to residual exposed OH groups. The low relative intensity of this band was in agreement with the low degree of hydroxylation of this surface (see Fig. 87). Correspondingly, only a weak 20 negative band could be detected in the OH stretching region of the subtraction spectrum (inset in Fig. 89).

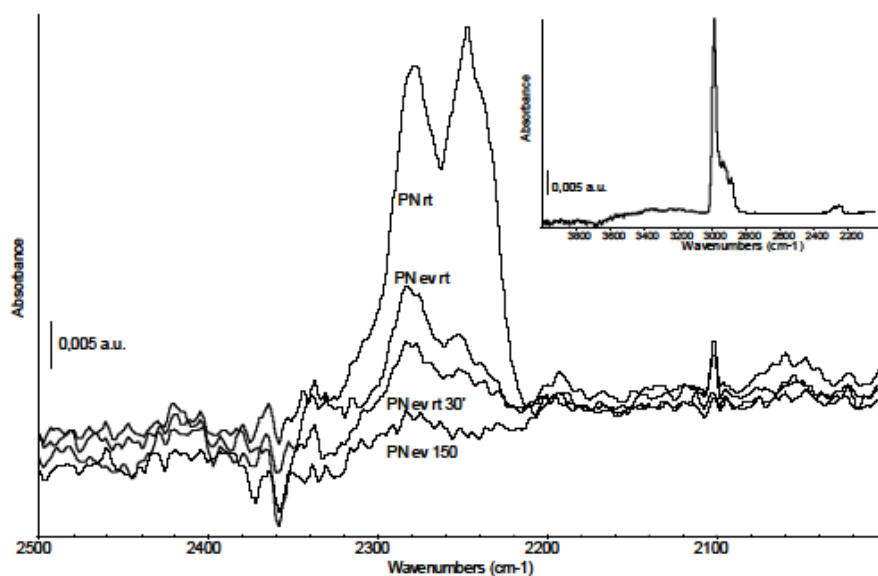


Figure 89 :FT-IR subtraction spectra of surface species arising from PN adsorption over the 10%Ni/TiO<sub>2</sub> reduced catalyst at room temperature and after prolonged outgassing. Inset: OH stretching region

As for the 10%Ni/SiO<sub>2</sub> FP-prepared sample reported surface spectra of the activated catalyst is shown in Fig. 90, where the typical features of silica (3745 cm<sup>-1</sup>, OH stretching mode, Si-O overtones in the 2000-1800 cm<sup>-1</sup> range, cut off near 1300 cm<sup>-1</sup>) were clearly visible. Reduction of the metal phase did not lead to any significant change of the spectrum. Possibly a weakening of the silanols band and a correspondingly increasing intensity of the H-bound hydroxyl groups could be the result of reduction (water vapour formed following reduction).

In the spectra recorded upon CO adsorption (Fig. 91, dotted line), the strong bands at 2160, 2140 and 2100 cm<sup>-1</sup> were due to CO interacting with OH groups and weakly physisorbed and they disappeared almost completely after outgassing at liquid nitrogen temperature. The intense and asymmetric band at 2047 cm<sup>-1</sup> together with the weak band centred at 1940 cm<sup>-1</sup> were due to terminal carbonyls and bridging carbonyls, respectively. Also for high loading and highly reduced Ni catalysts quite broad bands were usually observed upon CO adsorption at 2080-2020 cm<sup>-1</sup> and at 1930-1870 cm<sup>-1</sup>, typically assigned to terminal and bridging carbonyls on extended Ni metal particles [73-77]. The several weak components detected above 2000 cm<sup>-1</sup> suggest once again the formation of Ni<sup>+</sup> polycarbonyl species, although strongly reduced with respect to the Ni/TiO<sub>2</sub> catalyst. In particular, in the region 2000-2100 cm<sup>-1</sup> the weak bands at 2130 and 2090 cm<sup>-1</sup> were assigned to Ni<sup>+</sup>(CO)<sub>2</sub>, while shoulders at 2038 and 2070 cm<sup>-1</sup>, with similar relative intensities, could be due to NiO

polycarbonyls, such as  $\text{Ni}(\text{CO})_3$ , likely frozen precursors of the formation of  $\text{Ni}(\text{CO})_4$ . This may be seen as indication of the existence of atomically dispersed zerovalent nickel [77,78]. The relative intensities of the features here reported indicate that nickel was mainly present as metal. The detection of bridging species, not present in the  $\text{Ni}/\text{TiO}_2$  spectra, was an indication of larger particles formation.

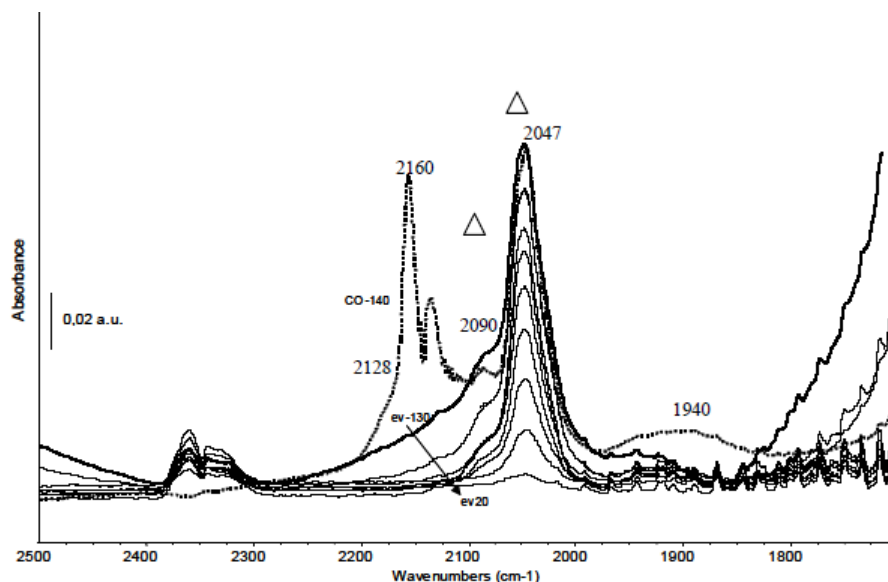


Figure 90 :FT-IR spectra of outgassed at 773 K and  $\text{H}_2$ -reduced 10%Ni/SiO<sub>2</sub> FP catalyst

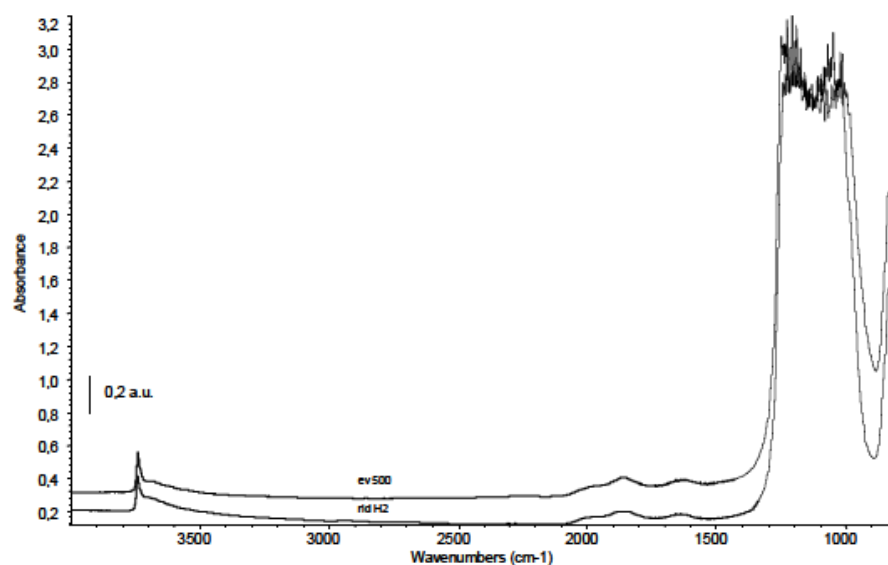


Figure 91:FT-IR subtraction spectra of surface species arising from CO adsorption over 10%Ni/SiO<sub>2</sub> reduced catalyst at liquid nitrogen temperature and after warming to room temperature. The activated surface has been subtracted

So the lower dispersion of metal active phase over SiO<sub>2</sub> support could be related to an increased Ni reducibility. This effect agrees with TPR results, where Ni over TiO<sub>2</sub> showed a larger reduction temperature range with respect to Ni over SiO<sub>2</sub> and with chemisorption data. PN adsorption over the reduced catalyst led to the spectra

reported in Figure 92. Two bands were detected in the CN stretching region: at 2250  $\text{cm}^{-1}$ , strong, and 2280  $\text{cm}^{-1}$ , by far weaker.

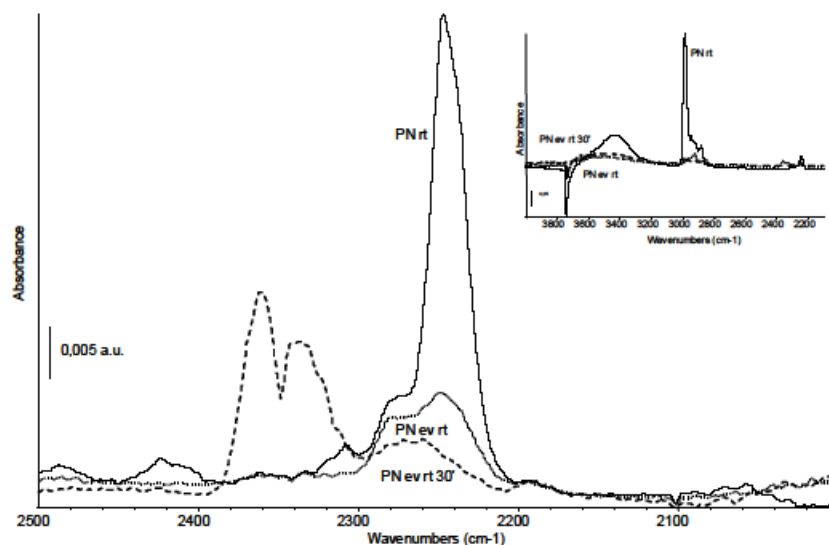


Figure 92 :FT-IR subtraction spectra of surface species arising from PN adsorption over reduced catalyst 10%Ni/SiO<sub>2</sub> FP at room temperature and after prolonged outgassing. The activated surface has been subtracted. Inset: OH stretching region

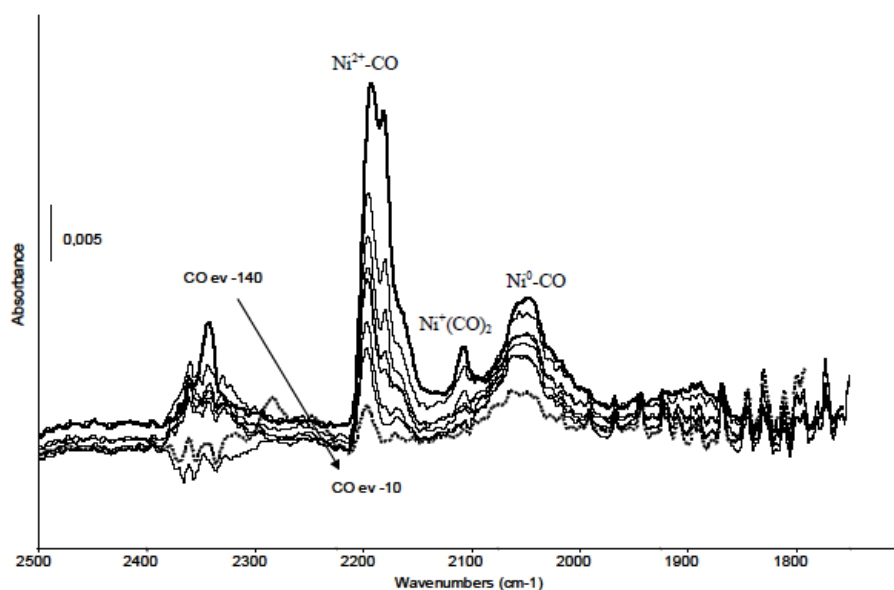


Figure 93 :FT-IR subtraction spectra of surface species arising from CO adsorption over 10%Ni/SiO<sub>2</sub> catalyst at liquid nitrogen temperature and after warming to room temperature. The activated surface has been subtracted.

The former disappeared already following outgassing at room temperature. The position and behaviour of these bands allowed their attribution to PN interacting with silanol groups (H-bound species, weakly held) and to PN interacting with Lewis

acidic centres, respectively (possibly the metal phase). CO adsorption at low temperature has been also performed over the outgassed catalyst, *i.e.* following a thermal treatment in vacuum and not in hydrogen (Fig. 93). This pretreatment resulted in the detection of three sharp bands at 2196, 2179, 2170  $\text{cm}^{-1}$ , thus in the spectral range typical of CO coordinated over  $\text{Ni}^{2+}$  and  $\text{Ni}^+$  ions species, as expected. In particular, the split of the high frequency band was an evidence of at least two kinds of  $\text{Ni}^{2+}$  ions. However, traces of Ni metal particles, likely formed during the preparation/pretreatment step could be detected, characterised by weak bands due to terminal carbonyls (see comparison in Fig. 94).

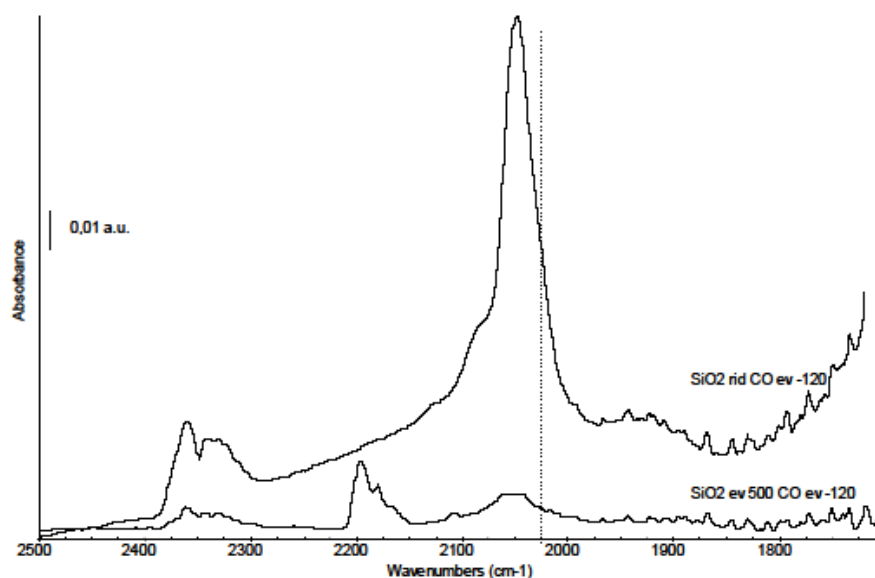


Figure 94: FT-IR subtraction spectra of surface species arising from CO adsorption over 10%Ni/SiO<sub>2</sub> catalyst reduced in H<sub>2</sub> and outgassed.

Skeletal spectra (Fig. 94) of the two catalysts showed the typical features of silica-based materials at 1100  $\text{cm}^{-1}$  (shoulder at 1250  $\text{cm}^{-1}$ ), 800 and 450  $\text{cm}^{-1}$  for the Ni/SiO<sub>2</sub> sample and of titania at 680  $\text{cm}^{-1}$ , broad, for the Ni/TiO<sub>2</sub> sample [79].

In contrast with the FP-prepared samples, the spectra of the T1C500 surface after heating at 500°C in vacuum had a very small transmittance window and showed a high noise. The subtraction spectra reported in Fig. 94 after CO adsorption showed only weak and broad bands between 2200 and 2180  $\text{cm}^{-1}$ , due to CO coordinated over ionic species (Ti ions).

Apparently, no metallic species characterised by bands below 2000  $\text{cm}^{-1}$  could be detected. The same sample following reduction does not allow any IR analysis due to the very low transmittance, if any. The same behaviour has been found for the T2C500 sample, whose spectra are not reported.

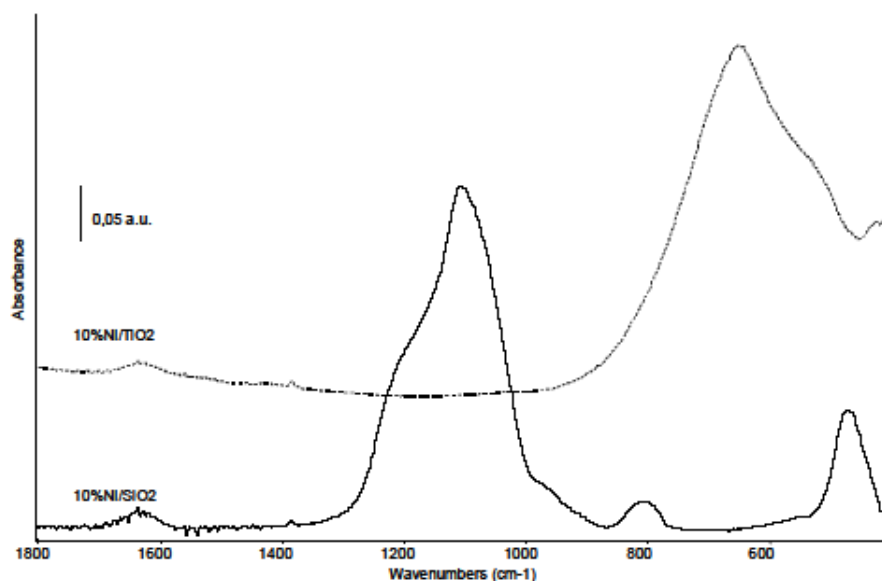


Figure 95 :FT-IR skeletal spectra of 10%Ni/TiO<sub>2</sub> and 10%Ni/SiO<sub>2</sub> catalysts prepared by FP.

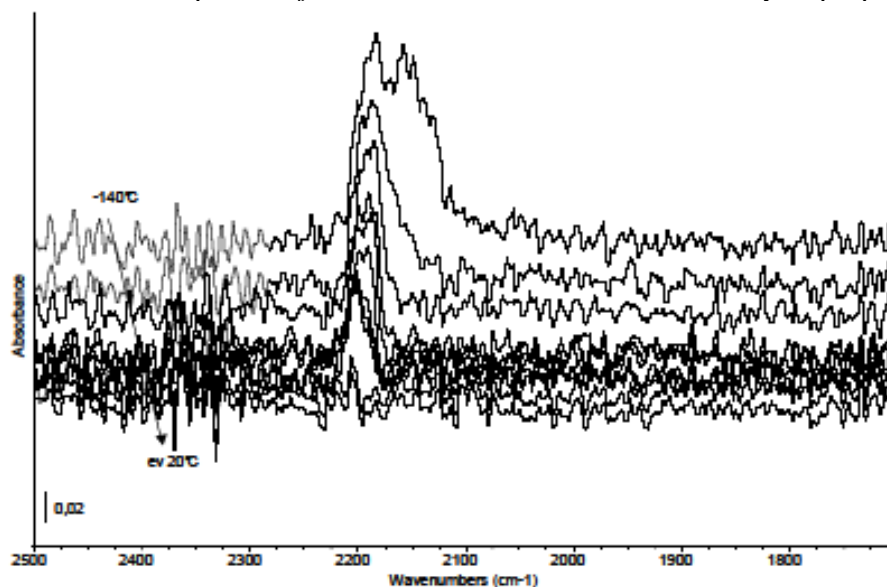


Figure 96 :FT-IR subtraction spectra of surface species arising from CO adsorption over TIC500 catalyst at liquid nitrogen temperature. The activated surface has been subtracted.

Sample T4C800 evidenced a broad and ill-defined band due to OH stretching. Low temperature CO adsorption gave rise to bands in the C-O spectral region: at 2156 cm<sup>-1</sup> (CO interacting with OH groups, possibly overlapped with CO adsorbed over Ni ions, and completely disappearing following outgassing at low temperature), at 2130 (weak), together with the band at 2095 cm<sup>-1</sup> (symmetric/asymmetric stretching modes of poly(di)-carbonyl species stable at low temperature and characterising a dispersed Ni fraction).

Bands at 2060, and possibly 2040 cm<sup>-1</sup>, were assigned to carbonyl species on Ni<sup>0</sup>

crystals, as well as the band at 2020 (shoulder) whose lower frequency suggested the assignment to larger Ni<sup>0</sup> particles. No bands due to CO coordinated over exposed Ti centres can be detected (about 2190 cm<sup>-1</sup>) and, correspondingly, no bands due to PN interacting with Lewis centres were observed.

PN adsorption led to the detection of one band only, due to H-bound species, disappearing following outgassing at room temperature. This can be due to the collapse of surface area in these samples and also to the formation of a titanate phase, as pointed out by XRD results. Features typical of the NiTiO<sub>3</sub> structure also appeared in the skeletal IR spectra Fig. 97, characterised by peaks at 530, 410 and 320 cm<sup>-1</sup> and in agreement with literature data [80]. The shoulder at 690 cm<sup>-1</sup> can be due to the rutile phase, also detected by XRD.

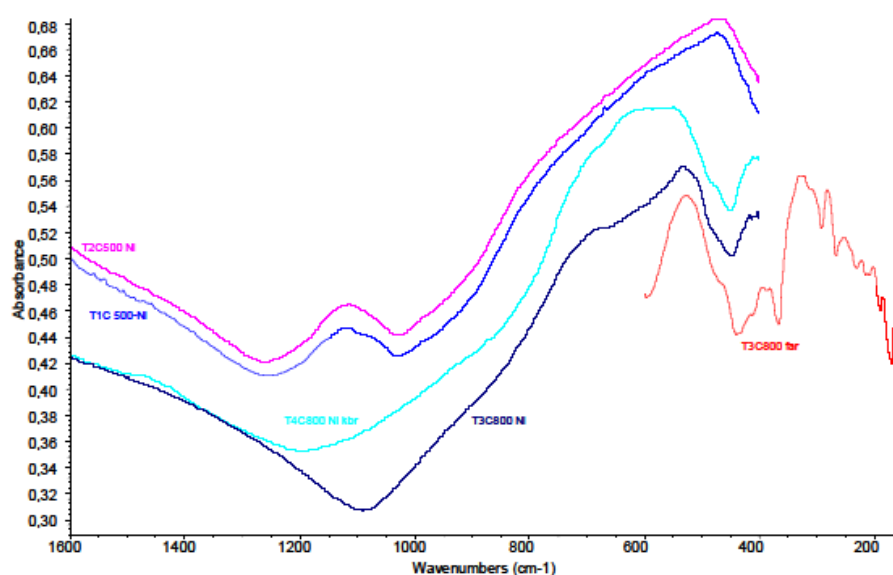


Figure 97: Skeletal and Far FT IR spectra of the Ti-based catalysts.

Another broad absorption around 610 cm<sup>-1</sup> was detected for the T4C800 sample, but not assigned. The spectra of T1C500 and T2C500 samples calcined at 500°C have been reported for comparison and show the broad absorption centred at 470 cm<sup>-1</sup>, characterising the titania anatase phase. These two spectra also show a broad absorption around 1100 cm<sup>-1</sup>, which may be ascribed to some impurities, maybe sulphates, as reported by XPS data for the T1C500 sample.

CO adsorption over T3C800 catalyst allowed the detection of weak and noisy bands in the carbonyl region, likely due to the very low surface area of this sample. However, it was possible to roughly detect the same features reported for the T4C800 sample. Thus, for both samples we were able to detect carbonyl coordinated over Ni metal particles formed already after reduction at 500°C, together with a

fraction of Ni ionic species (Ni strongly interacting with the surface and titanate species). This effect is in agreement with the TPR data indicating for these samples the main reduction peaks at temperatures above 600°C. Spectra of Z1C500 catalyst following activation did not show bands characterising zirconia isolated OH groups, thus pointing out the strong perturbation induced by Ni deposition (Fig. 98, inset).

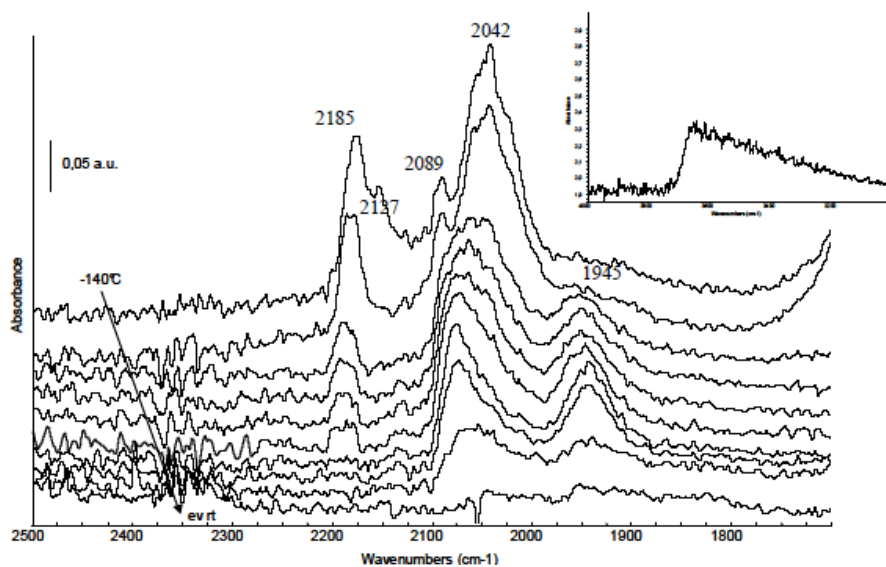


Figure 98 :FT-IR subtraction spectra of surface species arising from CO adsorption over Z1C500 catalyst at liquid nitrogen temperature. The activated surface has been subtracted. Inset: OH stretching region

CO adsorption led to the detection of a band at 2180  $\text{cm}^{-1}$ , with components at lower frequencies. This band decreased in intensity following outgassing and shifted to higher frequencies. This effect was in agreement with its attribution to CO coordinated over ionic species: carbonyls over  $\text{Zr}^{4+}$  and possibly  $\text{Ni}^{2+}$  ions, whose frequencies overlapped. A shoulder at 2150  $\text{cm}^{-1}$  has been assigned to CO adsorbed over a “NiO-like” phase whose enhanced electrophilicity was due to the effect of the support [81]. Low intensity bands at 2127 and 2089  $\text{cm}^{-1}$  were attributed to a dicarbonyl complex of  $\text{Ni}^+$ , while the main band at 2045  $\text{cm}^{-1}$  to CO coordinated over Ni metal particles. Upon out-gassing, this band became broader and the maximum shifted to higher frequencies. Simultaneously, a component at 1945  $\text{cm}^{-1}$  increased, suggesting that some reconstruction phenomena occurred, leading to the coalescence of Ni metal particles. As a consequence, two carbonyl bands remained in the spectrum after outgassing: they were assigned to linear and bridging carbonyl species over regular metal particles, possibly Ni(100) and/or Ni(111). This effect suggested that nickel particles consisted of high index planes favouring bridging CO



adsorption. On the other side, these facets, studied by IRAS spectroscopy, have been reported to be most stable on large Ni particles [82].

PN adsorption over the same catalyst (Fig. 99) led to the detection of a broad band at  $2274\text{ cm}^{-1}$ , due to nitriles coordinated over exposed  $\text{Zr}^{4+}$  acidic sites. The frequency of this band, slightly lower than in the case of PN over exposed Ti ions, was in agreement with the medium acidic strength of Zr ions sites.

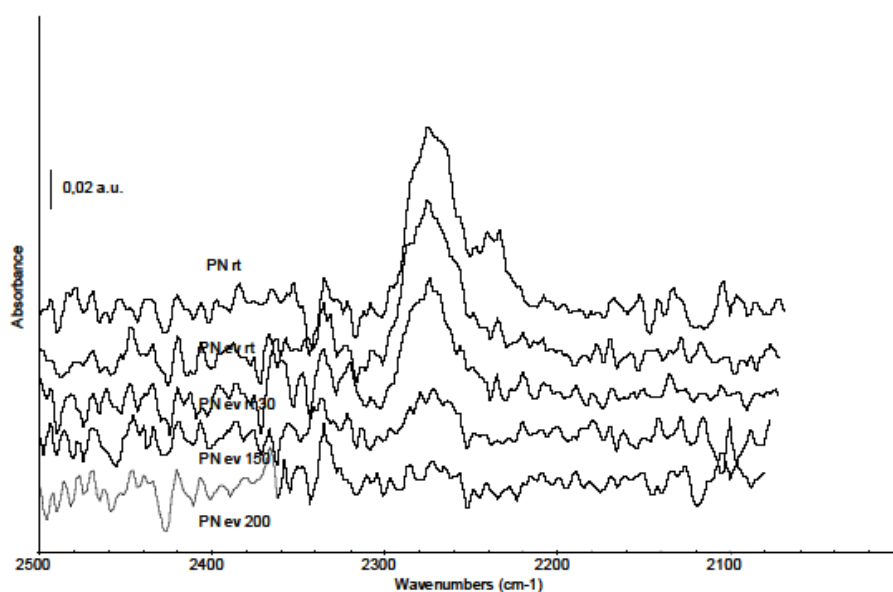


Figure 99 :FT-IR subtraction spectra of surface species arising from PN adsorption over Z1C500 catalyst at liquid nitrogen temperature. The activated surface has been subtracted.

After CO adsorption over Z2C800, three main bands could be detected at  $2190$ ,  $2062$  and  $1969\text{ cm}^{-1}$ , although very weak and noisy. The former was due to carbonyl over exposed Zr ions. This band decreased in intensity following outgassing and shifted to higher frequencies, in agreement with the proposed assignment. Bands below  $2100\text{ cm}^{-1}$  were assigned to CO on-top and bridging over Ni metal particles and can be compared with bands detected following CO adsorption and outgassing over the Z1C500 sample. PN adsorption over the same catalyst led to the detection of a weak and broad band at  $2275\text{ cm}^{-1}$ , due to nitrile coordinated over exposed  $\text{Zr}^{4+}$  acidic sites, in agreement with data from CO adsorption. Thus, with respect to the spectra of the Z1C500 sample, the metalcarbonyl species here detected were consistent with the formation of quite large Ni metal particles. We do not have any evidence of the “reconstruction” of the surface after CO adsorption (we proposed this effect to occur over the Z1C500 sample to explain the changes detected in the carbonyl spectra

upon outgassing and warming). Zr ions were exposed at the catalysts surface. The skeletal spectra of the zirconia based samples were completely consistent with the formation of monoclinic  $\text{ZrO}_2$  (band at  $745\text{ cm}^{-1}$ ).

As discussed for the FP-prepared  $\text{Ni/SiO}_2$  sample, CO adsorption at liquid nitrogen temperature over sample S1C500 gave rise to a main band at  $2155\text{ cm}^{-1}$ , due to H-bonded species, which corresponded to silanol negative band in the subtraction spectra, and to a lower intensity band around  $2134\text{ cm}^{-1}$ , due to liquid-like CO. As expected these bands readily disappeared upon outgassing (Fig. 100).

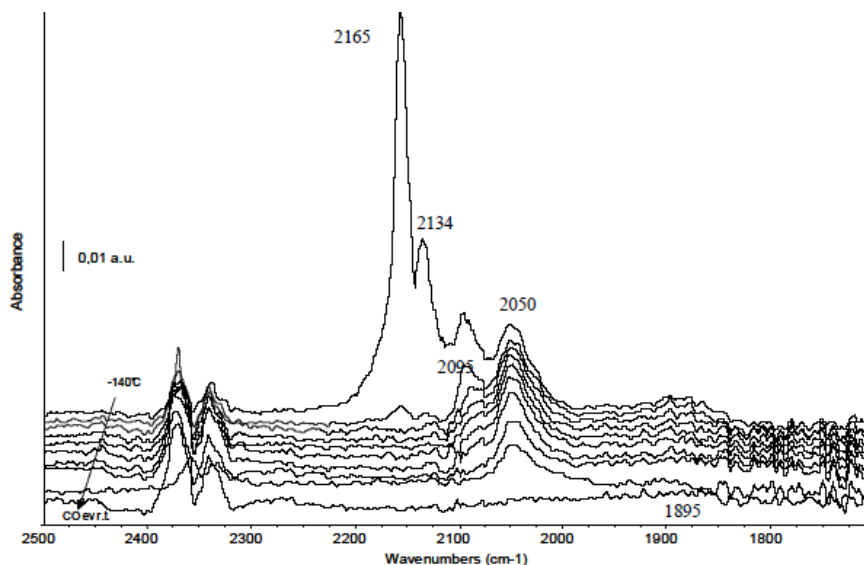


Figure 100 :FT-IR subtraction spectra of surface species arising from CO adsorption over S1C500 catalyst at liquid nitrogen temperature. The activated surface has been subtracted.

Bands at  $2095$  and  $2050\text{ cm}^{-1}$  were assigned to CO adsorption on top of Ni metal particles (corner or edges). However, the analysis of bands evolution upon outgassing allowed the assignation of the former band (more labile) to nickel species having ionic character, *i.e.*  $\text{Ni}^+(\text{CO})_2$ . In this case the corresponding asymmetric stretching band should be detected, very weak, around  $2130\text{ cm}^{-1}$ . Alternatively, this band could be due to small highly dispersed particles, which did not exhibit frequency characterising distinct facets. A weak and broad band due to bridging species could be detected at about  $1895\text{ cm}^{-1}$ . Its low frequency was in agreement with an assignation to both twofold and threefold sites.

PN adsorption, as discussed for the  $10\%\text{Ni/SiO}_2$  sample, led to a main band at  $2245\text{ cm}^{-1}$  due to PN H-bound and corresponding to a negative silanol band in the high frequency region (Fig. 101). No weak bands due to supported nickel were detected, confirming the results of chemisorption analysis.

No silanol bands could be detected following the reduction treatment for S2C800, but only a broad and strong signal around  $3700\text{ cm}^{-1}$ , tailing towards lower frequencies. In the spectra recorded following CO adsorption, strong bands at  $2155$  and  $2138\text{ cm}^{-1}$ , also in this case tailing towards lower frequencies, were attributed to CO interacting with OH groups and weakly physisorbed, and completely disappeared following outgassing. The strong band at  $2045\text{ cm}^{-1}$  was assigned to terminal carbonyls over Ni metal particles and the weak absorption at  $1885\text{ cm}^{-1}$  was ascribed to bridging carbonyls on extended Ni metal particles. Following outgassing upon warming, another component appeared at  $2000\text{ cm}^{-1}$ , thus in the frequency range characterising carbonyls over Ni metal particles possibly exposing different facets. The formation of polycarbonyls over ionic and metallic Ni clusters (bands at  $2130$ - $2090\text{ cm}^{-1}$ ) was strongly limited, if any. PN adsorption revealed, as expected, only H-bound species, readily disappearing following outgassing.

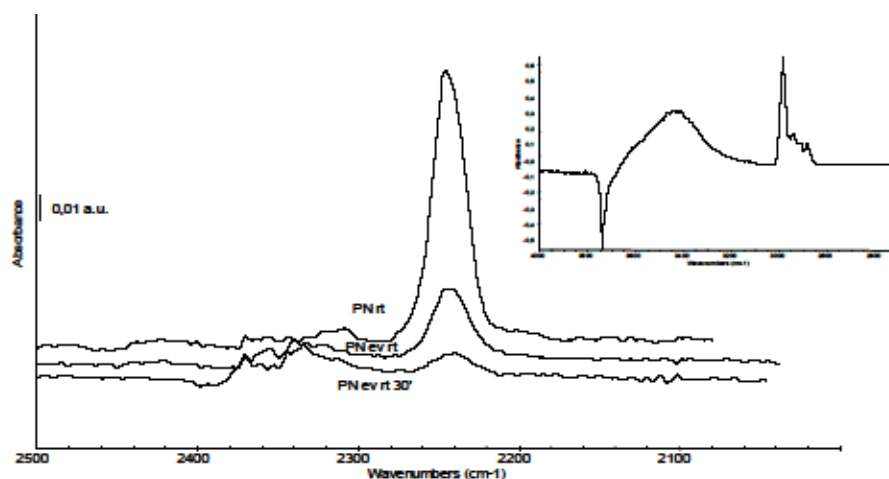


Figure 101: FT-IR subtraction spectra of surface species arising from PN adsorption over S1C500 catalyst. The activated surface has been subtracted. Inset: OH stretching region.

### **Co based catalysts:**

The skeletal IR spectra of this series of samples are reported in Figure 102.

As for the T samples (Fig. 102b), the broad band centred at  $450\text{ cm}^{-1}$  and tailing towards higher frequencies characterizes the anatase  $\text{TiO}_2$  phase, in agreement with XRD data. Moreover, we can clearly notice several sharp components at  $656$ ,  $557$  and  $458\text{ cm}^{-1}$ , superimposed to the main absorption. These bands are due to Cobalt-Oxygen vibrational modes of cobalt oxide species, likely  $\text{Co}_3\text{O}_4$ . The first band is associated with the  $\text{OB}_3$  vibration in the spinel lattice, where B denotes  $\text{Co}^{3+}$  in an octahedral hole. The second band is attributed to the  $\text{ABO}_3$  vibration, where A denotes the  $\text{Co}^{2+}$  in a tetrahedral hole [83-85]. Spectrum of sample T8 in the far-IR

region shows another component at  $267\text{ cm}^{-1}$ . The spectrum of sample T6 shows a broad band due to titania support, however bands due to cobalt oxides are also detected as weak shoulders. Moreover this sample shows other weak and complex absorptions between  $1200$  and  $1000\text{ cm}^{-1}$  possibly related to sulphate and/or Si-containing materials in the support.

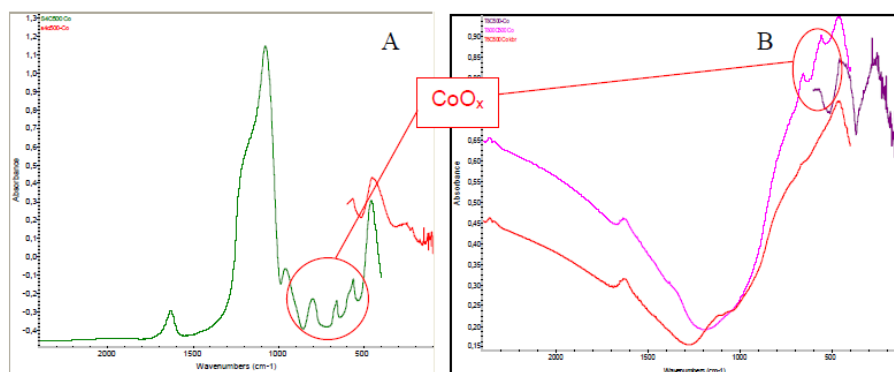


Figure 102: FT IR and far-IR skeletal spectra of Co-containing samples (a) S4C500 Co; (b) T6C500 and T8C500 Co samples

Silica support is characterized by the typical absorption at  $1078\text{ cm}^{-1}$  (with a shoulder at  $1200\text{ cm}^{-1}$ ), and by bands at  $802$  and  $460\text{ cm}^{-1}$  due to stretching and deformation modes of the  $\text{SiO}_4$  structural unit (Fig. 102a). The weak band at  $962\text{ cm}^{-1}$  is assigned to Si-OH and /or Si-O- deformation modes and is reported to be detected in the presence of a modifier or intermediate glass forming oxides. In a previous work, the presence of this band has been related to the interaction of Co oxides with the silica network. In fact, the higher the intensity of this band, the weaker the interaction of Co ions with silica matrix [86].

Adding Cobalt results in the detection of further sharp bands at  $660$  and  $565\text{ cm}^{-1}$ , both of them complex, assigned to  $\text{Co}^{\text{III}}$ -O bonds in cobalt oxide species, as in the case of T8 sample. The frequency is slightly shifted towards higher frequencies, with respect to the T8 sample spectrum. This effect can be due to a different morphology of the  $\text{CoO}_x$  phase. In the far-IR region another weak absorption at  $257\text{ cm}^{-1}$  can be detected (possibly due to  $\text{Co(II)}$ -O vibrational modes).

In Fig. 103 the spectra in the UV-Vis NIR region of all the Co containing samples are reported. Several strong absorptions are detected in the  $200$ - $1800\text{ nm}$  range.

As already reported, titania support only shows an absorption around  $380\text{ nm}$ , due to the  $\text{O}^{2-}\text{Ti}^{4+}$  charge transfer, while silica only shows weak absorptions below  $300\text{ nm}$ . Thus all the complex absorptions detected above  $400\text{ nm}$  are mainly related to the

presence of cobalt species.

In detail, for the sample T8, the one showing strong IR bands due to Co oxides, we detected two bands in the visible region at 484 and 705 nm, characterizing  $\text{CoO}_x$  clusters [87] and two very broad absorptions in the NIR region at 1310 (shoulder at 1220) and 1500 nm. These features are consistent with the spectra of supported  $\text{CoO}_x$  species and of pure  $\text{Co}_3\text{O}_4$  and  $\text{CoAl}_2\text{O}_4$  species.

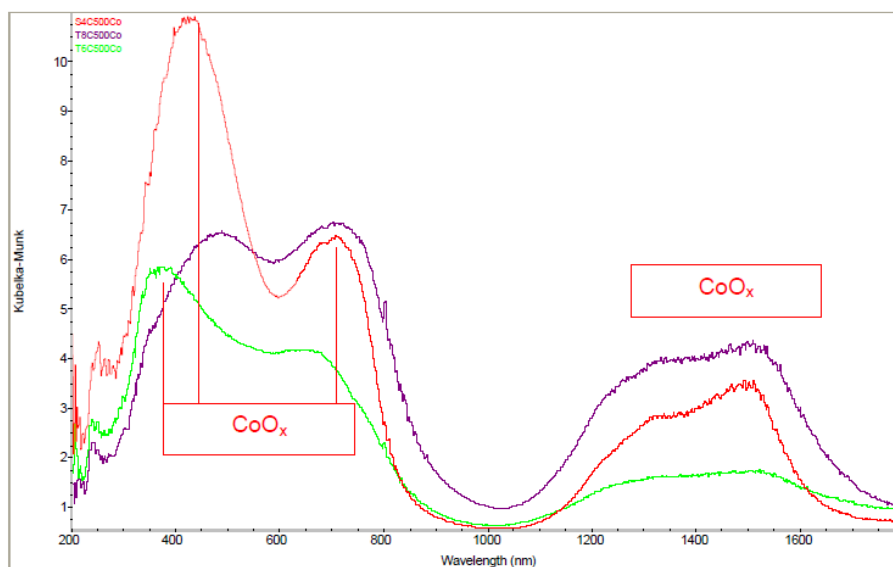


Figure 103: DR-UV-Vis NIR spectra of the Co-containing samples

Previous studies allow to assign absorptions near 420, 700 and 1310 nm to different d-d transitions of tetrahedrally coordinated  $\text{Co}^{2+}$ , as in the cobalt aluminate [84,88]. The strong band around 1300 nm could be related to the presence of massive  $\text{Co}_3\text{O}_4$ . The maximum tailing towards higher energies (i.e. the UV region) more evident in the T6 sample spectrum could be due to the octahedral  $\text{Co}^{3+}$ , as in  $\text{Co}_3\text{O}_4$ , but in this region also the titania absorption bands fall. As for the silica-based sample, the spectrum shows features intermediate between the two samples described before and the main band of the spectrum is now centred at 420 nm. The comparison amongst UV-Vis data suggests that the T8 sample was dominated by absorption of tetrahedrally coordinated  $\text{Co}^{2+}$ , while the spectrum of the T6 was dominated by a low frequency component which could be assigned to trivalent cobalt. In both samples  $\text{Co}_3\text{O}_4$  is formed. However FT IR data point out the increased Cobalt oxide massive formation in the sample T8. The same effect can be detected in the S4 sample. Moreover, in this sample formation of massive  $\text{CoO}_x$  species, weakly interacting with the silica network, is consistent with the detection of the  $950\text{ cm}^{-1}$  band and the features due to Co-O vibrational modes well defined in the  $650\text{-}550\text{ cm}^{-1}$  region. FT

IR spectra reported in Fig. 104 for the FP samples show only the features due to the oxide support: titania and silica.

Moreover we had evidence of a massive CoOx formation, characterized by sharp bands in the 650-550  $\text{cm}^{-1}$  region, neither over silica, nor over titania. Also in the UV Vis NIR region (Fig. 108) we noticed the main absorption related to the titania support (sample Co/TiO<sub>2</sub>) at 250 nm and a very weak absorption around 200 nm for silica support.

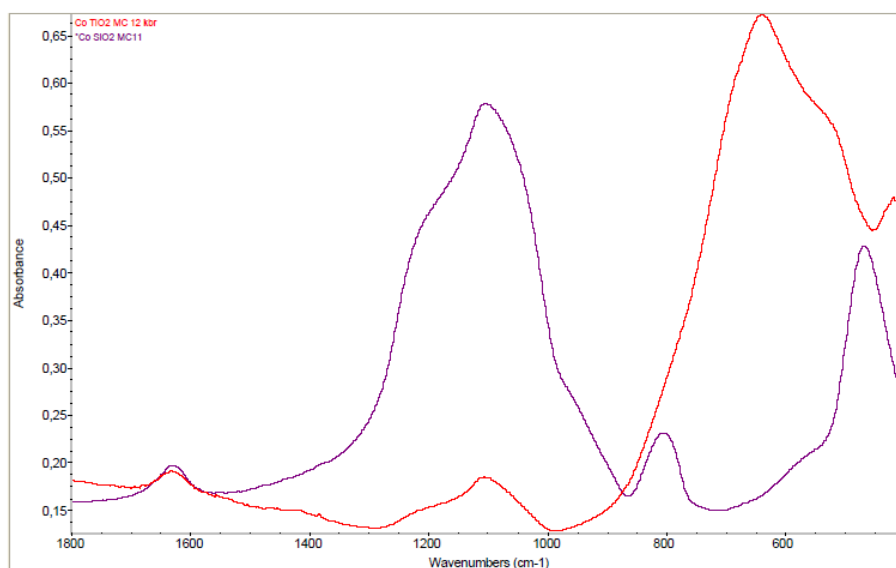


Figure 104: FT-IR skeletal spectra of FP Co containing spectra.

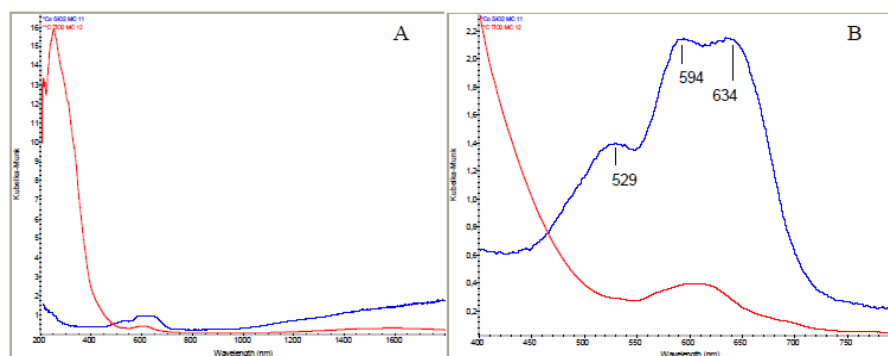


Figure 105: (a) DR-UV-Vis NIR spectra of the Co-containing samples- (b) Enlargement of the Visible region

Co doping leads to the detection of a triplet (529, 594, 634 nm, Fig. 105 enlargement) in the visible region for the Co-SiO<sub>2</sub> sample. These features, in close agreement with spectra reported by Esposito et al. [89], have been assigned to Co<sup>2+</sup> ions in tetrahedral environment, *i.e.* Co(O<sup>-</sup>)<sub>4</sub>, where the “ligands” come from the silica matrix. Splitting of these bands has been related to a lowered symmetry with respect to the regular tetrahedral configuration [89]. The same bands, although very weak can be

detected in the spectrum of Co-TiO<sub>2</sub> sample. The typical bands in the NIR region related to the presence of cobalt oxides cannot be detected. These features point out the presence of (mainly) Co<sup>2+</sup> ions in tetrahedral coordination incorporated in the support framework. This effect has been described for Cobalt supported over mesoporous silica and other silica-based materials, and for Co on alumina [87]. These results are consistent with TPR results where only reduction of CoO at high temperature can be detected for both samples.

All the samples analysed have been submitted to a mild reduction treatment at 550°C in hydrogen before any CO adsorption experiment.

The spectra reported in Figures 109 and 110 have been recorded following CO adsorption at low temperature over the Co-silica catalysts (impregnation and FP preparation). Over both catalysts, immediately after CO adsorption a main band is detected at 2157 cm<sup>-1</sup>, readily disappearing upon warming. This feature is due to CO interacting with silanol groups of the

support, and correspond to a negative band in the high frequency region. In addition to this band, the spectrum of sample 10%Co/SiO<sub>2</sub> prepared by FP shows a strong component at 2179 cm<sup>-1</sup>, with a shoulder at 2188 cm<sup>-1</sup> more clearly defined at decreasing CO coverage and ascribed to CO coordinated over surface Co<sup>2+</sup> ions. The highest frequency shoulder could be associated to the presence of some Co<sup>3+</sup> ions exposed at the surface, although bands in this frequency range have also been assigned to CO over Cobalt II ions.

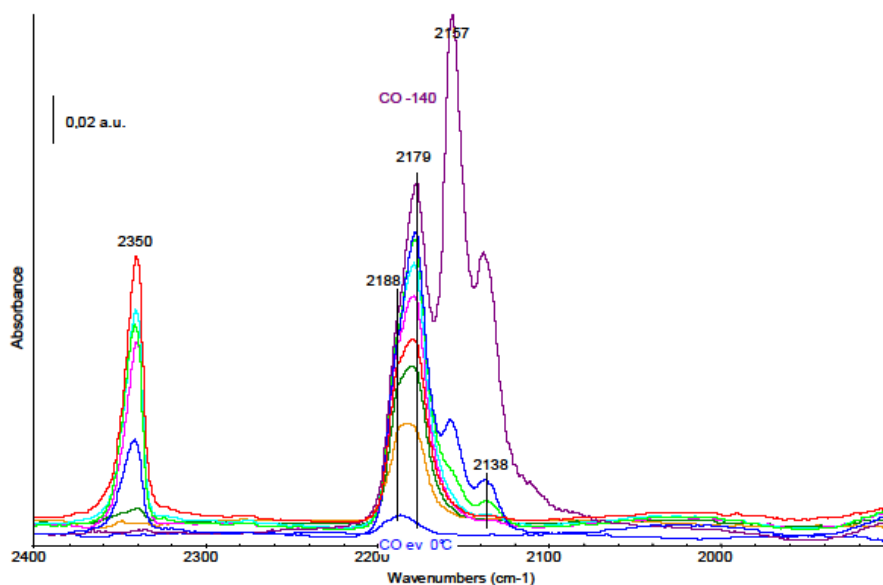


Figure 106: FT-IR spectra of surface species arising from low temperature CO absorption over H<sub>2</sub>-reduced FP Co/SiO<sub>2</sub> sample. The activated surface spectrum has been subtracted.

Another complex although weaker band around  $2138\text{ cm}^{-1}$  has been also assigned to CO coordinated over ionic Co, likely in an oxidation state lower than 2 [90]. The evidence of different component in the IR absorption bands can be due to the presence of cobalt ions in different environment [91]. The simultaneous  $\text{CO}_2$  formation at higher contact times (broad band centred at  $2350\text{ cm}^{-1}$ ) is due to CO oxidation over Cobalt ions which are at least partially reduced. Only traces of cobalt metal particles are revealed by CO coordination (very weak and broad band between  $2050$  and  $2000\text{ cm}^{-1}$ ). The detection of mainly cobalt ions following our reduction treatment is in agreement with TPR data which show the reduction of cobalt species to occur at high temperatures. As for the sample S4C500-Co (impregnated), bands at  $2177\text{ cm}^{-1}$  (very weak) and  $2136\text{ cm}^{-1}$  shifting towards lower frequencies ( $2120\text{ cm}^{-1}$ ) are due to CO coordinated over cobalt ions, as discussed above and in agreement with TPR results. Moreover, the spectrum we obtained also shows the presence of easily reduced metal centres characterised by a complex band centred at  $2064\text{ cm}^{-1}$  and tailing towards lower frequencies, thus within the frequencies range reported in the literature for CO coordinated over metal surface sites as Co-CO or  $\text{Co}(\text{CO})_n$  (Figure 107, inset).

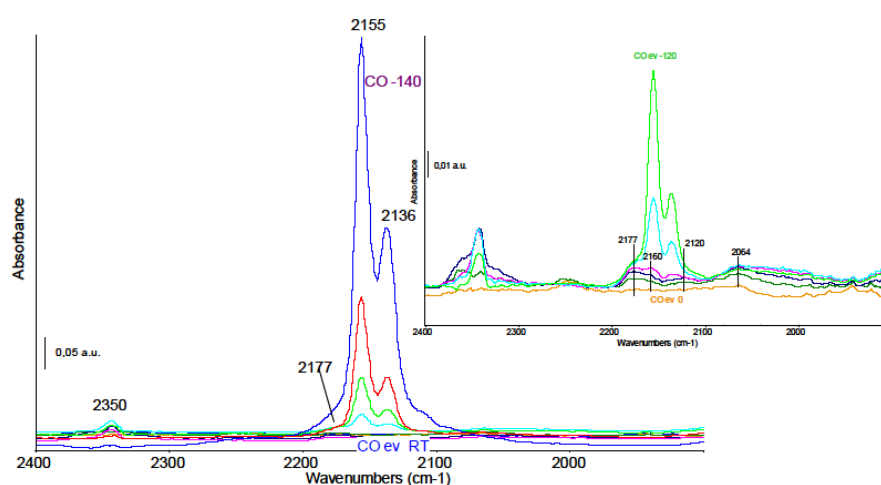


Figure 107: FT IR spectra of surface species arising from low temperature CO adsorption over  $\text{H}_2$ -reduced S3C500Co sample. The activated surface spectrum has been subtracted. Inset: magnification of the carbonyl species in the temperature range  $-120$ - $0^\circ\text{C}$ .



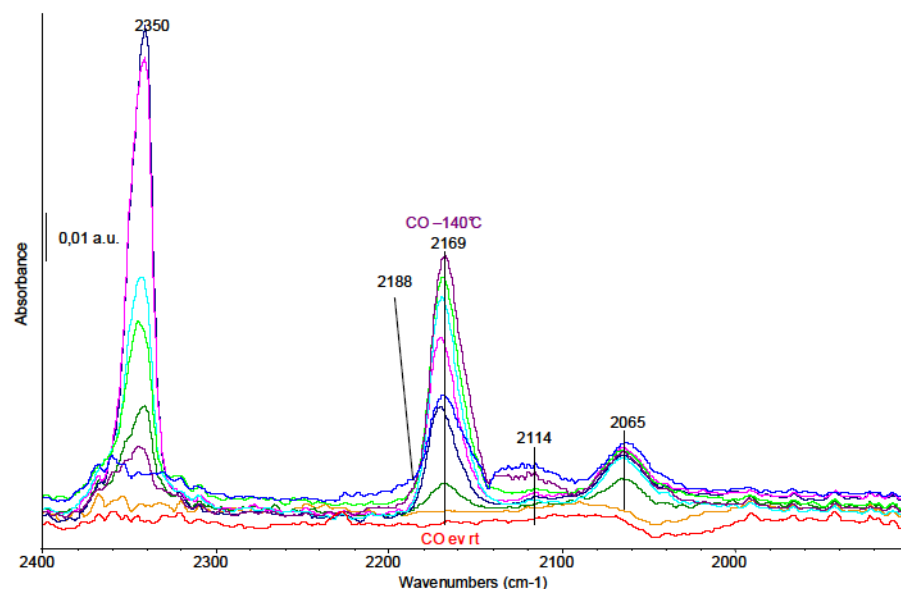


Figure 108: FT IR spectra of surface species arising from low temperature CO adsorption over H<sub>2</sub>-reduced 10%Co/TiO<sub>2</sub> sample. The activated surface spectrum has been subtracted

Accordingly, the amount of CO<sub>2</sub> formed by CO oxidation from residual Co ions, is here reduced with respect to the sample 10%Co/SiO<sub>2</sub> (weak band around 2350 cm<sup>-1</sup>). The comparison of spectra reported in Figures 102 and 107 indicates an increased reducibility of the cobalt oxides species detected over the impregnated samples, in agreement with TPR data. Several cobalt species can be detected at the catalysts surface.

Over the reduced sample FP 10%Co/TiO<sub>2</sub>, CO coordinated linearly over cobalt ions Co<sup>2+</sup> (band at 2169 cm<sup>-1</sup>), over partially reduced Co ions (weak band at 2114 cm<sup>-1</sup>) and over cobalt metal particles (band at 2065 cm<sup>-1</sup>). The absence of the high frequency band at 2180 cm<sup>-1</sup> (a shoulder at 2188 cm<sup>-1</sup> is barely visible) and the detection of the band due to CO linearly coordinated over cobalt metal particles at 2065 cm<sup>-1</sup> point out the increased reducibility of this catalyst with respect to the silica based sample. The reduction of the samples T8C500Co and T6C500Co leads to spectra showing almost zero.

Transmittance in the mid IR region (Figure 109, maximum T% = 0.60), possibly due to the extensive reduction of massive Co oxides at the surface. A similar behaviour was observed for Ni-based catalysts. In these experimental conditions, CO adsorption over the reduced surface just allows the detection of a weak band at 2152 cm<sup>-1</sup> due to CO interacting with OH groups of the support. On the other side, the high noise of the spectrum does not allow the detection of carbonyl species coordinated over Co ions or metal particles.

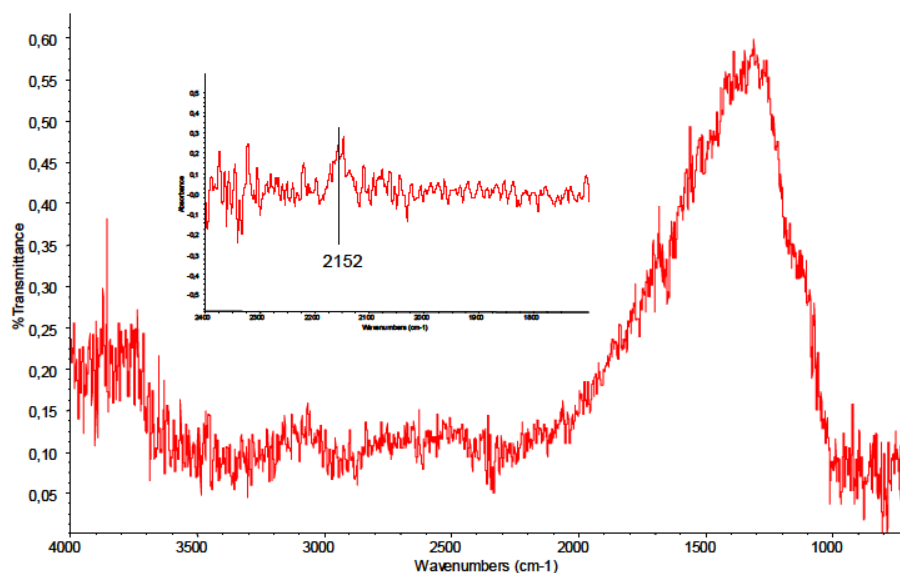


Figure 109: FT IR spectra of T6C500 Co sample following reduction in hydrogen at 500°C. Inset: surface species arising from CO adsorption at -140°C; the activated surface spectrum has been subtracted.

Spectra of the sample T9 show are even more noisy (not reported). In sum, support and preparation methods affect the morphology of supported Cobalt species:

Over the FP samples, Co/SiO<sub>2</sub> and Co/TiO<sub>2</sub>, no formation of massive cobalt oxides can be detected, Co is dispersed in the structure and over the catalyst supported on silica, it is mostly Co(II). In this catalyst, Cobalt oxide species are difficult to be reduced, while for the Si-based sample Co can be reduced by our mild reduction treatment, showing features typical of carbonyl species over metal particles.

As for the impregnated samples S and T, CoO<sub>x</sub> particles are formed both over titania and silica, weakly interacting with the support. The different intensities of the Co-O vibrational bands, clearly detected by the spectroscopic analyses, reflect the different Cobalt charge in the preparation methods for samples T6 and T8. Co<sup>III</sup> and Co<sup>II</sup> ions are present. Conversely, these species are more prone to reduction (at least for the S4C500 Co sample).

### **Cu based catalysts:**

In Figure 110 FT IR skeletal spectra of the titania and silica based samples (T9, T11, S3) are reported. The main bands observed are assigned to the lattice vibrational modes of the oxide supports. The presence of copper species in the form of copper oxides can be suggested by the very weak bands around 600 cm<sup>-1</sup> in the silica-based sample spectrum [92], while the same bands, if existing, can be masked by the

strong anatase bands in the titania-based spectrum. In the T11 preparation other weak bands in the 1300-1600  $\text{cm}^{-1}$  range are due to residual carbonate and nitrate species from the catalyst preparation.

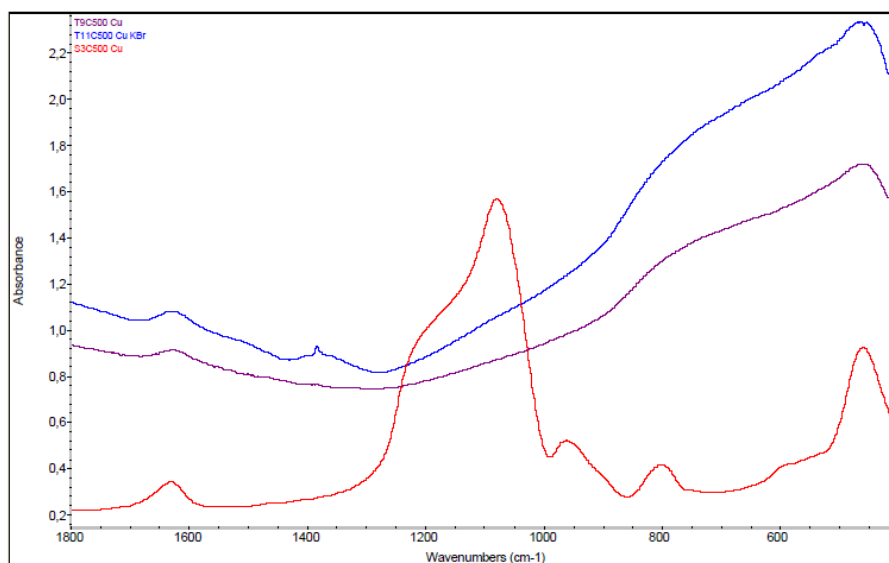
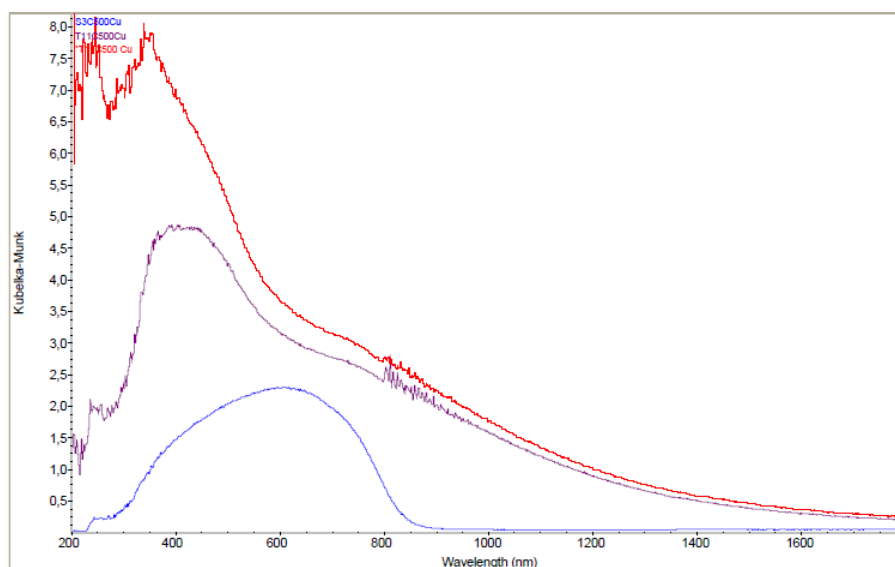


Figure 110: FT IR skeletal spectra of the Cu-containing T and S samples

Spectra in the UV-Vis-NIR region are reported in Figure 111. The spectrum of Cu supported over titania (sample T11) shows a main band centred between 420 and 500 nm, thus above the absorption edge characteristic of pure titania (anatase), with a shoulder tailing towards higher wavenumbers, in the NIR range. The former component has been tentatively assigned to  $\text{Cu}_2\text{O}$  layers-like species [93]. The absorption growing in the NIR spectral region can be due to the scattering effect.

The spectrum of the T9 sample shows the same absorption, although sharper and shifted towards lower wavenumbers. Moreover, another absorption at 236 nm can be observed.

The silica based S3 sample shows only a strong and unstructured absorption extending in the visible region, which has been associated to the presence of large Cu metal particles [93]. In fact, according to literature data, very large copper metal aggregates do not have specific signals in electronic spectra, but a diffuse absorption [94].



*Fig. 111: UV-Vis.-NIR spectra of the Cu-containing T and S samples*

FT IR skeletal spectra of the FP catalysts show features due to support titania (rutile) and silica oxides (Figure 112), too. The corresponding spectra in the UV-Vis-NIR region are reported in Figure 116. Cu supported over silica show a band pattern completely consistent with data from literature [95]. The broad band in the spectrum centred around 800 nm, as assigned to fundamental transition of small CuO particles, shifted with respect to the bulk absorptions by the small size effect. The broad absorption from 500 down to 300 nm has also been tentatively assigned to Cu<sub>2</sub>O layers like species, as in the previous case [95]. This latter absorption is absent in the titania based catalyst.

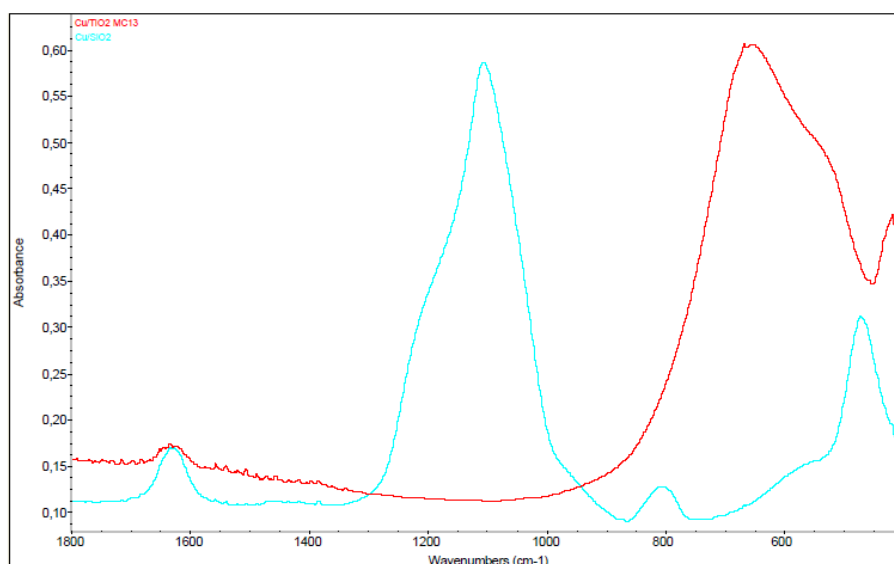


Fig. 112: FT IR skeletal spectra of the Cu-containing FP samples

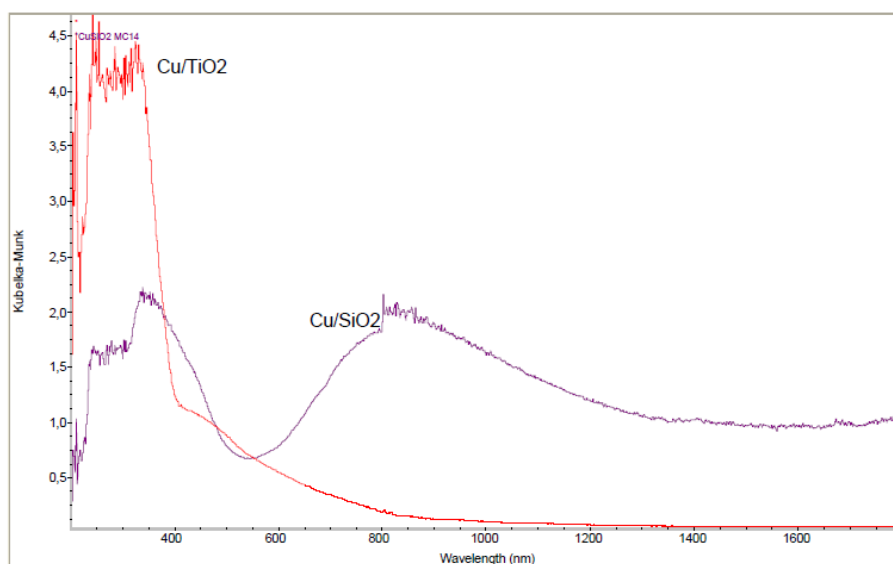
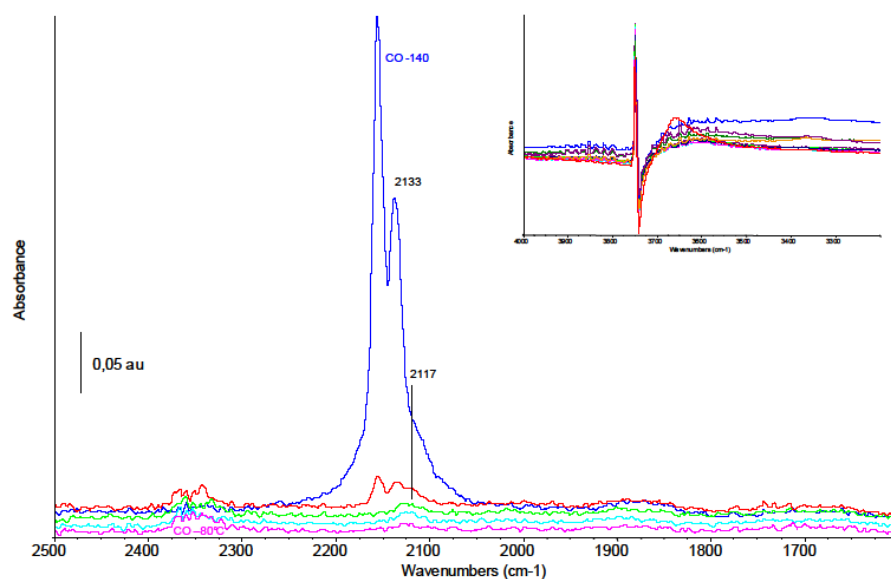


Fig. 113: UV-Vis.-NIR spectra of the Cu-containing FP samples

CO adsorption over reduced S3C500 Cu sample gives rise to a strong IR band due to CO interacting with silanol groups (strong band at  $2155\text{ cm}^{-1}$ ) and corresponding to a weak negative band in the subtraction spectrum in the OH stretching spectral region. Carbonyl species coordinated over residual  $\text{Cu}^{2+}$  ions are characterized by bands in the range  $2180\text{--}2150\text{ cm}^{-1}$ , thus can be masked by the strong CO---HO absorption [95-98]. Following outgassing this band disappears almost immediately, confirming its assignment to species weakly bound. The weaker component at  $2133\text{ cm}^{-1}$  is due to CO over residual oxidized copper  $\text{Cu}^+$  species.

The shoulder at  $2117\text{ cm}^{-1}$ , tailing towards lower frequencies, can be assigned to carbonyls over dispersed Cu metal particles, strongly interacting with the surface. Similar species have been described as carbonyls coordinated over two dimensional metal cluster (2D raft).



*Fig. 114: FT IR spectra of surface species arising from low temperature CO adsorption over  $H_2$  reduced S3C500Cu sample. Inset: OH stretching region. The activated surface spectrum has been subtracted.*

All these components are very labile and disappear following outgassing at such a low temperature as  $-80^\circ\text{C}$ . Obviously they correspond to very unstable species. The thermal behaviour allow their extensive assignation to reduced  $\text{Cu}/\text{Cu}^+$  species, although the frequency range of these bands is unusually high [99].

CO adsorption over T11 sample outgassed at  $500^\circ\text{C}$  and reduced in hydrogen at the same temperature has been carried out upon warming without outgassing (Figure 115a and b). The two series of spectra show common features, as discussed below, pointing out that the thermal treatment in vacuum itself allows the reduction of the metal particles. Copper species are thus very easily reducible.

At the lowest temperatures two main bands are detected at  $2156$  and around  $2100\text{ cm}^{-1}$ , both of them quite complex. The former is assigned to CO interacting with OH groups and a shoulder at  $2170\text{ cm}^{-1}$  can be due to exposed Ti ions form the support. The complexity of the  $2100$  band and its thermal behaviour deserve some discussion. Over alumina supported Cu catalyst, Escribano et al.[100] assigned a strong band at  $2115\text{ cm}^{-1}$  to carbonyls on copper ions or copper zerovalent clusters (which should correspond to the previously mentioned 2D raft) and another

component centred at  $2100\text{ cm}^{-1}$  and tailing towards lower frequencies to terminal carbonyls on copper zerovalent particles [101]. This assignment has been supported also by the different stability of these species to outgassing: it is in fact well known that carbonyls on reduced Cu adsorb weakly [102]. Features at lower frequencies are assigned to larger (and structured) metal particles, exposing different facets [95]. In our spectra the band is centred at  $2097\text{ cm}^{-1}$ , showing a shoulder around  $2085\text{ cm}^{-1}$ , and the position and thermal behaviour of these bands allow their assignment to Cu clusters and more structured Cu metal particles exposing mainly (110) facets. In the inset (Fig. 115) subtraction spectra allow to evidence the component at  $2085\text{ cm}^{-1}$ .

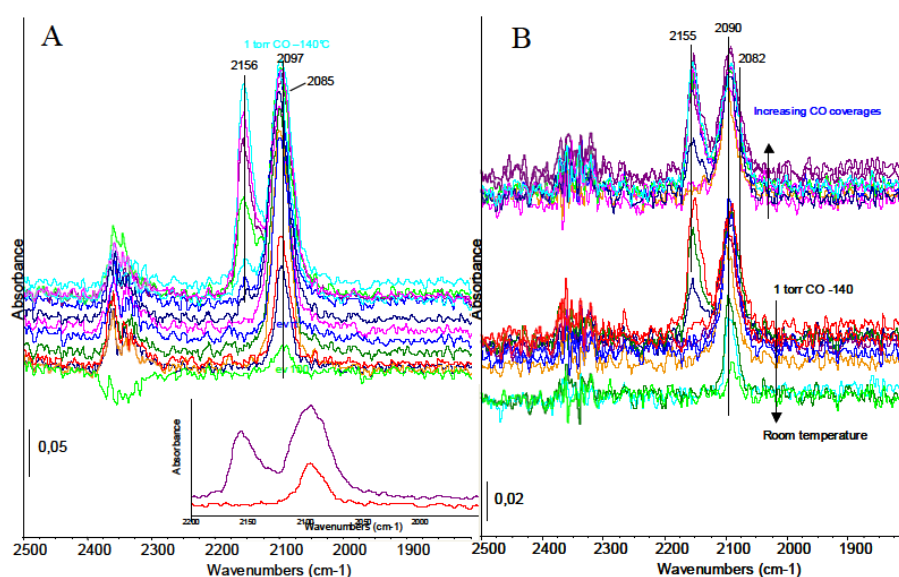


Figure 115: FT IR spectra of surface species arising from low temperature CO adsorption over T11C500Cu sample outgassed at  $500^{\circ}\text{C}$  (a) and reduced in  $\text{H}_2$  at the same temperature (b). The activated surface has been subtracted.

Reduction in hydrogen (Figure 115b), followed by CO adsorption, leads to the detection of the same bands centre at frequencies slightly lower, pointing out an increased electron density of these species. CO adsorption over the T9 sample leads to very similar results. The component at  $2170\text{ cm}^{-1}$  is assigned to CO coordinated over exposed Ti ions; the band at  $2150\text{ cm}^{-1}$  is due to CO H-bound to hydroxy groups of the support; the band at  $2102\text{ cm}^{-1}$ , with shoulder at  $2090\text{ cm}^{-1}$  and tailing towards lower frequencies, due to CO coordinated over Cu metal clusters and particles. Residual Cu ions are likely still present and lead to CO oxidation to  $\text{CO}_2$  even at such a low temperature (see complex band at  $2350\text{ cm}^{-1}$ ).

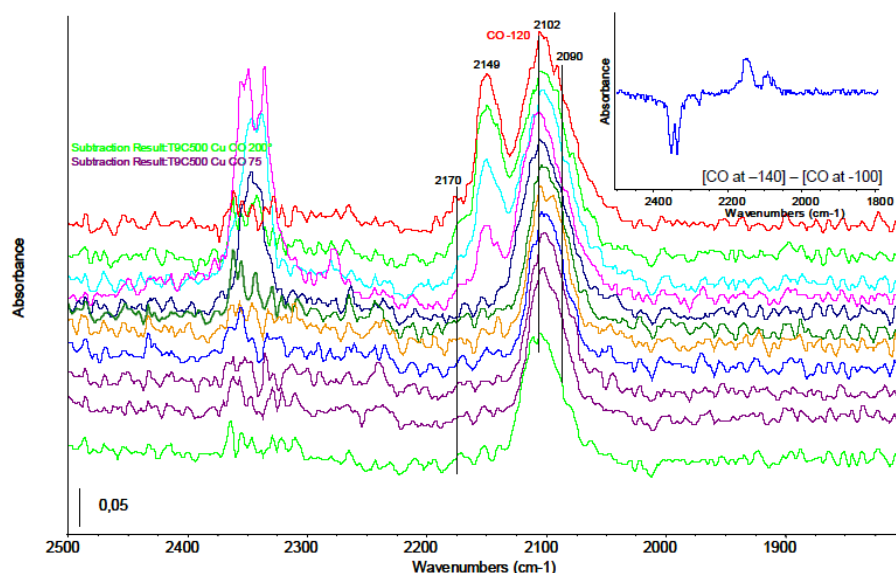


Fig. 116: FT IR spectra of surface species arising from low temperature CO adsorption over T9C500Cu sample. The activated surface has been subtracted.

The comparison of Figures 115 and 116 shows very similar features for CO adsorbed over T9 and T11 samples, *i.e.* high reducibility of a fraction of supported copper, leading to the formation of copper particles, metal clusters strongly interacting with the oxide support. However, the lower frequencies detected for the carbonyl bands over the T11 samples point out the formation of metal particles electron rich and/or exposing more defective facets. In Figure 117, spectra arising from CO adsorption over 10%Cu/SiO<sub>2</sub> sample outgassed in vacuum are reported. The 2156 cm<sup>-1</sup> band is assigned to CO interacting with silanols and corresponds to a negative band at 3742 cm<sup>-1</sup> in the high frequency region of the spectra. A strong band centred at 2117 cm<sup>-1</sup> and tailing toward lower frequencies is assigned to CO linearly coordinated over partially reduced copper species. This band decreases upon outgassing and warming to room temperature, shifting slightly to higher frequencies (2127 cm<sup>-1</sup>). CO adsorption at low temperature over the same sample previously reduced in hydrogen at 500°C leads to the spectra reported in Figure 114*b*. The main band is asymmetric and centred at 2129 cm<sup>-1</sup> and readily disappears following outgassing up to room temperature. Once again, its behaviour allows the assignation of this band to CO coordinated over Cu metal particles. The high frequency suggest the formation of an highly dispersed metal phase, strongly interacting with the surface, or the formation of rough metal particles. Actually the reported frequency is also consistent with formation of carbonyl over Cu<sup>+</sup> ions [100,103,104].



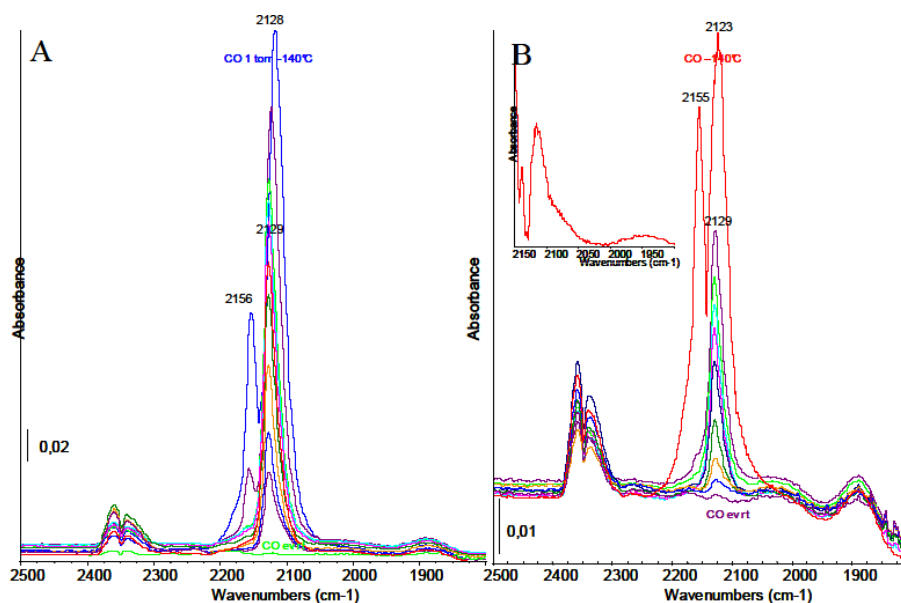


Figure 117: FT IR spectra of surface species arising from low temperature CO adsorption over 10%Cu/SiO<sub>2</sub> sample outgassed at 500°C (a) and reduced in H<sub>2</sub> at the same temperature (b).

CO adsorbed over the 10%Cu/TiO<sub>2</sub> sample (Figure 118) after outgassing at 500°C shows one main band at 2107 cm<sup>-1</sup> with a component at lower frequencies (2093 cm<sup>-1</sup>), due to carbonyl species adsorbed over metal particles having different morphology (likely, clusters and metal particles).

Reduction in hydrogen leads to the detection of a further shoulder around 2080 cm<sup>-1</sup>, observable only in the presence of CO, thus extremely labile. This feature should correspond to CO adsorbed over large Cu metal particles.

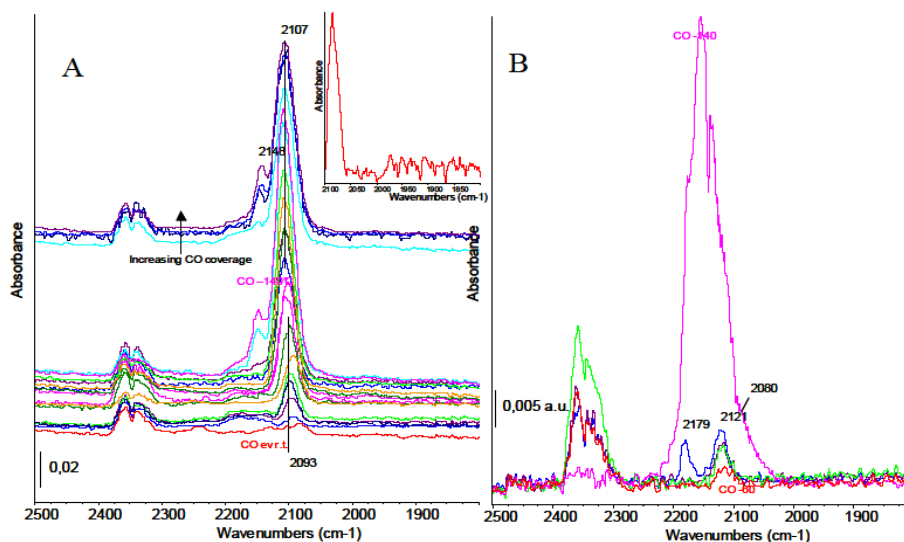


Figure 118: FT IR spectra of surface species arising from low temperature CO adsorption over 10%Cu/TiO<sub>2</sub> sample outgassed at 500°C (a) and reduced in H<sub>2</sub> at the same temperature (b).

## Activity test in Milan

### Activity test in Milan Results:

Parameters reported for each catalyst are the following:

$E_{in}$  (mol/min of ethanol pumped inside the reactor)

$E_{out}$  (mol/min of ethanol detected outside the reactor)

$F_n$  = mol/min of species n detected outside the reactor

$F_{tot}$  = mol flow of all the species detected outside the reactor

**Conversion%** =  $((E_{in} - E_{out}) / E_{in}) * 100$

**Cout%** =  $100 * ((2 * E_{in} - (F_{CO} + F_{CO_2} + F_{CH_4} + 2 * F_{CH_3CHO})) / (2 * E_{in}))$

**CO/CO<sub>2</sub>** =  $F_{CO} / F_{CO_2}$

**Sel n** =  $(F_n / \text{stoichiometric coefficient}) / (E_{in} - E_{out})$

**Productivity** =  $F_n / \text{of catalyst weight}$

### Blank test

Blank test	750 °C	500 °C
Conversion %	62	13
Cout %	100	90
CO/CO <sub>2</sub>	-	0.
H <sub>2</sub> (mol/min)/Kgcat	0.14	0
Sel CO <sub>2</sub> %	0	0
Sel CO %	9.8	7
Sel CH <sub>4</sub> %	0.16	0
Sel CH <sub>3</sub> CHO %	63	24
Sel CH <sub>2</sub> CH <sub>2</sub> %	33	0

Blank tests were led with the reactor filled with quartz grain, the experimental conditions are the same of all the activity test. At 750°C there was no formation of coke and few production of hydrogen ethanol is converted thermally only in acetaldehyde and ethylene, which is no longer observed in the activity tests. At 500°C only CO and acetaldehyde were detected, ethanol conversion was low and the C balance close at 90%

## Group 1

**Table 12 :key legend of the samples**

Name	Formula	Synthesis method
DAL8p2	10% Ni /Al <sub>2</sub> O <sub>3</sub>	Support made by FSP , Ni added by impregnation
DTi1	5% Ni /TiO <sub>2</sub>	Support made by FSP , Ni added by impregnation
DTi2	10% Ni /TiO <sub>2</sub>	Support made by FSP , Ni added by impregnation
DTi3	15% Ni /TiO <sub>2</sub>	Support made by FSP , Ni added by impregnation
FTi1	5% Ni /TiO <sub>2</sub>	Support+Ni one step FSP
FTi2	10% Ni /TiO <sub>2</sub>	Support+Ni one step FSP
FTi3	15% Ni /TiO <sub>2</sub>	Support+Ni one step FSP
LAD1	5% Ni /La <sub>2</sub> O <sub>3</sub>	Support made by FSP , Ni added by impregnation
LAD2	10% Ni /La <sub>2</sub> O <sub>3</sub>	Support made by FSP , Ni added by impregnation
LAD3	15% Ni /La <sub>2</sub> O <sub>3</sub>	Support made by FSP , Ni addde by impregnation
FLA1	5% Ni /La <sub>2</sub> O <sub>3</sub>	Support+Ni one step FSP
FLA2	10% Ni /La <sub>2</sub> O <sub>3</sub>	Support+Ni one step FSP
FLA3	15% Ni /La <sub>2</sub> O <sub>3</sub>	Support+Ni one step FSP
DPLN	LaNiO <sub>3</sub>	FSP

Table 13

DAL8P2	750 °C	500 °C	625 °C	750°C 2 <sup>nd</sup>
Conversion %	100	100	100	100
Cout %	100	46	70	98
CO/CO <sub>2</sub>	2.03	0.81	2.32	2.0
H <sub>2</sub> (mol/min)/Kg <sub>cat</sub>	1.29	0.54	0.35	1.18
Sel CO <sub>2</sub> %	31	19	20	35
Sel CO%	69	50	50	60
Sel CH <sub>4</sub> %	0	6.4	0.6	0
Sel CH <sub>3</sub> CHO%	0	0	0	0

Table 14

DTI1	750 °C	500 °C	625 °C	750°C 2 <sup>nd</sup>
Conversion %	100	90	100	100

Cout %	95	53	76	95
CO/CO <sub>2</sub>	10	1.85	7.90	30
H <sub>2</sub> (mol/min)/Kg <sub>cat</sub>	1.18	0.73	0.74	1.15
Sel CO <sub>2</sub> %	8	16	6	3
Sel CO%	85	30	52	88
Sel CH <sub>4</sub> %	1.17	2	1.28	3
Sel CH <sub>3</sub> CHO%	0	3	13	0

Table 15

DTi2	750 °C	500 °C	625 °C	750°C 2 <sup>nd</sup>
Conversion %	100	100	100	100
Cout %	98	68	85	96
CO/CO <sub>2</sub>	2.45	0.92	2.26	2.56
H <sub>2</sub> (mol/min)/Kg <sub>cat</sub>	1.29	0.97	1.11	1.31
Sel CO <sub>2</sub> %	28	30	25	27
Sel CO%	70	27	53	69
Sel CH <sub>4</sub> %	0	11	5	0.2
Sel CH <sub>3</sub> CHO%	0	0	2.56	0

Table 16

DTI3	750 °C	500 °C	625 °C	750°C 2 <sup>nd</sup>
Conversion %	100	90	100	100
Cout %	97	63	100	100
CO/CO <sub>2</sub>	2.4	0.39	2.0	2.37
H <sub>2</sub> (mol/min)/Kg <sub>cat</sub>	1.4	1.21	1.63	1.49
Sel CO <sub>2</sub> %	28	42	38	29
Sel CO%	68	69	16	69
Sel CH <sub>4</sub> %	0	4.5	0	0
Sel CH <sub>3</sub> CHO%	0	0	0	0

Table 17

FTI1	750 °C	500 °C
Conversion %	100	100

Cout %	97	65
CO/CO <sub>2</sub>	2.7	1.2
H <sub>2</sub> (mol/min)/Kg <sub>cat</sub>	1	1.1
Sel CO <sub>2</sub> %	27	25
Sel CO%	71	33
Sel CH <sub>4</sub> %	0	5
Sel CH <sub>3</sub> CHO%	0	0

Table 18

FTI2	750 °C	500 °C	625 °C	750°C 2 <sup>nd</sup>
Conversion %	100	84	100	100
Cout %	99	76	93	94
CO/CO <sub>2</sub>	2.6	0.6	2.2	4.5
H <sub>2</sub> (mol/min)/Kg <sub>cat</sub>	1.3	1.1	1.2	1.2
Sel CO <sub>2</sub> %	28	42	28	17
Sel CO%	71	25	62	76
Sel CH <sub>4</sub> %	0	10	3	0.8
Sel CH <sub>3</sub> CHO%	0	0	0	0

Table 19

FTI3	750 °C	500 °C	625 °C
Conversion %	100	100	100
Cout %	99	56	87
CO/CO <sub>2</sub>	2.8	0.7	3
H <sub>2</sub> (mol/min)/Kg <sub>cat</sub>	1.4	1.0	1.3
Sel CO <sub>2</sub> %	26	30	22
Sel CO%	74	22	65
Sel CH <sub>4</sub> %	0	3.2	0
Sel CH <sub>3</sub> CHO%	0	0	0

Table 20

LAD1	750 °C	500 °C	625 °C	750°C 2 <sup>nd</sup>
Conversion %	100	84	100	100

Cout %	87	60	78	98
CO/CO <sub>2</sub>	1.9	0.9	1.5	2.2
H <sub>2</sub> (mol/min)/Kg <sub>cat</sub>	1	0.3	1.5	1.7
Sel CO <sub>2</sub> %	23	18	30	31
Sel CO%	46	16	47	68
Sel CH <sub>4</sub> %	0.2	0.5	1	0
Sel CH <sub>3</sub> CHO%	0	8	0	0

Table 21

LAD2	750 °C	500 °C	625 °C	750°C 2 <sup>nd</sup>
Conversion %	100	100	100	100
Cout %	100	81	100	100
CO/CO <sub>2</sub>	2.3	1	2.5	2.6
H <sub>2</sub> (mol/min)/Kg <sub>cat</sub>	1.31	1	0.91	1.52
Sel CO <sub>2</sub> %	30	36	33	28
Sel CO%	68	36	74	73
Sel CH <sub>4</sub> %	0	8	3	1.6
Sel CH <sub>3</sub> CHO%	0	1.6	0	0

Table 22

LAD3	750 °C	500 °C	625 °C	750°C 2 <sup>nd</sup>
Conversion %	100	100	100	100
Cout %	100	71	93	83
CO/CO <sub>2</sub>	2.4	0.6	1.4	1.9
H <sub>2</sub> (mol/min)/Kg <sub>cat</sub>	1.5	1.2	1.5	1.3
Sel CO <sub>2</sub> %	31	42	38	27
Sel CO%	69	25	53	55
Sel CH <sub>4</sub> %	0	4	2	1
Sel CH <sub>3</sub> CHO%	0	0	0	0

Table 23

FLA1	750 °C	500 °C	625 °C	750°C 2 <sup>nd</sup>
Conversion %	100	100	100	100

Cout %	94	79	92	97
CO/CO <sub>2</sub>	2.3	1.2	1.7	2.2
H <sub>2</sub> (mol/min)/Kg <sub>cat</sub>	1.4	0.63	1.5	1.4
Sel CO <sub>2</sub> %	29	26	31	30
Sel CO%	65	31	65	66
Sel CH <sub>4</sub> %	0	1.7	0.6	0.9
Sel CH <sub>3</sub> CHO%	0	11	0	0

Table 24

FLA2	750 °C	500 °C	625 °C	750°C 2 <sup>nd</sup>
Conversion %	100	74	100	100
Cout %	100	91	98	100
CO/CO <sub>2</sub>	2.6	0.7	1.6	2.5
H <sub>2</sub> (mol/min)/Kg <sub>cat</sub>	1.44	0.9	1.4	1.4
Sel CO <sub>2</sub> %	29	42	38	28
Sel CO%	75	31	60	70
Sel CH <sub>4</sub> %	0	7	2	0
Sel CH <sub>3</sub> CHO%	0	7.6	0	0

Table 25

FLA3	750 °C	500 °C	625 °C	750°C 2 <sup>nd</sup>
Conversion %	100	100	100	100
Cout %	95	89	100	100
CO/CO <sub>2</sub>	2.2	0.6	1.6	2.4
H <sub>2</sub> (mol/min)/g <sub>cat</sub>	1.3	1.2	1.4	1.4
Sel CO <sub>2</sub> %	30	51	38	36
Sel CO%	66	31	56	59
Sel CH <sub>4</sub> %	0.7	9.8	2.6	2.5
Sel CH <sub>3</sub> CHO%	0	0	0	0

Table 26

DPLN	750 °C	500 °C	625 °C	750°C 2 <sup>nd</sup>
------	--------	--------	--------	-----------------------

Conversion %	100	100	100	100
Cout %	100	88	98	99
CO/CO <sub>2</sub>	2.6	0.8	1.6	2.5
H <sub>2</sub> (mol/min)/g <sub>cat</sub>	1.3	1.2	1.3	1.3
Sel CO <sub>2</sub> %	28	43	36	29
Sel CO%	72	37	64	73
Sel CH <sub>4</sub> %	0	7.7	1.6	0
Sel CH <sub>3</sub> CHO%	0	0	0	0

A first comparison is between samples with the same Ni loading on different supports prepared by impregnation. The comparison of tests at 750°C for all these catalyst is reported in Figure 119. 100% of conversion and very low formation of carbon are visible and productivity of H<sub>2</sub> was the same for all the catalysts. The same catalysts tested at 500°C showed that even if the conversion was 100% Ni/Al<sub>2</sub>O<sub>3</sub> showed the worst productivity of H<sub>2</sub> and worst carbon balance (below 50%), due to extensive coke formation over the support, as expected due to high acidity. La<sub>2</sub>O<sub>3</sub> based catalysts showed the most resistant towards coking and the highest H<sub>2</sub> productivity, while TiO<sub>2</sub>-based catalyst gave the best CO/CO<sub>2</sub> ratio though also in this case no satisfactory C-out% balance was achieved. After this first comparison Al<sub>2</sub>O<sub>3</sub> based catalyst were no longer tested.

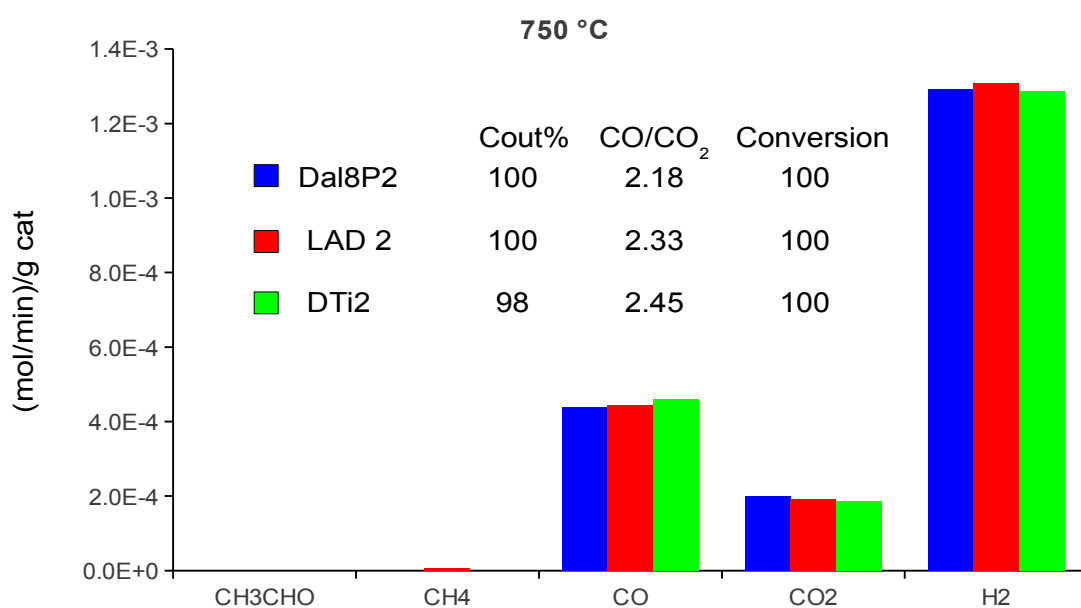


Figure 119: productivity at 750°C of 10%Ni supported on Al<sub>2</sub>O<sub>3</sub>(Dal8P2); TiO<sub>2</sub>(DTi2) and on



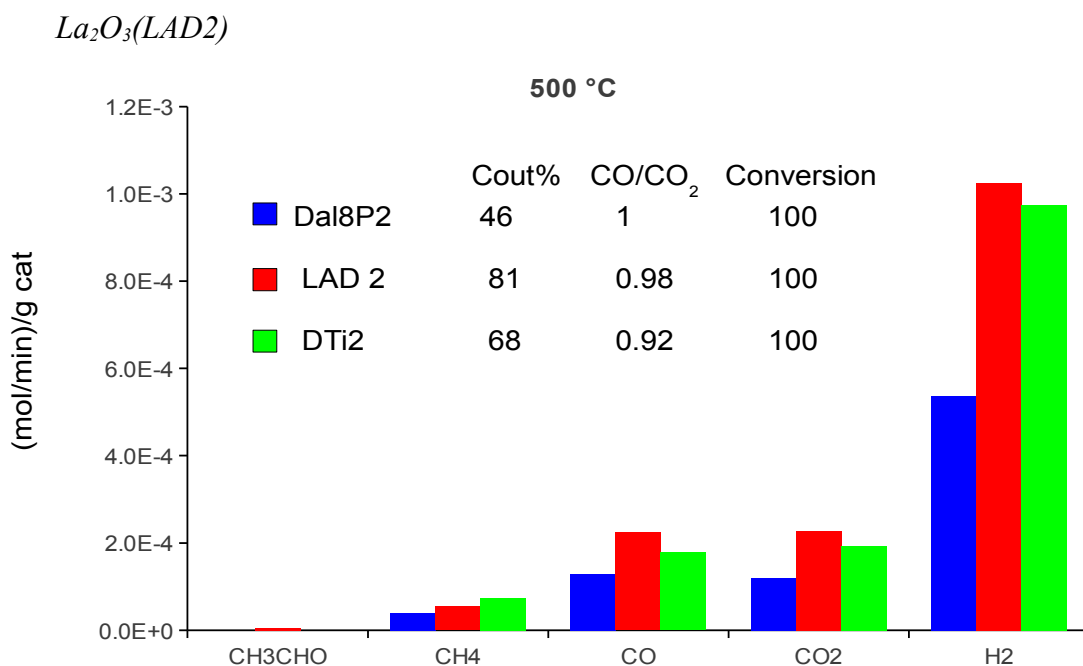


Figure 120: productivity at 500°C of 10%Ni supported on  $Al_2O_3$ (Dal8P2);  $TiO_2$ (DTi2) and on  $La_2O_3$ (LAD2)

In Figure 121 and 122 comparisons between FP made catalysts and impregnated ones are reported.

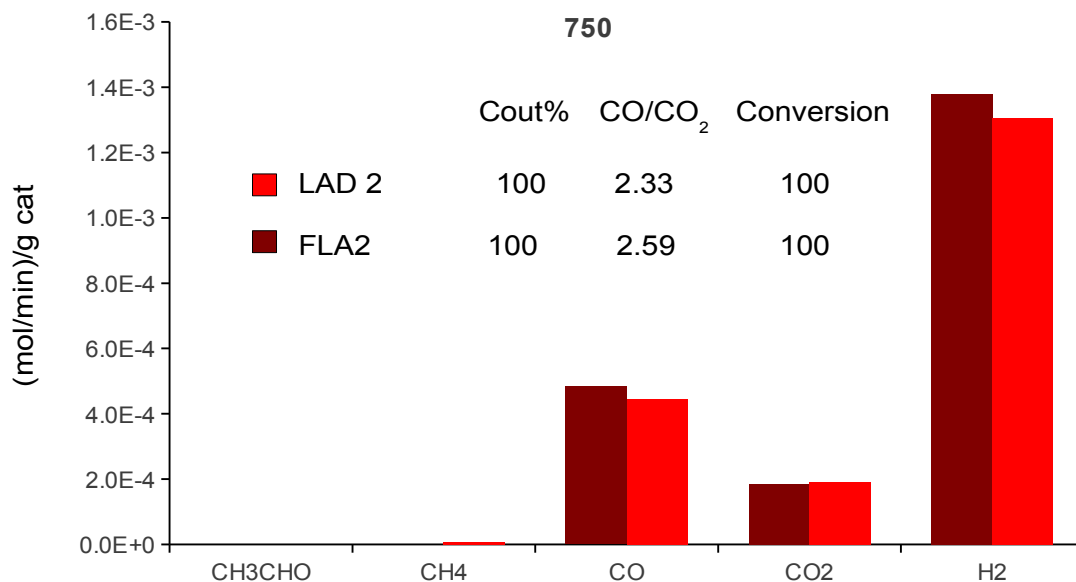


Figure 121a: productivity at 750°C of 10%Ni/ $La_2O_3$ (LAD2) made by impregnation and it's corresponding FP made sample(FLAD2)

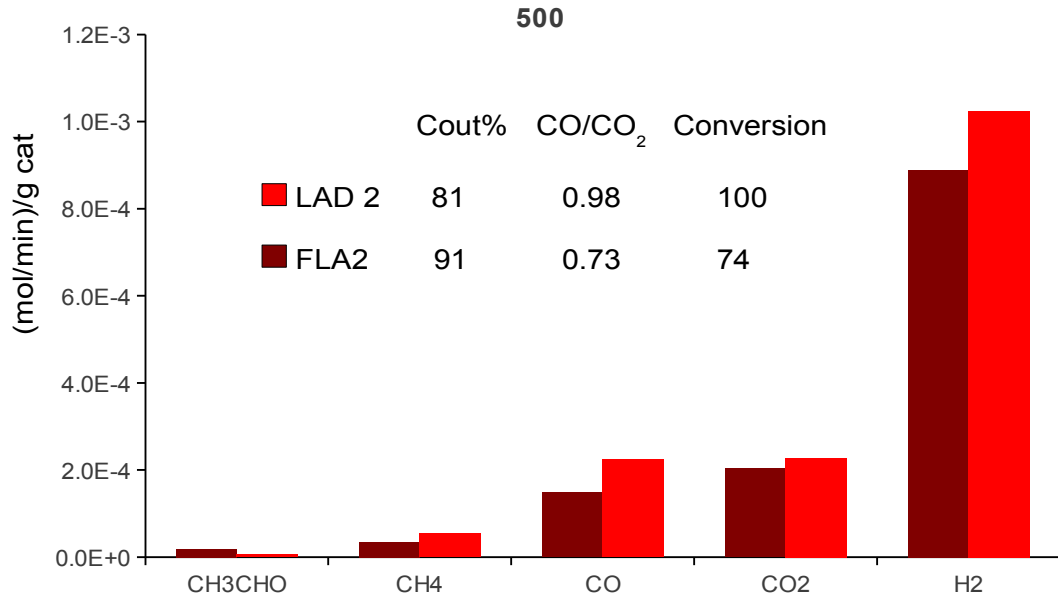


Figure 121b: productivity at 500°C of 10%Ni/La<sub>2</sub>O<sub>3</sub>(LAD2) made by impregnation and it's corresponding FP made sample(FLAD2)

For La based catalysts it could be observed that FP made catalysts at 750°C (figure 121a) led to quite the same catalytic activity of the impregnated ones, the small increase observed in the H<sub>2</sub> production is due to a slightly better conversion of water. In the comparison of 500°C (Figure 121b) impregnated catalysts show an higher productivity for H<sub>2</sub> and complete conversion of ethanol, while the FP made sample showed a better CO/CO<sub>2</sub> and a better Cout%. FLA2 showed a good resistance towards coking and a better efficiency in H<sub>2</sub> production since it's conversion of ethanol was 26% lower than the one of LAD2, but the difference between the two productivities was only 10%., only.

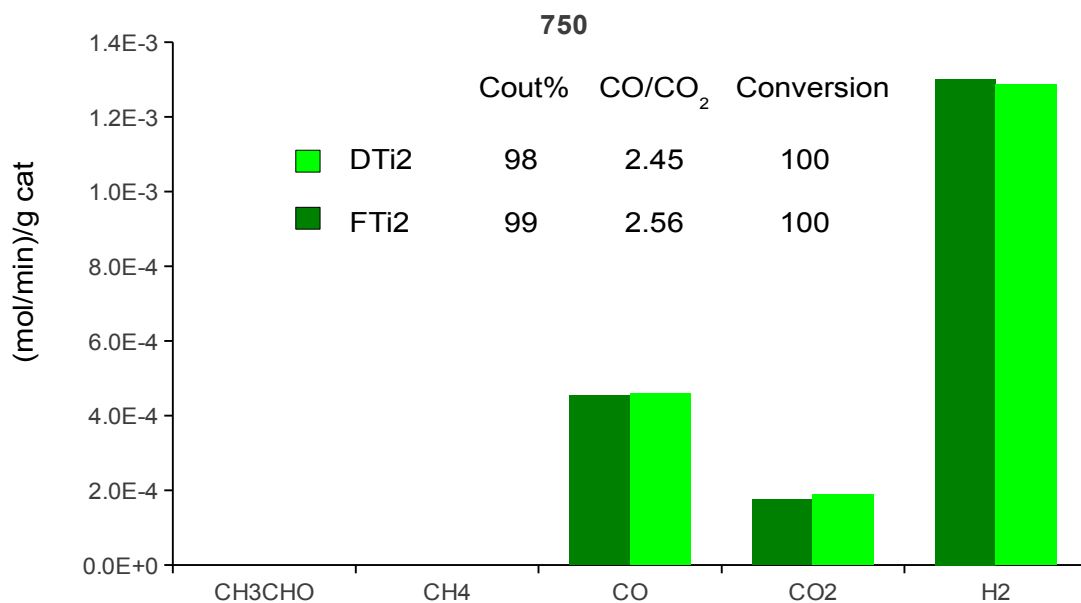


Figure 122a: productivity at 750°C of 10%Ni/TiO<sub>2</sub>(DTI2) made by impregnation and it's corresponding FP-made sample( FTI2)

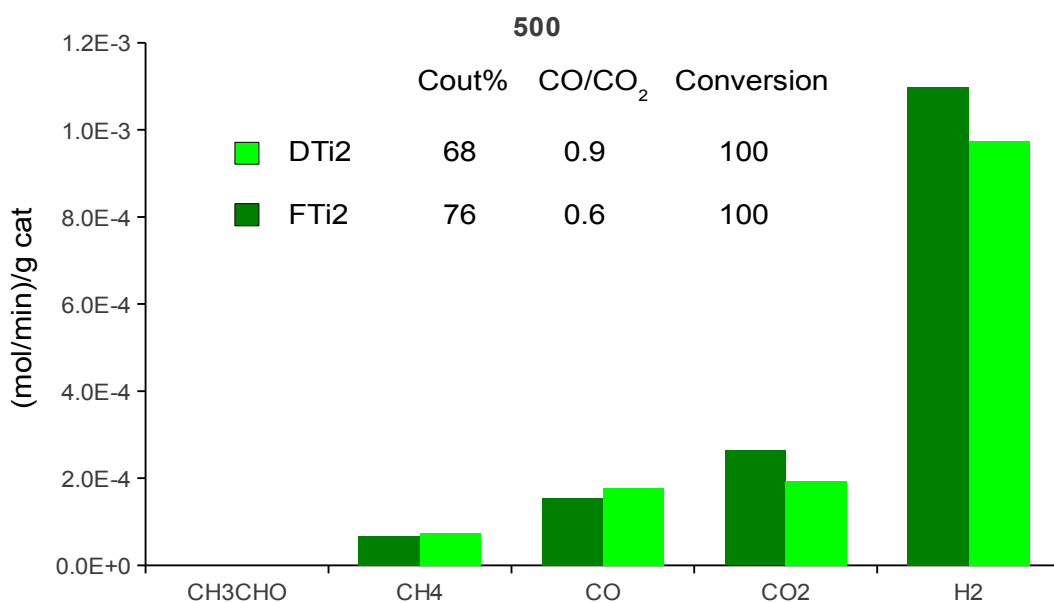


Figure 122b: productivity at 500°C of 10%Ni/TiO<sub>2</sub>(DTI2) made by impregnation and it's corresponding FP-made sample( FTI2)

At 750°C Figure 122a, showed quite the same catalytic performance, instead at 500°C it was more evident that the FP catalyst generated less carbon on it's surface since the Cout% balance was higher (Figure 122b) . Productivity of hydrogen was higher and the CO/CO<sub>2</sub> lower indicating that the contribution of WGS to the whole H<sub>2</sub> production at 500°C was higher for the FP catalysts than for it's corresponding impregnated ones. The higher surface area of the FP catalysts may favour the WGS

activity during operation at low temperature leading to better CO/CO<sub>2</sub> ratio with unaffected other parameters.

In general all the FP made catalysts (both lanthanum and titanium based) showed a better coke resistance at both temperatures. This may be due to the higher metal dispersion usually achieved with such samples with respect to the impregnated ones. Indeed, small Ni clusters demonstrated much more resistant towards coking.

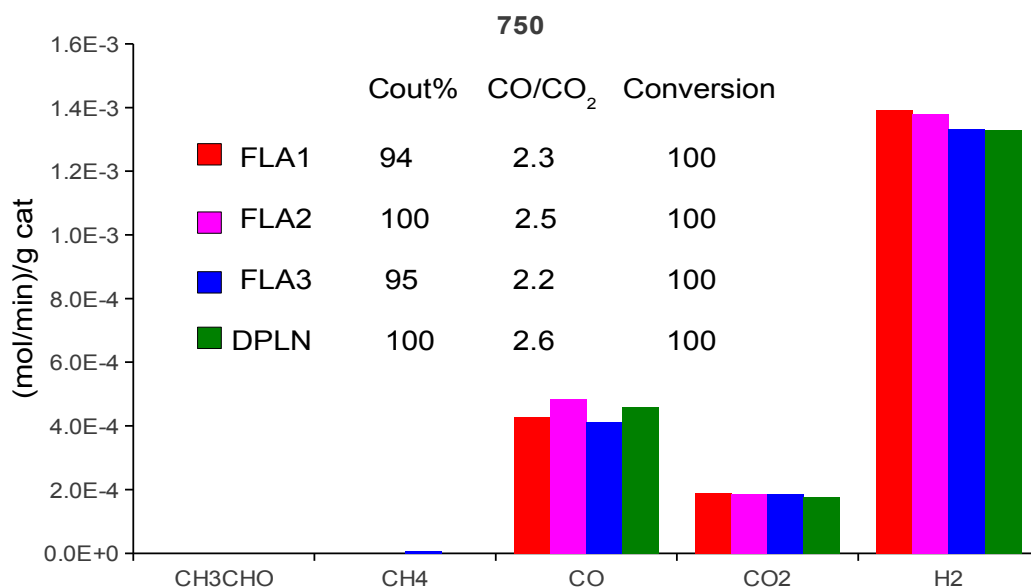


Figure 123a: productivity at 750°C of FP X%Ni/La<sub>2</sub>O<sub>3</sub> (X=5 (FLA1); 10(FLA2) ;15(FLA3); FP made LaNiO<sub>3</sub> (DPLN)

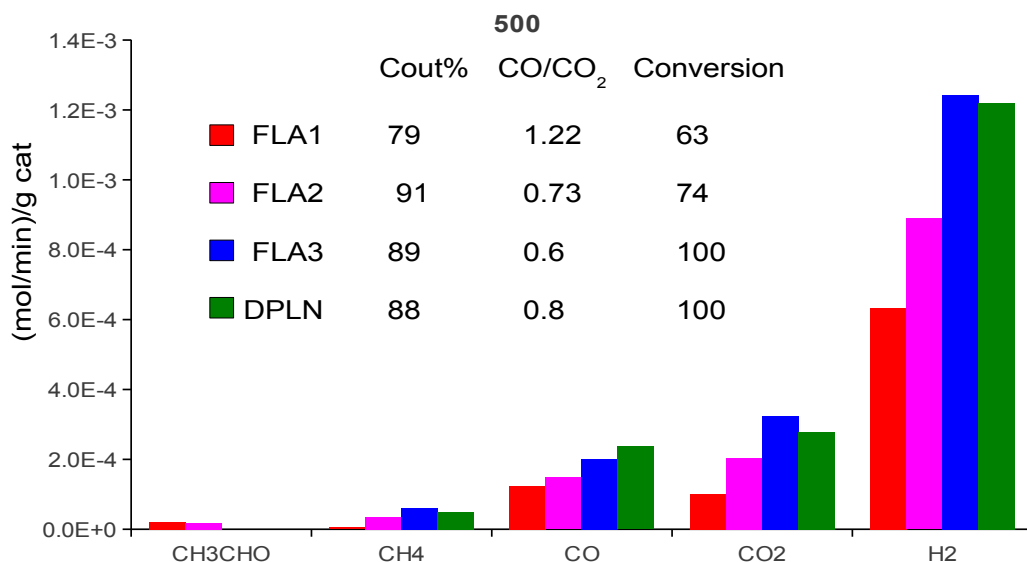


Figure 123b: productivity at 500°C of FP X%Ni/La<sub>2</sub>O<sub>3</sub> (X=5 (FLA1); 10(FLA2) ;15(FLA3); FP made LaNiO<sub>3</sub> (DPLN)

At 750°C for all the La based catalyst ( Figure 123a) an increase of Ni loading seems not to be directly connected to the improvement of catalytic behaviour. The best productivity was indeed achieved with FLA1 (5% Ni), which gave the highest water conversion. Cout% balance was over 95% for all the catalysts.

At 500°C the relationship between catalytic performances and Ni loading looks more evident. From 5 to 15wt% (FLA1-FLA3) there was an increase of ethanol conversion from 63% to 100%. H<sub>2</sub> productivity increased as well and the CO/CO<sub>2</sub> ratio decreased, suggesting that the WGS contribution to the general H<sub>2</sub> production increased with nickel amount. Cout% increased as well even if 10% and 15% reached quite the same value, comparable with the blank test. Figure 123b also points out that increase in the Ni loading decreased the selectivity towards CH<sub>3</sub>CHO, favouring it's full reforming.

DPLN was added since it is the La based catalyst with the highest Ni Content (La:Ni = 1:1 mol/mol). It's catalytic behaviour was quite similar to LaD3 even if it's CO/CO<sub>2</sub> was a bit higher. This could indicate that DPLN with is Ni loading around 35 wt% was more active for the low temperature SR (products H<sub>2</sub> and CO) than for the WGS (products H<sub>2</sub> and CO<sub>2</sub>).

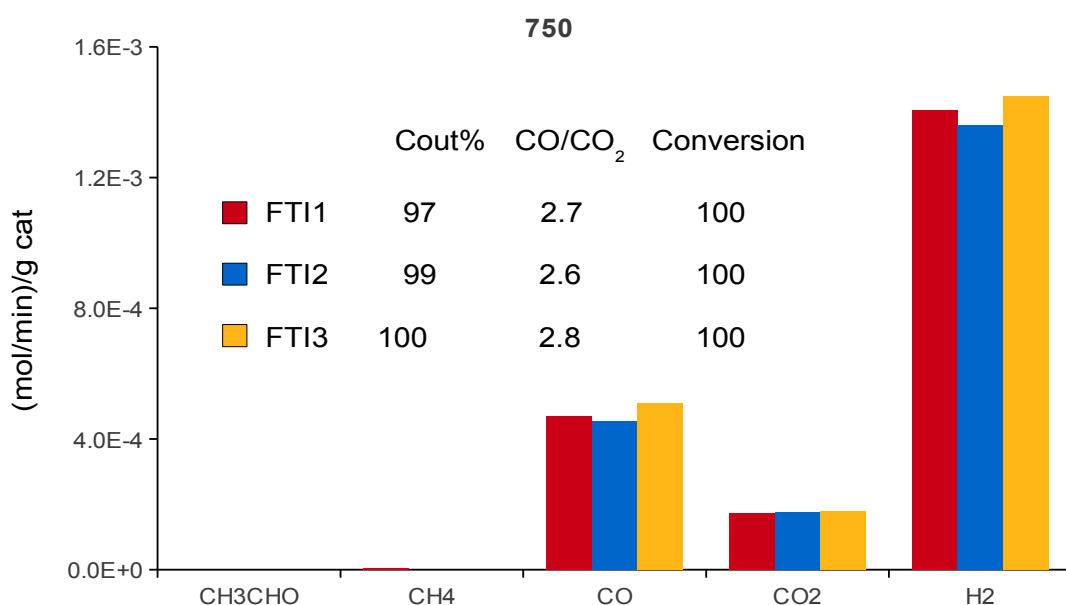


Figure 124a: productivity at 750°C of FP X%Ni/TiO<sub>2</sub>(X=5 (FTI1); 10(FTI2) ;15(FTI3))

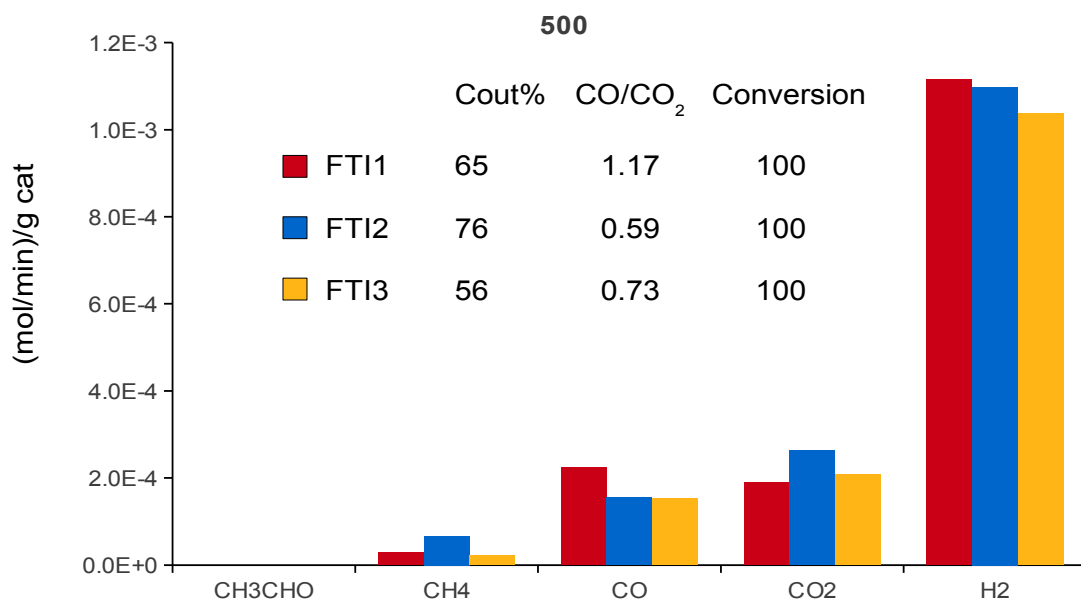


Figure 124b: productivity at 500°C of FP X%Ni/TiO<sub>2</sub>(X=5 (FTI1); 10(FTI2) ;15(FTI3))

TiO<sub>2</sub>-based catalysts tested at 750°C (Figure 124a) showed the catalytic performances are quite the same independently on the Ni loading. At 500°C (Figure 124b) the behaviour was different since the highest H<sub>2</sub> productivity was reached with the 5% Ni (FT1) that possessed also the highest CO productivity. FTI2 shows the best catalytic performance with H<sub>2</sub> productivity quite similar to the one of FTI1, best Cout% balance and low CO/CO<sub>2</sub> ratio indicating that FT2 possesses a good activity also for WGS.

Therefore, the main results obtained with this first group of catalyst are the following:

i) comparing the three supports, La<sub>2</sub>O<sub>3</sub> showed the highest coke resistance while TiO<sub>2</sub> usually exhibited a better CO/CO<sub>2</sub> ratio. FP made catalysts were characterised by better resistance towards coking and CO/CO<sub>2</sub> ratio than the corresponding impregnated ones, and in some case they also showed higher hydrogen productivity. Among this group the best catalysts for SR 500°C were 15%Ni/La<sub>2</sub>O<sub>3</sub> (FLA3) and 10%Ni/TiO<sub>2</sub> (FTI2). Likely, the easier formation of a mixed oxide when supporting Ni over lanthana and the consequent lower reducibility of part of the active phase requires to add a higher amount of metal to reach the same activity of the titania-supported samples. However, the higher surface acidity of the titania loaded samples, exhibited as both titanols and Lewis a.s. provokes a higher consumption of the substrate (lower Cout balance).

## Group 2

**Table 27 : key legend of the samples**

Name	Formula	Synthesis method
FLC	LaCoO <sub>3</sub>	one step FSP
MC12	10% Co /TiO <sub>2</sub>	Support+Co one step FSP
MC13	10% Cu /TiO <sub>2</sub>	Support+Cu one step FSP
MC10	10% Ni /SiO <sub>2</sub>	Support+Ni one step FSP
MC11	10% Co /SiO <sub>2</sub>	Support+Co one step FSP
MC14	10% Cu /SiO <sub>2</sub>	Support+Cu one step FSP
MC15	10% Ni /ZrO <sub>3</sub>	Support+Ni one step FSP

**Table 28**

FLC	750 °C	500 °C	625 °C	750°C 2 <sup>nd</sup>
Conversion %	100	96	100	100
Cout %	97	82	100	98
CO/CO <sub>2</sub>	2.1	0.8	1.4	2
H <sub>2</sub> (mol/min)/Kg <sub>cat</sub>	1.23	0.94	1.34	1.34
Sel CO <sub>2</sub> %	30	34	38	30
Sel CO%	63	30	54	61
Sel CH <sub>4</sub> %	6	5	5	6
Sel CH <sub>3</sub> HO%	0	11	0	0

**Table 29**

MC12	750 °C	500 °C	625 °C
Conversion %	100	32	63
Cout %	94	90	88
CO/CO <sub>2</sub>	24	2	7
H <sub>2</sub> (mol/min)/Kg <sub>cat</sub>	0.7	0	0.2
Sel CO <sub>2</sub> %	3.2	1.7	1.9
Sel CO%	75	4	13
Sel CH <sub>4</sub> %	7	0	2
Sel CH <sub>3</sub> HO%	0	40	54

**Table 30**

MC13	750 °C	500 °C	625 °C
------	--------	--------	--------

Conversion %	100	15	36
Cout %	98	100	99
CO/CO <sub>2</sub>	8	nd	1.6
H <sub>2</sub> (mol/min)/Kg <sub>cat</sub>	0.32	0	0
Sel CO <sub>2</sub> %	0.4	0	3.7
Sel CO%	16	0	6
Sel CH <sub>4</sub> %	6	0	0
Sel CH <sub>3</sub> HO%	39	90	91

Table 31

MC10	750 °C	500 °C	625 °C
Conversion %	100	100	100
Cout %	99	89	100
CO/CO <sub>2</sub>	1.7	0.9	1.1
H <sub>2</sub> (mol/min)/Kg <sub>cat</sub>	1.4	0.5	1.4
Sel CO <sub>2</sub> %	36	50	49
Sel CO%	63	29	54
Sel CH <sub>4</sub> %	0	0	0
Sel CH <sub>3</sub> HO%	0	7.5	0

Table 32

MC11	750 °C	500 °C	625 °C	750°C 2 <sup>nd</sup>
Conversion %	100	73	100	95
Cout %	100	99	100	95
CO/CO <sub>2</sub>	1.6	0.6	1.6	1.5
H <sub>2</sub> (mol/min)/Kg <sub>cat</sub>	1.24	0.64	1.24	1.27
Sel CO <sub>2</sub> %	40	43	40	40
Sel CO%	65	25	65	60
Sel CH <sub>4</sub> %	0.42	0.83	0.42	2
Sel CH <sub>3</sub> HO%	0	31	0	0

Table 33

MC14	750 °C	500 °C	625 °C
Conversion %	100	10	68



Cout %	89	90	72
CO/CO <sub>2</sub>	10	nd	0.15
H <sub>2</sub> (mol/min)/Kg <sub>cat</sub>	0.31	0	0
Sel CO <sub>2</sub> %	2.3	nd	21
Sel CO%	21	nd	4
Sel CH <sub>4</sub> %	8	nd	1
Sel CH <sub>3</sub> HO%	20	0.8	40

Table 34

MC15	750 °C	500 °C	625 °C
Conversion %	100	75	100
Cout %	97	94	100
CO/CO <sub>2</sub>	2.18	0.73	1.83
H <sub>2</sub> (mol/min)/Kg <sub>cat</sub>	1.22	0.65	1.25
Sel CO <sub>2</sub> %	32	36	43
Sel CO%	69	27	57
Sel CH <sub>4</sub> %	0	8	1.3
Sel CH <sub>3</sub> HO%	0	8.4	0

The catalytic performance of FLC and DPLN, both lanthanum-based perovskites are compared in Figure 125.

At 750°C (Figure 125a) Co only brought a small improvement in the CO/CO<sub>2</sub> ratio but there a decreasing of the H<sub>2</sub> productivity and of the resistance of the catalyst to coke formation was observed. Indeed Cout% of FLC was lower than for DPLN.

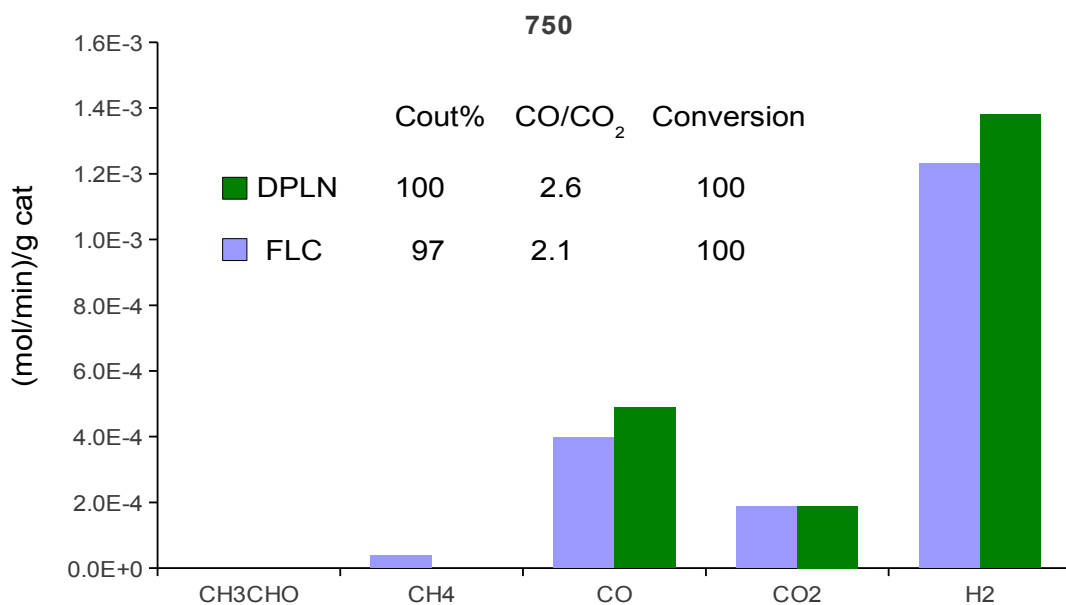


Figure 125a: productivity at 750°C of FP-prepared LaNiO<sub>3</sub>(DPLN);LaCoO<sub>3</sub>(FLC)

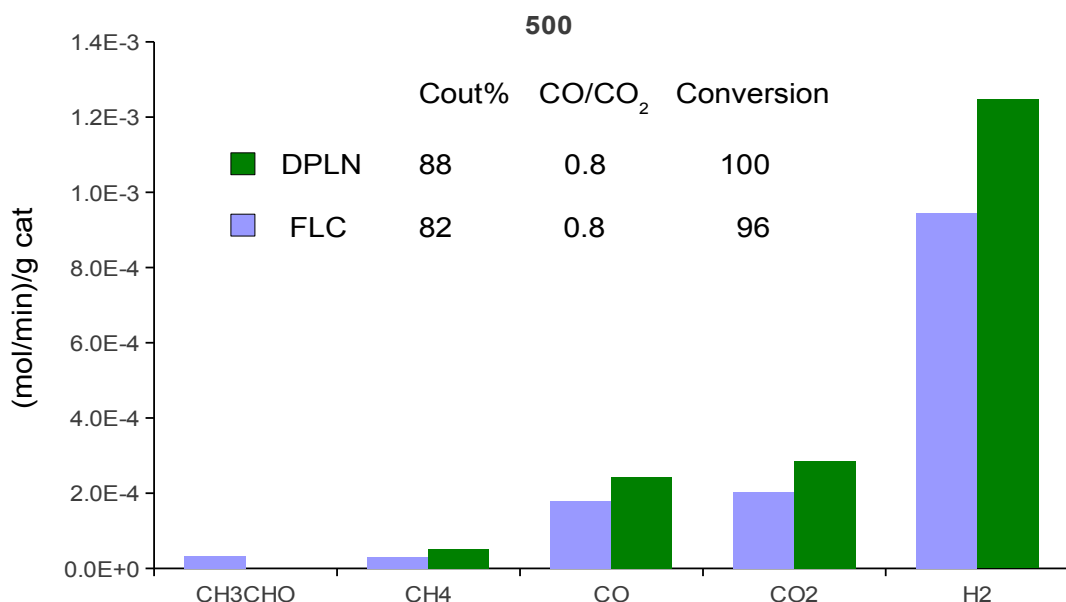


Figure 125b: productivity at 500°C of FP-prepared LaNiO<sub>3</sub>(DPLN);LaCoO<sub>3</sub>(FLC)

At 500°C LaCoO<sub>3</sub> (Figure 125b) showed ethanol conversion, H<sub>2</sub> productivity and CO<sub>2</sub> productivity lower than for LaNiO<sub>3</sub>. Performance. This is contrasting with what reported by Llorca et al. [13] who indicate Co as an active phase suitable for low temperature operation. The results here observed for the perovskite-like precursor have been also confirmed by supporting Co on other supports in different loading (*vide infra*).

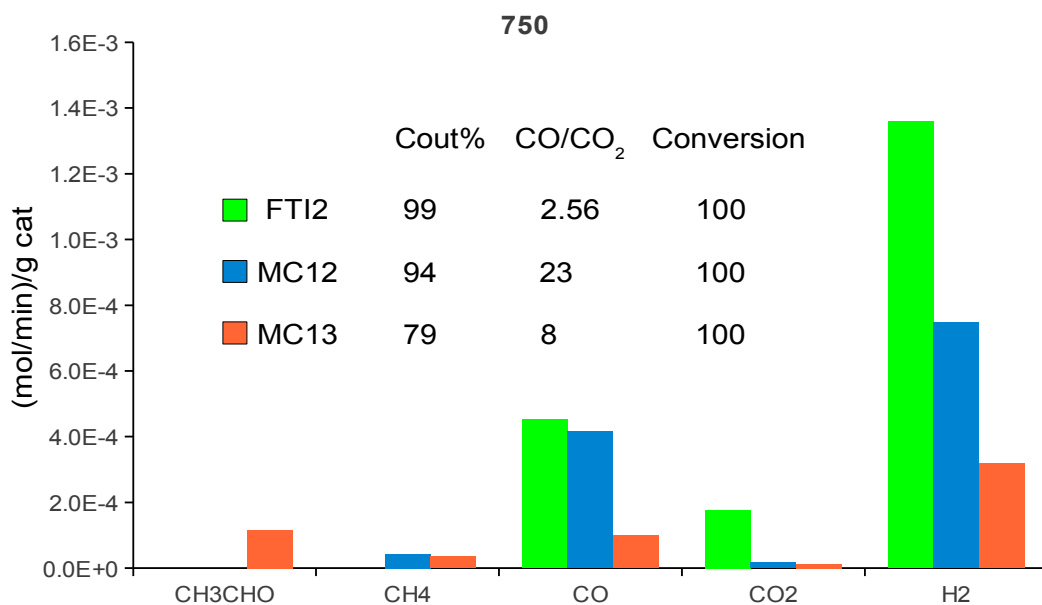


Figure 126: productivity at 750°C of FP 10%Ni/TiO<sub>2</sub>(FTI2);10%Co/TiO<sub>2</sub>(MC12); 10%Cu/TiO<sub>2</sub>(MC13)

Figure 126 reports the comparison between 10%Co/TiO<sub>2</sub> (MC12), 10%Cu/TiO<sub>2</sub> (MC13) and 10%Ni/TiO<sub>2</sub> (FTI2 group 1). The activity of Ni was much higher than the one of the two other catalyst. At 500°C MC12 and MC13 do not produce any H<sub>2</sub> as shown in Tables 29 and 30. So with TiO<sub>2</sub> as support Co and Cu showed almost completely inactive for ESR.

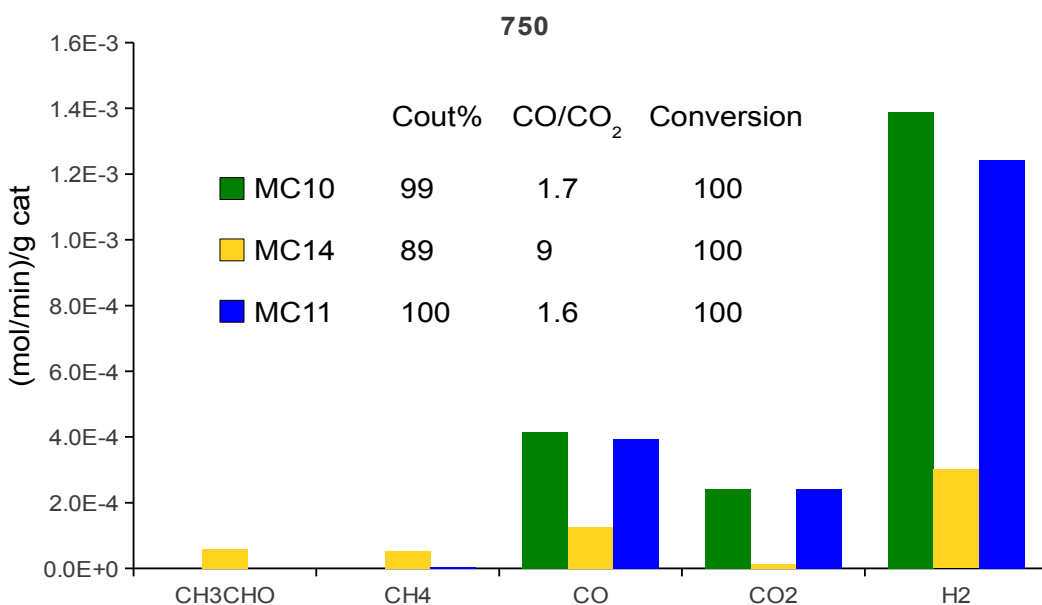


Figure 127a: productivity at 750°C of FP 10%Ni/SiO<sub>2</sub>(MC10);10%Co/SiO<sub>2</sub>(MC11); 10%Cu/SiO<sub>2</sub>(MC14)

The activity of the catalysts with support  $\text{SiO}_2$  and different active phase (Ni, Co or Cu) is compared in Figure 127(a,b). Cu showed the worst  $\text{H}_2$  productivity, negatively join to the lowest carbon balance and highest  $\text{CO}/\text{CO}_2$ . Co (MC11) gave rise to a slightly better result but as it is for the previous comparison, Ni confirmed the best active phase as for  $\text{H}_2$  productivity. At  $500^\circ\text{C}$  (Figure 127b) the better activity of Ni was even more evident since Cu did not produce hydrogen at all, Co produced less  $\text{H}_2$  than Ni and showed a lower ethanol conversion, though the carbon balance was higher. It is indeed well known the higher activity towards the formation of carbon fibers and filaments of Ni.

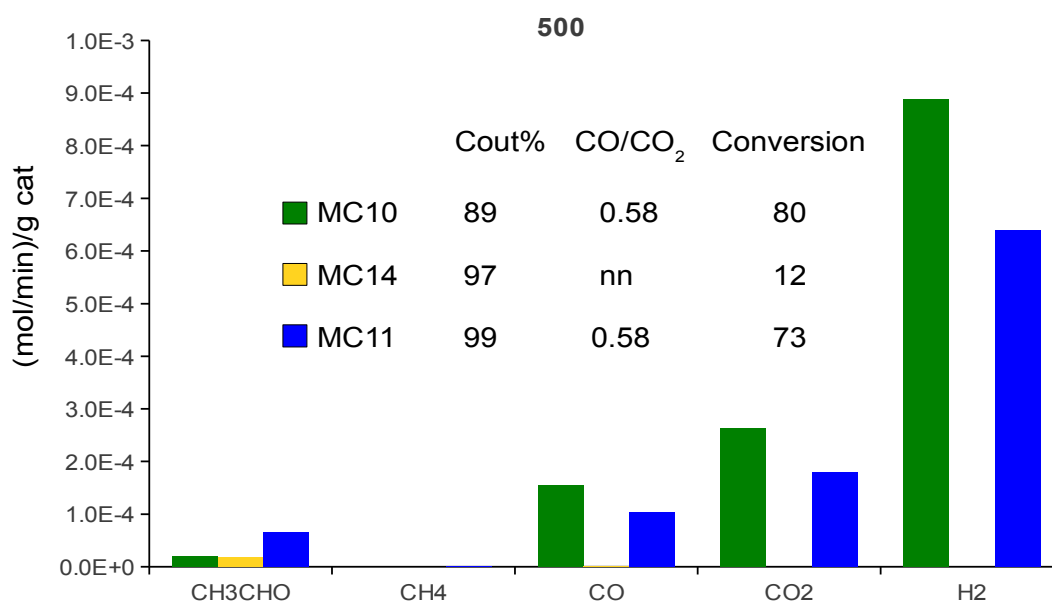


Figure 127b: productivity at  $500^\circ\text{C}$  of FP 10%Ni/ $\text{SiO}_2$ (MC10); 10%Co/ $\text{SiO}_2$ (MC11); 10%Cu/ $\text{SiO}_2$ (MC14)

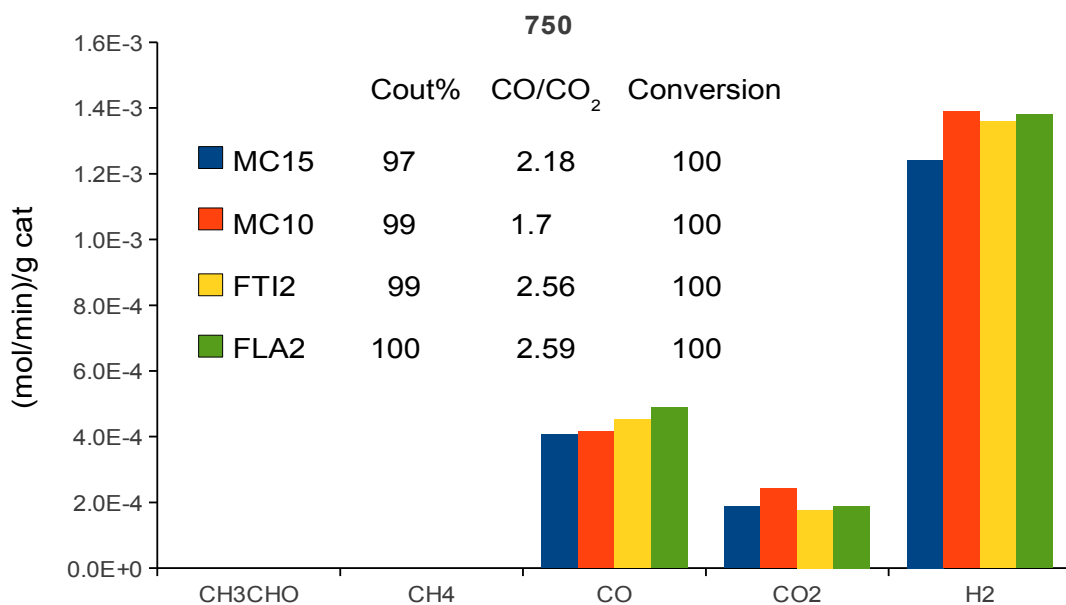


Figure 128a: productivity at 750°C of FP 10%Ni/ZrO<sub>2</sub>(MC15); 10%Ni/SiO<sub>2</sub>(MC10); 10%Ni/TiO<sub>2</sub>(FTI2); 10%Ni/La<sub>2</sub>O<sub>3</sub>(FLA2)

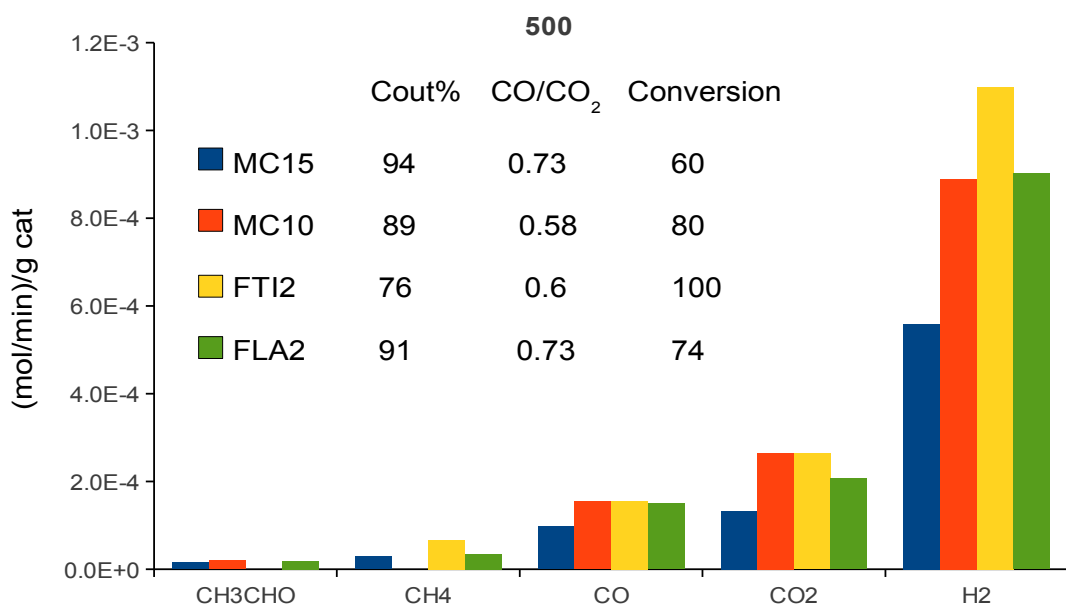


Figure 128b: productivity at 500°C of FP 10%Ni/ZrO<sub>2</sub>(MC15); 10%Ni/SiO<sub>2</sub>(MC10); 10%Ni/TiO<sub>2</sub>(FTI2); 10%Ni/La<sub>2</sub>O<sub>3</sub>(FLA2)

The comparison among 4 catalysts with Ni amount (10wt%) and synthesised by direct FP synthesis on different supports (ZrO<sub>2</sub>, SiO<sub>2</sub>, TiO<sub>2</sub> and La<sub>2</sub>O<sub>3</sub>) is proposed in Fig.128. At 750°C all the catalyst showed the same performance, only ZrO<sub>2</sub> showed a quite lower H<sub>2</sub> productivity probably due to the low Cout balance of the sample.

At 500°C only the titania supported sample reached the complete conversion and the best CO/CO<sub>2</sub>. By contrast, the zirconia supported catalyst showed the lowest H<sub>2</sub>

productivity as a consequence of its lowest conversion, however accompanied by the best C out% balance. Silica and lanthana loaded samples led to quite the same H<sub>2</sub> productivity and C out % balance, the latter with a lower CO<sub>2</sub> productivity than the former, which also led to complete reforming of CH<sub>4</sub>.

Summarising, the substitution of Ni with Co or Cu do not increase the efficiency of the catalyst. Cu showed to be the worst active phase among the three metals at 500°C, mainly producing CH<sub>3</sub>CHO with almost nil H<sub>2</sub> productivity.

Furthermore the support deeply influenced the catalytic performance.

TiO<sub>2</sub> showed complete conversion and high H<sub>2</sub> productivity, even if the Cout% balance was unsatisfactory.

ZrO<sub>2</sub> showed the lowest conversion and as consequence the lowest H<sub>2</sub> productivity but, it possessed the highest resistance to coking since its Cout % balance was the highest.

La<sub>2</sub>O<sub>3</sub> showed incomplete conversion joined to a good H<sub>2</sub> productivity and a very good Cout% balance, similar to the one of ZrO<sub>2</sub>

SiO<sub>2</sub> showed a slightly lower Cout% than La and Zr but H<sub>2</sub> productivity very good with CO and CO<sub>2</sub> as the only by-products.

Among all the support La and Si seems the most promising for low temperature SR since they achieved a good H<sub>2</sub> productivity joined to an acceptable Cout%, finely tunable by using different water-ethanol ratio or contact time.

### Group 3

In this group all the activity test made on catalyst made by University of Venice (UniVe) are reported. Those catalyst were made by incipient wetness impregnation of supports prepared via liquid phase synthesis. Ni, Co and Cu were used as active phase supported on SiO<sub>2</sub>, TiO<sub>2</sub> and ZrO<sub>2</sub>. Such catalysts could be also divided into categories one for high temperature (calcined at 800°C) and for low temperature SR (calcined at 500°C).

Table 35 key legend of the samples

Name	Formula	Synthesis method
T1C500	7.8%Ni/TiO <sub>2</sub>	Incipient wetness impregnation+ calcination 500°C

T2C500	7.5%Ni/TiO <sub>2</sub>	Incipient wetness impregnation+ calcination 500°C
T3C800	7.3%Ni/TiO <sub>2</sub>	Incipient wetness impregnation+ calcination 800°C
T4C800	6.7%Ni/TiO <sub>2</sub>	Incipient wetness impregnation+ calcination 800°C
T6C500	6.6%Co/TiO <sub>2</sub>	Incipient wetness impregnation+ calcination 500°C
T8C500	9.6%Co/TiO <sub>2</sub>	Incipient wetness impregnation+ calcination 500°C
T9C500	5.6%Cu/TiO <sub>2</sub>	Incipient wetness impregnation+ calcination 500°C
T11C500	5.6%Cu/TiO <sub>2</sub>	Incipient wetness impregnation+ calcination 500°C
S1C500	9.2%Ni/SiO <sub>2</sub>	Incipient wetness impregnation+ calcination 500°C
S2C800	8.9%Ni/SiO <sub>2</sub>	Incipient wetness impregnation+ calcination 800°C
S3C500	6.7%Ni/TiO <sub>2</sub>	Incipient wetness impregnation+ calcination 500°C
S4C500	7.8%Co/SiO <sub>2</sub>	Incipient wetness impregnation+ calcination 500°C
Z1C500	9.7%Ni/ZrO <sub>2</sub>	Incipient wetness impregnation+ calcination 500°C
Z2C800	8.8%Ni/ZrO <sub>2</sub>	Incipient wetness impregnation+ calcination 800°C

Table 36

T1C500	500°C	400°
Conversion %	38	nd
Cout %	79	nd
CO/CO <sub>2</sub>	0.05	nd
H <sub>2</sub> (mol/min)/Kg <sub>cat</sub>	0.03	nd
Sel CO <sub>2</sub> %	6	nd
Sel CO%	0.15	nd
Sel CH <sub>4</sub> %	0	nd
Sel CH <sub>3</sub> CHO%	16	nd

Table 37

T2C500	500°C	400°C
Conversion %	25	nd
Cout %	81	nd
CO/CO <sub>2</sub>	0	nd
H <sub>2</sub> (mol/min)/Kg <sub>cat</sub>	0	nd

Sel CO <sub>2</sub> %	7	nd
Sel CO%	0	nd
Sel CH <sub>4</sub> %	0	nd
Sel CH <sub>3</sub> CHO%	16	nd

Table 38

T3C800	750°C	500°C	625°C	750°C 2 <sup>nd</sup>
Conversion %	100	100	96	100
Cout %	10	70	88	100
CO/CO <sub>2</sub>	16	0.86	4.79	13
H <sub>2</sub> (mol/min)/Kg <sub>cat</sub>	1.5	0.91	0.76	1.41
Sel CO <sub>2</sub> %	5	26	9	4
Sel CO%	87	22	46	82
Sel CH <sub>4</sub> %	9.5	10	8	9.3
Sel CH <sub>3</sub> CHO%	0	3	16	0

Table 39

T4C800	750°C	500°C	625°C
Conversion %	100	96	100
Cout %	96	72	94
CO/CO <sub>2</sub>	1.77	1.83	1.98
H <sub>2</sub> (mol/min)/Kg <sub>cat</sub>	1.2	0.76	1.1
Sel CO <sub>2</sub> %	33	30	23
Sel CO%	60	40	68
Sel CH <sub>4</sub> %	1.9	7	3.5
Sel CH <sub>3</sub> CHO%	0	0.24	0

Table 40

T6C500	500°C	400°C
Conversion %	48	nd
Cout %	89	nd
CO/CO <sub>2</sub>	0	nd
H <sub>2</sub> (mol/min)/Kg <sub>cat</sub>	0	nd
Sel CO <sub>2</sub> %	14	nd



Sel CO%	0	nd
Sel CH <sub>4</sub> %	0	nd
Sel CH <sub>3</sub> CHO%	52	nd

Table 41

T8C500	500°C	400°C
Conversion %	70	18
Cout %	89	96
CO/CO <sub>2</sub>	1	1.6
H <sub>2</sub> (mol/min)/Kg <sub>cat</sub>	0.3	0
Sel CO <sub>2</sub> %	12	3.4
Sel CO%	11.5	4.4
Sel CH <sub>4</sub> %	3.5	1.1
Sel CH <sub>3</sub> CHO%	52	49

Table 42

T9C500	500°C	400°C
Conversion %	57	nd
Cout %	51	nd
CO/CO <sub>2</sub>	15	nd
H <sub>2</sub> (mol/min)/Kg <sub>cat</sub>	0.36	nd
Sel CO <sub>2</sub> %	1.2	nd
Sel CO%	18	nd
Sel CH <sub>4</sub> %	7	nd
Sel CH <sub>3</sub> CHO%	17	nd

Table 43

T11C500	500°C	400°C
Conversion %	11	nd
Cout %	94	nd
CO/CO <sub>2</sub>	0.46	nd
H <sub>2</sub> (mol/min)/Kg <sub>cat</sub>	0	nd

Sel CO <sub>2</sub> %	7	nd
Sel CO%	3	nd
Sel CH <sub>4</sub> %	0	nd
Sel CH <sub>3</sub> CHO%	70	nd

Table 44

S1C500	500°C	400°C	300°C
Conversion %	100	83	23
Cout %	100	79	83
CO/CO <sub>2</sub>	0.6	1	1.4
H <sub>2</sub> (mol/min)/Kg <sub>cat</sub>	1.3	0.5	0
Sel CO <sub>2</sub> %	48	21	2
Sel CO%	26	20	3
Sel CH <sub>4</sub> %	15	23	3
Sel CH <sub>3</sub> CHO%	0	2	13

Table 45

S2C800	750°C	500°C	625°C	750°C 2 <sup>nd</sup>
Conversion %	100	100	100	100
Cout %	100	75	99	100
CO/CO <sub>2</sub>	1.8	0.5	1.2	1.8
H <sub>2</sub> (mol/min)/Kg <sub>cat</sub>	1.38	1.03	1.37	1.42
Sel CO <sub>2</sub> %	38	49	35	38
Sel CO%	64	25	64	65
Sel CH <sub>4</sub> %	0	0	0	0
Sel CH <sub>3</sub> CHO%	0	0	0	0

Table 46

S3C500	500	400
Conversion %	36	nd
Cout %	94	nd
CO/CO <sub>2</sub>	0	nd

H <sub>2</sub> (mol/min)/Kg <sub>cat</sub>	0	nd
Sel CO <sub>2</sub> %	20	nd
Sel CO%	0	nd
Sel CH <sub>4</sub> %	0	nd
Sel CH <sub>3</sub> CHO%	56	nd

Table 47

S4C500	500	400
Conversion %	100	28
Cout %	93	98
CO/CO <sub>2</sub>	0.78	1.07
H <sub>2</sub> (mol/min)/Kg <sub>cat</sub>	0.95	0.1
Sel CO <sub>2</sub> %	36	8
Sel CO%	28	9
Sel CH <sub>4</sub> %	8	3
Sel CH <sub>3</sub> CHO%	16	74

Table 48

Z1C500	500°C	400°C	300°C
Conversion %	100	81	27
Cout %	91	53	74
CO/CO <sub>2</sub>	0.6	0.4	0
H <sub>2</sub> (mol/min)/Kg <sub>cat</sub>	1.2	0.25	0
Sel CO <sub>2</sub> %	45	12	0
Sel CO%	27	5	0
Sel CH <sub>4</sub> %	19	3	0
Sel CH <sub>3</sub> CHO%	0	7	3

Table 49

Z2C800	750°C	500°C	625°C
Conversion %	100	100	100
Cout %	97	87	90

CO/CO <sub>2</sub>	2.3	0.6	1.4
H <sub>2</sub> (mol/min)/Kg <sub>cat</sub>	1.35	1.17	1.43
Sel CO <sub>2</sub> %	46	29	37
Sel CO %	67	27	53
Sel CH <sub>4</sub> %	0	11	0
Sel CH <sub>3</sub> CHO %	0	0	0

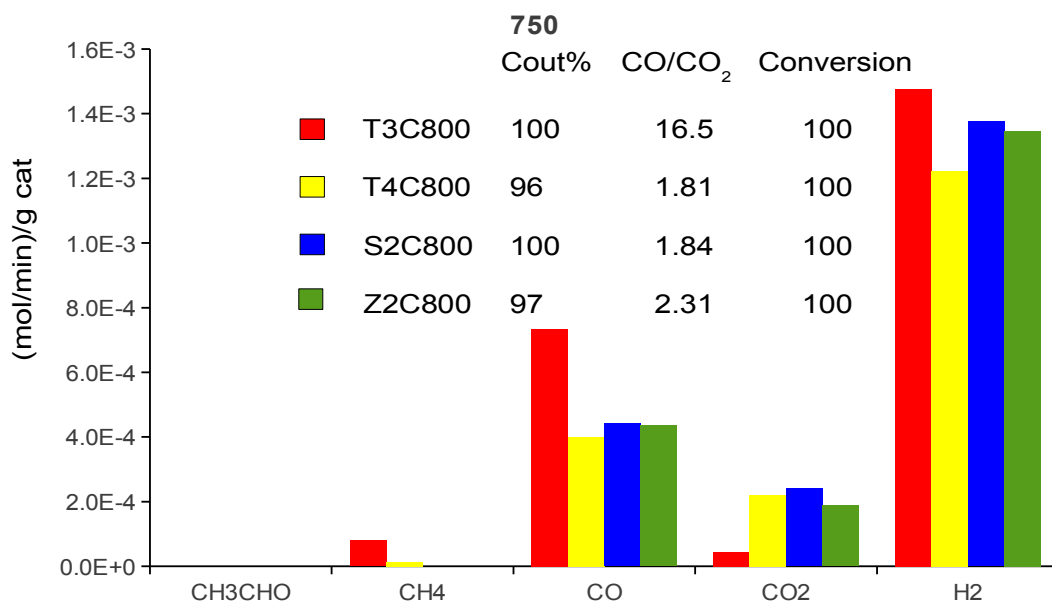


Figure 129a: productivity at 750° C of catalysts calcined at 800°C; 10%Ni/TiO<sub>2</sub>(T3C800,T4C800); 10%Ni/SiO<sub>2</sub>(S2C800); 10%Ni/ZrO<sub>2</sub>(Z2C800)

The catalytic performance of all the catalyst calcined at 800°C are compared in Figure 129. Among the two Ni/TiO<sub>2</sub> T3C800 showed the best H<sub>2</sub> productivity and to a better Cout balance. The main difference between T4 and T3 is that T3 showed a very poor selectivity for CO<sub>2</sub> coupled to a very high productivity for CO.

S2C800 and Z2C800 seems to have quite the same catalytic performance but as for FP catalysts (Fig. 129a) TiO<sub>2</sub> help to reduce the CO/CO<sub>2</sub> ratio while SiO<sub>2</sub> showed a better productivity of H<sub>2</sub>, even if in this case also ZrO<sub>2</sub> showed a very high productivity.

As for the test at 500°C T4C800 showed a better coke resistance and an higher CO productivity than T3C800 (Figure 129b). Even if T3C800 showed a better conversion than T4C800. S2C800 was more active than TiO<sub>2</sub> as observed with FP made samples SiO<sub>2</sub> increased the productivity of H<sub>2</sub> compared to TiO<sub>2</sub>; even if in this case

also the CO/CO<sub>2</sub> ratio improved. As It was for it's corresponding FP-made sample (MC15) Z2C800 showed the highest resistance to coking if compared to Si and Ti. Nevertheless in this case it also reached the complete conversion of ethanol increasing it's H<sub>2</sub> productivity.

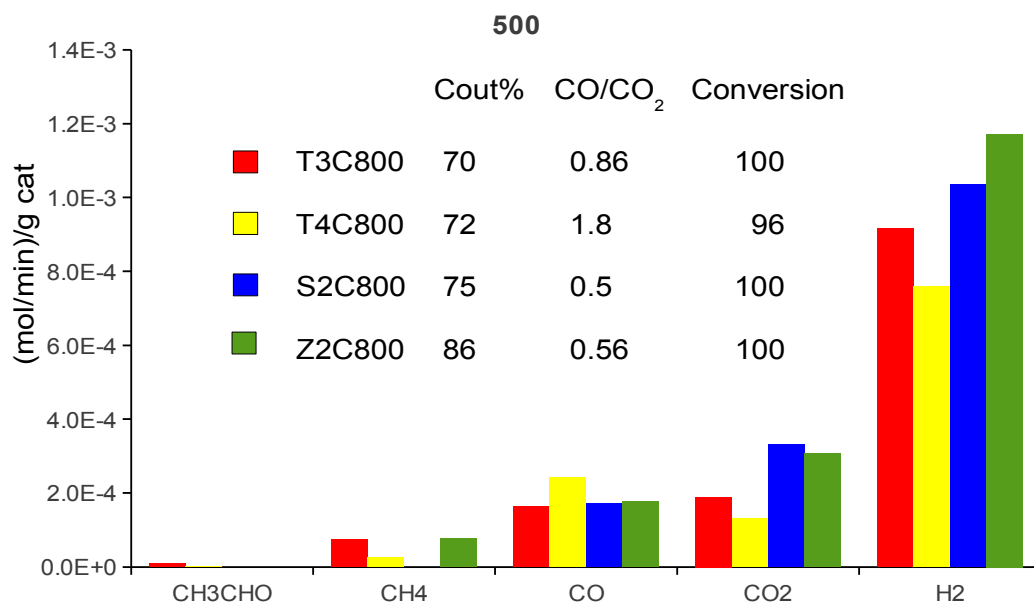


Figure 129b: productivity at 500° C of catalysts calcined at 800°C; 10%Ni/TiO<sub>2</sub>(T3C800,T4C800); 10%Ni/SiO<sub>2</sub>(S2C800); 10%Ni/ZrO<sub>2</sub>(Z2C800)

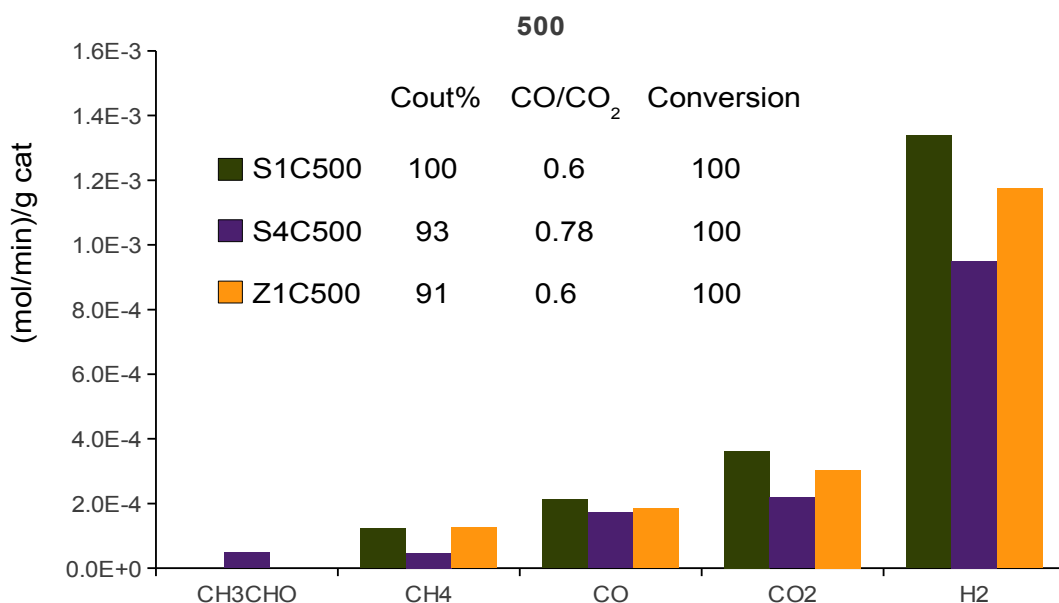


Figure 130a: productivity at 750° C of catalysts calcined at 500°C; 10%Ni/SiO<sub>2</sub>(S1C800, S4C500); 10%Ni/ZrO<sub>2</sub>(Z1C500)

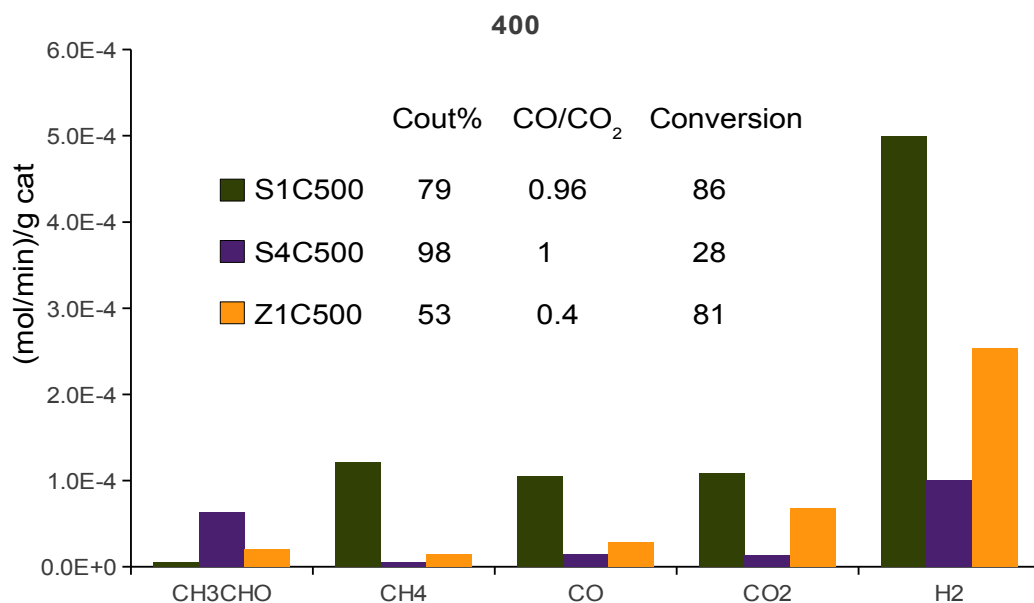


Figure 130b: productivity at 500° C of UniVe catalysts calcined at 500°C; 10%Ni/SiO<sub>2</sub>(S1C800, S4C500); 10%Ni/ZrO<sub>2</sub>(Z1C500).

The activity of most catalysts calcined at 500°C was very poor at 500°C and negligible at 400°C and 300°C. Some relevant comparisons are reported in figure Figure 130.

At 500°C Ni supported on silica (S1C500) proved to be more active than cobalt on silica (S4C500). As shown in Figure 130a the higher H<sub>2</sub> production of Ni catalysts is due to the complete conversion of ethanol to CO, CO<sub>2</sub> and CH<sub>4</sub> without CH<sub>3</sub>CHO. Comparing the same active phase on two different supports SiO<sub>2</sub> (S1C500) and on ZrO<sub>2</sub> (Z1C500), Figure 130a, it could be seen that SiO<sub>2</sub> granted a better coke resistance at 500°C than ZrO<sub>2</sub> and this caused an increase of H<sub>2</sub> productivity. The activity tests at 400°C are also compared in Figure 130b. Ni proved again the most active meta with a higher conversion respect to Co. At 400 °C silica gave rise to a better coke resistance (higher Cout%) and this caused an increase of H<sub>2</sub> productivity. It must be noticed that Cout% of Z2500 at 400°C was averaged over 8 h-on-stream. Values fluctuating from 80 to 126 %, indicating partial self-cleaning during time-on-stream.

The activity of 3 catalyst made by wetness impregnation and their corresponding ones made by FP are compared in Figure 131.

As for TiO<sub>2</sub> based catalysts preparation by FP increased very much the catalytic activity: high H<sub>2</sub> productivity, high coke resistance and complete conversion ( T3C800

also reached complete conversion, but coupled with the lowest resistance to coking). Compared to the two catalysts made by impregnation, FTI2 was characterised by higher activity for WGS (low CO/CO<sub>2</sub> ratio).

For S2C800 and MC10 the situation was different, impregnation on SBA-15 increased the resistance to coke formation and increased led to the complete ethanol conversion towards CO, CO<sub>2</sub> and CH<sub>4</sub> (no presence of CH<sub>3</sub>CHO was detected in S2C800 products).

Z2C800 reached complete conversion and the lowest CO/CO<sub>2</sub> ratio, among all the samples in Figure 131. Its corresponding FP made (MC15) instead showed a lower conversion, together with a lower activity for WGS (higher CO/CO<sub>2</sub> ratio) but a much better resistance towards coking.

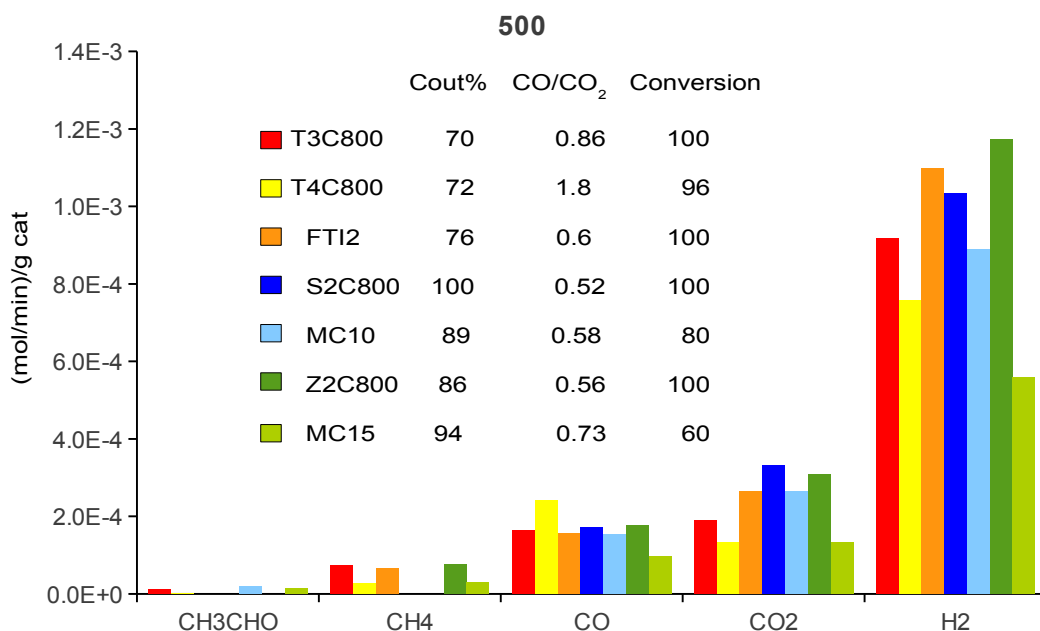


Figure 131: Comparison of productivity at 500° C of catalysts calcined at 800°C vs FP made samples: 10%Ni/SiO<sub>2</sub>(S1C800, S4C500; FTI2); 10%Ni/ZrO<sub>2</sub>(Z2C800; MC10); 10%Ni/SiO<sub>2</sub>(Z2C800; MC10).

As enlightened for group 2, Ni confirmed the most active active phase and its substitution with Co did not bring any improvement to the catalytic performance and with Cu heavily decreased the activity. Samples calcined at 800°C were more active than samples calcined at 500°C. Comparing samples calcined at 800°C and their corresponding FP made counterparts one may conclude that, depending on the support:

FP synthesis improved the whole catalytic activity for TiO<sub>2</sub>

Impregnation on SBA-15 increased the catalytic activity but not the resistance, while for Zr<sub>2</sub>O impregnation increased the H<sub>2</sub> productivity, the ethanol conversion and the CO/CO<sub>2</sub> ratio, but the FP synthesis strongly improved the resistance towards coking.

#### Group 4

Table 50 key legend of the samples

Name	Formula	Synthesis method
MC2	10% Ni/La <sub>0.6</sub> Zr <sub>1.4</sub> O <sub>3</sub>	FSP
MC3	La <sub>0.8</sub> Sr <sub>0.2</sub> NiO <sub>3</sub>	FSP
MC5	La <sub>0.7</sub> Ce <sub>0.3</sub> NiO <sub>3</sub>	FSP
MC6	10% Ni/La <sub>0.6</sub> Ce <sub>1.4</sub> O <sub>3</sub>	FSP
MC8	3%Pt/CeO <sub>2</sub>	FSP

Table 51

MC2	750 °C	500 °C	625 °C
Conversion %	100	99	100
Cout %	95	93	100
CO/CO <sub>2</sub>	2.19	0.72	1.47
H <sub>2</sub> (mol/min)/Kg <sub>cat</sub>	1.24	1.17	1.43
Sel CO <sub>2</sub> %	28	47	40
Sel CO%	62	34	59
Sel CH <sub>4</sub> %	0	12	0.6
Sel CH <sub>3</sub> CHO%	0	0.42	0

Table 52

MC3	750 °C	500 °C	625 °C
Conversion %	100	100	100
Cout %	94	94	100
CO/CO <sub>2</sub>	2.27	0.55	1.39
H <sub>2</sub> (mol/min)/Kg <sub>cat</sub>	1.29	1.28	1.42
Sel CO <sub>2</sub> %	29	52	40
Sel CO%	65	28	56
Sel CH <sub>4</sub> %	0.37	14	5
Sel CH <sub>3</sub> CHO%	0	0	0



Table 53

MC5	500 °C	625 °C
Conversion %	100	100
Cout %	89	98
CO/CO <sub>2</sub>	0.4	1.4
H <sub>2</sub> (mol/min)/Kg <sub>cat</sub>	1.25	1.42
Sel CO <sub>2</sub> %	52	40
Sel CO%	24	56
Sel CH <sub>4</sub> %	14	0.41
Sel CH <sub>3</sub> CHO%	0	0

Table 54

MC6	750 °C	500 °C	625 °C
Conversion %	100	100	100
Cout %	97	92	92
CO/CO <sub>2</sub>	2.2	0.5	1.4
H <sub>2</sub> (mol/min)/Kg <sub>cat</sub>	2.17	1.54	1.43
Sel CO <sub>2</sub> %	31	49	38
Sel CO%	67	26	54
Sel CH <sub>4</sub> %	0	17.2	0
Sel CH <sub>3</sub> CHO%	0	0	0

Table 55

MC8	750 °C	500 °C	625 °C
Conversion %	100	33	94
Cout %	95	87	88
CO/CO <sub>2</sub>	2.3	0.48	2.2
H <sub>2</sub> (mol/min)/Kg <sub>cat</sub>	1.3	0	1.0
Sel CO <sub>2</sub> %	29	12	31
Sel CO%	67	6.3	33.3
Sel CH <sub>4</sub> %	0	2.5	4
Sel CH <sub>3</sub> CHO%	0	43	11

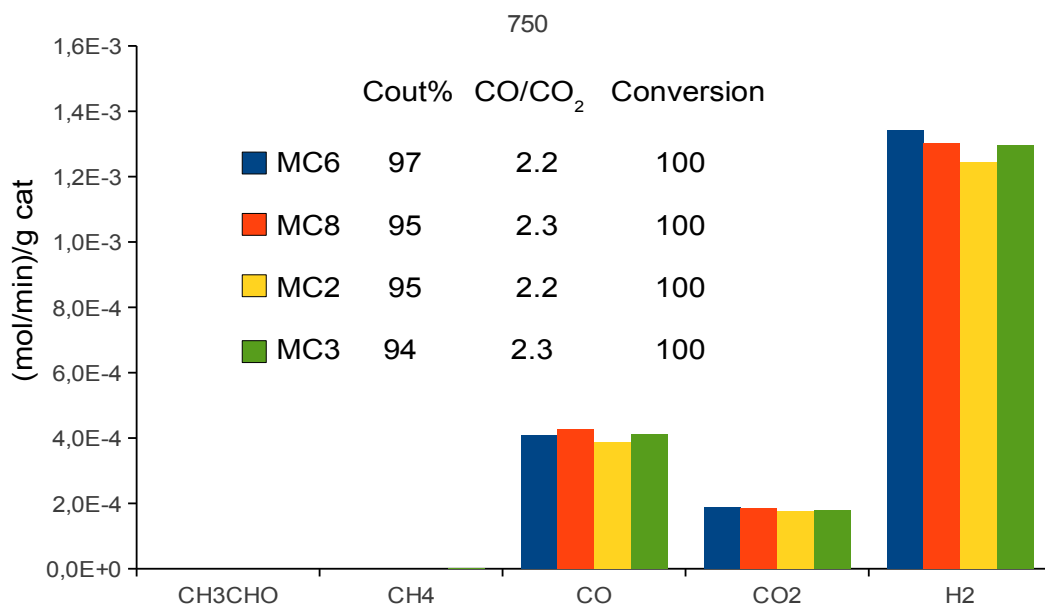


Figure 132a: Comparison of productivity at 750° C of FP made 10% Ni/La<sub>0.6</sub>Ce<sub>1.4</sub>O<sub>3</sub> (MC6); 3%Pt/Ce<sub>2</sub>O<sub>3</sub> (MC8); 10% Ni/La<sub>0.6</sub>Zr<sub>1.4</sub>O<sub>3</sub> (MC2) and La<sub>0.8</sub>Sr<sub>0.2</sub>NiO<sub>3</sub> (MC3)

All the catalysts almost seem to have the same activity at 750°C (Figure 132a) .

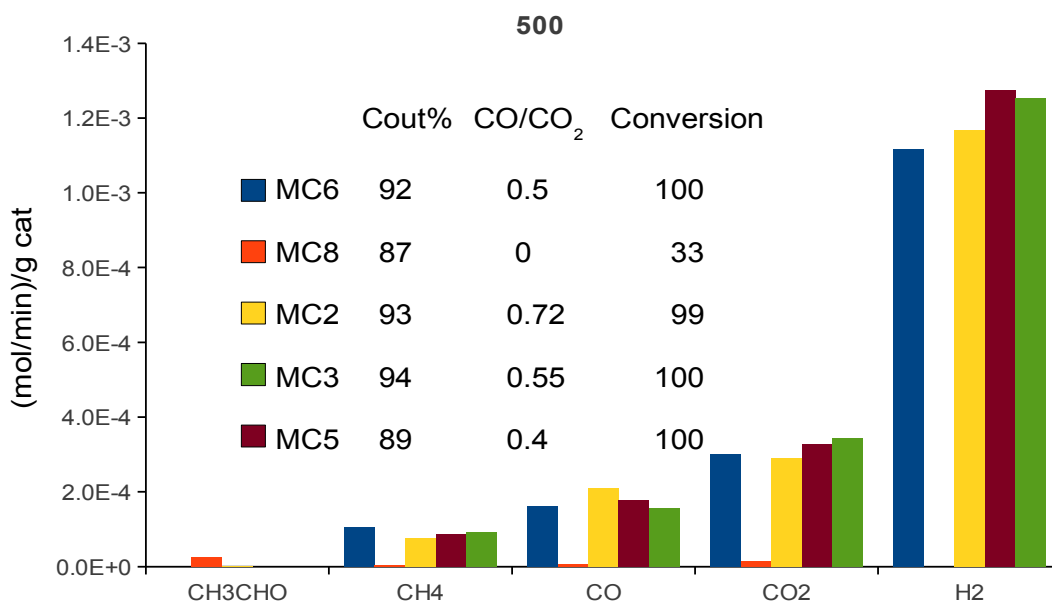


Figure 132b: Comparison of productivity at 500° C of FP made 10% Ni/La<sub>0.6</sub>Ce<sub>1.4</sub>O<sub>3</sub> (MC6); 3%Pt/CeO<sub>2</sub> (MC8); 10% Ni/La<sub>0.6</sub>Zr<sub>1.4</sub>O<sub>3</sub> (MC2); La<sub>0.8</sub>Sr<sub>0.2</sub>NiO<sub>3</sub> (MC3) and La<sub>0.7</sub>Ce<sub>0.3</sub>NiO<sub>3</sub> (MC5)

The behaviour of the catalysts was markedly different at 500°C. First of all, the Pt based catalyst (MC8) showed the worst performance among all the catalysts with a very low conversion and high selectivity to CH<sub>3</sub>CHO and seems to work better as

ethanol de-hydrogenation catalyst than as SR catalyst. The best productivity of H<sub>2</sub> was achieved using the MC5 sample perovskite-like catalyst in which 30% of the La atoms were substituted by Ce. This led to high productivity despite the Cout% balance that smaller than for the other catalysts. MC3 showed H<sub>2</sub> productivity quite smaller and a CO/CO<sub>2</sub> bigger than MC5, but a better Cout%. MC3 and MC5 are compared to the pure LaNiO<sub>3</sub> (DPLN group 1) in Figure 15 at 500°C. Substituting part of the La atoms with Sr (MC3) or with Ce (MC6), H<sub>2</sub> productivity increase and CO/CO<sub>2</sub> decrease. These two factors could indicate an increased in the WGS activity that follow the trend Sr < Ce. More interestingly insertion of Sr with the respect to the undoped perovskite markedly improved coke resistance.

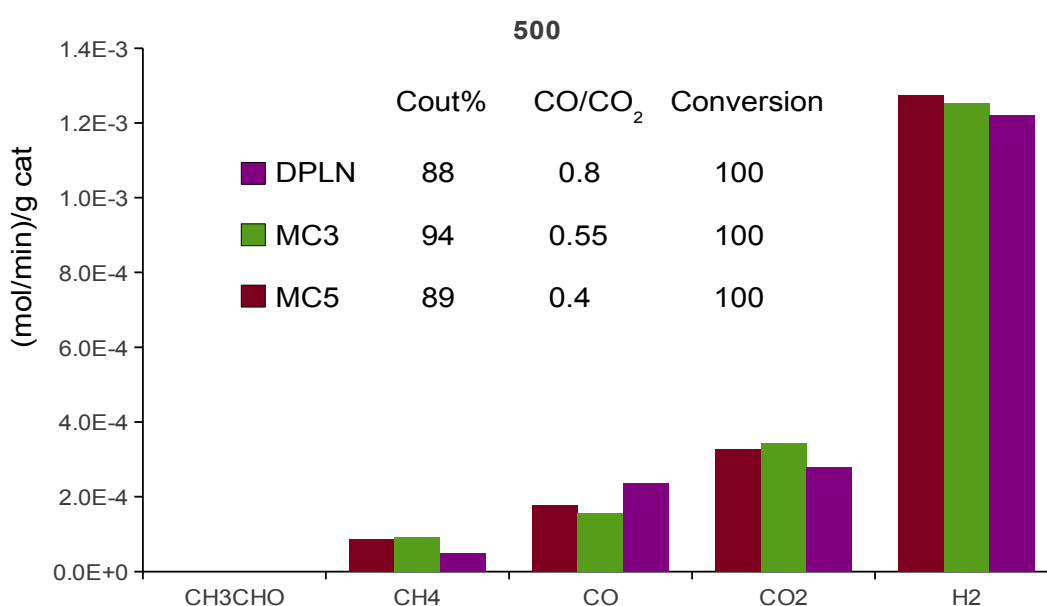


Figure 133: Comparison of productivity at 500° C of FP ma  $La_{0.8}Sr_{0.2}NiO_3$  (MC3);  $La_{0.7}Ce_{0.3}NiO_3$  (MC5) and  $LaNiO_3$  (DPLN)

Pt tested at 500°C was not particularly active as ESR catalysts, but mostly as a dehydrogenation one.

The insertion of Ce inside the perovskite structure of LaNiO<sub>3</sub> caused an increase in the WGS activity, but a decrease in the coke resistance. Instead doping with Sr provoked a lower increase in the WGS activity, but a satisfactory improvement of the resistance towards coking.

### Activity test in Belfast :

The samples analysed were those of group 1, but since not all the samples were from the same batch of the original catalysts they are here re-named. Two more catalysts were added, in particular 15% Co/La<sub>2</sub>O<sub>3</sub> and 15%Cu/La<sub>2</sub>O<sub>3</sub> to investigate the effect of different active phase on lanthanum oxide and the loading was chosen on the basis of the results of Group 1.

Table 56 key legend of the samples

Name	Formula	Synthesis method
BLa1	5%Ni/La <sub>2</sub> O <sub>3</sub>	Support+Ni one step FSP
BLa2	10%Ni/La <sub>2</sub> O <sub>3</sub>	Support+Ni one step FSP
BLa3	15%Ni/La <sub>2</sub> O <sub>3</sub>	Support+Ni one step FSP
BLaNi	LaNiO <sub>3</sub>	one step FSP
BTi1	5%Ni/TiO <sub>2</sub>	Support+Ni one step FSP
BTi2	10%Ni/TiO <sub>2</sub>	Support+Ni one step FSP
BTi3	15%Ni/TiO <sub>2</sub>	Support+Ni one step FSP
BLa3Co	15%Co/La <sub>2</sub> O <sub>3</sub>	Support+Co one step FSP
BLa3Cu	15%Cu/La <sub>2</sub> O <sub>3</sub>	Support+Cu one step FSP

Table 57

BLa1	500 °C
Conversion %	85
Cout %	77
CO/CO <sub>2</sub>	0.36
H <sub>2</sub> (mol/min)/Kg <sub>cat</sub>	2.7
Sel CO <sub>2</sub> %	42
Sel CO%	15
Sel CH <sub>4</sub> %	14
Sel CH <sub>3</sub> CHO%	2

Table 58

BLa2	500 °C
Conversion %	98
Cout %	77
CO/CO <sub>2</sub>	0.4
H <sub>2</sub> (mol/min)/Kg <sub>cat</sub>	2.7
Sel CO <sub>2</sub> %	42
Sel CO%	17
Sel CH <sub>4</sub> %	16
Sel CH <sub>3</sub> CHO%	1

Table 59

BLa3	500 °C
Conversion %	92
Cout %	98
CO/CO <sub>2</sub>	0.27
H <sub>2</sub> (mol/min)/Kg <sub>cat</sub>	3.0
Sel CO <sub>2</sub> %	62
Sel CO%	11
Sel CH <sub>4</sub> %	22
Sel CH <sub>3</sub> CHO%	0

Table 60

BLaNi	500 °C
Conversion %	100
Cout %	95
CO/CO <sub>2</sub>	0.18
H <sub>2</sub> (mol/min)/Kg <sub>cat</sub>	3.5
Sel CO <sub>2</sub> %	40
Sel CO%	11
Sel CH <sub>4</sub> %	33
Sel CH <sub>3</sub> CHO%	0

Table 61

BTi1	500 °C
Conversion %	71
Cout %	75
CO/CO <sub>2</sub>	0.27
H <sub>2</sub> (mol/min)/Kg <sub>cat</sub>	2.2
Sel CO <sub>2</sub> %	42
Sel CO%	11
Sel CH <sub>4</sub> %	11
Sel CH <sub>3</sub> CHO%	2

Table 62

BTi2	500 °C
Conversion %	99
Cout %	77
CO/CO <sub>2</sub>	0.23
H <sub>2</sub> (mol/min)/Kg <sub>cat</sub>	3.1E <sup>-3</sup>
Sel CO <sub>2</sub> %	46
Sel CO%	11
Sel CH <sub>4</sub> %	20
Sel CH <sub>3</sub> CHO%	0

Table 63

BTi3	500 °C
Conversion %	99
Cout %	65
CO/CO <sub>2</sub>	0.2
H <sub>2</sub> (mol/min)/Kg <sub>cat</sub>	2.9
Sel CO <sub>2</sub> %	41
Sel CO%	8
Sel CH <sub>4</sub> %	15
Sel CH <sub>3</sub> CHO%	0

Table 64

BLa3Co	500 °C
Conversion %	65
Cout %	59
CO/CO <sub>2</sub>	0.4
H <sub>2</sub> (mol/min)/Kg <sub>cat</sub>	2.0
Sel CO <sub>2</sub> %	24
Sel CO%	7
Sel CH <sub>4</sub> %	1
Sel CH <sub>3</sub> CHO%	3

Table 65

BLa3Cu	500 °C
Conversion %	33
Cout %	87
CO/CO <sub>2</sub>	0.014
H <sub>2</sub> (mol/min)/Kg <sub>cat</sub>	0.7
Sel CO <sub>2</sub> %	44
Sel CO%	0.6
Sel CH <sub>4</sub> %	0.7
Sel CH <sub>3</sub> CHO%	1.2

The comparison between the catalysts based on TiO<sub>2</sub> and on La<sub>2</sub>O<sub>3</sub> are reported in Figures 134 and figure 135 respectively. In general all these catalysts showed bigger CO<sub>2</sub> productivity and a lower CO/CO<sub>2</sub> than catalysts analysed in group 1 (Figure 123b, 124b). This indicates higher contribution of WGS to the production of H<sub>2</sub>. This could be due to the fact that in this series the catalysts were tested only at 500°C only, so the catalyst experienced a lower thermal stress, showing more active for WGS. As already observed for Group 1, x%/TiO<sub>2</sub> catalysts possessed a lower CO/CO<sub>2</sub> ratio, but a lower resistance towards coke formation than the corresponding x%/La<sub>2</sub>O<sub>3</sub>. As for TiO<sub>2</sub> series (Figure 134) the best catalyst confirmed 10%Ni/TiO<sub>2</sub>, which showed the best Cout% balance and the highest H<sub>2</sub> productivity.

For the La based series (Figure 135), as the Ni percentage increased the catalytic performance improved, but in this series LaNiO<sub>3</sub> (BLANi) was the only catalyst reaching complete ethanol conversion, though Cout% was lower than for the other

samples. This may be due to the milder activation performed before these tests, that coupled with the stability of the mixed oxide likely left a higher amount of Ni enclosed as mixed oxide and not available for the reaction.

This is also the reason why a lower Ni is needed to reach complete conversion with Ni supported over titania, which forms a less stable mixed oxide and is characterised by easier reducibility.

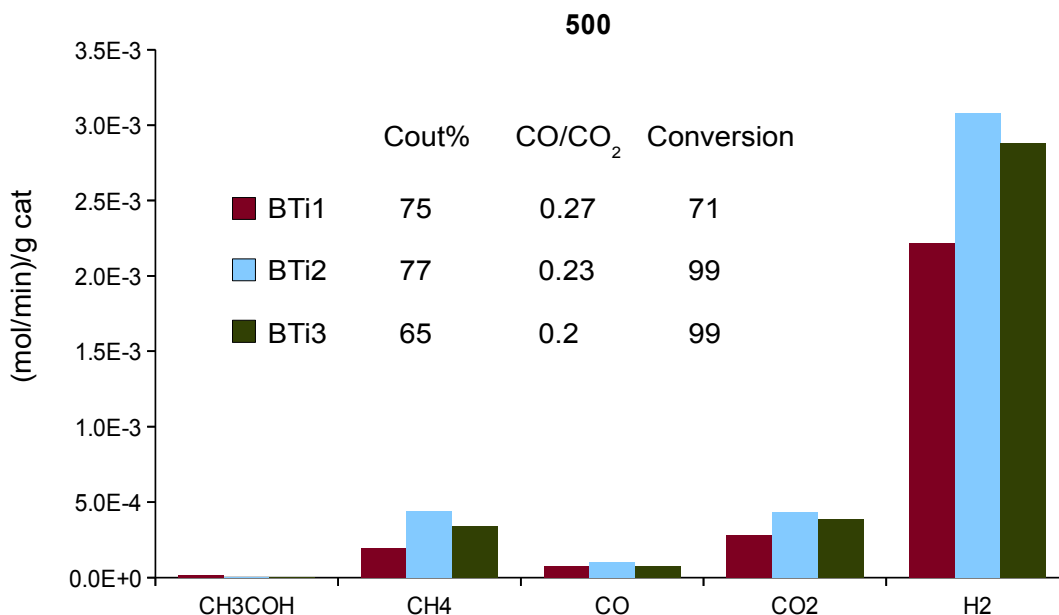


Figure 134: productivity at 500°C of FP X%Ni/TiO<sub>2</sub> (X=5 (BTi1); 10(BTi2) ;15(BTi3)) tested in Belfast

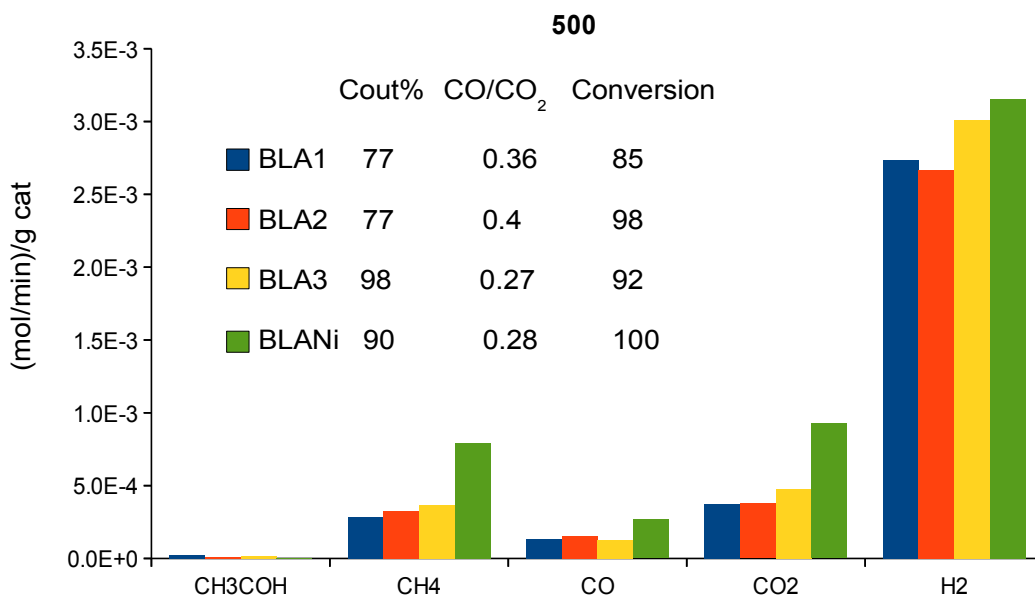


Figure 135: productivity at 500°C of FP X%Ni/La<sub>2</sub>O<sub>3</sub> (X=5 (BLA1); 10(BLA2) ;15(BLA3); FP made LNiO<sub>3</sub> (BLANi)



The comparison between the activity of 3 catalysts supported on  $\text{La}_2\text{O}_3$  with different active phase is reported in Figure 136. As observed in previous comparisons Co (Bla3Co) exhibited a lower activity than Ni, while Cu (Bla3Cu) lead to the lowest conversion and productivity of  $\text{H}_2$ .

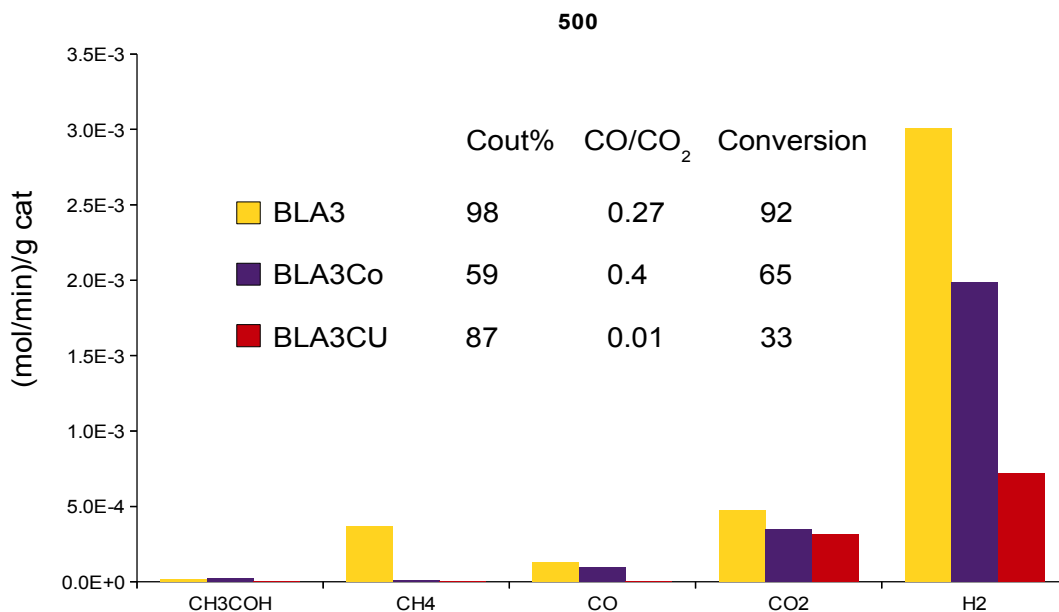


Figure 136: Productivity at 500°C of FP made 15%Ni/La<sub>2</sub>O<sub>3</sub> (BLA3); 15%Co/La<sub>2</sub>O<sub>3</sub> (BLA3Co) and 15%Cu/La<sub>2</sub>O<sub>3</sub> (BLA3Cu)

Among all the catalysts the most promising seems to be LaNiO<sub>3</sub> (BLaNi) that also showed an interesting trend in the Cout% balance, that could suggest an “auto-cleaning” behaviour towards the carbon formed over its surface. (Figure 137)

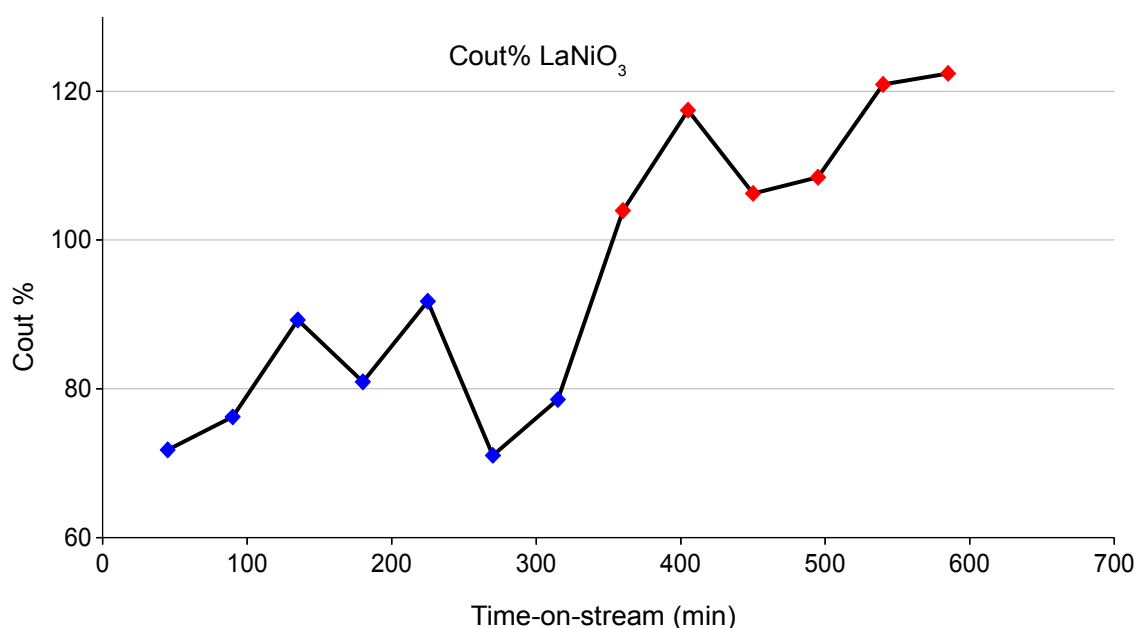


Figure 137: Time-on-stream Cout% balance at 500°C of LaNiO<sub>3</sub>, whole test duration 10h. First analysis made at min 15, other analysis made every 35 minutes.

To verify whether LaNiO<sub>3</sub> really eliminates the coke formed during the first hours-on-stream, a test lasting 35h hours was divided into 7 sub-tests to see how the activity of the catalyst changed every 5 hours-on-stream.

After each sub-test the catalyst was collected and weighted to see the increase of its mass due to carbon formation. The result are reported as Weight % = 100 [(mass of catalyst after the test – mass of catalyst before the test)/ mass of catalyst before the test].

**TABLE 66: Results of the 7 tests of LaNiO<sub>3</sub> at 500°C**

h-on-stream	C out %	Weight %	CO/CO <sub>2</sub>	H <sub>2</sub> (mol/min)/Kg <sub>cat</sub>	Sel CO <sub>2</sub> %	Sel CO%	Sel CH <sub>4</sub> %
5	84	17	0.31	2.92	38	12	33
10	88	48	0.29	3.16	40	11	34
15	92	74	0.28	3.30	42	13	35
20	92	102	0.30	3.23	41	13	35
24,7	90	106	0.29	3.16	41	12	34
30	93	131	0.32	3.33	42	14	34
35	100	169	0.35	3.34	44	16	38

The results of this activity test are reported in table 66.

As regards H<sub>2</sub> productivity there is no sign of deactivation as time-on-stream increased, CO/CO<sub>2</sub> ratio become more stable after 20h and only a slight increase of 5% H<sub>2</sub> productivity was observed.

Cout balance % and the increase in the weight of the sample are summarised in the first two columns of Table 66. The weight of the sample increased with time-on-stream and the general trend of the Cout% suggest an increase of the C out balance.

This could mean a progressive deactivation of the sites more active for coking.

Results of this test do not confirm the hypothesised auto-cleaning behaviour of LaNiO<sub>3</sub>, even if the carbon balance of the sample improved as the time-on-stream, but it enlightened a high resistance towards coke formation since the catalytic performance of LaNiO<sub>3</sub> slightly improved with time-on-stream. Likely, the active sites

more active for coking progressively deactivated, but they were not the most active sites for ESR, since no decrease of conversion and hydrogen productivity was observed.

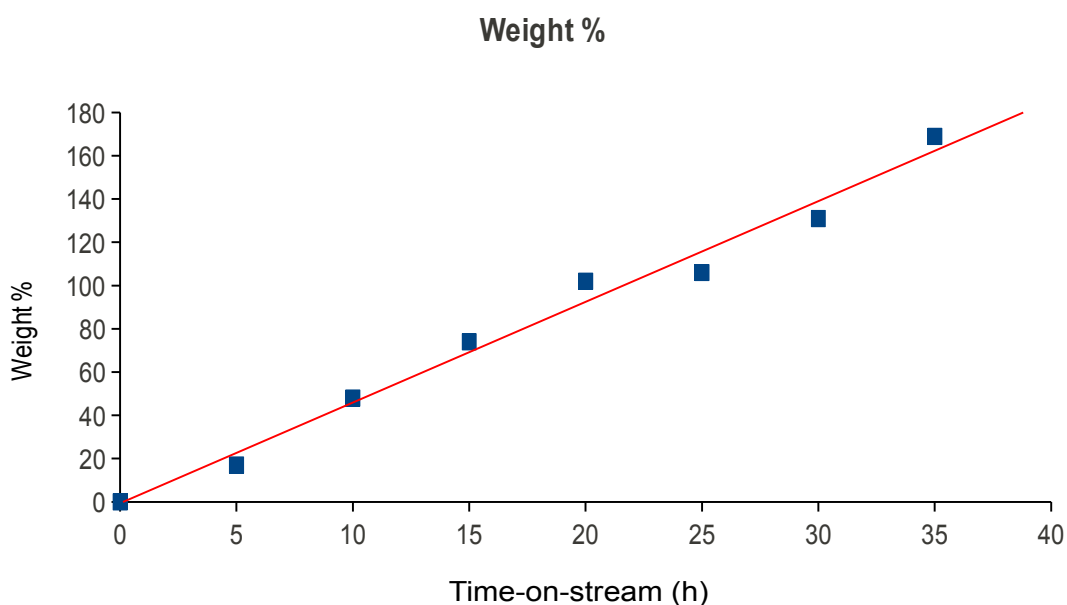


Figure 138: Weight% v.s time-on-stream at 500°C of  $\text{LaNiO}_3$ , whole test duration 35h. Value of weight% balance every 5 hours.

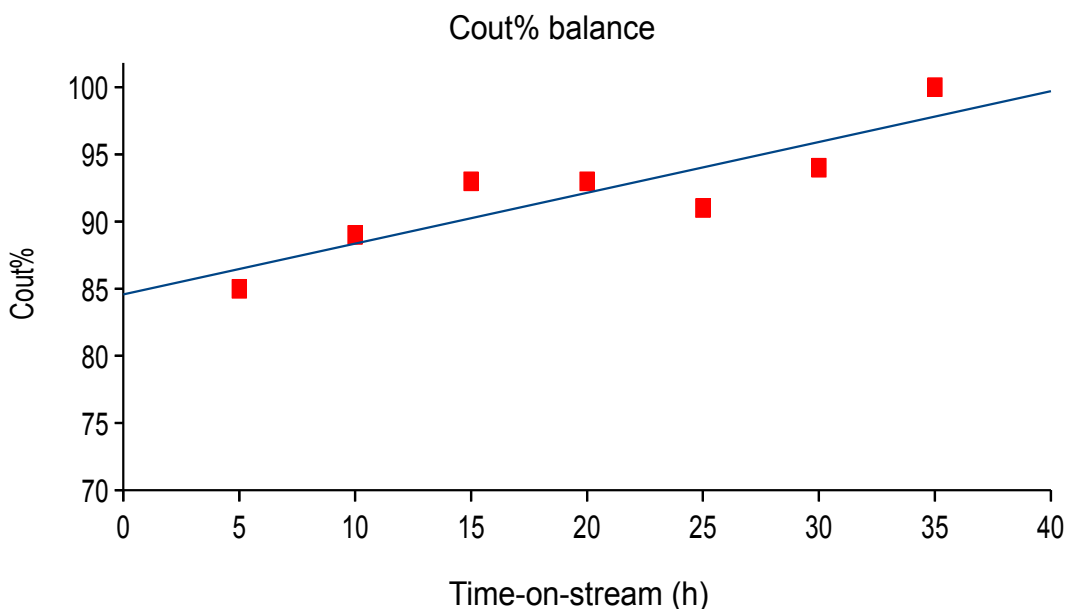


Figure 139: Time-on-stream Cout balance% at 500°C of  $\text{LaNiO}_3$ , whole test duration 35h. Value of Cout balance% balance every 5 hours.

To further test the resistance of  $\text{LaNiO}_3$ , two additional tests with different contact time were performed. The flow of water/ethanol mixture and of gases was kept

constant, but the amount of catalyst charged in the reactor was reduced first to 100 mg and for the second test to 50 mg. Tests were made at 500°C for 24h. As shown in Figure 140 the first effect of the reduction of contact time was the reduction of ethanol conversion with time-on-stream, even if after 24h at the lowest contact time (test 50mg) conversion after was still around 70%.

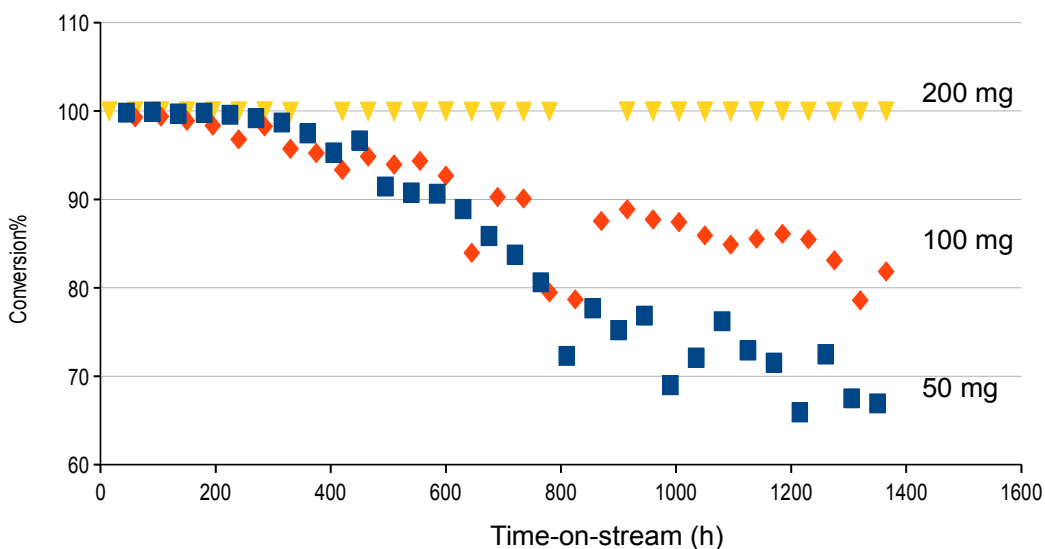


Figure 140: Comparison of different contact time: conversion % vs. time-on-stream at 500°C

Total flow of ethanol fed to the reactor was 0.24 mmol/min so the maximum yield of H<sub>2</sub> possible was 1.4 mmol/min so the max H<sub>2</sub> productivity for each test was:

50mg=28 (mmol/min)/g of catalysts

100mg=14 (mmol/min)/g of catalysts

200mg=7 (mmol/min)/g of catalysts

H<sub>2</sub> productivity measured for each test after 24h-on-stream were:

50mg=11.8 (mmol/min)/g of catalysts

100mg=6.65 (mmol/min)/g of catalysts

200mg=3.40 (mmol/min)/g of catalysts

Looking the ratio between the actual and the maximum theoretical productivity one obtains:

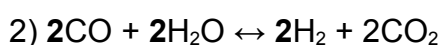
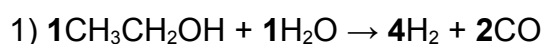
$$50\text{mg} = 42\% \quad 100\text{mg} = 47\% \quad 200\text{mg} = 49\%$$

Therefore decreasing the contact time leads to a progressive decreasing of the ethanol conversion and as consequence of the productivity of H<sub>2</sub>.

Comparison between those tests shows that LaNiO<sub>3</sub> is a very active and stable catalyst, since even under the most “deactivating” conditions (lowest contact time

50mg) conversion of ethanol was still around 70%.

To achieve the maximum yield of H<sub>2</sub> for mol of CH<sub>3</sub>CH<sub>2</sub>OH converted, the stoichiometry of reaction 1 and 2 requires 3 mol of water for each mol of ethanol.



So for all the tests described in previous paragraphs a mixture H<sub>2</sub>O:CH<sub>3</sub>CH<sub>2</sub>OH 3:1 mol/mol (CH<sub>3</sub>CH<sub>2</sub>OH 52 vol%) was used. Since LaNiO<sub>3</sub> is meant to be a catalyst for bio ethanol steam reforming which as raw product is very diluted (H<sub>2</sub>O/C<sub>2</sub>H<sub>5</sub>OH = 8.4 mol/mol), some tests were made back to Milan at 500°C using different steam to ethanol ratio: 5:1 mol/mol (CH<sub>3</sub>CH<sub>2</sub>OH 39 vol%) and 10:1 mol/mol (CH<sub>3</sub>CH<sub>2</sub>OH 24 vol %). The results are reported in Table 50. These tests were also carried out to enhance the resistance towards coking by intensifying the gasification of cumulated coke

**Table 67 Results of activity test with different steam to ethanol ratio**

Water/ethanol (mol/mol)	3:1	5:1	10:1
Conversion %	100	100	100
C <sub>out</sub> %	94	99	100
CO/CO <sub>2</sub>	0.62	0.32	0.12
H <sub>2</sub> /ethanol converted	3.8	3.9	4.2
Sel CO <sub>2</sub> %	51	67	81
Sel CO%	31	21	9
Sel CH <sub>4</sub> %	12	10	8
Sel CH <sub>3</sub> CHO%	0	0	0

As shown in Table 67, the CO production dramatically decreased as the amount of water in the reagents increased. At the same time, selectivity towards CO<sub>2</sub> increased due to higher activity for WGS H<sub>2</sub> productivity increased as well. Most important, an increase of water amount in the feed increased the activity for CH<sub>4</sub> reforming and improved C balance, one of the most pressing problems when operating at low

temperature.

# **Chapter 5 Integrated energy co-generation device**

A Device for the co-generation of thermal and electric was installed c/o the Dept. of Physical Chemistry and Electrochemistry of Università degli Studi di Milano, on the basis of a collaboration with Helbio S.A. Hydrogen and Energy Production Systems (supplier of the unit) and some sponsors (Linea Energia S.p.A., Parco Tecnologico Padano and Provincia di Lodi).

This device is composed by GH2-BE-5000 unit connected to a polymer electrolyte membrane fuel-cell (PEM). The device has a nominal output of 5 kW electrical power + 5kW thermal power with heat recovery. This system is designed to produce energy for civilian de-localized uses, variable electricity and heat loads and discontinuous applications.

GH2-BE-500 unit layout is depicted in Figure 141. It is less compact than possible commercial units, due to the need of gas sampling and internal inspection during the testing campaign.



*Figure 141: GH2-BE-500 unit installed c/o the Dept. of Physical Chemistry and Electrochemistry of Università degli Studi di Milano*

The PEMFC connected meets the power requirements. Indeed, these cells are considered suitable since their development is in a semi-commercial stage, their power density is comparatively higher than other FC, they operate at low temperature (ca. 80°C) and hence they do not require long start-up periods, demonstrating adaptable also for emergency devices. Nevertheless, CO poisoning of the Pt-based electrodes is a serious drawback when H<sub>2</sub> is derived from organic feed-stocks. The fuel processor here adopted is designed to decrease CO concentration below 20 ppm in the reformat, suitable to feed PEMFC operating around 80°C.

Scale of the process is 5kw electric and 5kw thermal as peak output, but further scale up are planned to reach 100kw both electric and thermal. The goal of the testing campaign is to demonstrate the feasibility of this device as emergency power generator or for de-localized domestic energy generation.

## **GH2-BE-500 unit**

GH2-BE-500 unit consists of a series of six reactors connected in series, as sketched in Fig. 142 (auxiliary equipment, interconnections and heat recovery systems were not reported for simplicity). Bioethanol from grapes (Alcoplus, 99.0 vol%) was diluted to 96.0 vol% with deionised water before feeding the unit. Ethanol with 96 vol% concentration was not directly purchased from the supplier due to purity reasons. The alcohol was fed to a heat exchange reactor (shell and tubes) containing both the steam reforming catalyst and a commercial combustion catalyst. After evaporation on an electrical heater, ethanol was mixed with air for feeding the combustion side and with water vapour to feed the hydrogen production line. The latter reacting mixture was first fed to a pre-reformer, then to the main reforming reactor. Heat recovery is active between these two units. Two reactors for water gas shift and two for methanation follow are connected in series to purify the reformat gases from CO. Heat exchange with air blowers is provided between each of them to progressively lower the reaction temperature. Excess water is condensed at the outlet of the last reactor by cooling at ca. 80°C. A pressure relief valve allows to set the reformat discharge pressure depending on the FC requirement.

A gas sampling point is available after each reactor. Products analysis was carried out by means of an Agilent 7890 GC equipped with FID and TCD detector and with PoraplotQ and Molecular Sieves columns. The analytical method allows the quantification of ethanol, water, H<sub>2</sub>, CO, CO<sub>2</sub> and CH<sub>4</sub>. The detection of acetaldehyde, ethylene, ethane and acetic acid is also possible, though they were almost never observed in the products. A methanation device is used before the FID detector to reliably quantify traces of CO (last steps of the purification section).



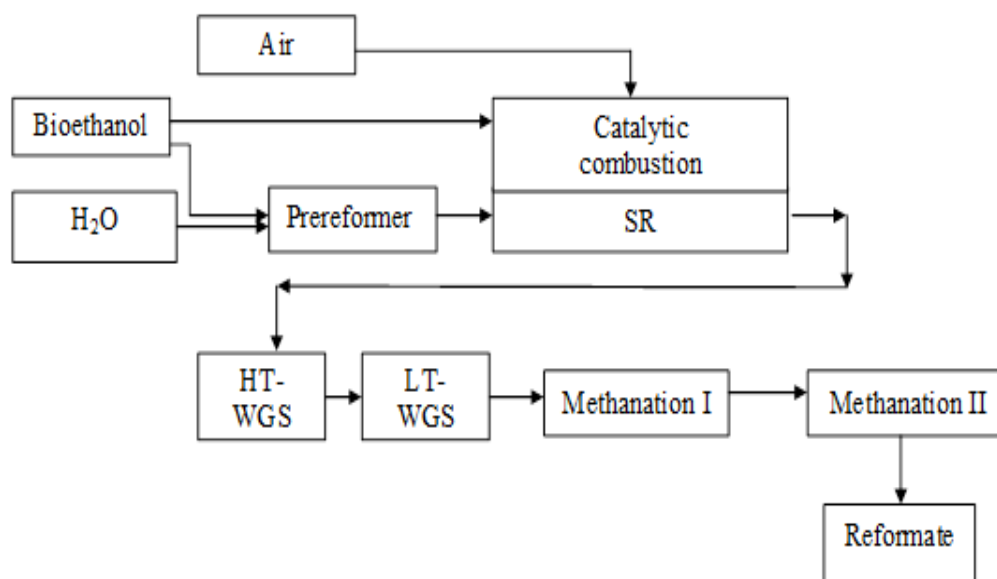


Figure 142: scheme of the GH2-BE-500 unit

The pre-reforming stage (figure 142) operates with a Helbio SA proprietary catalyst at 300-350°C, GHSV = 1900 h<sup>-1</sup>, leading to rather full ethanol conversion into H<sub>2</sub>, CO and CH<sub>4</sub>. By contrast, the main reformer is operated between 550 and 750°C, GHSV = 7700 h<sup>-1</sup>, allowing the conversion of the produced CH<sub>4</sub> and of possible residual ethanol.

Reactor heating is accomplished by combustion of part of the ethanol over a commercial combustion catalyst. The latter is loaded in the tubes of a heat exchanger type reactor, hosting the reforming catalyst pellets in the shell side.

The water/ethanol ratio in this case has been set to ca. 5.5 mol/mol, to prevent extensive coking and to drive the WGS equilibrium towards CO removal.

Pressure at the outlet of the processor has been at first adjusted to 0.8 bar(g) by using two relief valves, in order to feed the FC module. Additional tests have been also carried out at higher pressure, *i.e.* 0.95 bar(g), with similar results.

An example of gas composition after each reactor is reported in Table 68, as vol% on a dry basis.

**Table 68 : Gas composition after the unit reactors**

Compound	Prereformer	Reformer	HT-WGS	LT-WGS
H <sub>2</sub>	59	73	73	74
CO	1	10	1.5	0.4
CO <sub>2</sub>	21	17	24	24.4
CH <sub>4</sub>	19	-	1.5	1.2

H<sub>2</sub> concentration was *ca.* 60% after the first pre-reforming stage, as expected since a high methane yield was achieved by ethanol decomposition, but reaction temperature was too low to achieve its full reformation. The latter was accomplished in the subsequent reforming reactor, where methane was fully converted. However, the CO/CO<sub>2</sub> ratio increased due to the thermodynamically unfavourable conditions for the WGS reaction.

H<sub>2</sub> purity is a fundamental task for its use in fuel cells. Indeed, depending on the FC type selected, different poisons should be carefully eliminated to prevent rapid and irreversible deactivation of the FC catalyst. H<sub>2</sub> purification was first accomplished by water gas shift (WGS), splitted in two reactors, high-temperature (HT) and low temperature (LT), WGS stages. The former is operated around 350°C for kinetic reasons and it converts *ca.* 90% of CO, the remaining portion being abated in a LT-WGS stage at 280°C to shift the equilibrium towards *ca.* 0.3-1% CO. Gas composition out-flowing from both WGS reactors is summarised in Table 68. Some methane formed due to methanation of CO or CO<sub>2</sub> and H<sub>2</sub> concentration was higher than 70% on a dry basis. However the most important datum is CO level, kept below 2 vol% after the former WGS stage and below 0.5 vol% after the latter. Such purity level is suitable to feed the HT-PEMFC.

By contrast, a further purification stage is required to meet the higher H<sub>2</sub> purity demand of low temperature PEMFC (CO<20 ppm), here accomplished by two selective methanation reactors, connected in series and operated at 215 and 210°C respectively. The CO amount was quantified in the last three reactors by using the

methanation-FID device of the GC, which allows a detection limit down to 2 ppmv. CO concentration decreased from 0.4 vol% after the LT-WGS stage, to *ca.* 15 and 10 ppmv respectively after the first and second methanation reactors. Therefore, the present fuel processor demonstrated suitable for H<sub>2</sub> production with enough purity for LT-PEMFC (CO < 20 ppmv) .

### **General observation**

The fuel processor operated under fixed reaction conditions only. At 100% capacity the hydrogen production to feed a 5 kW<sub>e</sub> PEM-FC is ~6.5 Nm<sup>3</sup>/h H<sub>2</sub>. This requires 44 and 98 g/min as feeding flow rates of ethanol 96 vol% and of demineralised water, respectively. Based on this value, the total system efficiency would be *ca.* 22.5 %, calculated on electrical power output only and according to ethanol LHV. This result is much better than 17.5 % reported in the literature for a smaller system (250 W), with a similar layout [105].

### **Observations and improvements**

Future experimentation will be carried out on a recently developed high temperature PEM fuel cell (HT-PEMFC), operating at 160-180°C. The increase of the FC working temperature represents an advantage for a higher quality heat output and above all for a much lower sensitivity to CO (depending on power loading even 2 vol% CO or more may be tolerated). This would allow to sensibly simplify the present reactors layout by dropping both the methanation units. Major drawbacks are a lower reliability of HT-PEMFC due to lacking experience and more critical operation when frequent start-up and shut down occur.

Our testing over SR catalysts indicates that it is possible to achieved the amount of H<sub>2</sub> required by the PEM-FC even working at 500°C. This temperature joint to the new HTPEM-FC which will work at around 180°C could bring many improvements to the

whole system : first of all a strong reduction of the CO amount inside the reformat gases that will bring a simplification of the device layout reducing the number of the reactors for CO abatement. Furthermore, it will decrease the amount of ethanol consumed for the catalytic combustion since the temperature required will be 250°C lower than the ones set up currently.

## **Chapter 6: Conclusions**

### **Working temperature**

By comparing the different reaction conditions it is possible to conclude that at 750°C the differences among the samples flatten and the system approaches the

equilibrium behaviour. When tested at 500°C the catalysts differentiate from one another. Usually at this temperature the formation of coke is the most pressing problem and the contribution of WGS is more visible (lower CO/CO<sub>2</sub> ratio). Activity at 625°C showed some differences among the samples, some of these differences are due to the partial deactivation of the catalysts when tested at 500°C. The fourth test made at 750°C after a second activation some case showed better results than the first 750°C test this is due to the fact that some catalyst required more time at temperature to stabilise their activity. As enlightened by the test made in Belfast activity at 500°C immediately after activation (at 750°C for 1h with H<sub>2</sub>), without testing at 750°C before, reduces coke formation and increases the CH<sub>4</sub> selectivity and this is due to a lower thermal stress of the sample.

## Synthesis methods

At 750°C the effect of FP synthesis on the catalytic performances of the samples was negligible as already observed comparing the different temperatures all the samples showed quite the same activity.

The effect of the synthesis method were more visible at 500°C: the FP made catalysts seem to promote WGS more effectively (high H<sub>2</sub> productivity, joint to smaller CO/CO<sub>2</sub>) than their corresponding impregnated one. They also showed always a better resistance towards coking.

This could be explained looking at the XRD analysis of the samples as prepared and after the activation process (800°C for 1h). For examples 10 wt%Ni/TiO<sub>2</sub> catalysts after activation are mainly composed by rutile and metallic Ni. This is the same native composition of the FP made samples while the impregnated catalyst were mainly composed by anatase. Change of structure could cause a loss in the original SSA of the sample as confirmed by BET analysis. The same considerations hold for the samples obtained by incipient wetness impregnation and calcined at 500°C, whose surface area was *ca.* double than for the FP prepared ones, but it dropped to a few m<sup>2</sup>/g after calcination at 800°C. Moreover the synthesis by FP generates high dispersion of the active phase improving the resistance of the sample to coke formation [105-107] and possibly favouring the WGS reaction.

## Specific surface area

The specific surface area widely variable for the full set of samples, depending on one hand on support nature, on the other hand on calcination temperature. By neglecting at first the effect of the chemical composition of the sample on catalytic activity, a slight decrease of water conversion with increasing surface area was observed at 750°C, the other parameters being independent on SSA. This trend was confirmed at 625°C, coupled with a slight increase of carbon balance with increasing surface area, and at 500°C when additionally H<sub>2</sub> productivity was found to roughly increase with this property.

## Metal reducibility

H<sub>2</sub> productivity and C balance roughly decreased and CO/CO<sub>2</sub> ratio increased accordingly when decreasing metal reducibility (higher initial and final reduction temperatures). At first sight, at 500°C a lower productivity than expected was observed for some FP prepared samples, which were characterised by very low reduction temperatures. However, the TPR-TPO-TPR cycles evidenced a higher reduction temperature during the second reduction cycle, particularly for the TiO<sub>2</sub> supported sample. Metal reducibility has been already addressed as one of the most important parameters affecting catalytic activity [106,107], though this parameter may be also influenced by a strong interaction with the support [108].

## Active phase

A general trend could be observed in the activity of the different active phase used . Especially at 500°C the activity follow this trend Cu < Co < Ni

## Supports

*TiO<sub>2</sub>*:

Compared to the other supports at 500°C TiO<sub>2</sub> showed the best conversion (100%) coupled with low CO/CO<sub>2</sub> and the worst resistance towards coking. The titania supported samples demonstrated unstable when calcined at 500°C, due to surface reconstruction of the active phase and the support. Some better results have been achieved at higher temperature, though sample T3C800 proved satisfactory only when tested at 750°C. Even in this case this sample showed a good H<sub>2</sub> productivity, but very high values of the CO/CO<sub>2</sub> ratio, which may be compatible with a considerable activity for the dry reforming of ethanol. The best performing catalyst among the titania supported ones was that prepared by flame pyrolysis, which also sufficiently promoted the WGS reaction, though its low temperature activity was not fully satisfactory.

#### *La<sub>2</sub>O<sub>3</sub>:*

Compared to the other supports at 500°C La<sub>2</sub>O<sub>3</sub> didn't reach the complete conversion even if it showed a good resistance towards coking and good H<sub>2</sub> productivity. FP made samples improved their activity as the Ni loading increased.

As enlightened by the XRD analysis (Figure 31) the amount of Ni influence the presence of the mixed oxide La<sub>2</sub>NiO<sub>4</sub> in the structure of the as prepared sample. After activation La<sub>2</sub>NiO<sub>4</sub> disappeared even if not completely and some small reflections were still visible. LaNiO<sub>3</sub> was the best catalyst among the series of La based catalysts and tested for 35h enlighten a progressive improvement of the catalytic activity with time-on-stream due to the progressive deactivation of the most active site for coke generation. De-Lima et al [104] observed that after reduction LaNiO<sub>3</sub> lost its perovskitic structure generating high dispersed Ni metallic particle on La supports [106-107]. Dispersion of Ni obtained by reducing a perovskite precursor was higher than the one obtained from NiO supported samples. The high resistance towards coking is due to the high dispersion of Ni derived by the reduction of the perovskite. Some advantages were achieved by partially substituting La with Ce or Sr. Ce generated an increase of the H<sub>2</sub> productivity and an improvement of the CO/CO<sub>2</sub> ratio, Nevertheless the resistance to coking decreased. Instead Sr doping improved the catalytic performance of the pure LaNiO<sub>3</sub> even increasing resistance to coke formation. As observed by XRD analysis (Figure 48, 49) insertion of Sr inside the

structure did not change the structure while the insertion of Ce reduced the amount of perovskite inside the sample. This reduction lead to a lower dispersion of Ni<sup>0</sup> and subsequently a lower C% out balance. It has to be noticed that the presence of mixed oxide in the structure of the catalyst is also the cause of the not complete conversion of ethanol in the tests at 500°C and of the strict correlation of the catalytic activity with the amount of Ni. Since part of the Ni remains in the perovskitic structure , even after activation, to acquire the right amount of metallic nickel over the surface it's necessary to increase the total amount of nickel in the sample

#### SiO<sub>2</sub>:

Silica proved an interesting support both if prepared in mesoporous form or as amorphous

dense nanoparticles by FP. One of its main advantages was the absence or low selectivity

to by-products, especially methane. This support, especially when calcined at high temperature, was characterised by low water conversion. The sample calcined at low temperature was very interesting, since characterised by the highest H<sub>2</sub> productivity. Furthermore, even if the carbon balance was still not constantly closing to 100%, this catalyst showed a peculiar self-cleaning behaviour consisting in periodical coke accumulation and gasification, which did not alter sensibly its catalytic performance.

The best results as for carbon balance, productivity and lower CO/CO<sub>2</sub> ratio were attained with the FP prepared 10%Ni/SiO<sub>2</sub> .By contrast, sample S1C500 gave much better results than S2C800, showing that a bit higher Ni reducibility may improve the low temperature activity of those samples. However, this may not be favourable in absolute, *e.g.* considering the overall sample stability. The best conversion and coke resistance showed by the catalysts made by impregnation is due also to the fact that as detect by FT-IR analysis, the acid sites are localized only over the support while in the FP made catalyst there are two different kinds of acid sites, localized on the support or on the active phase. So in S1C500 and S2C800 coke formation took place only over the support and the active sites for the hydrogen production were not affected.

#### ZrO<sub>2</sub>:



Zirconia also proved an interesting support, especially when tested at the highest temperatures, showing stable behaviour and good H<sub>2</sub> productivity without by-products. It should be noticed that when prepared by FP it showed poor conversion of ethanol, but very good C<sub>out</sub> % balance during the most critical testing at low temperature. However, it is interesting to notice that Z1C500 and Z2C800 samples at 500°C showed perfectly overlapping results, indicating that the calcination temperature did not affect the final catalyst performance. This result is supported by the very similar physical-chemical properties of these samples. 10wt%Ni/ZrO<sub>2</sub> is one of the two catalyst that showed a good activity at 400°C showing the best CO/CO<sub>2</sub> ratio if even improvements of catalyst formulation are needed, together with an optimisation of the reaction conditions (for example increasing the water/ethanol feeding ratio or modifying the contact time).

## Surface acidity

Support interaction with water and its acidity may play a role in the activation of the reactants and in catalyst resistance towards coking, strong acid sites being responsible of

ethanol dehydration and subsequent ethylene polymerisation [110]. Lewis acidity was predominant in the case of titania- and zirconia-supported samples, with medium strength acid sites. By contrast silanols characterised all the silica supported samples, except S2C800, and poor Lewis acidity was only due to Ni ions. In every case, the absence of strong acid sites prevented from severe deactivation of the catalyst. No preferred nature of acid sites (Lewis or Brønsted) may be invoked to explain coke formation, especially during testing at 500°C, when the phenomenon was more relevant. However, when Lewis acidity was limited and predominantly due to Ni ions (S1C500) a self cleaning action was also observed. Therefore, provided that strong surface acidity is ruled out, no tight relationship between acidity and coking may be drawn, as already well pointed out by Liguras *et al.* [111].

## General conclusions

According to pilot projects on stationary PEM fuel cell systems, characterised by 5 kW<sub>electric</sub> power size and efficiency variable from 0.35 to 0.41, H<sub>2</sub> consumption has been reported between 3.5 and 4.1 Nm<sup>3</sup>/h [111]. One of the main object of this project was to find out a catalysts that could work with a stationary fuel cell at 500°C. According to the highest productivity here reported at each temperature we may estimate that the production of 4 Nm<sup>3</sup>/h of H<sub>2</sub> requires ca. 2.2 kg of the S1C500 or 2.4 kg of LaNiO<sub>3</sub> catalyst operated at 500°C.

S1C500 may be a promising solution provided that the modulation of reaction conditions or an optimised catalyst formulation further improves the carbon balance.

LaNiO<sub>3</sub> seems more promising since it reached an higher Cout% balance and tested with higher water/ethanol ratio already showed an improvement of the catalytic activity with no decreasing of the coke resistance. The CO/CO<sub>2</sub> of the pure LaNiO<sub>3</sub> was higher than S1C500 but substitution with Sr of part of La seems to be a promising way to increase the activity of WGS even without changing the operating conditions. If the reaction temperature is increased to 625°C also both the samples Z2C800 and 10wt%Ni/SiO<sub>2</sub> may be selected, requiring ca. 2.0 kg of catalyst. There is no real advantage in operating at 750°C since H<sub>2</sub> productivity does not increase appreciably (a higher reforming activity is counterbalanced by an unfavourable thermodynamics of the WGS one) and therefore similar installation costs for the catalyst are required, while evident drawbacks are higher variable costs for reactor heating and for purification from CO.

## Appendix 1 :proceedings and publications

## Proceedings:

- 1) "From biomass to energy: hydrogen-based technology by bio-ethanol reforming", I. Rossetti, C. Biffi, G. Faita, G.F. Tantardini, M. Raimondi, L. Forni, International Workshop on Distributed Energy Systems, Università di Milano, 6 Aprile 2009.
- 2) "From biomass to energy: H<sub>2</sub> based technology from bioethanol" I. Rossetti, C. Biffi, G. Faita, M. Raimondi, G.F. Tantardini, L. Forni, 17th European Biomass Conference & Exhibition, Hamburg, Germany, 2009.p. 2194
- 3) "Electric and thermal energy co-generation from renewable primary sources" C. Biffi, I. Rossetti and L. Forni. In-GAP-NANOCAT-III summer school, Trondheim(NO) 21-26 June 2009
- 4) "Electric and thermal energy co-generation from renewable primary sources" C. Biffi, I. Rossetti and L. Forni. PCAM" Chemistry and Physics of Materials for Energetics" summer school, Università della Bicocca Milano (IT) 14-19 september 2009
- 5) "Integrated 5KWe + 5KWt PEM-FC generator from bioethanol : A demonstrative project" I. Rossetti , C. Biffi, L. Forni, G. F. Tantardini, G.Faita, M. Raimondi, ASME 2010 Eight International Fuel Cell Science, Engineering and Technology Conference FuelCell 2010 Brooklyn, New York, June 14-16, 2010
- 6) "Hydrogen production by steam reforming of bio-ethanol" C. Biffi, I. Rossetti, G.F. Tantardini, L. Forni, XVI National Congress of Catalysis, GIC 2010, Palermo (IT) 19 - 23 September 2010
- 7) "Hydrogen production by steam reforming of bio-ethanol" I. Rossetti, C. Biffi, G. F. Tantardini, L. Forni, Catalysis for Renewable Sources: fuel, energy, chemicals" Tsars Village, St. Pietroburgo Russia, 27 June-3 July 2010
- 8) "La<sub>2</sub>O<sub>3</sub> -supported catalyst for the steam reforming of bioethanol" C. Biffi, I. Rossetti, G. F. Tantardini, L. Forni, X Scuola GIC 2010, Palermo (IT), 15 - 18 Settembre 2010
- 9) "Ni based catalyst for Ethanol Steam Reforming (ESR)" C. Biffi, I. Rossetti, A. Goguet, XXIV Congresso Nazionale della Società Chimica Italiana , Lecce (IT), 11 - 16 Settembre 2011

## Publications:

- 1) "Prospettive della cogenerazione di energia da bioetanolo"  
C. Biffi, I. Rossetti, G.F. Tantardini, G. Faita, M. Raimondi, L. Forni, Rivista Italiana del Combustibili, La rivista dei combustibili e dell'industria chimica, 64 (2010) 44-45.

- 2) "Oxygen non stoichiometry in perovskitic catalysts for the flameless combustion of methane", I. Rossetti, C. Biffi, L.Forni, Chem. Eng. J. 162 (2010) 768
- 3) "La-Ag-Co perovskites for the catalytic flameless combustion of methane" O. Buchneva, I. Rossetti, C. Biffi, M. Allieta, A. Kryukov, N. Lebedeva, Appl. Catal. A: General 370 (2009) 24– 33
- 4) "Effect of sulphur poisoning on perovskite catalysts prepared by flame pyrolysis" I.Rossetti, O. Buchneva, C. Biffi and R. Rizza, Appl. Catal. B: Environmental (2009), 89 (3-4), 383-390
- 5) "H<sub>2</sub> production by steam reforming of bioethanol", C. Biffi and I. Rossetti Catalysis in Industry 6 (2011) 66
- 6) "5 kWe + 5 kWt PEM-FC Generator From bio-ethanol: first findings from a demonstrative project" I. Rossetti, C. Biffi, L. Forni, G. F. Tantardini, G. Faita, M.Raimondi, E.Vitto, D. Alberti, A. Salogni Applied Energy, submitted
- 7) "Ni-SiO<sub>2</sub> and Ni/ZrO<sub>2</sub> Catalysts for the steam reforming of bioethanol" I.Rossetti, C. Biffi, C. Bianchi, V. Nichele, M. Signoretto, E. Finocchio, G. Ramis G. Garbarino, A. Di Michele, In preparation

## Bibliography

- [1] V.A. Goltsov, T.N. Veziroglub, L.F. Goltsovaa, Int. J. Hydrogen Energy , 31 (2006) 153 – 159
- [2] Y. Guo, S.Z. Wang, D.H. Xu, Y.M. Gong, H.H. Ma, X.Y. Tang, Renew. Sust. Eergy

Rev., 14 (2010) 334–343

- [3] M. Ni, M. K.H. Leung, K. Sumathy, D.Y.C. Leung, *Int. J. Hydrogen Energy*, 31 (2006) 1401 – 1412
- [4] D.J.R Rostrup-Nielsen, *J.Catal.*, 33 (1974) 184
- [5] H Brejc, E. Supp In: *Ullmann's Encyclopedia of Industrial Chemistry*, B .Elvers, S .Hawkins, M. Ravenscroft, J. F. Rounsaville, G. Schulz, Vol. A12 (1989) 207
- [6] P. Corbo, F. Migliardini, *J. Natural Gas Chem.*, 18(2009)9–14
- [7] F. Rosillo-Calle, A. Walter *Energy for Sustainable Development*, Volume X No. 1 (2006) 7-19
- [8] S. Cavallaro, *Energy & Fuels*, 14 (2000) 1195-1199
- [9] M.C. Sánchez-Sánchez, R.M. Navarro, J.L.G. Fierro , *International Journal of Hydrogen Energy*, 32 (2007) 1462 – 1471
- [10] A. Haryanto, S. Fernando, N. Murali, S. Adhikari, *Energy & Fuels*, 19 (2005) 2098-2106
- [11] G.A. Deluga, J.R. Salge, L.D. Schmidt, X.E. Verykios, *Science*, 303 (2004) 993-997
- [12] A.N.Fatsikostas, X.E.Verykios, *J. Catal.*, 225 (2004) 439-452
- [13] J. Llorca, P.R. de la Piscina, J. Sales, N. Homs, *Direct Chem. Comm.*, (2001), 641-642.
- [14] J.C. Vargas, F. Sternenberg, A.C. Roger, A. Kiennemann, Presented in the Technical Program, Pisa, Italy, May 16-19, 2004.
- [15] F. Frusteri, S. Freni, V. Chiodo, G. Bonura, S. Donato, S.Cavallaro, Presented in the Technical Program, Pisa, Italy, May 16- 19, 2004.

- [16] J. Llorca, J.-A. Dalmon, P. R.de la Piscina, N.Homs, *Applied Catalysis A*, 243 (2) (2003) 261-269.
- [17] F. Haga, T. Nakajima, H. Miya, S. Mishima, *Catal. Lett.*, 48 (1997) 223-227.
- [18] J. Llorca , P. R.de la Piscina, J.-A. Dalmon , J. Sales, N. Homs, *Appl. Catal.*, B 43 (4) (2003) 355-369.
- [19] E. Vanhaecke, A.C. Roger, J.C. Vargas, A. Kiennemann, 1st European Hydrogen Energy Conference, Grenoble, France, September 2-5, 2003.
- [20] M.S. Batista, R.K. S. Santos, E.M.Assaf, J.M.Assaf, E. A.Ticianelli, *J. Power Sources*, 134 (1) (2004) 27-32.
- [21] A. Kaddouri, C. Mazzocchia, *Catal. Commun.*, 5 (6) (2004) 339-345.
- [22] F. Marino, M. Boveri, G. Baronetti, M. Laborde, *Int. J. Hydrogen Energy*, 29 (2004) 67-71.
- [23] A. Therdthianwong, T. Sakulkoakiet, S. Therdthianwong, *Science Asia*, 27 (2001) 193-198.
- [24] F. Marino, M. Boveri, G. Baronetti, M. Laborde *Int. J. Hydrogen Energy*, 26 (7) (2001) 665- 668.
- [25] F. Frusteri, S. Freni, V. Chiodo, L. Spadaro, G. Bonura, S. Cavallaro, *DGMK Tagungsbericht*, 2003; pp 163-170.
- [26] V. Fierro, V. Klouz, O. Akdim, C. Mirodatos, *Catal. Today*, 75 (1-4) (2002) 141-144.
- [27] V. Klouz, V. Fierro, P. Denton, H. Katz, J. P. Lisse, S. Bouvot-Mauduit, C. Mirodatos, *J. Power Sources*, 105 (1) (2005) 26-34.
- [28] H. Idriss, *Met. Rev.*, 48 (3) (2004) 105- 115.

- [29] S. Cavallaro, *Energy Fuels*, 14 (2000) 1195-1199.
- [30] M. Toth, M. Domok, J. Raskox, A. Hancz, A. Erdohelyi, Presented in the Technical Program, Pisa, Italy, May 16-19, 2004.
- [31] C. Diagne, H. Idriss, A. Kiennemann, *Catal. Commun.*, 3 (12) (2002) 565-571.
- [32] O. Khasalev, A. Bansal, S. Kocha, J.A. Turner, In DOE Hydrogen Program Review; United States Department of Energy (DOE): Washington, DC, 1999.
- [33] J.N. Armor, *Review Appl. Catal. A* , 176 (1999) 159-176.
- [34] P. Y. Sheng, H. J. Idriss, *Vac. Sci. Technol. A* , 22 (4) (2004) 1652-1658.
- [35] D. Srinivas, C. V. V. Satyanarayana, H. S. Potdar, P. Ratnasamy, *Appl. Catal. A*, 246 (2) (2003) 323-334.
- [36] N.R.C. F. Machado, R.C.P. Rizzo, P.P.S. Peguin, *Acta Sci.*, 26 (6) (2002) 1637-1642.
- [37] D. Morton, J. C. David, *Chem. Commun.*, 4 (1987) 248-249.
- [38] D. Morton, D.J. Cole-Hamilton, I.D. Utuk, M. Paneque-Sosa, L. Manuel, J. Chem. Soc., *Dalton Trans.*, 3 (1989) 489-495.
- [39] V.V. Galvita, V.D. Belyaev, V. A. Semikolenov, P. Tsiakaras, A. Frumin, V. A. Sobyenin, *React. Kinet. Catal. Lett.*, 76 (2) (2002) 343-351.
- [40] J. Comas, F. Marino, M. Laborde, N. Amadeo, *Chem. Eng. J.*, 98 (1- 2) (2004) 61-68.
- [41] A. N. Fatsikostas, D.I. Kondarides, X.E. Verykios, *Catal. Today*, 75 (1-4) (2002) 145-155.

- [42] D.K. Liguras, K. Goundani, X.E. Verykios, *J. Power Sources*, 130 (2004) 30–37
- [43] D.K. Liguras, K. Goundani, X. E. Verykios, *Int. J. of Hydrogen Energy* 29 (2004) 419 – 427
- [44] A. Casanovas, C. de Leitenburg, A. Trovarelli, J. Llorca *Catal. Today*, 138 (2008) 187–192.
- [45] M. Domínguez, E. Taboada, E. Molins, J. Llorca, *Catal. Today*, 138 (2008) 193–197.
- [46] G.L. Chiarello, I. Rossetti, L. Forni, P. Lopinto, G. Migliavacca *App. Catal. B: Environmental*, 72 (2007) 227–232
- [47] G.L. Chiarello, I. Rossetti, L. Forni, P. Lopinto, G. Migliavacca, *App. Catal. B: Environmental* 72 (2007) 218–226
- [48] G.L. Chiarello, I. Rossetti, P. Lopinto, G. Migliavacca, L Forni, *Catal. Today*, 117 (2006) 549–553
- [49] G.L. Chiarello, I. Rossetti, L. Forni *J. Catal* 236 (2005) 251–261
- [50] L. Fabbrini , A. Kryukov, S. Cappelli, G.L. Chiarello, I. Rossetti, C. Oliva, L. Forni *J. Catal.* 232 (2005) 247–256
- [51] I. Rossetti, C. Biffi, L. Forni *Chem. Eng.*, 162 (2010) 768–775
- [52] O. Buchneva, I. Rossetti, C. Biffi, M. Allieta, A. Kryukov, N. Lebedeva, *App. Catal. A: General*, 370 (2009) 24–33
- [53] I. Rossetti, O. Buchneva, C. Biffi, R. Rizza, *App. Catal. B: Environmental*, 89 (2009) 383–390



- [54] JCPDS Database <http://www.icdd.com/>
- [55] K.Hadjiivanov, M.Mihaylov, N. Abadjieva, D.Klissurski., J. Chem. Soc., Farady Trans., 94 (1998) 3711.
- [56] J. Juan-Juan, M.C. Román-Martínez, M.J.Illán-Gómez., Appl. Catal. A: General, 355 (2009) 27.
- [57] Y.Q. Song, D.H. He , B.Q. Xu, Appl. Catal. A: General, 337 (2008) 19
- [58] V. García, J.J. Fernández, W. Ruíz, F. Mondragón, A. Moreno, Catal. Commun., 11 (2009) 240.
- [59] Q.G. Yan, W.Z. Weng, H.L. Wan, H. Toghiani, R.K. Toghiani, C.U. Pittman, Jr., Appl.Catal. A: General, 239 (2003) 43.
- [60] S. Zhang, J. Wang, X. Wang, J. Natur. Gas Chem., 17 (2008) 179.
- [61] M.J. Lazaro, Y. Echevoyen, C. Alegre, I. Suelvea, R. Moliner, J.M. Palacios, Int. J.Hydrogen Energy, 33 (2008) 3320.
- [62] B. Jongsomjit, T. Wongsalee, P. Praserthdam, Catal. Commun., 6 (2005) 705–710.
- [63] S. Guerrero, I. Guzmán, G. Aguila, P. Araya, *Catal. Commun.*, **11** (2009) 38–42.
- [64] M. Lindo, A.J. Vizcaino, J.A. Calles, A. Carrero, Int. J. Hydrogen Energy, 35 (2010) 5895.
- [65] S. He, Q. Jing, W. Yu, L. Mo, H. Lou, X. Zheng, Catal. Today, 148 (2009) 130.
- [66] S. Sun, N. Tsubaki, K. Fujimoto, Appl. Catal. A: General, 202 (2000) 121–131.
- [67] F. Boubekr, A. Davidson, S. Casale, P. Massiani, Micropor. Mesopor. Mater. (2010)

- [68] S.S. Reddy, B.D. Raju, A.H. Padmasri, P.K.S. Prakash, K.S.R. Rao, *Catal. Today* 141(2009) 61–65.
- [69] E. M. Fixman, M. C. Abello, O. F. Gorriz, L. A. Arrua, *Appl. Catal. A: General*, 319 (2007)111–118.
- [70] Y.Q. Song, D.H. He , B.Q. Xu, *Appl. Catal. A: General*, 337 (2008) 19.
- [71] V. García, J.J. Fernández, W. Ruíz, F. Mondragón, A. Moreno, *Catal. Commun.*, 11(2009) 240
- [72] K. I. Hadjivanov, G. N. Vayssilov., *Adv. Catal.*, 47 (2002) 307.
- [74] L. Kubelková, J. Nováková, N. I. Jaeger, G. Schulz-Ekloff, *Appl. Catal. A: General*, 95 (1993) 87.
- [75] S. Derrouiche, D. Bianchi, *Appl. Catal. A: General*, 313 (2006) 208.
- [76] V. Sanchez Escribano, M.A. Larrubia Vargas, E. Finocchio, G. Busca, *Appl. Catal. A:General*, 316 (2007) 68-74.
- [77] M.A. Vannice, in *Catalysis, Science and Technology*, J.R. Andeson, M. Boudart, Eds.,Vol. 3, 1982, Springer Verlag, p.139.
- [78] C. Resini, T. Venkov, K. Hadjiivanov, S. Presto, P. Riani, R. Marazza, G. Ramis, G.Busca, *Appl. Catal. A: General*, 353 (2009) 137.
- [79] M. Garcia Dieguez, E. Finocchio, M.Á. Larrubia, L.J. Alemany, G. Busca, *J. Catal.*,274 (2010) 11.
- [80] G. Busca, C. Resini, *Encyclopedia of Analytical Chemistry*, R.A. Meyers (Ed.), Wiley and Sons Ltd., Chichester, 2000, pp.10984.
- [81] M.I. Baraton, G. Busca, M.C. Prieto, G. Ricchiardi, V. Sanchez Escribano, J.

Solid State Chem, 112 (1994) 9.

- [82] M. Mihaylov, K. Charakova, K. Hadjiivanov, *J. Catal.*, 228 (2004) 273.
- [83] K. Coulter, X. Xu, D.W. Goodman, *J. Phys. Chem.*, 98 (1994) 1245
- [84] G. Busca, R. Guidetti and V. Lorenzelli, *J. Chem. Soc., Faraday Trans.*, 86 (1990), 989-994
- [85] E. Finocchio, T. Montanari, C. Resini, G. Busca, *J. Mol. Cat. A: Chemical* 204–205 (2003) 535–544
- [86] C-W. Tang, C-B. Wang, S-H. Chien, *Thermochimica Acta* 473 (2008) 68–73
- [87] S. Esposito, M. Turco, G. Ramis, G. Bagnasco, P. Pernice, C. Pagliuca, M. Bevilacqua, A. Aronne *Journal of Solid State Chemistry*, 180 (2007) 3341-3350.
- [88] L.F. Liotta, G. Pantaleo, A. Macaluso, G. Di Carlo, G. Deganello *Applied Catalysis A: General* 245 (2003) 167–177.
- [89] M. Zayat, D. Levy, *Chem. Mater.* 12 (2000) 2763.
- [90] M. Kato, T. Ikeda, T. Kodaira, S. Takahashi, *Microporous and Mesoporous Materials* 142 (2011) 444–453
- [91] K. Hadjiivanov, G. Vayssilov, *Adv. Catal.* 47 (2002) 307-511
- [92] L.E.S. Rygh, O.H. Ellestad, P. Klæboe and C.J. Nielsen, *Phys. Chem. Chem. Phys.* 2
- [93] J.A. Gadsden, *Infrared Spectra of Minerals and Related Inorganic Compounds*, Butterworths eds., Reading Mass., USA, 1975
- [94] F. Boccuzzi, S. Coluccia, G. Martra, N. Ravasio, *J. Catal.* 184 (1999) 316-326

- [95] A.N. Pestryakov, V.P. Petranovskii, A. Kryazhov, O. Ozhereliev, N. Pfeander, A. Knop-Gericke *Chemical Physics Letters* 385 (2004) 173–176.
- [96] G. Busca, *J. Mol. Catal.* 43 (1987) 225–236
- [97] A. Dandekar and M. A. Vannice, *J. Catal.*, 178, 621–639 (1998).
- [98] A. Gervasini, M. Manzoli, G. Martra, A. Ponti, N. Ravasio, L. Sordelli, F. Zaccheria, *J. Phys. Chem. B*, 110, 7851–7861 (2006)
- [99] K. Hadjiivanov, T. Tsoncheva, M. Dimitrov, C. Minchev, H. Knözinger, *Appl. Catal. A: General* 241 (2003) 331–340
- [100] V. Sanchez-Escribano, L. Arrighi, P. Riani, R. Marazza, G. Busca, *Langmuir*, 22 (2006) 9214–9229
- [101] Tz. Venkov, K. Hadjiivanov *Catalysis Communications* 4 (2003) 209–213
- [102] T. Tsoncheva, Tz. Venkov, M. Dimitrov, C. Minchev, K. Hadjiivanov, *J. Mol. Catal. A: Chemical* 209 (2004) 125–134
- [103] S. Derrouiche, D. Bianchi, *Appl. Catal. A: General*, 313 (2006) 208
- [104] S. M. de Lima, A. M. da Silva, L. O. O. da Costa, J. M. Assaf, Gary Jacobs, B. H. Davis, L. V. Mattos, F. B. Noronha; *Applied Catalysis A: General* 377 (2010) 181–190
- [105] G. Valderrama, M.R. Goldwasser, C.U. de Navarro, J.M. Tatiboué, J. Barrault, C. Batiot-Dupeyrat, et al. *Catal. Today*. 107 (2005) 785–791. [104] T. Aicher, J. Full, A. Schaadt, *Int. J. Hydrogen Energy*, 34 (2009) 8006.
- [106] S.Q. Chen, Y. Liu, *Int. J. Hydrogen Energy*, 34 (2009) 4735

- [107] F. Frusteri, S. Freni, V. Chiodo, L. Spadaro, G. Bonura, S. Cavallaro, J. Power Sources, 132 (2004) 139
- [108] S.M. Lima, J.M. Assaf, M.A. Pen˜ a, J.L.G. Fierro, Appl. Catal. A. 311 (2006) 94–104.
- [109] A.C. Furtado, C.G. Alonso, M. Pereira Cant˜ ao, N.R.C. Fernandes-Machado, Int. J. Hydrogen Energ., 34 (2009) 7189
- [110] D. Liguras, D. Kondarides, X. Verykios, Appl. Catal. B: Environmental, 43 (2003) 345.
- [111] C. Resini, T. Venkov, K. Hadjiivanov, S. Presto, P. Riani, R. Marazza, G. Ramis, G. Busca, Appl. Catal. A: General, 353 (2009) 137